Year : 2023

Glacier meltwater–groundwater connectivity in alpine proglacial areas : the case of the Otemma glacier

Müller Tom

Müller Tom, 2023, Glacier meltwater–groundwater connectivity in alpine proglacial areas : the case of the Otemma glacier

Originally published at : Thesis, University of Lausanne

Posted at the University of Lausanne Open Archive http://serval.unil.ch
Document URN : urn:nbn:ch:serval-BIB_0D86F40FF2ED1

UNIL | Université de Lausanne

FACULTÉ DES GEOSCIENCES ET DE L'ENVIRONNEMENT

Institut des dynamiques de la surface terrestre (IDYST)

Glacier meltwater–groundwater connectivity in alpine proglacial areas : the case of the Otemma glacier

THÈSE DE DOCTORAT

présentée à la

Faculté des Géosciences et de l'Environnement
de l'Université de Lausanne

pour l'obtention du grade de

Docteur en Sciences de l'environnement

par

Tom Müller

Directeur de thèse
Prof. Dr. Bettina Schaefli

Co-directeur de thèse
Prof. Dr. Stuart N. Lane

Jury

Président du jury :	Prof. Dr. Gregoire Mariethoz (UNIL)
Expert interne :	Prof. Dr. Torsten Vennemann (UNIL)
Expert externe :	Prof. Dr. Peter Molnar (ETH Zurich)
Expert externe :	Prof. Dr. Masaki Hayashi (University of Calgary)

Lausanne, 26 mai 2023

UNIL | Université de Lausanne
Faculté des géosciences et de l'environnement
bâtiment Géopolis bureau 4631

IMPRIMATUR

Vu le rapport présenté par le jury d'examen, composé de

Président de la séance publique :	M. le Professeur Grégoire Mariéthoz
Président du colloque :	M. le Professeur Grégoire Mariéthoz
Directrice de thèse :	Mme la Professeure Bettina Schaefli
Co-directeur de thèse :	M. le Professeur Stuart Lane
Expert interne :	M. le Professeur Torsten Vennemann
Expert externe :	M. le Professeur Peter Molnar
Expert externe :	M. le Professeur Masaki Hayashi

Le Doyen de la Faculté des géosciences et de l'environnement autorise l'impression de la thèse de

Monsieur Tom MÜLLER

Titulaire d'un
Master en Sciences et Ingénierie de l'Environnement
de l'Ecole Polytechnique Fédérale de Lausanne (EPFL), SUISSE

intitulée

GLACIER MELTWATER–GROUNDWATER CONNECTIVITY IN ALPINE PROGLACIAL AREAS: THE CASE OF THE OTEMMA GLACIER

Lausanne, le 26 mai 2023

Pour le Doyen de la Faculté des géosciences et de l'environnement

Professeur Grégoire Mariéthoz

Summary

High-Alpine water resources are subject to rapid changes in the context of climate change. There, rapid glacier melt, combined with reduced snow accumulation and earlier snowmelt, will lead to a modification of the flow regime with a shift of the peak discharge to earlier months and reduced flow in summer. The extent of such changes has been thoroughly studied for large basins, as water resource availability is of key importance to maintain favorable ecological conditions (residual flow requirements) and for human purposes so as hydropower production, drinking water or irrigation. At a more local scale however, and specifically in the case of small alpine glaciated catchments, changes in water supply are accompanied by strong geomorphological processes. In particular, the production and release of glacial sediments and their paraglacial reworking lead to the formation of a range of proglacial landforms in which water, from different sources, may infiltrate. While recent studies have recognized its role to sustain water availability, the groundwater dynamics in such environments is still heavily understudied. It remains particularly challenging to assess how such systems may react to climate change since limited process understanding of the hydrogeological functioning of such catchments has been provided.

In this study, based on a case Study in the Swiss Alps, the Otemma glacier, I developed an integrated analysis framework based on a wide range of field data and modelling to obtain detailed insights into (i) the hydrological response at the catchment-scale; (ii) a detailed perceptual model of the assemblage of different hydrogeological units with an assessment of the timescales at which they provide baseflow; (iii) a focused study on a key understudied landform, (iv) an estimation of the seasonal water contributions from rain, snow- and icemelt and (v) a perceptual model of groundwater connectivity between landforms.

We show that the functioning of recently deglaciated proglacial areas is governed by multiple hydrogeological structures, which release water at different timescales and seasons. Steep superficial landforms mostly transmit rain and meltwater especially during the early melt season and have a rapid discharge recession of the order of days. As water converges towards the bottom of the valley, we observe a diversity of water sources, either generated by rapid surface flow, slow bedrock leakages or rapid subsurface flow in the coarse hillslope deposits. Flatter deposits, such as the outwash plain, appear to have a larger potential to release groundwater at seasonal timescales (weeks to months). However, based on a more complex modelling framework, we estimated a rather limited mobile storage, leading to limited baseflow. They may however have a more significant ecological value. Finally, we identified that, with about 75 mm of storage in summer, the largest groundwater aquifer at an annual scale is located in bedrock fractures. Results show that baseflow in winter is mostly dominated by the connection of such a bedrock aquifer to a subglacial sediment system which slowly releases water in winter and maintains a residual baseflow of the order of 0.5 mm d^{-1}.

In the context of rapid glacier retreat, we expect the formation of more superficial deposits and flat outwash plains. Here, the formation of potential future outwash plains are not expected to provide a significant additional baseflow. Overall, at the seasonal scale, an extension of superficial deposits will not greatly modify the active groundwater storage at the catchment-scale, so that drier conditions are expected, especially in late summer, due to earlier snowmelt and reduced surface available for icemelt. In that perspective, while catchment-scale bedrock storage should not significantly change and bedrock exfiltration will maintain a limited baseflow seasonally, the mechanisms of bedrock recharge and drainage remain more uncertain. In particular, the effect on recharge of the interplay between more liquid precipitation and earlier and more ephemeral snow and early soil development are still poorly understood. Moreover, the gradual disconnection of the bedrock aquifer system from the subglacial system due to glacier recession may also prove to increase drainage rates and thus lead to faster baseflow recession in winter.

As a conclusion, we showed that multiple landforms store and transmit water at varying timescales from days in the hillslopes, to weeks in flatter glacial deposits and to months in the bedrock. Each of these processes may be of interests for future research and we have here provided a detailed framework to understand and to assess these landforms in other alpine catchments.

Acknowledgements

During this research, I had the chance to be able to rely on my supervisors, colleagues, students and a large number of friends who have always been supportive and inspired me in many ways.

First I would like to sincerely thank my both main supervisors Bettina and Stuart, who gave me a lot of freedom during these last four years, trusting my decisions and helping me to direct this research. I felt very responsible to orientate this research based on my interests and ideas, and they were always available to give a rapid feedback when I was usually late with deadlines. I enjoyed having both of their specific expertise which pushed me to adapt and learn from different fields where I was less proficient. Discussions were always inspiring and greatly contributed to improve the quality of my ideas and the content of my research. From a personal perspective, I always found that my personal life was always respected, they always put my private interests first and did not push me during some more difficult periods.

Secondly I will thank my friends at the farm, Mélodi, Ivanna, Clément, Timothée, Baptiste, Ivo with whom I went through these crazy four years. While we all invested a lot of energy to live together, I think the balance between this work and the farm made these years really special. You also always respected the moments when I was absent or when I needed more focus, but you also helped me to often change my mind. I learnt a lot with you in all regards in these last years and I am very thankful for that.

I would like to thank Mauro Fischer who embarked with a lot of motivation in this project. He helped me launch all glacier related field measurements which was of great use for this study. He was also very available to discuss ideas on glaciological topics which also helped me to deepen my understandings in this field.

I thank Emily Voytek who conducted the first geophysical surveys in Otemma, experimented different methods and taught me how to conduct such investigations in the following years.

The extensive field work was only possible thanks to the great effort of our field camp manager, Boris Ouvry and Floreana Miesen who organized everything very efficiently which helped me to focus on my specific field equipment and not to care about helicopter transport or the recipe of the evening menu ! We also had a lot of good memories, with Boris and Mélanie watching movies under the tent during really bad weather and Floreana when we discovered the field camp buried in the snow for example !

Then, I thank my PhD colleagues who also worked in Otemma, Pascal, Mattéo, Davide, Matt, Jamal with whom we shared many ideas, labor time in the field, data and good moments under the tent in the evening, cheers ! There are too many memories to say more.

Data collection would not have been possible by legions of bachelor and master students ! I would like to thank in particular Anna Tassaux and her supervisor Stephanie Grand for her help in collecting and analyzing geochemical samples and for her expertise in weathering processes. Vera Girod for conducting the ablation measurements. Isabel Herr for her drone work on the glacier. Léa Rodari, Valentin Tanniger (Skull King!) and Luca Eiholzer for their help with sampling, performing ERT under the rain and trying to make the field mass spectrometer work. Giulia Murgia, Loic Perez and Clément Gaspoz for covering most of the ERT transects during the first year. Bastien, Johanna and Tibor for some good moments too ! Many others participated, Ella, Alissa, Lara, Gwendoline, Margaux, Frédéric, Pierre, Adrijan, Mattia, Lila, Linnea and likely others I have forgotten.

A special thank to our field and laboratory technicians, Laetitia Monbaron, Micaela Faria and Aurélien Ballu for their valuable help in analyzing samples, organizing or developing field equipment.

I thank Prof. Torsten Vennemann for the water isotopes analysis and some interesting discussions.

I thank Prof. James Irving and Prof. Christophe Lambiel for lending the ERT equipment.

I also would like to thank Marianne Milano for whom I supervised the exercises of the bachelor hydrology

course. Teaching was a very motivating activity which I enjoyed to do with her a lot.

Finally the PhD experience would not be the same without precious PhD and postdoc friends: my office mates in Lausanne, Anthony Michelon, Marie-No and Clémence (I just can't separate you), Harsh Beria, Moctar Dembélé, Wolfgang Wicker, Pauline Rivoire and in Bern, Natalie Ceperley, Tobias Wechsler, Malve Heinz. Then all my other PhD friends, the older (donkey) crew : Pascal, Gabriel, Nath, Zoneibe, Gilles, Seba, Laurent, John, Ben, Femi. And the newer ones: Pau, Javier, Mars, Janbert, Bryce, Joanne, Pierre-Louis, Nora, Lila, Isabel, Davide, Jamal, Mathilde, Matt, Naz, Tibor... and the ones I apparently cannot recall here.

Of course I would like to thank my parents, Pascale and Philippe, my sister, Line, her husband, Yann and the kids, Zia and Mano. You always supported my choices and, although I was always busy somewhere, it was every time nice to spend family moments with lots of love... and wine !

I would like to give a special thought for Maéva who accompanied me during the major part of these four years. It was not always easy to deal with me putting lots of efforts and mental energy in this work rather than in other things. I went through these years also a lot thanks to you, thanks to our discussions and will always cherish all the good and bad moments we spent together.

I also thank Selma who helped me go through the last months of this work without much pressure. Your presence helped me a lot to change my mind and remain positive and motivated until the end !

Finally, a big thanks to all my old friends, who accompanied me for many years and contributed to who I am and thus to this work immensely: Léon, Maryke, Géo, Justine, Laura, Arémis, Jon, Pablo, Amapola, Camille, Amaya, Sarah.

To my two cyclofriends, Guillaume and Victor. bééèh !

And to Clément, Mélo, Stefi, Robin, Kaboul, Paul who also inspired me in many ways, as well as all of my friends from EPFL and beyond !

Financial support

This research has been supported by the Schweizerischer Nationalfonds zur Förderung der Wissenschaftlichen Forschung (grant no. 200021_182065).

List of Figures

List of Tables

Abbreviation

- **DEM** : Digital Elevation Model
- **ELA** : Equilibrium line altitude
- **EC** : Water electrical conductivity
- **LIA** : Little ice age
- **m asl** : meters above see level
- **PCA** : Principal component analysis
- **ROS** : Rain on snow
- **SWE** : Snow water equivalent

Contents

Figure 1: Picture of the field basecamp during a stormy afternoon. The Otemma glacier can be seen at the back.

1 Introduction

1.1 Alpine water availability in a context of climate change

In a context of rapid climate change, water resources availability in terms of amounts and seasonality is a major contemporary challenge from perspectives for the society, as well as ecosystem and biodiversity preservation. In the specific context of Switzerland, recent studies (Brunner et al., 2019) have shown that water scarcity is becoming critical in the Plateau region, especially during summer, mainly due to reduced annual precipitation and a high water demand for irrigation. Water extraction is increasingly limited by the need to maintain favorable ecological conditions (residual flow requirements) as prescribed by Swiss legislation (WPA, 2022). In Alpine regions, water scarcity is more critical in late fall (after the melt season) or during the winter and early spring when ice and snowmelt are low. Here, potential water scarcity can in particular come into play in connection to hydropower production, whose storage infrastructure in high Alpine regions is designed to shift water from the high streamflow season (summer) to the high electricity demand season (winter).

Due to the general increasing trend of precipitation with elevation and due to the storage and redistribution of snow- and ice-melt during dryer summer months, the European Alps are often described as the water tower of Europe (Viviroli et al., 2007): They have the potential to provide water to downstream areas during droughts (Huss, 2011; Van Tiel et al., 2021).

Accordingly, significant changes in water quantities and seasonality due to future changes in the distribution of rain, snow and ice melt can be expected. First, a shift from snow-dominated to rainfall dominated conditions will occur. With warmer air temperatures, solid precipitation will shift to higher elevations and the seasonal snowpack duration will decrease in general. At lower elevations, winter snow accumulation will be reduced and melt increased such that snowpacks are thinner and more ephemeral (Klein et al., 2016). In all regions, earlier snowmelt and a longer snow free season will lead to a shift of stream regimes, with more discharge during winter and spring, an earlier monthly peak discharge in late spring or summer and a decreasing summer flow, especially towards the late season (Beniston et al., 2018; Hanus et al., 2021). Additionally, there may be general reduction of the mean annual streamflow due to a shift from snow to rain dominated regimes (Berghuijs et al., 2014).

While projected warming trends are relatively well constrained by future climate scenarios, precipitation changes show more natural variability in space and time, so that down-scaling of climate models leads to more uncertainty in precipitation projections (Fatichi et al., 2014). Nonetheless, regional climate models in Europe point towards an increase of precipitation in February to April and a decrease in August (Brunner et al., 2019; Fatichi et al., 2014).

Glaciers are also rapidly retreating worldwide. Ice volume loss between 2017 and 2100 is estimated to amount to 63±15 % and 94±8 % in the European Alps for the lowest and highest emission climate change scenarios (RCP2.6, RCP8.5) (Zekollari et al., 2019). Peak annual runoff from glacier melt will be reached between 2010 and 2060 across the world (Huss and Hock, 2018). Thanks to recent advances in satellite and airborne remote-sensing, combined with new modelling approaches, the characterization of ice extent (Pfeffer et al., 2014), thickness (Frey et al., 2014; Grab et al., 2021) and glacier volume (Farinotti et al., 2019a) has been significantly improved, allowing more accurate predictions of future ice melt. Whilst peak discharge estimates are well constrained by glacio-hydrological models fed with scenarios from general circulation and regional climate models, processes linked to ice flow and their degree of supraglacial debris accumula-

tion remain much less well understood. Indeed, several studies have shown the increasing importance of the isolating effect of debris, limiting the recession of their length and volume (Ferguson and Vieli, 2021; Jouvet et al., 2011). Related uncertainties may have important implications as heavily debris-covered glaciers or rock glaciers, may supply a steady, limited baseflow by conserving more ice or by providing large sediment storage (Wagner et al., 2021), which may prove essential for local ecological communities (Brighenti et al., 2019a) or for hydropower.

1.2 A more global perspective on alpine resources

Beyond the specific context of the European Alps and Switzerland, many local populations rely heavily on alpine water resources, with about a sixth of the world population living in snow-dominated regions with limited reservoir storage capacity (Barnett et al., 2005). On a global scale, water towers in the southern tropical Andes and western Asia are the most vulnerable due to large glacier reserve and a strong dependence of local communities on these glacier water resources (Immerzeel et al., 2020). The monthly changes in glacier melt compared to the basin-scale runoff are also expected to be the largest in those regions, with a reduction between 20 to 40 % by the end of the century under a medium emission scenario (RCP4.5) (Huss and Hock, 2018). Peak glacier runoff depends largely on the considered regions and on future climate scenarios. In general, smaller glaciers in Europe, South America and Canada have already passed peak water or will reach it in the coming decade. Larger glaciers at high elevation in Asia will reach peak water between 2050 and 2070 (Nie et al., 2021) and by the end of the century for high latitude glaciers in Northern Canada and Alaska (Huss and Hock, 2018). In some areas, the degree of debris cover may limit glacier retreat. For example, the Karakoram mountain range, which stores the largest volume of Asia, is expected to retain between 45 % (RCP8.5) and 80 % (RCP2.6) of its mass by 2100 due to their heavy debris-covered tongues (Kraaijenbrink et al., 2017).

In combination with glacier melt changes, regions where a dry period occurs during current peak melt are mostly vulnerable to future changes. The southern tropical Andes experience a semi-arid climate with very limited precipitation from April to September (Vuille et al., 2018). There, glacier melt contribution to streamflow is currently high only in the vicinity of large glaciers, where an estimated small upland rural population of 0.75 million depend on meltwater for small-scale agriculture and domestic use (Buytaert et al., 2017). A few large cities rely more heavily on glacier melt, such as La Paz (Bolivia), where water supply from glaciers was estimated to be 15 % annually, but could be as high as 85 % of the monthly flow during a drought (Buytaert et al., 2017). With the addition of potential economical conflicts related to water allocation for larger hydropower projects, it appears therefore, that in the tropical Andes, mostly rural, poor, local communities at high elevations will be mostly impacted by future glacier recession.

Regions where lowland populations heavily depend on mountain water for irrigation are also expected to be strongly impacted by changes in snow melt seasonality and reduced ice melt (Viviroli et al., 2020). In fact, it was shown that the projected changes in water consumption due to fast population increase is the main driver that pushes the largest number of people towards an insufficient dependency on mountain waters, especially in African and Asian basins (Viviroli et al., 2020). The Indus, Ganges and Brahmaputra regions show the currently largest rural population relying on mountain resources (Viviroli et al., 2020). In the eastern Himalayas, the summer monsoon leads to abundant precipitation during the ablation season, resulting in limited seasonal contribution from glacier melt. In the upper western Himalaya and the Indus basin, characterized by a more arid climate and more winter precipitation, mountain snow and ice melt represents about 60 % of the annual discharge, with an estimated 129 million farmers relying on meltwater for rice, cotton and sugar cane production (Biemans et al., 2019). By the end of 21st century, water availability is expected to increase in the Indus basin, due to a projected increase in summer monsoon precipitation and in ice melt. Nevertheless, the water demand is projected to increase due to socio-economic development so that unsustainable groundwater extraction is expected to increase by 7 and 14 % in the Indus and Ganges river basin under RCP8.5 (Wijngaard et al., 2018).

1.3 Groundwater, the missing component

From the different mountain regions discussed above, glaciers and to some extent snow act as a major natural reservoir storing water during the cold season and redistributing it during warmer, potentially dry periods.

Recent studies started to discuss the role of groundwater storage in mitigating to some extent the impact of seasonal low-flows by providing a natural, underground water storage. However, direct observations of groundwater storage are challenging especially in remote mountainous regions, and accordingly,that most studies rely on indirect methods to quantify related potential storage. At the regional-scale, based on discharge recession analysis, Andermann et al. (2012) estimated that groundwater storage in Nepal could account for 10 % of annual streamflow, with a response time of 45 days, which they attribute to fractured bedrock. Another modeling study in the northern Himalayas estimated an annual groundwater contribution of 27 % (Yao et al., 2021). In Switzerland, Staudinger et al. (2017) showed a linear increase in catchment-scale dynamic storage with elevation, suggesting a large potential storage in mountainous regions, without a clear allocation of this storage to a hydrogeological unit. In glaciated catchments, the interactions between ice melt and groundwater are only recently being discussed. Indeed, studies showed that large areas of previously ice-covered till and bedrock are becoming exposed in proglacial areas, leading to frequent geomorphological changes (Heckmann and Morche, 2019) and to the emergence of landforms prone to groundwater storage (Hayashi, 2020).

In this context, the processes of groundwater recharge, storage and release appear as key components to provide a better understanding of future low-flow conditions at all spatial-scales. In high headwater catchments, groundwater may buffer droughts and maintain surface water availability essential to local ecosystems (Milner et al., 2017). At regional-scale, groundwater exfiltration may lead to higher baseflow and downstream groundwater recharge during drought periods, an essential source of water for the various water uses discussed here. (Vuille et al., 2018). It appears nonetheless that the processes of recharge as well as the dominant hydrogeological units responsible for groundwater storage remain largely unknown, so that most large-scale glacio-hydrological studies tend to neglect this component in Alpine environments.

Reasons that might explain a certain disconnection of glacio-hydrological research in mountain environments from groundwater research include i) the assumed dominance of water storage above ground (in the form of snow and ice); ii) the current absence of groundwater-sustained summer low-flows in such environments, which typically show a summer high flow; iii) the wide-spread use of conceptual hydrological models with highly simplified representations of groundwater (e.g. Huss et al., 2008; Schaefli et al., 2014) and iv) the historical representation of glaciers overlying impervious bedrock.

1.4 The ecological importance of groundwater

It is clear today that glacier-influenced streamflow will decrease in the future, especially due to declining icemelt contributions. To mitigate the seasonal shift in peak discharge and summer low flows, the construction of reservoirs in newly formed proglacial areas was proposed (Farinotti et al., 2016). Such areas have a world-wide large storage and hydropower potential (Farinotti et al., 2019b), with an estimated 39 % having an acceptable economic, environmental and technical suitability. The construction of such new reservoirs should however consider a series of ecological aspects. First, future new proglacial areas are expected to be composed of bare rock walls and coarse sediments with unvegetated soils with little ecological interest, leading to some studies claiming for a limited environmental value (Farinotti et al., 2016, 2019b). Such an assessment seems not to take into account future elevational shifts of ecological niches (You et al., 2018) and future ecological succession in such zones (Miller and Lane, 2018; Roncoroni et al., 2019). It is indeed likely that future proglacial areas with sufficient sediment deposition will lead to the creation of large floodplains instead of lakes, offering a large diversity of unique habitats (Hauer et al., 2016) once glacier disturbance has decreased by the end of the century. While the impact of climate change and retreating ice may have a strong impact on water availability, and promote the idea of increasingly dry alpine environments, groundwater storage in superficial glacial deposits may, on the other hand, store and release water on seasonal timescales and therefore promote more favorable habitats.

Understanding the contribution of groundwater to baseflow is therefore of crucial importance for the ecology of high Alpine environments (Heckmann et al., 2016; Levy et al., 2015). Where glacier melt is near its peak, kryal (glacier-fed) habitats face very poor food availability and harsh environmental conditions, limiting species richness and promoting cold-based specialists (Brighenti et al., 2019b). However, krenal (groundwater-fed) habitats may be present in the vicinity of the braided river network, usually on terraces or close to debris fans, where disturbance is reduced and where groundwater provides nutrients, water and higher temperatures (Crossman et al., 2011; Ward et al., 1999). Krenal habitats may also appear temporarily in spring and autumn in areas dominated by kryal water sources during summer; in ecosystem terms, these periods are known as "windows of opportunity" when habitat is temporarily suitable for life (Brighenti et al., 2019b; Uehlinger et al., 2010).

Due to the complexity and heterogeneity of krenal habitats, certain zones within proglacial floodplains can become hotspots of aquatic biodiversity, and these appear to be strongly related to both water availability and disturbances (Miller and Lane, 2018; Windsor et al., 2017). In particular, groundwater may play a major role in enhancing microbial activity and the development of microbes and biofilms, which have an essential role for the onset of vegetation succession (Miller and Lane, 2018). Indeed, by stabilizing sediments, transforming organic material, fixing nitrogen and promoting biochemical weathering of rocks, they can provide nutrients for primary producers and foster soil development. They furthermore may enhance a strong biogeomorphologic effect, thus leading to a strong feedback into the morphology and the water cycle of such environments (Roncoroni et al., 2019).

Once glaciers retreat sufficiently, the reduced contribution of glacier melt to streams is expected to decrease disturbances and to increase the contribution from groundwater, generally leading to water with higher temperatures, more solutes and more organic matter from terrestrial sources (Brighenti et al., 2019b). Such habitat amelioration is expected to support autochthonous production and more complex food webs, which will result in an increase in the α-diversity but the appearance of more generalist bacteria, limiting endemic species and habitat heterogeneity and thus reducing the β-diversity and γ-diversity, especially in the case of kryal habitats (Brighenti et al., 2019a; Huss et al., 2017). In this context, groundwater will increasingly shape the thermal and hydrochemical state of both kryal and krenal habitats, may sustain water availability during droughts and will contribute to maintain habitat heterogeneity through different flow paths and water sources. Brighenti et al. (2019a), for e.g., showed how permafrost and rock glaciers can provide colder waters which provided refuges for species adapted to previously glacier-sourced colder water.

1.5 Research gaps

While the importance of groundwater in recently deglaciated catchments is being acknowledged with the emergence of related review papers (Glas et al., 2018; Vincent et al., 2019; Vuille et al., 2018), more research is needed. Presently, most studies still either analyze groundwater contributions at a larger scale at the outlet of a catchment (e.g. Cochand et al., 2019; Engel et al., 2016, 2019; Hood and Hayashi, 2015; Penna et al., 2017), without a clear vision of the hydrogeology of the landforms responsible for such storage, or they alternatively focus on the hydrological functioning of specific landforms. This lack of a general hydrogeological conceptual model for Alpine deglaciating catchments emerges from the difficulty of hydrogeological characterization intrinsic to these remote areas and from the site specific variability of geomorphological features, which mainly depend on the type of bedrock (Carrivick et al., 2018), the shape (slope and width) of the glacier valley, the glacier sediment production rate and the local climate (Carrivick and Heckmann, 2017; Maisch et al., 1999).

Only few perceptual models of the hydrogeology of such glaciated headwater catchments have been proposed to our knowledge: (i) in the Canadian Rockies a series of papers studied the hydrogeology of different proglacial structures (rock glacier, moraine, talus slope) and were summarized in the paper of Hayashi (2020); ii) in the Cordillera Blanca in Peru a suite of studies focused on the role of groundwater for stream flow in different proglacial valleys (Baraer et al., 2015; Glas et al., 2018; Gordon et al., 2015; Somers et al., 2016) and iii) in the Swiss Alps, it is worth mentioning a relatively old review of the hydrological behavior of proglacial landforms by Parriaux and Nicoud (1990).

To our opinion and as suggested by others (Heckmann et al., 2016; Vincent et al., 2019), there is still a lack of integrative studies that (i) intercompare the drainage rates and potential storage volumes of different landforms ; (ii) propose a framework to characterize the timing, amount and location of the transmission of different water sources (rain, snow, ice) to these landforms and between each of them; (iii) compare if the documented response of individual landforms can explain the observed catchment-scale behavior in terms of runoff amounts, timing and geochemistry; (iv) propose a unifying theory for the geomorphological and hydrological evolution of such rapidly evolving catchments.

1.6 Research objectives

In this research, we aim to better characterize the hydrology of the proglacial area emerging from a typical alpine valley glacier lying on a crystalline metamorphic terrain in the Swiss Alps. We specifically aim to unravel the interactions of different hydrogeological units at the catchment-scale in order to quantify the current and future potential of groundwater storage in such areas. Based on a case study in the Swiss Alps, we aim to characterize the current functioning of the different landforms based on an assessment of the mechanisms of water storage and release (Wagener et al., 2007). Furthermore, we aim to identify water pathways within the catchment and to which extent different sources of water (rain, snowmelt, icemelt) contribute to seasonal groundwater recharge.

The main question of this research is the following :

- What is the hydrogeological functioning of recently deglaciated proglacial areas in a context of rapid glacier retreat, fast paraglacial adjustments and changing climatic conditions ?

The focus of this work will be on the proglacial area emerging from a laterally-constrained Alpine temperate glacier on crystalline terrains. Such areas are especially relevant for alpine hydrology as temperate valley glaciers are the most common and largest glaciers of most alpine regions and show relatively similar geomorphological processes, leading to probably comparable water dynamics. Metamorphic rocks comprise the main geology of most high mountain chains and have to be separated from other geologies such as karstic systems with very different hydrological functioning. To answer the overall research question, the following subquestions will be studied :

- Where does groundwater recharge occur in glaciated catchments and in which hydrogeological units ?
- Which sources of water (rain, snowmelt, icemelt) recharge the aquifer and how does recharge evolve across seasons ?
- What are the hydrological functions (storage, release) of these storage units ?
- How will changing water sources availability (less ice-melt, earlier snowmelt) affect groundwater storage and baseflow ?

1.7 Case study

This research focuses on an extensive field-based assessment of the hydrogeomorphological processes of the Otemma glacier catchment in the Haut Val de Bagnes (VS, Switzerland) (Fig. 1.1). The catchment outlet was defined as the location of a small hydroelectrical water intake managed by the *Force Motrice de Mauvoisin* and constructed in the early 1960s right at the former glacier front (Fig. 1.2 (GS3)). From the end of the Little Ice Age (LIA) in 1850 to 1960, the glacier length had retreated by about 450 m. The rate of length recession increased after 1970 with an additional change of more than 2000 m, or about 40 m per year (GLAMOS (1881-2020)). With an equilibrium line altitude (ELA) located at around 3200 m asl (estimated for 2020 and 2021), a long flat main tongue and a small accumulation zone, the glacier is retreating rapidly, with an estimated complete melt of the main tongue by 2060 (Gabbi et al., 2012). The catchment has an area of 30.4 km^2, a mean elevation of 3005 m a.s.l. (2350 m to 3780 m) and a glacier coverage of 45 % in 2019 (adapted from GLAMOS (1881-2020)). The glacier possesses two medial moraines, which deliver supraglacial and

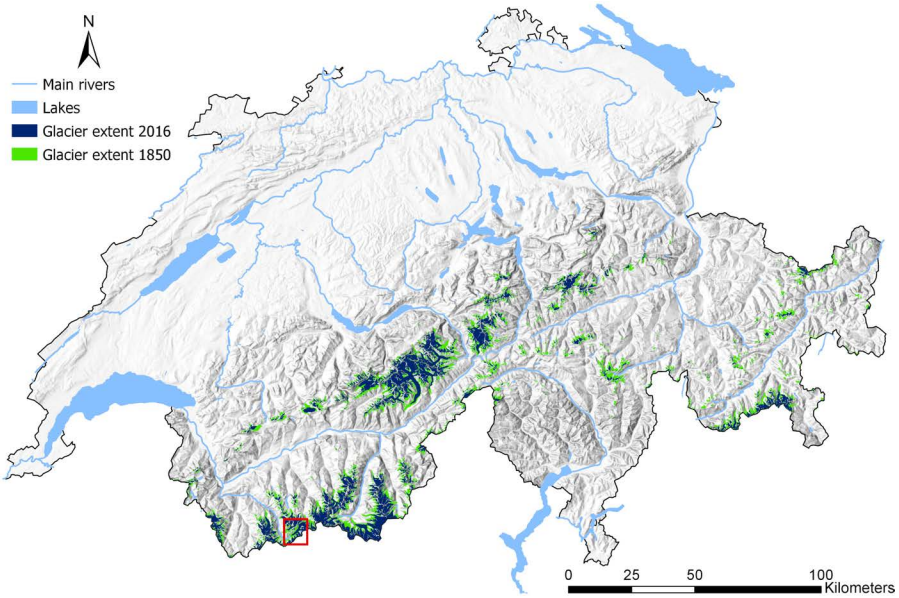

Figure 1.1: Overview of Switzerland with location of the Otemma glacier catchment (red rectangle). The glacier extents of year 1850 and 2016 are also highlighted based on the Swiss Glacier Inventory (GLAMOS (1881-2020)). The basemap data is provided by SwissTopo (2020b).

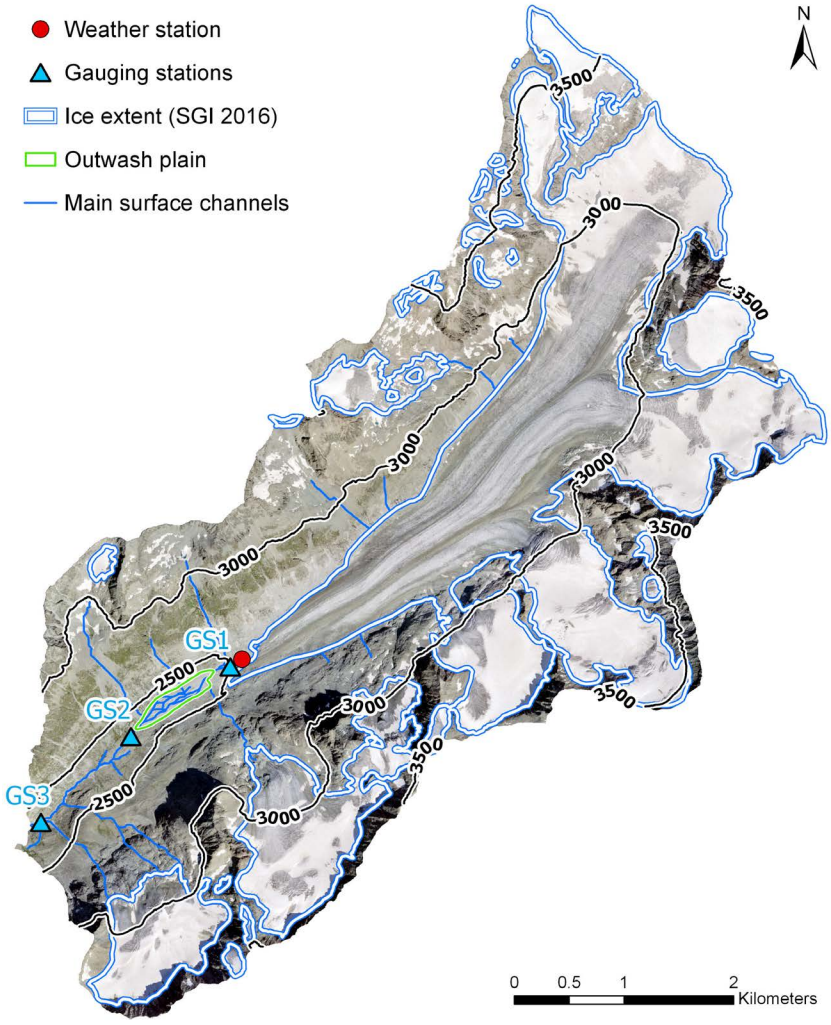

Figure 1.2: Overview of the Otemma glacier catchment. The three installed river gauging stations (GS) and weather station are also shown. GS3 corresponds to the location of a small hydropower water intake. The orthoimage is provided by SwissTopo (2020a) and the glacier extent from the Swiss Glacier Inventory (SGI2016) (GLAMOS (1881-2020))

englacial sediments to the glacier tongue especially in its more shaded southern part which gradually becomes heavily debris-covered. Except from this area, the glacier mostly consists of relatively clean ice with an average debris cover of about 10 % (estimated from Linsbauer et al., 2021).

The geology of the underlying bedrock is composed of gneiss and orthogneiss from the Late Paleozoic with some granodiorite inclusions (Burri et al., 1999). The main geomorphological forms comprise bedrock, with some vegetation cover above the LIA limit (46 %), steep slopes (30 % post-LIA lateral moraines and 10 % talus slopes), gently sloping debris fans and morainic deposits (13 %) and a flat glaciofluvial outwash plain (0.9 %). One main subglacial channel at the glacier snout supplies meltwater to a large, highly turbid and turbulent stream, which quickly reaches a mildly slopping (1 to 2 %) outwash plain composed of non-consolidated sandy-gravelly sediments. In this part, the stream forms a braided river network with a mosaic of bars and terraces until it converges in a bedrock confined channel about 1 km downstream and until the hydropower intake. A few tributaries from small hanging glaciers or lateral valleys also contribute to the river discharge during the melt season.

1.8 Methodology and thesis structure

Three years of extensive data collection campaigns where conducted in the summers from 2019 to 2021 in the glacier forefield. A base camp was installed about 1 km downstream of the current glacier foot, which allowed an easy access to the research area. Occasional field visits were also conducted in winter, but were limited due the difficulty of access and avalanche risks. Based on data collected during those three years, four research papers were written which constitutes the main scientific content of this thesis. Figure 1.3 provides a comprehensive overview of all methods used in this research, where and how they were applied (within a simplified representation of a glaciated catchment) and in which of the research papers (thesis chapters) they are discussed. The field methods used for this research are classified in three main categories : i) methods assessing the catchment-scale response; ii) methods evaluating single landform hydrological behavior and iii) methods looking at the types of water sources and the connectivity between landforms. In the following, we briefly discuss all field methods.

1.8.1 Catchment-scale response

The hydrological response of a catchment is usually studied based on streamflow observations made at its outlet. Based either on analysis of the river hydrograph (Kirchner, 2009) or on the chemical composition of the water (Penna et al., 2014), such approaches allow to either characterize the catchment-scale groundwater storage, estimate the contribution of different water sources (rain, snowmelt, icemelt, groundwater) (Carroll et al., 2018; Engel et al., 2016; He et al., 2019) or can be used to calibrate glacio-hydrological models, e.g. to provide an estimation of the current or future hydrological regime (Huss et al., 2008). While catchment-scale analysis provides an important assessment of the current integrated response of the overall catchment, it usually provides little information on the internal processes responsible for its behavior. In this work, we therefore propose to analyze the catchment-scale response together with an assessment of the individual behavior of its internal hydrogeological units. This provides a better process understanding and more realistic view on future hydrological trends, which we present in Chapt. 3.

Streamflow We studied the hydrological behavior of the Otemma catchment based on streamflow observations at the catchment oulet (GS3 in Fig. 1.2). Extensive literature exists on the relationship between discharge recession and the catchment-scale groundwater storage. Such a recession analysis method was applied to analyze the catchment-scale response from 2006 to 2017, to assess potential changes due to glacier retreat and to estimate the overall theoretical groundwater storage.

In addition to the catchment outlet, two other gauging stations (GS1, GS2, see Fig. 1.2) were installed from 2019 to 2022, where we observed discharge together with water temperature and water electrical conductivity. Discharge near the glacier snout was used as an input parameter of a 3D model of the outwash plain aquifer (Chapt. 4) and for the evaluation of the glacio-hydrological model (Chapt. 5).

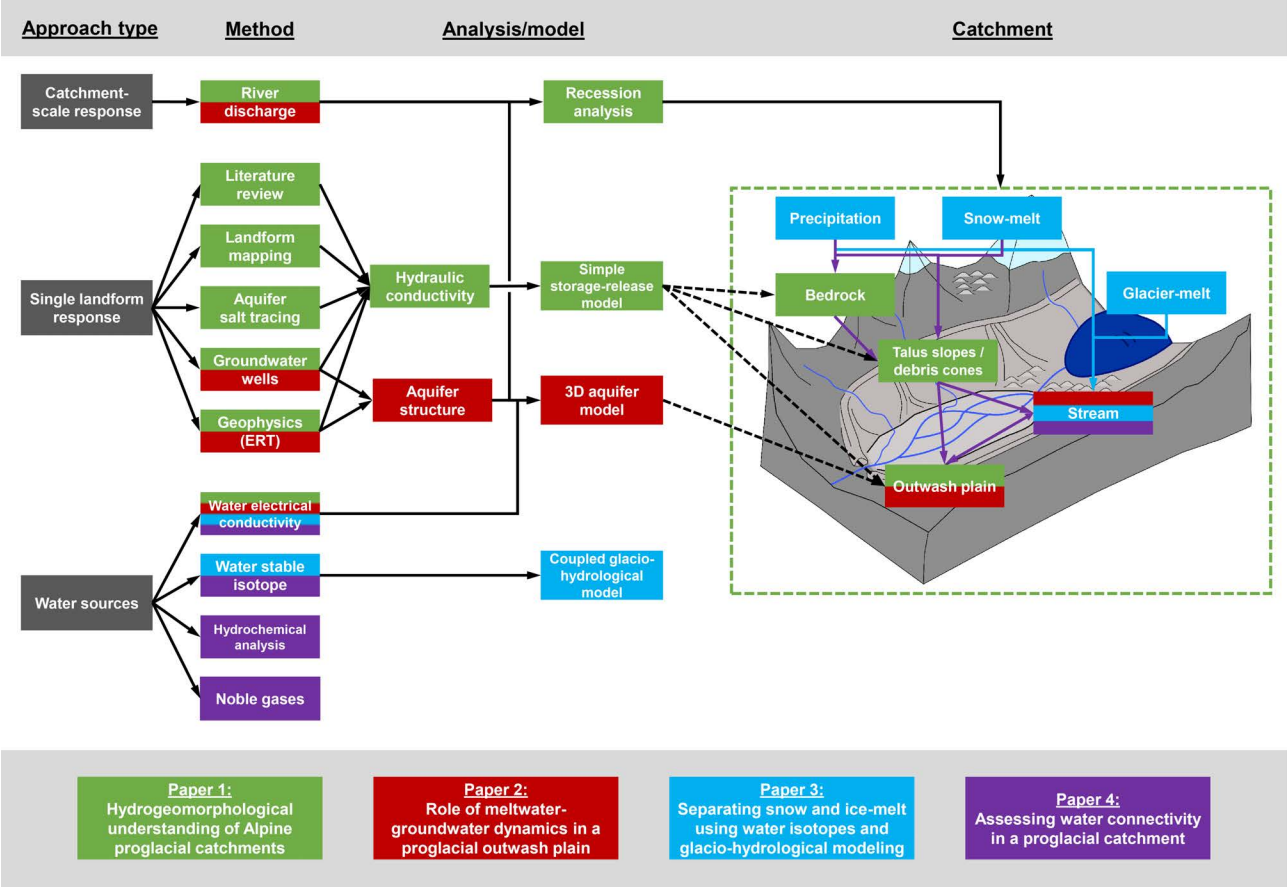

Figure 1.3: Overview of the methods and main modelling framework used in this thesis, highlighting where they were applied in the glaciated catchment of Otemma. A simplified representation of the glaciated catchment is shown on the right, highlighting the main landforms. The colors of the boxes and arrows show in which paper each method was used. The four papers are illustrated by the bottom boxes.

1.8.2 Single landform functioning

Glaciated catchments are characterized by a complicated assemblage of superficial geomorphological landforms, which have different potential to store and release water from different origins (rain, snowmelt, icemelt). Since such landforms are changing or emerging rapidly with glacier retreat, the future hydrological response of such catchments is expected to change due to the structural modifications of its internal structures. It appears therefore that a detailed understanding of each hydrogeological unit is needed to project the future behavior of glaciated catchments. In particular, we focused our work on aquifers which may maintain seasonal baseflow by storing large water amounts and releasing it at long timescales (several weeks to years).

We address the characterization of such aquifers in the first two research papers provided in this thesis. We rely on multiple low invasive field method, which are briefly discussed hereafter.

Literature review Alpine hydrology is rapidly advancing, with a recent more extensive focus on groundwater and landform hydrogeology (e.g. Hayashi, 2020). By summarizing estimated water hydraulic conductivities and aquifer responses found in the literature and including them in a simple framework, a first-order comparison of their hydrological functioning can be provided. Nonetheless, the literature on the hydrological role of some landforms, such as the outwash plain, was found here to be limited, and we therefore focused a part of this research on a detailed assessment of their hydro-geomorpohological functioning. A detailed literature review is provided in Chapt. 2

Landform mapping In addition to the literature review, by identifying the extent and thickness of different landforms in the Otemma catchment, an assessment of their potential maximal groundwater storage can be provided, as proposed in other alpine catchments (e.g. Hood and Hayashi, 2015). It remains however difficult to estimate their actual storage as aquifers are typically not fully saturated. For this reason, we developed a simple storage-release model to provide a more realistic assessment of the seasonal storage of different parts of the catchment. This is discussed in Chapt. 3.

Aquifer tracing The transit time of groundwater in an aquifer can be estimated by measuring the travel time of a tracer and based on Darcy's Law, the hydraulic conductivity can be inferred. We used the method proposed by Kobierska et al. (2015a) to estimate the hydraulic conductivity of the outwash plain by injecting salt in the aquifer and using Electrical Resistivity Tomography (see below) to detect the movement of the salt plume. This is discussed in Chapt. 3.

Geophysics Electrical Resistivity Tomography (ERT) is a typical geophysical method allowing to detect low resistivity (fine sediments, water) and high resistivity (bedrock, ground-ice) layers in the underground by applying an electrical current to an array of electrodes inserted into the ground and was used successfully in other Alpine studies (e.g. Harrington et al., 2018; Muir et al., 2011). It is particularly well suited to measure the depth of the sediment aquifer formed by the outwash plain in the Otemma catchment. This method allowed to estimate the volume of this aquifer, which was used to develop a 3D aquifer model of the interactions between the glacial stream and the aquifer. This is discussed in Chapt. 4.

Groundwater wells We installed eight shallow (2-3m deep) fully-screened groundwater wells in the outwash plain and continuous monitored the aquifer head. From those results, we determined the general groundwater flow direction and the aquifer behavior during the recession periods. Based on the diel groundwater variations propagated from the icemelt-induced river fluctuations, the hydraulic conductivity was estimated following the work of Magnusson et al. (2014) and was compared with the aquifer tracing method (see above). Finally, the groundwater observations were also used to calibrate the 3D aquifer model presented in Chapt. 4.

1.8.3 Water sources and connectivity

While the previous methods allow to characterize the mechanisms of water storage and release, they provide little information on the sources of water, how they are recharged and connected between each other. Knowledge about the source of the recharge appears especially important in a context of climate change and the expected change in the snow and ice-melt seasonality. The following methods were used to assess the current partitioning of the different water sources into the main stream or in different hydrogeological units inside the catchment.

Water stable isotopes Water stable isotopes are typically used to detect the different sources of water (snow, ice, precipitation). Numerous studies in high Alpine catchments have been conducted (e.g. Penna et al., 2017; Schmieder et al., 2018), but the spatio-temporal variability in the isotopic composition of the end-members is challenging leading to large uncertainties (Zuecco et al., 2019). We collected water isotopes in multiple locations in the Otemma catchment. The composition of the water sources were collected monthly during the summer season mostly, at multiple locations for snow and ice to assess their spatial variability. At the three gauging stations, isotope waters were sampled during the whole snow-free season, usually twice a day. Based on those data, a coupled isotope-glacio-hydrological model was developed to assess the partitioning of the water sources, discuss the uncertainty due to the snowmelt isotopic variability and provide recommendations for the use of water stable isotopes in such environments (Chapt. 5). Waters were also analysed from the outwash plain and in hillslope tributaries to assess how such landforms are recharged (Chapt. 6).

Water electrical conductivity The electrical conductivity of water (EC) is usually used in combination to H- and O-isotopes of water to estimate the share of groundwater at the catchment outlet (e.g. Penna et al., 2017; Schmieder et al., 2018). Since chemical weathering may occur at the contact with sediments or bedrock, EC cannot be considered as a conservative tracer. Moreover, defining the EC value of different groundwater aquifers is challenging, as multiple aquifers may have different values and may be difficult to access. In this work, EC is only used for a qualitative assessment of groundwater contribution in different parts of the catchment or for comparison with other approaches.

Geochemical analysis Water-rock interactions are well known to modify the geochemical composition of dissolved solutes in surface and groundwaters (e.g. Anderson, 2007). By analyzing solute concentrations in various parts of the catchment, the weathering conditions of different water sources can assessed. The weathering rates of different lithologies may change due to groundwater contact time as well as due to other factors, and it may therefore be possible to trace the source or flowpaths of the groundwater (Baraer et al., 2015). This method provided valuable information on the water connectivity between different landforms and on the different proportion of groundwater flow from different groundwater compartments. This is discussed in Chapt. 6.

Noble gases Assessing the contribution from the hillslopes to the outwash plain is challenging since potentially significant infiltration may occur below ground. Moreover, a traditional water isotope mixing model cannot yield further information because the isotopic compositions of all involved water sources (main stream, lateral tributaries, groundwater) may be similar in Alpine catchments. As proposed in the work of Schilling et al. (2021), noble gases can be used to estimate the contribution from hillslope water against the glacial stream based on water temperatures at the point of recharge. We investigated this new method by installing a portable mass-spectrometer (Brennwald et al., 2016) during the summer 2021, which continuously analyzed the water composition of three groundwater wells along a transect from the stream to the hillslopes. This is discussed in Chapt. 6.

1.8.4 Complementary studies in the Otemma catchment

Alongside the work presented here, four other research projects were conducted in Otemma catchment, mostly focusing on the eco-geomorphological processes and sediment production and transport with the following main topics: i) the role of biofilm as ecosystem engineer of a glacial floodplain (Roncoroni et al., 2019, 2022); ii) geometry and dynamics of subglacial channels (Egli et al., 2021); iii) proglacial forefield dynamics and bedload transport (Mancini et al., 2021); and iv) subglacial sediment export (Jenkin et al., 2022).

1.9 Thesis structure

This thesis is subdivided into six main chapters. The first chapter provides a more extensive literature review on the state-of-the-art of hydrological and geomorphological process understanding in an Alpine glaciated catchment. It provides an in-depth description of the typical geomorphological landforms, their structure and hydrological functioning and concludes with a preliminary synthesis of their relative importance in such environments. The four next chapters correspond to the four research papers elaborated during this work and cover the methods presented in Fig. 1.3. The final chapter provides a synthesis of this work, summarizing the major findings and highlighting potential questions which may be addressed in future research.

The four main research papers are summarized hereafter.

Research article 1, published in HESS on 02 Dec 2022 :

Müller, T., Lane, S. N., and Schaefli, B.: Towards a hydrogeomorphological understanding of proglacial catchments: an assessment of groundwater storage and release in an Alpine catchment, Hydrol. Earth Syst.

Sci., 26, 6029–6054, https://doi.org/10.5194/hess-26-6029-2022, 2022.

The first chapter provides a comparison of the hydrological catchment-scale response based on discharge recession analysis in order to estimate the overall theoretical groundwater storage and response timescale. It then analyses the response of all landforms inside the Otemma catchment based on a literature review as well as additional field data from the outwash plain aquifer and provides a simple model to estimate their potential storage. Based on the comparison between both approaches, we highlight an important missing water storage compartment from our landform-based analysis, which we attribute to bedrock storage. While the overall results appear robust, it also opens new questions regarding the role of the outwash plain and bedrock storage, which are then further investigated in the following papers 2 and 4.

Research article 2, submitted to HESS on 24 Dec 2022, in review :

Müller, T., Roncoroni, M., Mancini, D., Lane, S. N., and Schaefli, B.: Current and future role of meltwater-groundwater dynamics in a proglacial Alpine outwash plain, EGUsphere, 2023, 1–34, https://doi.org/10.5194/egusphere-2022-1503, 2023

Based on the outcome of the first paper, this article focuses on the aquifer formed by the outwash plain, the interactions with the glacial stream and its importance to maintain baseflow. For this purpose, a 3D model (MODFLOW) was set-up to simulate the aquifer behavior during two years and was calibrated based on different field observations using an automated parameter estimation model (PEST). On the basis of this model, we show the currently limited dynamic storage of such aquifers. We finally attempt to identify future potential new emerging outwash plains due to glacier retreat and discuss their combined cascading effect on river discharge.

Research article 3, ready for submission to HESS :

Evolution of the stable isotope compositions of snow and ice melt waters and their impact on improving glacio-hydrological models in highly glaciated catchments

This research article builds on the extensive isotopic data obtained at the glacier outlet and for snow and ice to discuss the use of water stable isotopes to separate snow and ice-melt in such a highly glaciated catchment. For this purpose, we developed a simplified glacio-hydrological model which simulates all water fluxes as well as the isotopic composition of snowmelt, icemelt and rain. The model is calibrated based on snow and ice mass balance measurements obtained between 2020 and 2021 and snow cover maps from satellite imagery. The model ultimately allows us to simulate the integrated isotopic composition of snowmelt, icemelt and rain at the catchment outlet, which we compare with the measured isotopic composition of the river to estimate their contribution. We finally show the significant uncertainty linked to this isotopic approach, which we compare with results from the glacio-hydrological model.

Research article 4, in preparation for submission :

An assessment of subglacial and proglacial groundwater connectivity using a multi natural tracers analysis in a highly glaciated catchment

This chapter explores groundwater connectivity in the proglacial and subglacial zone of the Otemma catchment. For this purpose, we mainly compare observations from three different types of natural tracers : i) water stable isotopes; ii) geochemical and EC data and iii) noble gases. Based on the previous chapters, we show that the nature of the most significant groundwater storage at a seasonal scale remains unclear. Moreover, while the modelling work highlighted the seasonal groundwater dynamics of the outwash plain, the relative contribution from hillslope recharge could be better estimated based on natural tracers. We therefore combine different natural tracers to identify the signature of different groundwater compartments and

assess how they affect groundwater storage in the outwash plain or in the stream composition at the glacier outlet. While each method shows clear limitations, their combined interpretation, compared to results from the previous work, allows to propose a perceptual model of a coupled bedrock-subglacial groundwater system. This last chapter finally allows to evaluate the results from the previous works with a more direct approach and contributes to a more integrated understanding of the current hydrogeological functioning of a typical highly glaciated catchments.

1.10 Data availability

All field data acquired during this work have been published in Zenodo in different datasets. Weather data are available in Müller (2022a), stream observations (discharge, EC and temperature) in Müller and Miesen (2022), groundwater observations (water head and temperature) in Müller (2022b), geophysical surveys in Müller (2022c) and finally isotopes and EC data various catchment locations in Müller (2023).

All codes required for a detailed data analysis or the development of models are provided as Supplements to each research article.

For the purpose of field data collection, I developed a range of low-cost automatic sensors, which were used to record groundwater levels or air temperature, air pressure and rainfall. A description of these sensors was presented in (Müller et al., 2022b). In addition, tutorials and codes are accessible at `https://github.com/tomuelle/DIYweatherstation`.

2 State of research

In this chapter, we review current literature on the geomorphological processes which lead to the formation of superficial deposits in alpine environments. We then review the hydrological functioning of those landforms based on the knowledge gained from the geomorphological processes leading to their formation and discuss, based on the latest literature, the timescales and potential volumes of groundwater that they may store and release. We start this chapter with an overview of current research which analyzes the catchment-scale response of proglacial catchments and then discuss each proglacial landforms in more details.

2.1 Catchment-scale hydrological functioning of proglacial areas

Proglacial margins are characterized by a strong seasonal streamflow regime, with low-flow during winter, conditioned by below-zero air temperatures and near ubiquitous snow cover. The onset of snowmelt leads to a gradual streamflow increase in spring, with the highest flows and the largest diurnal fluctuations (Lane and Nienow, 2019) occurring after near complete snow disappearance and the development of a strong subglacial channelized stream network (Werder et al., 2013). In autumn, the decreasing air temperature and solar radiation limit ice melt and lead to the onset of snowfall, which explains the return to winter baseflow. The relative contribution of precipitation, snow-melt, ice-melt and groundwater during each season is to date not well understood and greatly depends on the glacier coverage (Schmieder et al., 2018; van Tiel et al., 2020a). Historically, high Alpine catchments were considered as "Teflon basins" where all water inputs are quickly directed into streams (Williams et al., 2015). This vision was supported by a highly simplified representation of the geology of the system : an impervious bedrock with very coarse glacial deposits having little retention capacity. Some studies have started to address this lack of understanding at the catchment-scale, using end-member mixing model or water balance approaches.

For instance, water stable isotopes have been increasingly used as a conservative tracer to quantify the contribution of different water sources (Beria et al., 2018; Michelon et al., 2023). They are often combined with other geochemical tracers such as electrical conductivity (EC) or chloride (Crossman et al., 2011) to build three-component mixing models. Based on such models, (Penna et al., 2014) showed a delayed contribution of snowmelt to spring water compared to stream water, and a peak snow contribution of up to 92 % during July and August, when most of the snow had disappeared from the catchment. These observations suggest relatively long groundwater recharge times and challenge the "Teflon hypothesis". Groundwater contribution was also shown to contribute significantly to streamflow, from a minimum of 20 % during summer for a 25 % glaciated catchment and up to 90 % in autumn (Engel et al., 2016; Penna et al., 2017). A growing groundwater contribution with distance downstream (decreasing percentage of glacier cover) is also observed in summer, from 20 % to 50 % for sub-catchments of 25 % to 4 % glaciated surface (Penna et al., 2017). However, the choice of end-members, as well as the spatial distribution and timing of sampling has resulted in uncertainties in such studies (Schmieder et al., 2018). The use of EC as a tracer of groundwater may be questioned, since groundwater EC may not be homogeneous in groundwater, due to preferential flow paths (Zuecco et al., 2019), and does not take into account possible enrichment, due to the rock-water interactions during infiltration or due to fast hyporheic exchanges (Kalbus et al., 2006). Isotope analyses have been used to assess groundwater travel time distributions using various models (McGuire et al., 2005), but long continuous time series are needed (Benettin et al., 2017), which limits their feasibility during winter in snow-covered areas. One tentative study (Schmieder et al., 2019) identified a mean response time of 28 days for a small groundwater dynamic storage in a 34 % glaciated, crystalline catchment, but was com-

bined with a much larger "mobile storage" (see Staudinger et al., 2017) with a mean transit time of 9.5 years, indicating both a fast catchment response and a much slower subsurface storage reservoir. Finally, isotope-aided glacio-hydrological models may also provide more reliable estimates of the contribution of different compartments at the catchment-scale (He et al., 2019).

There are also water balance-based approaches for groundwater storage quantification in highly glacierized catchments that attempt to characterize all incoming (snow melt, precipitation, glacier melt) and outgoing fluxes (streamflow, evapotranspiration, sublimation). Hood and Hayashi (2015) used a dense snow survey to characterize maximal snow depth and density, combined with a snowmelt model and snow transects in a small 4 % glaciated catchment and found an early groundwater storage increase of 60-100 mm by the end of June, and a gradual storage decrease in August and September that they attributed to drainage of extensive proglacial moraines. Using a similar approach, Cochand et al. (2019) used airborne LIDAR scanning to estimate maximum snow height distribution in a small headwater catchment with two small rock glaciers (1.5 % coverage) and showed an early summer snowmelt-related groundwater storage increase of 300±60 mm, attributable to an evaporitic rock layer, which sustained baseflow during a 7-month long recession period.

While studies at the catchment-scale provide valuable understanding of the overall hydrological functioning of such glaciated proglacial margins (e.g. Andermann et al., 2012; Cochand et al., 2019; Engel et al., 2016, 2019; Hood and Hayashi, 2015; Penna et al., 2017), the internal mechanisms responsible for such behavior remain difficult to identify, making future predictions difficult in such geomorphologically dynamic systems. In particular, as the importance of groundwater in recently deglaciated catchments has been acknowledged in recent review papers (Glas et al., 2018; Vincent et al., 2019), there is a need for a clearer view of the hydrogeological functioning of their landforms, which is discussed hereafter.

2.2 Proglacial landforms as drivers of groundwater storage

Current proglacial margins are usually defined based on the Little Ice Age, LIA, (1850) glacier extent (Heckmann et al., 2019). The geomorphological processes occurring here (also called "paraglacial" processes) can be separated into (i) gravitational processes linked to glacial debuttressing and rock slope failure (Grämiger et al., 2017), debris flow (Ballantyne, 2002) and freeze-thaw cycles (Haeberli et al., 2006) (ii) glaciofluvial processes linked to river erosion, transport and deposition of sediments and neighboring landforms (Lane et al., 1996; Maizels, 2002); and (iii) processes associated with relict ice and its melt-out (Evans et al., 2006).

2.2.1 Sediment origin

Due to high glacial erosion rates, on the order of 0.1 to 10 mm yr-1, on crystalline bedrock (Guillon et al., 2015; Hallet et al., 1996) and the efficiency of subglacial channeled streams to transport sediments, sediments of glacial origin (also called "till") provide the main sediment source to proglacial areas (Guillon et al., 2015). The majority of subglacial sediments are produced at the bedrock-ice interface due to glacier erosion through glacial abrasion, glacial plucking or quarrying or the chemical erosion of meltwater(Bennett, 2009) and are then deposited or transported by a number of mechanisms including basal ice regelation, upward faulting and folding (Alley et al., 1997) or by subglacial streams (Swift et al., 2005). Regardless of their degree of consolidation, most glacial tills are classified as diamicton, referring to a poorly sorted mix of medium to coarse sediments contained in a matrix of fines (Evans et al., 2006). The basal debris layer that forms under glaciers is called hereafter traction till and is affected by high ice pressure and shear stress, leading to a more compacted and more impervious material. Traction till can be distinguished from subglacial melt-out till, which refers to englacial sediments released by basal melting deposited without deformation (Evans et al., 2006). Such melt-out till has a similar particle distribution but is less packed and contains fewer fines.

Alternatively, sediments can be derived directly from rockwalls erosion and be transported downslope to non-glaciated areas. Their particle shape is more angular and non-spherical and their size distribution is distinct from glacial sediments and are usually lead to coarser and less compacted landforms (Fischer and Hubbard, 1999; Sass, 2006).

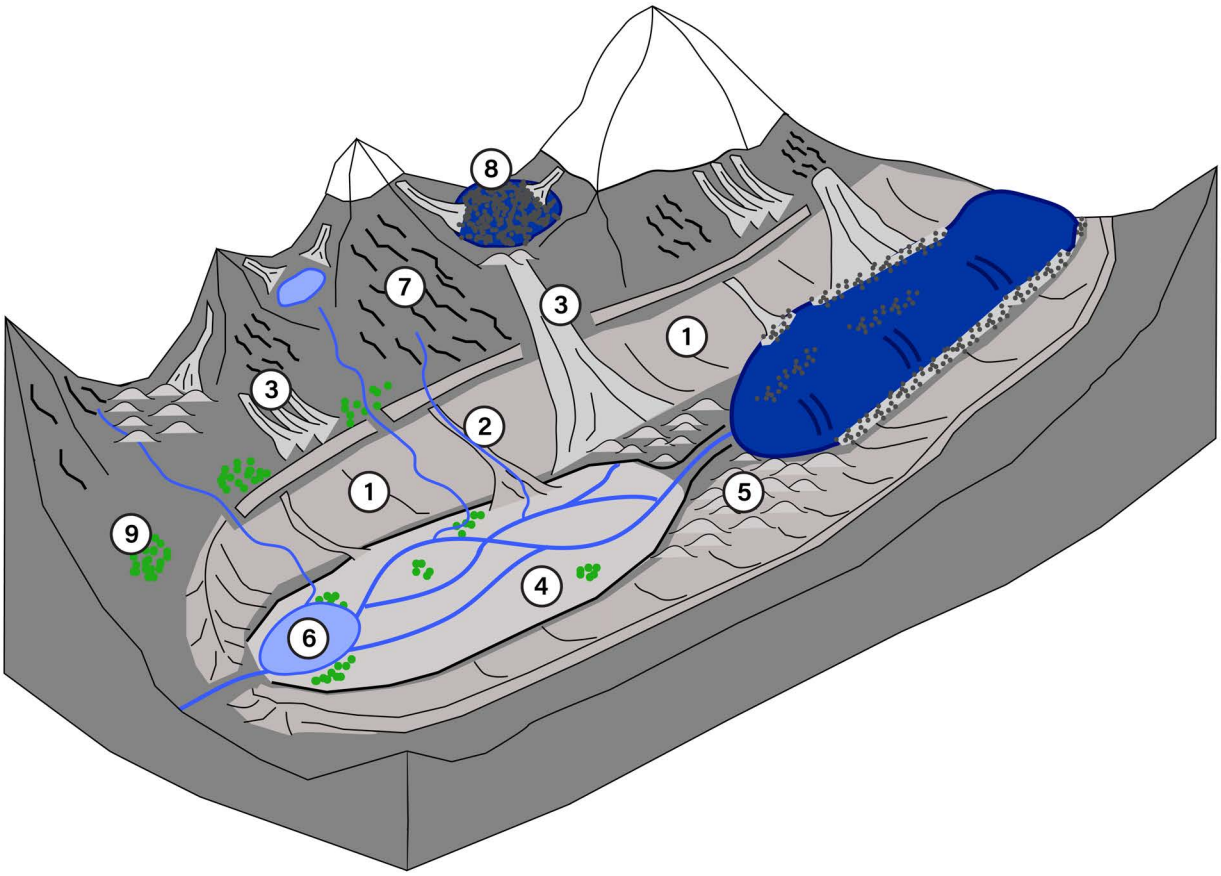

Figure 2.1: General overview of geomorphological landforms typical of proglacial zones. (1) Lateral moraine (grey); (2) debris cone; (3) talus slope (light grey); (4) fluvial outwash plain; (5) glacial deposit (till); (6) proglacial lake; (7) apparent bedrock (dark grey); (8) debris-covered rock glacier; (9) vegetation patches. Snow on the mountain tops is in white, and the glacier is in blue on the right (figure inspired by the work of Temme (2019)).

2.2.2 Landform assemblages

Landform assemblages in proglacial margins are complex and have been created by the history of glacial advances and retreats and complex paraglacial reworking processes. A typical landform assemblage is proposed in Fig. 2.1. In the following, we discuss each landform first from a geomorphological perspective and then highlight their main hydrological mechanisms in terms of water storage and release.

2.2.3 Slope related landforms

2.2.3.1 Lateral moraine deposits, debris cones and alluvial fans

Lateral moraine deposits form by three main processes: i) subglacial and supraglacial sediment deposition during glacial retreat; ii) gravity and fluvial flow leading to reworking in steep parts (>30 °(Dusik et al., 2019)) and creation of gullies (Mancini and Lane, 2020) and iii) glacier readvance that erodes earlier deposits and "plasters" the remaining deposits (Lukas and Sass, 2011; Lukas et al., 2012). Lateral moraines are mainly composed of a non-sorted mix of fine to coarse materials and potentially have a more consolidated till. The paraglacial reworking of the moraine leads to sediment accumulation on previous glacial deposits in the lower part of the lateral moraine (Mancini and Lane, 2020). This process leads to the formation of debris cones which are composed of poorly sorted sediments and have a typical slope angle of 12-25 °(Ballantyne, 2002). Their sedimentological signature is similar to the underlying moraine deposits, although the surface deposits are usually less compacted. Alluvial fans are distinguished from debris flow based on their gentler slope (<15 °) and are usually composed of sediments from both debris flow and fluvial deposition. Although their sedimentological structure may not be exactly similar, the hydrology of lateral moraine deposits and

subsequent debris cones is usually considered similar to glacial till deposited at the valley bottom and will be discussed in chapter 2.2.4.1.

2.2.3.2 Talus slopes

Talus slopes are similar to debris-cones with the exception that their debris originates from rock slope failures and is not linked to glaciogenic materials. Depending on their scale, these landforms may flow above or may be mixed with lateral moraine deposits or glaciofluvial sediments. Talus slope debris is coarser than morainic material, more angular and usually less compact. It accumulates downslope as stratified layers, usually sitting on previous soils or moraine formations in its lower part and directly on the bedrock on the upper part of the talus (Sass, 2006, 2007).

There is no clear consensus in the literature about the importance of talus slopes for groundwater storage, release and hence baseflow contributions. Clow et al. (2003) suggests that talus slopes may be composed of a finer more compacted layer in their lower parts and are overlain by a coarser upper layer. They concluded that talus slopes contributed up to 75 % of winter baseflow. Liu et al. (2004) also pointed out the importance of talus slopes but mainly by transmitting snowmelt to downslope parts of the catchment leading to little water retention and thus limited contribution to winter baseflow. Muir et al. (2011) reported a fast hydraulic conductivity and a very little capacity to maintain baseflow for more than a few days (response time of about 1 day) due to their coarse texture and only calculated a very thin saturated layer (<3 cm) at the talus-bedrock interface. Based on geophysical investigations, they could not observe any finer sediment layer at their base. However, they observe a dominance of pre-event water during storms which they attribute to a mechanism of water storage in bedrock depressions, based on a typical "fill & spill" mechanism (Tromp-Van Meerveld and McDonnell, 2006). What should be retained here is that : (i) talus slopes are composed of coarse material and have very high hydraulic conductivity (Muir et al., 2011); ii) a finer layer characterized by more storage capacity may be present at their base if talus slopes cover other landforms such as glacial deposits (Baraer et al., 2015; Sass, 2006); iii) talus slopes play an important role in transmitting snowmelt and precipitation and may store water in depressions or in the underlying fractured bedrock(Liu et al., 2004; Muir et al., 2011); iv) talus slopes should not be confused with lateral moraine deposits since they are much coarser (Rogger et al., 2017).

2.2.4 Glaciofluvial landforms

2.2.4.1 Glacial deposits (till)

In the flatter valley bottom, glaciers deliver substantial amounts of sediments. Glacier retreat commonly leads to deposits that comprise tills stacked on top of each other. Traction till usually represents the lowest layer and is the most consolidated and fine material (Eyles et al., 1983; Hammer and Smith, 1983). Subglacial melt-out till may be released near the glacier front (Hart, 1998), leading to a less compacted stratified diamicton (Eyles et al., 1983). Generally, in Alpine environments, basal traction till was reported to be very thin and rather discontinuous (<1m (Brand et al., 1987; Iverson et al., 1994; Kulessa et al., 2005)), so that a strong decreasing hydraulic gradient with depth is unlikely (Lukas, 2012). Therefore, glacial till deposits are mostly constituted by a stratified diamicton composed of silt to sandy-gravelly sediments (Rogger et al., 2017) and should be less compacted than lateral moraines due to the absence of a "plastering" mechanism.

Strong groundwater-surface water interactions in glacial tills have been observed. For example, in Alaska, 46 % of annual stream discharge was lost to a till aquifer and was the main contributor for lowland winter runoffs (Liljedahl et al., 2017). Three studies on proglacial moraines in the Swiss Alps (Kobierska et al., 2015a,b; Magnusson et al., 2014) documented an aquifer alimented by the stream and a groundwater table close to the surface ($< 1m$) flowing parallel to the stream. Due to an aquifer thickness of 10 m and a response time of a slow reservoir of 29 days, they showed that this type of aquifer may provide substantial baseflow during the low-flow season.

2.2.4.2 Outwash plain

Subglacial streams usually come in contact with glacial deposits at the glacier tongue. Due to strong diel streamflow variations and occasional large floods, a strong reworking of the valley floor occurs, with a succession of phases of erosion and aggradation and a usual eluviation of fines (Marren, 2005). Where the valley slope is low, stream power decreases and sediment sorting occurs (Miall, 1977), with coarser sediments deposited in the proximal region and finer sandy material deposited further downstream (Zielinski and Van Loon, 2003). If the accommodation space is large, thick deposits of sandy-gravelly material will lead to the creation of bars and of a braided stream network, eventually leading to the creation of so-called glaciofluvial outwash plains (Maizels, 2002), which may play an important role as sediment traps (Baewert and Morche, 2014; Lane et al., 2017). They are composed of heterogeneous layers of non-consolidated silty-sandy and gravely facies (Anderson, 1989; Ballantyne, 2002), and they usually sit on previously deposited reworked glacial till, composed of a finer diamicton layer (Maizels, 2002). The burial of ice blocks is also a common phenomenon, leading to the formation of "kettle holes" (Maizels, 1977).

The hydrology and ecology of such plains has been mostly studied in ice-caps glaciers, where they form large "sandur" (Levy et al., 2015; Macdonald et al., 2016; Robinson et al., 2008). They are considered as large productive aquifers and experience important surface-water groundwater interactions, with glacier meltwater contributing to wells up to 500 meters from the stream (Ó Dochartaigh et al., 2019). In Alpine regions, proglacial outwash plains were less studied, probably because of their smaller size and only recent appearance. A few studies explored their geomorphological importance showing their potential role as sediment trap and sensitivity to extreme events (Baewert and Morche, 2014; Lane et al., 2017). Small outwash plains in the Alps were shown to behave similarly to larger sandur by collecting water from multiple sources and maintaining various groundwater-fed river channels in autumns and winter, promoting habitat heterogeneity and high biodiversity (Crossman et al., 2011; Malard et al., 1999; Ward et al., 1999). A study in a late Pleistocene glaciofluvial plain also showed a large water storage capacity and a slow aquifer depletion rate during a seasonal drought, where groundwater exfiltration contributed up to 35 % of total runoff while it only represented 3 % of its total area (194 km^2) (Käser and Hunkeler, 2016). However, recent proglacial outwash plains emerging after the LIA are expected to be smaller and store less sediments, reportedly in the order of tens of meters (Kobierska et al., 2015b; Otto et al., 2009; Rogger et al., 2017).

2.2.4.3 Proglacial lakes

Proglacial lakes usually form behind a natural barrier which can originate from: (i) an overdeepening in the bedrock; ii) a frontal moraine-dam; iii) an ice-dam or iv) a landslide-dam (Otto, 2019). Many small proglacial lakes are ephemeral due to their gradual filling with sediments or sudden rupture of natural dams which may cause extreme events such as glacier lake outburst floods (GLOFs) (Nie et al., 2018). They act as sediment traps for all types of sediments, mainly from fluvial origin through sedimentation of the suspended load, from melt-out of ice blocks or from debris from the valley sides. The most common moraine-dammed lakes are usually composed of glaciofluvial sediments forming annual layers of coarser material (silt/sand) in summer and finer deposits in winter, which can be overlain by more outwash sediments once the lake becomes filled with sediments (Ballantyne, 2002). Due to the fine nature of their sediments, proglacial sediments in lakes are usually rather unproductive, but may constitute important natural water reservoirs (Parriaux and Nicoud, 1990).

2.2.5 Permafrost related landforms

2.2.5.1 Permafrost

Permafrost is defined as a ground state where temperature is at or below 0 °C for a minimum of two years (Haeberli et al., 2006). The frozen material is usually located a few meters below an active-layer of unfrozen sediments and plays an important role in stabilizing slopes and moraines and thus limiting sediment transport. Increased permafrost thawing due to warmer temperature is expected to reduce slope stability, leading to further reworking of hillslopes and hazardous events such as landslides or moraine-dam lakes breaches (Haeberli et al., 2017), and may also be a source of water for high Alpine environments (Gärtner-Roer and

Bast, 2019). While permafrost thaw does not yield large water volumes due to their slow melt (Harrington et al., 2018), permafrost may effectively act as an impervious layer limiting deeper water infiltration. For instance, Rogger et al. (2017) modelled the future groundwater storage capacity after the complete melt of permafrost in a small glaciated catchment and estimated a 19 % increase of runoff during the autumn recession period due to the absence of ice.

2.2.5.2 Rock and debris-covered relict glaciers

Rock glaciers are periglacial landforms intrinsic to the presence of permafrost and their future role for providing water supply and chemical compounds has been stressed recently (Brighenti et al., 2019a). Rock glaciers may be classified based on the genetic origin of their ice and debris into two types: i) rock glaciers derived from talus slope processes under permafrost conditions and ii) heavily debris-covered relict glaciers in permafrost free zones. Berthling (2011) addresses this by defining rock glaciers as "the visible expression of cumulative deformation by long-term creep of ice/debris mixtures under permafrost conditions". Accordingly, degenerating melting debris-covered glaciers are excluded from this definition because of the absence of permafrost conditions. These formations are recognized as ice-cored moraines and have a similar composition to glacial till deposits, usually with a more important depletion of fine materials (Haeberli et al., 2006). Most rock glaciers are thus slope-derived in permafrost zones and are created by the burial of surface snow and ice by debris from talus slopes. They are composed of a matrix of coarse blocky sediments with a lack of fine materials and a frozen core of fine-grained to larger sediments (Haeberli et al., 2006).

Most studies on ice-cored moraines have shown a hydrological response composed of a fast and slow groundwater component and could sustain substantial winter baseflow (Langston et al., 2011). Harrington et al. (2018) completed a multimethod analysis of such rock glacier where they showed a 1 to 2 m saturated finer basal layer with a response time of 20 days overlain by a coarser layer having a much higher hydraulic conductivity. Winkler et al. (2016) reported a similar behavior, but with a basal less conductive layer attributed to traction till. Wagner et al. (2021) further discussed the role of rock glaciers to store important water amounts due to their relatively large coverage in Austrian Alps and to provide baseflow with average residence times of 7 to 23 months.

2.3 Synthesis

In the context of the present thesis, the most relevant conclusions from the above detailed literature review can be summarized as follows:

1. Due to their aquifer structure and their fast hydraulic conductivity, talus slopes appear to have very short transit times, meaning a rapid transmission of water and little retention. They most probably do not store water but rather transmit it from or to other landforms. Some water may however be stored in the underlying fractured bedrock (Harrington et al., 2018; McClymont et al., 2011).

2. The storage capacity of glacial deposits appears to depend to some extent on the aquifer slope (hydraulic gradient). Lateral moraines may potentially sustain baseflow during shorter droughts, while deposits located in flatter areas may store water for longer periods. Due to their large spatial extent in proglacial areas, their capacity to sustain winter baseflow is probably linked to the amount of water recharge during the melt period. The effect of rapid groundwater recharge from early summer snow melt reported before is most likely linked to these glacial deposits.

3. The behavior of rock glaciers is less clear. Most studies report large volumes of coarse material, which is probably reflected by the short transit times in the work of Harrington et al. (2018). However, longer transit times were also reported linked to a finer basal layer (Wagner et al., 2021). The storage capacity of rock glaciers probably depends on the depth of this basal layer and on the spatial extent of such landforms.

4. Few hydrological studies exist in Alpine outwash plains. They may store a considerable volume of silty-sandy sediments and thus may constitute productive aquifers, although this may be countered

by the relatively thin cover of sediment which is typical of current deglaciating Alpine valleys. Based on the strong surface water-groundwater interactions that are reported in the literature, we can assume that their water storage remains generally near saturation until late summer, in opposition to most other landforms. This would support the hypothesis that outwash plains have a considerable hydrological significance. More data on their physical properties and their hydrogeomorphological behavior are however needed.

5. The amount of water stored directly in the fractured bedrock is the largest unknown in proglacial areas because groundwater seepage through deep fractures probably occurs underneath other landforms. Such fractures may be large due to the glacier debuttressing (Bovis, 1990; Grämiger et al., 2017) but only few studies have investigated their importance (Andermann et al., 2012; Cochand et al., 2019).

Figure 2.2: Picture of the main catchment research area from the downstream end of the outwash plain in front of the Otemma glacier.

3

Research paper 1

Towards a hydrogeomorphological understanding of proglacial catchments: an assessment of groundwater storage and release in an Alpine catchment

Tom Müller[1,2], Stuart N. Lane[1], and Bettina Schaefli[1,2,3]

[1]Institute of Earth Surface Dynamics, Lausanne, University of Lausanne, Switzerland

[2]Institute of Geography (GIUB), University of Bern, 3012 Bern, Switzerland

[3]Oeschger Centre for Climate Change Research (OCCR), University of Bern, 3012 Bern, Switzerland

Received: 18 March 2022 – Discussion started: 25 April 2022

Revised: 31 August 2022 – Accepted: 7 November 2022 – Published: 2 December 2022

Hydrol. Earth Syst. Sci., 26, 6029–6054, 2022

https://doi.org/10.5194/hess-26-6029-2022

The chapter provides a comparison of the hydrological catchment-scale response based on discharge recession analysis in order to estimate the overall theoretical groundwater storage and response timescale. It then analyses the response of all landforms inside the Otemma catchment based on a literature review as well as additional field data around the outwash plain aquifer and provide a simple model to estimate their potential storage. Based on the comparison between both approaches, we highlight an important missing compartment from our landform-based analysis which we suggest to attribute to bedrock storage. While the overall results appear robust, it also opens new questions regarding the role of the outwash plain and bedrock storage which are then further investigated in the following chapters.

Abstract

Proglacial margins form when glaciers retreat and create zones with distinctive ecological, geomorphological and hydrological properties in Alpine environments. There is extensive literature on the geomorphology and sediment transport in such areas as well as on glacial hydrology, but there is much less research into the specific hydrological behavior of the landforms that develop after glacier retreat in and close to proglacial margins. Recent reviews have highlighted the presence of groundwater stores even in such rapidly draining environments. Here, we describe the hydrological functioning of different superficial landforms within and around the proglacial margin of the Otemma glacier, a temperate Alpine glacier in the Swiss Alps; we characterize the timing and amount of the transmission of different water sources (rain, snowmelt, ice melt) to the landforms and between them, and we compare the relationship between these processes and the catchment-scale discharge. The latter is based upon a recession-analysis-based framework. In quantifying the relative groundwater storage volumes of different superficial landforms, we show that steep zones only store water on the timescale of days, while flatter areas maintain baseflow on the order of several weeks. These landforms themselves fail to explain the catchment-scale recession patterns; our results point towards the presence of an unidentified storage compartment on the order of 40 mm, which releases water during the cold months. We suggest attributing this missing storage to deeper bedrock flowpaths. Finally, the key insights gained here into the interplay of different landforms as well as the proposed analysis framework are readily transferable to other similar proglacial margins and should contribute to a better understanding of the future hydrogeological behavior of such catchments.

3.1 Introduction

Glaciated catchments are highly dynamic systems characterized by complex physical, chemical and biological interactions at multiple scales ranging from local processes in the glacier ice to regional effects transmitted from the glacier forefield to downstream regions (Carrivick and Heckmann, 2017; Miller and Lane, 2018). In such environments, where nutrients and energy are limited and climate variations are large, glaciers provide water (Huss et al., 2017), sediments (Hallet et al., 1996) and organic carbon (Brighenti et al., 2019b) to downstream areas, which sustain a high regional biodiversity (Milner et al., 2009). At the regional scale, glaciers provide a number of ecological services essential for human society, such as water supply for drinking water purposes and irrigation, hydropower or cultural services (Beniston et al., 2018; Haeberli and Weingartner, 2020). Water resource availability is undergoing strong seasonal modifications due to climate warming, with rapid glacier retreat worldwide (Milner et al., 2017), e.g., an estimated volume loss of 84 ± 15 % by 2100 in the European Alps (Huss et al., 2017). Peak annual runoff from glacier melt will be reached between 2010 and 2060 across the world (Huss and Hock, 2018), and the subsequent reduction of ice available to melt, together with more liquid precipitation and earlier snowmelt (Klein et al., 2016; Lane and Nienow, 2019), will cause a change in streamflow regimes, with a shift in the flow magnitude and in the timing of high flows to earlier months (Beniston et al., 2018; Berghuijs et al., 2014; Gabbi et al., 2012; Lane and Nienow, 2019).

While numerous discussions of the implications of cryosphere changes have been published (e.g., Beniston et al., 2018; Huss et al., 2017; Immerzeel et al., 2020), the role of groundwater is typically neglected in many glaciohydrological studies in Alpine environments (Vuille et al., 2018). This is surprising given the rapidly growing body of literature on groundwater–snowmelt interactions, e.g., for environments with regular droughts (Fayad et al., 2017; Jefferson et al., 2008; Van Tiel et al., 2021), as well as regional studies highlighting large groundwater contributions to streamflows in the Andes (Vuille et al., 2018) and in the Himalayas (Andermann et al., 2012; Yao et al., 2021). Recent studies started to tackle this issue by estimating groundwater contribution at the catchment scale or by analyzing the hydrological processes of specific landscape units. At the catchment scale, water-stable isotopes as well as other geochemical tracers were used to identify groundwater contributions of 20 % to 50 % for sub-catchments with 25 % to 4 % glaciated cover (Engel et al., 2016, 2019; Penna et al., 2017). While those studies provide interesting insights into the role of groundwater to sustain baseflow, the allocation of storage to specific hydrological units remains unclear. This is problematic as such systems are subject to rapid geomorphological changes, with large areas of previously ice-covered till and bedrock becoming exposed in proglacial margins (Heckmann and Morche, 2019), leading to the emergence of new landforms that have high groundwater storage potential (Hayashi, 2020). Thus, studies focusing on the integrated catchment-scale response provide little information on the internal mechanisms which maintain baseflow, and they therefore cannot predict future changes in groundwater storage and its contribution to streamflow.

Other studies have approached this issue by characterizing the structure and hydrological response of specific geomorphological units in terms of water partitioning, storage and release (Wagener et al., 2007). Those unconsolidated superficial landforms are formed by different glacial and slope processes, have different internal structures and sedimentology and create a complex mosaic of landforms in glaciated catchments, which we summarize in Fig. 3.1.

A recent comprehensive study of the hydrogeological processes in such geomorphological landforms was provided in the work of Hayashi (2020). Here, we only retain some key information. Morainic material can be deposited both on slopes or in flatter areas. They are composed of a non-sorted mix of fine to coarse materials, which may contain more consolidated till (Ballantyne, 2002). Where they are in contact with a stream network, complex interactions occur and relatively deep aquifers (10 m depth) can be formed, which may sustain baseflow during dry periods (Kobierska et al., 2015b; Magnusson et al., 2014). Heavily debris-covered relict glaciers lead to the formation of rock glaciers. They were shown to consist mainly of a coarse layer with high hydraulic conductivity but contain a 1 to 2 m basal layer of finer water-saturated sediments, which can store significant water amounts (Harrington et al., 2018; Wagner et al., 2021; Winkler et al., 2016). In flat valley bottoms, fluvial deposition of sandy–gravelly material will lead to the creation of so-called glaciofluvial outwash plains (Maizels, 2002). They collect water from multiple sources and maintain

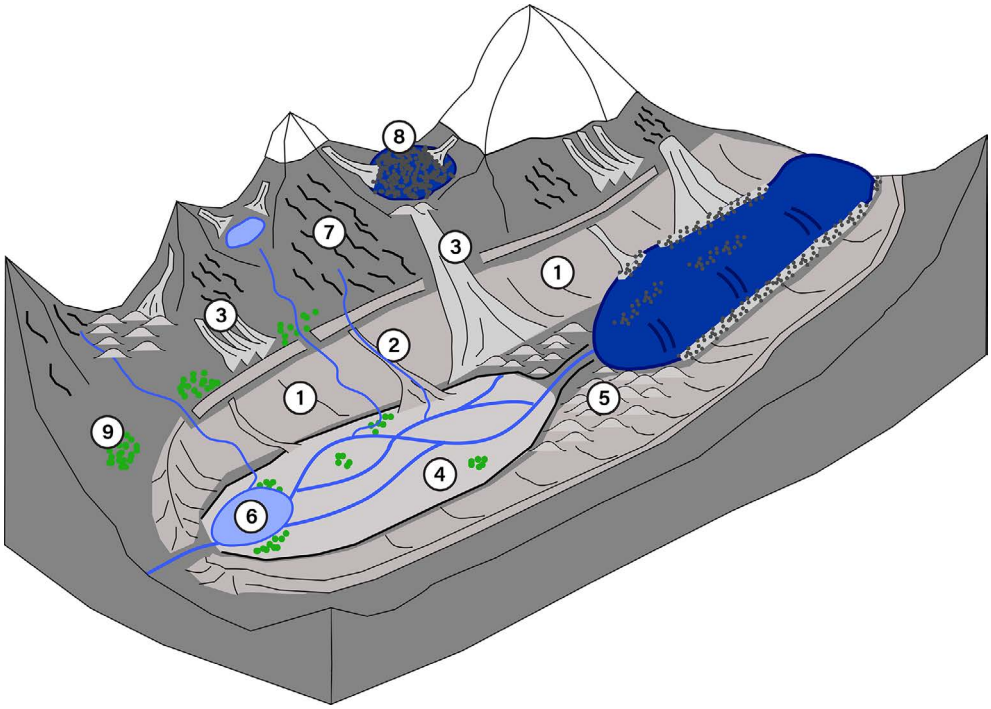

Figure 3.1: General overview of geomorphological landforms typical of proglacial zones. (1) Lateral moraine (grey); (2) debris cone; (3) talus slope (light grey); (4) fluvial outwash plain; (5) glacial deposit (till); (6) proglacial lake; (7) apparent bedrock (dark grey); (8) debris-covered rock glacier; (9) vegetation patches. Snow on the mountain tops is in white, and the glacier is in blue on the right (figure inspired by Temme (2019)).

groundwater-fed river channels in fall, promoting habitat heterogeneity and high local biodiversity (Crossman et al., 2011; Hauer et al., 2016; Malard et al., 1999; Ward et al., 1999). Older outwash plains were shown to have strong interactions with glacier-fed streams (Mackay et al., 2020; Ó Dochartaigh et al., 2019) and to provide upward groundwater exfiltration contributing between 35 % and 50 % to river baseflow (Käser and Hunkeler, 2016; Schilling et al., 2021). On hillslopes, debris not linked to glaciogenic origin comes from rock slope failures, leading to the formation of talus slopes. These talus slopes are composed of coarser debris than morainic material, showing thereby little water retention capacity and fast water transfer to downstream units (Muir et al., 2011).

Those studies provide key information on the groundwater dynamics of selected units; they are, however, rarely integrated into a perceptual model that brings together knowledge of all units, which compares their relative storage volumes and their contribution to streamflow and thereby explains the overall catchment-scale hydrological response. To our knowledge, only a limited number of studies propose an integrated description of the hydrogeological behavior of proglacial margins: in the Canadian Rockies a series of papers studied the hydrogeology of different proglacial structures and were summarized in the work of Hayashi (2020); in the Cordillera Blanca in Peru a suite of studies (Baraer et al., 2015; Glas et al., 2018; Gordon et al., 2015; Somers et al., 2016) focused on the role of groundwater for streamflow in different proglacial valleys, and in the Swiss Alps, there is a review of the hydrological behavior of proglacial landforms by Parriaux and Nicoud (1990).

From our perspective, but as also highlighted by others (Heckmann et al., 2016; Vincent et al., 2019), there is still a need for integrative studies that (i) document the hydrological functioning of proglacial landforms with appropriate metrics, (ii) propose a framework to characterize the timing, amount and location of the transmission of different water sources (rain, snow, ice) to these landforms and between each of them, (iii) compare whether the documented response of individual landforms can explain the observed catchment-scale behavior in terms of streamflow amounts, timing and geochemistry and (iv) propose a unifying theory for the geomorphological, ecological and hydrological evolution of such rapidly evolving catchments.

Within this paper, we propose a framework to address the first three of the above-mentioned points. First, we present field observations from the Otemma catchment and our case study in the Swiss Alps (Sect. 3.2.1)

and discuss the different hydrological behaviors observed around the outwash plain, based on electrical conductivity data, direction of groundwater flowpaths and an estimation of hydraulic conductivity (Sect. 3.3.1). We then propose a methodology to characterize the hydrological behavior of the different superficial landform storages by assessing their storage–discharge relationship based on recession analysis and a literature review of the timescales of their hydrological response (Sect. 3.3.3). Applied to our case study, we quantify the seasonal storage and discharge capacity for each landform with a simple model (Sect. 3.3.5). Finally, we perform a multi-year recession analysis at the catchment outlet to analyze the catchment-scale hydrological response (Sect. 3.3.2) and compare the estimated catchment-scale storage with the storage of each landform obtained from the previous analysis.

3.2 Study site and field methods

3.2.1 Site description

With an ice-covered area of about 14 km^2, the Otemma glacier (45°56′03″ N, 7°24′42″ E) in the western Swiss Alps is amongst the 15 largest glaciers of Switzerland (Fischer et al., 2014). The glacier is characterized by a relatively flat tongue, which has retreated by about 2.3 km since the Little Ice Age (LIA) and 50 m yr^{-1} since 2015 (GLAMOS (1881-2020)). A recent study suggested an almost complete glacier retreat by 2060 (Gabbi et al., 2012).

A Tyrolean-type water intake (GTZ, 1989) has been constructed for hydropower production about 2.5 km downstream of the current glacier terminus and is used in the present study as the outlet of what we call the Otemma basin (Fig. 3.2b). It has an area of 30.4 km^2, a mean elevation of 3005 m a.s.l. (2350 to 3780 m) and a glacier coverage of 45 % in 2019 (adapted from GLAMOS (1881-2020)).

The geology of the underlying bedrock is composed of gneiss and orthogneiss from the Late Paleozoic Era with some granodiorite inclusions (Burri et al., 1999). The main geomorphological forms comprise bedrock, with some vegetation cover above the LIA limit (46 %), steep slopes (30 % post-LIA lateral moraines and 10 % talus slopes), gently sloping debris fans and morainic deposits (13 %) and a flat glaciofluvial outwash plain (0.9 %) (Fig. 3.2b). One main subglacial channel at the glacier snout provides water to a large, highly turbid and turbulent stream, which quickly reaches a flat outwash plain composed of sandy–gravelly sediments; this leads to a braided river network, which eventually converges in a more confined channel about 1 km downstream and extends to the hydropower intake. A few tributaries from small hanging glaciers or valleys also contribute to river discharge during the snow-free season.

3.2.2 Hydrometeorological data

In July 2019, we installed an automatic weather station (Fig. 3.2a) at the glacier snout at an elevation of 2450 m a.s.l., which recorded with a 5 min resolution air temperature, humidity, atmospheric pressure (Decagon VP-4) and liquid precipitation (Davis tipping rain gauge). After July 2020, total incoming shortwave radiation was also recorded by the device (Apogee SP-110). For the present analysis, winter solid precipitation data were provided by SwissMetNet, the Swiss automatic monitoring network, using information from the Otemma station (2.7 km from the glacier snout) or the Arolla station (10 km from the glacier snout). Data with a detailed description are available on Zenodo (Müller, 2022a).

3.2.3 Hydrological data

Hourly river stage was recorded from 2006 to 2018 at the water intake corresponding to the catchment outlet (GS3, Fig. 3.2a) by the local hydropower company (Force Motrice de Mauvoisin, FMM); corresponding discharge was estimated using a theoretical stage–discharge relationship provided by FMM. We post-processed the data by in-filling data gaps related to regular sediment flushing events (of duration < 1 h) with linear interpolation. Winter discharge was also recorded, although a data gap usually occurred from October to December.

In August 2019, we installed three river gauging stations, one in the vicinity of the glacier snout (GS1), one

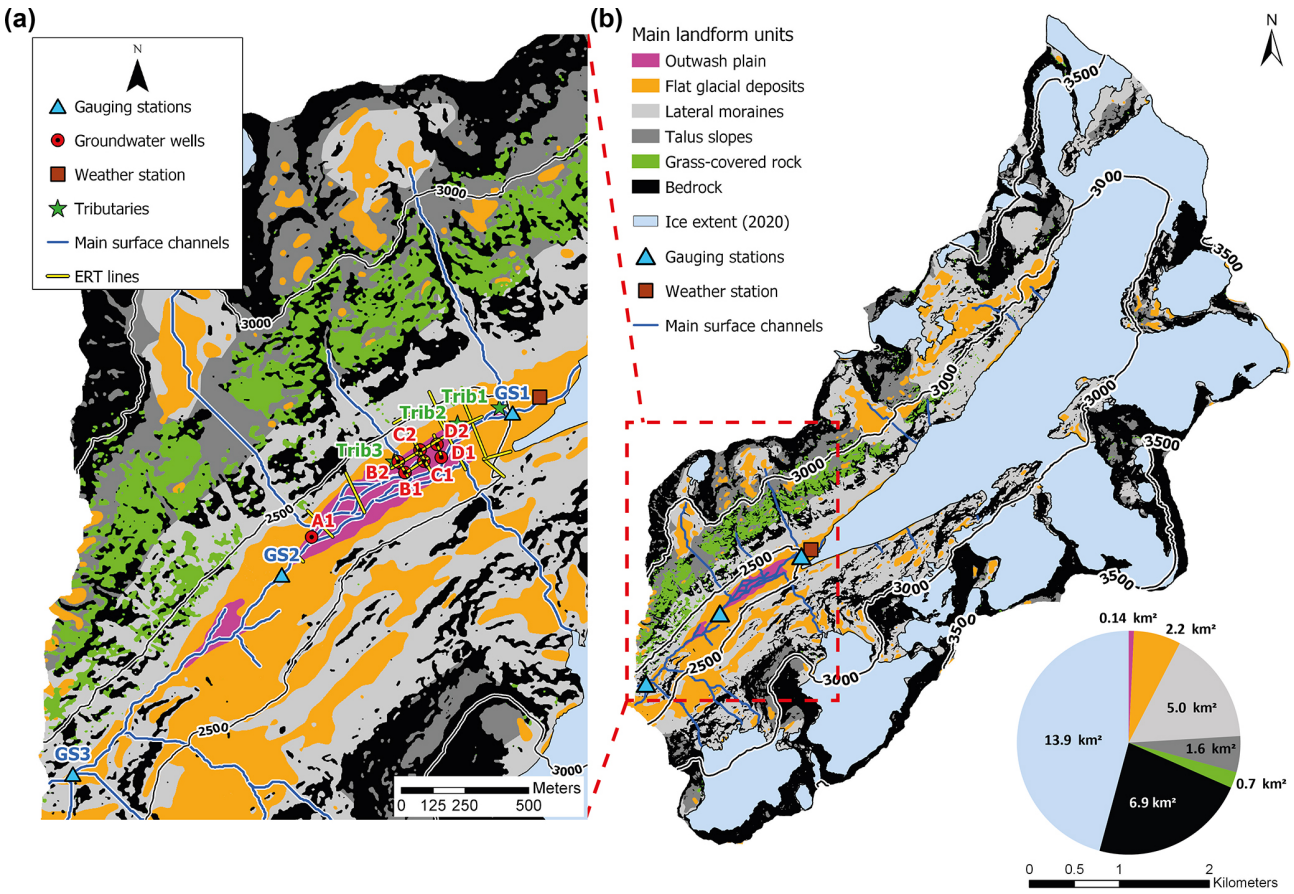

Figure 3.2: **(a)** The zoom-in window shows the field measurement stations installed between 2019 and 2021 as well as the ERT lines. The outwash plain is located between gauging stations 1 and 2 (GS1 and GS2). **(b)** Overview of the Otemma catchment classified based on its main geomorphological landforms (see Sect. 3.3.4). The pie chart shows the surface area of each unit.

at the end of the outwash plain (GS2) and one at the catchment outlet (GS3) (Fig. 3.2a). River stage, water electrical conductivity (EC) and water temperature were recorded continuously at 10 min intervals using an automatic logger (Keller DCX-22AA-CTD). Periodic EC and discharge measurements were also made in many tributaries and water sources, with a main focus on three representative tributaries along the outwash plain. Finally, we installed seven groundwater wells consisting of fully screened plastic tubes at an averaged depth of 1.5 to 2 m in the outwash plain, which covered four transects (A to D) perpendicular to the river in the direction of the base of the hillslope. Water table elevation was recorded in each well at a 10 min interval using SparkFun MS5803-14BA pressure sensors. Sensor bias was verified and corrected by bimonthly manual groundwater stage measurements. A more detailed description of the data is available on Zenodo (Müller and Miesen, 2022).

3.2.4 Electrical resistivity tomography

Electrical resistivity tomography (ERT) was used to map the sediment structure in the outwash plain. We performed a total of 21 lines from 2019 to 2021 using a Syscal Pro Switch 48 from Iris Instruments (Fig. 3.2a). The electrode array consisted of 48 electrodes with a spacing between 1.5 and 4 m, and dipole–dipole (DD) and Wenner–Schlumberger (WS) schemes were systematically used for better data interpretation. We processed the data using the open-source pyGIMLi python library (Rücker et al., 2017). All data inversions were calculated using a robust scheme (L1 norm) with different regularization strength (lambda from 1 to 100) to assess overfitting and underfitting. The depth of the outwash plain sediments was estimated by performing multiple transects in different parts of the outwash plain and by identifying the transition from water-saturated sediments with a resistivity value between 500 and 2000 Ω m and the bedrock layer with a resistivity of 4000 to 7000 Ω m, similar to other studies (e.g., Harrington et al., 2018; Langston et al., 2011).

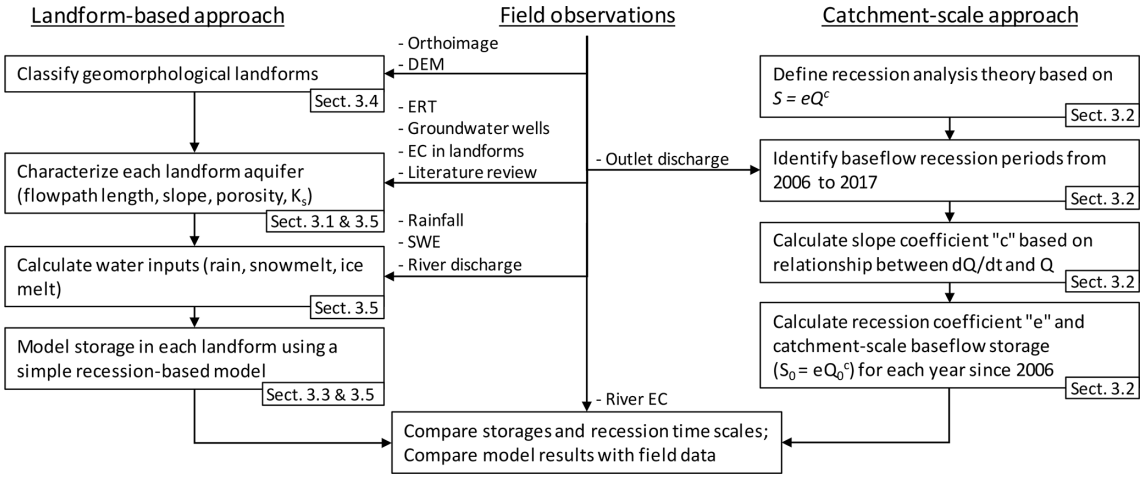

Figure 3.3: Sketch of the adopted workflow, separated between field observations and landform-based and catchment-based methods. The corresponding sections in the methodology are also highlighted. All abbreviations are detailed in the text.

More detailed information on the data, results, codes and maps is available on Zenodo (Müller, 2022c).

3.3 Data analysis methods

In this study we used two frameworks based on recession theory to analyze both the catchment-scale hydrological response and the response of individual landforms. These two approaches were applied to our case study in the Swiss Alps using various field data, and we ultimately compare the results obtained from both methods together and against field observations. The workflow of the overall methodology is summarized in Fig. 3.3.

3.3.1 Estimation of hydraulic conductivity in the outwash plain

While some literature exists to characterize most geomorphological landforms in glaciated catchments, data on post-LIA outwash plains in Alpine environments are scarce. We therefore used two different methods to estimate the saturated hydraulic conductivity (K_s) of the outwash plain.

The first method applied the pressure wave diffusion method documented in the work of Magnusson et al. (2014). Given a certain hydraulic diffusivity (D), this method was used to relate the aquifer head variations (h) at a distance x from the stream to the diel stream stage cycles ($h_{x=0}$) generated by ice melt. It furthermore made use of a simplified 1D Boussinesq equation, where advective fluxes were neglected (Eq. 3.1). This procedure is only valid for relatively flat aquifers with a thick unconfined saturated layer and where evapotranspiration losses can be neglected (Kirchner et al., 2020), which makes this approach well-suited for high-elevation outwash plains. By comparing the phase shift (time lag) and the amplitude dampening between the river stage and the groundwater signals, the aquifer hydraulic diffusivity (D) was estimated and related to K_s using the aquifer thickness (B) and assuming that the specific yield (S_y) was similar to the aquifer porosity (Eq. 3.2).

$$\frac{\delta h}{\delta t} = D\frac{\delta^2 h}{\delta x^2} \tag{3.1}$$

$$D = \frac{K_s B}{S_y} \tag{3.2}$$

For this analysis, we used the two upstream and downstream well transects (B and D; see Fig. 3.2a) for two periods: during high flow in mid-August 2019 and during a lower-flow period in mid-September 2019. An additional groundwater well "B3" on transect B was also used for this analysis. The 1D partial differential equation was solved using a central-differencing scheme in space and a Crank–Nicolson method in

time, imposing the measured river stage variations as a boundary condition. Prior to solving the equation, both river stage and groundwater heads were detrended by substracting the linear trend of each dataset as suggested by Magnusson et al. (2014). We then calibrated the model parameter D using a Monte Carlo approach where we minimized the root mean square error and maximized the Spearman rank correlation between observed and modeled groundwater heads. Hydraulic conductivity was finally calculated based on the aquifer thickness estimated by ERT, and porosity was estimated by measuring saturated water content (Decagon 5TM) at five locations in the upper sediment layer.

A second independent estimation of the hydraulic conductivity was obtained with salt tracing, using ERT time lapse with a measurement cycle of about 30 min. We injected 3 kg of salt dissolved in 15 L of water in a 1 m-deep pit in the center of the outwash plain and recorded the timing of the passage of the salt plume at a downstream transect (distance 9.38 m) using ERT, similarly to the work of Kobierska et al. (2015a). We only installed one ERT line perpendicular to the groundwater flow consisting of 48 electrodes with a 1 m spacing. Hydraulic conductivity can be calculated by solving Darcy's law for the mean pore velocity as follows:

$$v_\mathrm{p} = \frac{K_\mathrm{s}}{\theta_s}\frac{\mathrm{d}h}{\mathrm{d}x}, \tag{3.3}$$

where $\frac{\mathrm{d}h}{\mathrm{d}x}$ is the aquifer gradient, θ_s is the aquifer porosity and v_p is the mean pore velocity corresponding to the travel distance divided by the travel time of the center of gravity of the salt plume.

3.3.2 Catchment-scale recession analysis

We analyzed the storage–discharge relationship at the catchment scale by using a classical recession analysis during periods when both water inputs (snow, rain) as well as outputs (evapotranspiration) can be neglected, i.e., during periods when discharge is only related to aquifer storage (Clark et al., 2009; Kirchner, 2009). Following Kirchner (2009), we describe the recession behavior of the aquifer storage with a nonlinear storage (S)–discharge (Q) function,

$$S = eQ^c, \tag{3.4}$$

whose derivative, using $\frac{\mathrm{d}S}{\mathrm{d}t} = -Q$, is given by

$$-\frac{\mathrm{d}Q}{\mathrm{d}t} = \frac{1}{\mathrm{ce}}Q^{(2-c)}. \tag{3.5}$$

This is usually summarized as $-\frac{\mathrm{d}Q}{\mathrm{d}t} = aQ^b$, where $a = 1/\mathrm{ce}$ is the recession coefficient and $b = 2 - c$ is the slope coefficient (Santos et al., 2018). The release behavior of the catchment-scale storage was characterized by identifying zones where the slope of the relationship between the rate of change ($-\frac{\mathrm{d}Q}{\mathrm{d}t}$) and discharge ($Q$) is constant in the logarithmic scale, which allowed calculation of the slope coefficient b.

We performed the recession analysis for the 12-year period of discharge data provided by FMM at the catchment outlet (GS3). The recession periods were automatically selected by identifying periods where flow is constantly decreasing for at least 10 d and is extended until the first increase in flow. The discharge recession data were smoothed (moving average with a span of 50 % of a given recession period) to remove small step-like decreases or small drops due to sensor failures, so that only the averaged trends are analyzed. Finally, we plotted the relationship between ($-\frac{\mathrm{d}Q}{\mathrm{d}t}$) and discharge ($Q$), and we average the recession points from all years in bins with an equal number of points (we selected 100), as suggested in the work of Kirchner (2009), to which we apply a linear regression (nonlinear least squares method, MATLAB R2019a). This procedure allowed estimation of the slope coefficient b. Once b is identified, we fitted a power-law function on the raw discharge data (without any smoothing) for each winter recession, using the analytical solution of Eq. (3.5) in order to estimate the recession coefficient e. Finally, this allowed us to relate the maximum baseflow discharge Q_0 to the catchment-scale baseflow storage S_0 using Eq. (3.4).

3.3.3 Assessing the hydrological response based on aquifer characteristics and recession analysis

Similarly to the catchment-scale recession analysis, the same relationship between storage and discharge can be applied to specific landforms, which allows estimation of the rate of water storage and release in

different parts of a glaciated catchment. For instance, the form of the water table in an aquifer can be linked to the shape and physical properties of the landform (Troch et al., 2013). Using some simplifications, the Boussinesq equation (Boussinesq, 1904) provides a physically based means of estimating the temporal variation of the aquifer table along a one-directional aquifer and thus allows estimation of discharge based on the groundwater gradient and physical properties of the aquifer (Harman and Sivapalan, 2009a). For flat aquifers with homogeneous conductivity, a slope b of 1.5 ($c = 0.5$) is common for the late recession (Rupp and Selker, 2006). Here, an analytical solution of the Boussinesq equation was proposed, leading to the discharge solution (Rupp and Selker, 2005; Wittenberg and Sivapalan, 1999) shown in Eqs. (3.6) and (3.7).

$$S = eQ^{0.5} \tag{3.6}$$

$$Q_t = Q_0(1 + \alpha t)^{-2} \tag{3.7}$$

$$\alpha = \frac{Q_0^{0.5}}{e} \approx \frac{K_s h_m}{\phi L^2} \tag{3.8}$$

A physical description of α was proposed (Eq. 3.8) based on the aquifer conductivity (K_s) and porosity (ϕ), the aquifer length (L) and the aquifer thickness at distance L (h_m) (Dewandel et al., 2003; Rupp and Selker, 2005; Stewart, 2015).

In the case of a significantly sloping aquifer (> 10°), a value $b = 1$ is usually proposed for the late drainage (Muir et al., 2011; Rupp and Selker, 2006). In this case, if the aquifer thickness was small enough, the aquifer flux would be mostly advective and conducted by the bedrock slope (Harman and Sivapalan, 2009b), so that discharge recession becomes linear (Eqs. 3.9 and 3.10). Due to the nonlinearity of the Boussinesq equation, the parameter α could only be approximated using numerical linearization approaches (Hogarth et al., 2014; Verhoest and Troch, 2000). In this study we used one of the simplest proposed descriptions for α (Eq. 3.11), similar to the previous one, where only h_m/L (the aquifer slope) is replaced by $\sin(\theta)$ and θ is the bedrock slope (Berne et al., 2005; Harman and Sivapalan, 2009a; Rupp and Selker, 2006).

$$S = eQ \tag{3.9}$$

$$Q_t = Q_0 e^{-\alpha t} \tag{3.10}$$

$$\alpha = \frac{1}{e} \approx \frac{K_s \sin(\theta)}{\phi L} \tag{3.11}$$

In both equations (Eqs. 3.7 and 3.10), the rate of aquifer decline can be related to a recession constant ($1/\alpha$), corresponding to the characteristic response time of the aquifer. Based on this approach, we reviewed the range of estimated hydraulic conductivity values reported in recent studies for typical landforms in glaciated catchments. Combined with realistic aquifer properties (slope, porosity, aquifer length) for each type of landform, we applied the proposed relationships for flat (Eq. 3.8) or sloping aquifers (Eq. 3.11) and finally assessed the recession timescales ($1/\alpha$) at which different storage compartments provide water for baseflow.

3.3.4 Superficial landform classification

Landform classification was performed by combining a visible band orthoimage from 2020 with a 10 cm resolution (SwissTopo, 2020a) and a 2 m resolution digital elevation model (DEM) (SwissTopo, 2019). We calculated the slope from the DEM and classified it in categories as suggested in the work of Carrivick et al. (2018): < 8° for outwash plains; 8–22° for mildly sloping glacial deposits and debris cones; 22–42° for lateral moraines below the LIA limit and talus slopes above the LIA limit; > 42° for bedrock. We then downscaled the orthoimage to 2 m and combined the RGB bands with an additional band corresponding to the slope classes. We manually identified small zones corresponding to the main landform features and performed a supervised classification using a random tree classifier (ArcGIS Pro v2.3). We finally calculated the median class for a moving window of 10 cells by 10 cells (20 × 20 m) to smooth out noise in the results. A specific class for grass was used, since many grass patches were identified above the LIA line on shallow soils on top of bedrock. Lateral moraines below the LIA line were distinguished from coarser debris talus slopes with similar slopes in zones where glaciers were absent during the LIA. The glacier extents from 1850 (LIA limit) and 2016 are provided by the Swiss Glacier Inventory 2016 (Linsbauer et al., 2021). The results are presented in Fig. 3.2b.

3.3.5 Landform-based model of the hydrological response of single geomorphological units

Based on the previously discussed recession theory (Sect. 3.3.3), we propose a simple methodology to estimate the seasonal storage and discharge contribution of each individual superficial landform storage compartment in the Otemma catchment. In order to estimate the maximum water storage, we used the total area (A_i) of each classified landform (Sect. 3.3.4) and an estimation of their sediment thickness, similarly to other studies (Hood and Hayashi, 2015; Rogger et al., 2017). Sediments are however never fully water-saturated, so that it remained difficult to estimate the maximum aquifer thickness for each landform. To overcome this limitation, we defined a simple hydrological model where we simulated a realistic daily water input (Q_{in}) in the form of rain (P_{rain}) and snowmelt (P_{snow}) and estimated storage (S) and outflow discharge (Q_{out}) based on the nonlinear storage–discharge relationship (Eq. 3.4). We defined c based on the landform slope and estimated e following Eq. (3.8) or (3.11) using realistic hydrological characteristics of each landform: hydraulic conductivity was based on our measurements (Sect. 3.3.1) or from a review of the literature, while the aquifer slope and length were estimated for each landform based on our landform classification by manually measuring the averaged landform length (Fig. 3.2b).

Following this approach, we defined Eqs. (3.12) to (3.14) in order to simulate the seasonal storage and discharge over a whole year.

$$\frac{\delta S_t}{\delta t} = Q_{\text{in,t}} - Q_{\text{out,t}}, \tag{3.12}$$

$$Q_{\text{in,t}} = \left(\left(P_{\text{snow,t}} + P_{\text{rain,t}}\right) A_i + Q_{\text{glacier,t}}\right) / A_{\text{catchment}}, \tag{3.13}$$

$$Q_{\text{out,t}} = \left(\frac{S_t}{e}\right)^{1/c}, \tag{3.14}$$

where $\frac{\delta S}{\delta t}$ is the change in storage in mm d^{-1}, $Q_{\text{in,t}}$ is the daily water input at time t and $Q_{\text{out,t}}$ is the generated daily output discharge based on the nonlinear storage–discharge equation. P_{snow} and P_{rain} are the daily snowmelt and daily liquid precipitation in mm d^{-1}, A_i is the area of each landform, Q_{glacier} is the daily river discharge from the glacier in L d^{-1} and $A_{\text{catchment}}$ is the total catchment area in square meters. Finally, e is the recession parameter estimated based on α (Eq. 3.8 or 3.11) and c the slope coefficient (1 for slopping aquifers > 10° and 0.5 for flatter aquifers). In these equations, the landform storage (S_t) was scaled by dividing the volume by the entire catchment area, which allowed ready comparison of the storage associated with each landform.

The snowmelt input was modeled with a snow accumulation routine (rain transitions to snow from an air temperature between 1 and 2 °C) and a degree-day model for daily snowmelt estimation following Gabbi et al. (2014), with a degree-day melt factor of 6.0 mm °C^{-1} d^{-1} when air temperature is higher than 1 °C. The catchment was separated into 50 m elevation bands with a calibrated temperature lapse rate of 0.5 °C 100 m^{-1} and a precipitation lapse rate of +10 % 100 m^{-1}. Winter precipitations from SwissMetNet were adapted using a correction factor for each year. The melt parameters, precipitation correction factor and lapse rates were estimated by minimizing the error between modeled and observed snow water equivalent (SWE) based on 92 snow depth measurements and two snow pits for density measurements made near the maximum snow accumulation on 28 May 2021. It was further calibrated by matching the snowline limit during the snowmelt season as suggested in Barandun et al. (2018), based on daily 3 m resolution Planet images (Planet Team, 2017). Snowmelt and rain inputs were considered to recharge entirely the whole aquifer (no surface flow), and there was no routing or water exchange between the different landforms, so that our estimates represent the maximum potential storage linked to a realistic maximum recharge.

In the case of the outwash plain, an additional glacier melt input (Q_{glacier}) was provided, since this is the only landform directly recharged by the river network in Otemma. Only a small fraction of the total river discharge was allowed to recharge the outwash plain aquifer. An infiltration rate of 100 L s^{-1} (2 % of mean summer discharge) from May to October was used, estimated from dilution gauging along the stream and preliminary modeling results. This amount was also found to realistically approximate the rate of recharge observed using the groundwater wells. Finally, the maximum storage (sediment thickness) of the reservoirs cannot be exceeded in any landform.

Based on the three sources of water (rainwater, snowmelt, glacial stream), a small routine was also added

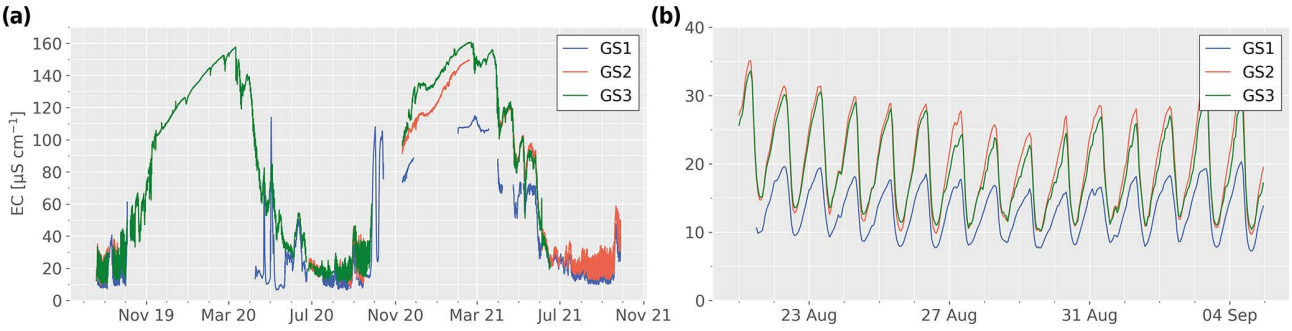

Figure 3.4: **(a)** Streamflow electrical conductivity (EC) at the three gauging stations (GS1 to GS3) during 2 years. **(b)** Zoom-in window showing the EC for the first 20 d of measurement. Large gaps in winters are due to sensor failures.

to calculate the source water partitioning in each landform. At each time step, the reservoir was assumed to be fully mixed and a water amount for each water source was removed, proportional to the estimated partitioning at the previous time step and so that the total water removed equates the calculated discharge ($Q_{\text{out},t}$). The amount of water recharge from each source is then added, and a new partitioning is calculated. This allowed tracking of the seasonal contribution of different water sources in each landform.

3.4 Results

3.4.1 Water electrical conductivity

3.4.1.1 Stream observations

Streamflow EC in the Otemma catchment shows strong seasonal and diel cycles driven by snowmelt and glacier melt (Fig. 3.4). During summer, when discharge is highest, streamflow EC remains very low, with small diel variations on the order of 10 to 20 μS cm^{-1} (Fig 3.4b). During this period, EC is strongly negatively correlated with river discharge, with maximum streamflow EC in the morning. There is an EC increase between the glacier snout (GS1) and the end of the outwash plain (GS2) but little change further downstream. Indeed, during summer high flow, the EC difference between GS2 and GS3 is very limited, with EC at GS3 consistently smaller by a few μS cm^{-1} in the morning when EC is maximal. This decrease is likely due the contribution of the two main surface tributaries fed by ice melt from the southwestern-most hanging glacier (see Fig. 3.2), where water is characterized by low EC. Additionally, this very limited change in EC could indicate little contribution from groundwater with higher EC in this zone compared with the larger increase in EC observed in the outwash plain region (GS1 to GS2).

After November, EC increases gradually during the whole winter (Fig 3.4a), until the first onset of snowmelt in early spring. Similar to the summer, there is a difference in EC between GS1 and GS2, which becomes larger as EC at GS1 increases less rapidly in March 2021. A small EC difference between GS2 and GS3 only occurs during the very low-flow conditions from mid-November to March. This EC increase suggests that, during winter, the contribution of ice melt from the hanging glaciers is likely very limited, so that some groundwater contributions from the hillslopes become dominant and contribute to increasing the stream EC between GS2 and GS3. The change appears however smaller than between GS1 and GS2, suggesting less groundwater contribution in this zone, similar to the observation in the summer.

3.4.1.2 Hillslope and groundwater observations

We monitored the EC of selected landforms as well as of different water sources. The averaged snowmelt EC was 5.1 ± 2.5 μS cm^{-1} based on 28 snowpack samples collected during the snowmelt season in the outwash plain and on the glacier surface up to 2850 m a.s.l. Surface ice-melt samples show EC values of 5.7 ± 4.3 μS cm^{-1} based on 29 samples. The average rain EC value is 31.6 ± 11.3 μS cm^{-1} based on 11 samples. The reason for a slightly higher EC in rain than snowmelt is not known but has also been reported in other studies (Zuecco et al., 2019).

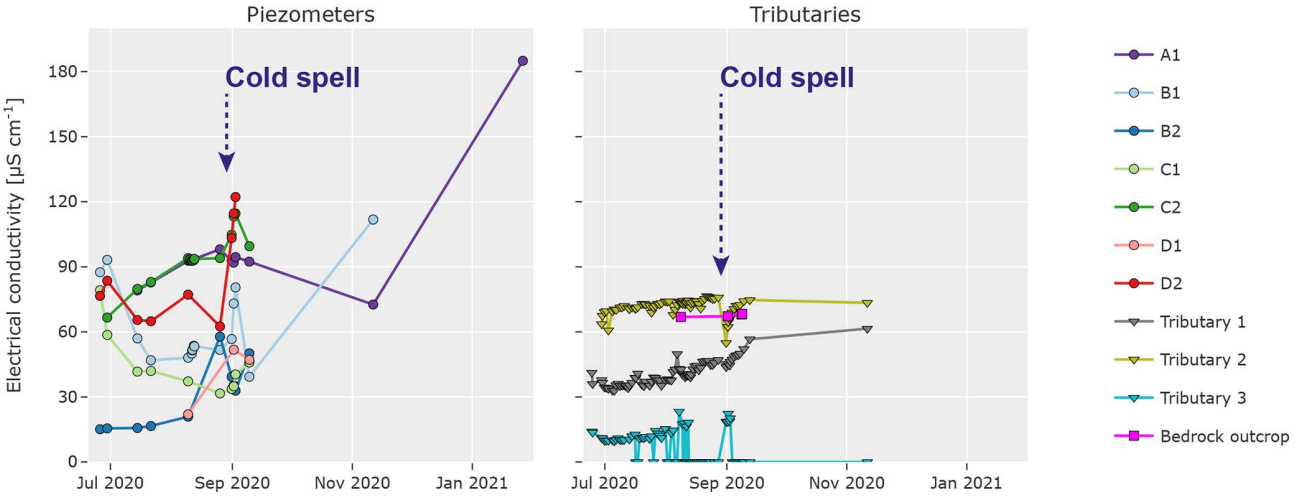

Figure 3.5: Temporal evolution of EC at seven wells (A1 to D2) in the outwash plain, in three tributaries as well as one bedrock spring (see Fig. 3.2a for the location). Values of 0 for tributary 3 indicate no surface flow. A cold spell resulting in snowfall over the whole catchment is indicated by the dark blue arrow.

Tributaries on the side of the outwash plain show only limited change in EC during summer (Fig. 3.5) but present different trends. Tributary 1 is located below a hanging valley, likely containing buried ice or permafrost and snow at high elevation, leading to a perennial superficial flow. The relatively low EC of this tributary seems to indicate a marginal groundwater contribution, with probably only a short contact time between the morainic material and meltwater in the higher part of the catchment. Tributary 2 exfiltrates from sediments at the base of the lateral moraine, and its EC is only slightly higher than the bedrock exfiltration, suggesting that this tributary is mainly fed by water stored in the bedrock which infiltrates in the coarse sediments of the lateral moraine and re-emerges at the base of the outwash plain. During a cold spell (30 August), accompanied by a heavy rain event (42 mm) on the preceding day, a small drop in EC in tributary 2 can be observed and is likely related to an increased water storage in the lateral moraines, which empties in a few days. Tributary 3 maintains low EC close to the value of snowmelt and becomes dry in August, indicating its direct dependence on snowmelt transmitted by overland flow with hardly any contact time with the sediments.

The EC measured in the groundwater wells shows much stronger variations, both spatially and temporally (Fig. 3.5). In the upper part of the outwash plain (wells B, C, and D), groundwater EC near the stream is low and similar to the stream EC, indicating strong stream infiltration to the outwash plain. Near the hillslopes, EC is higher and also larger than the tributaries, indicating either contribution from deeper hillslope exfiltrations with higher EC or river contribution with long flowpaths from the stream network. During the cold spell, river discharge decreased and groundwater EC became larger in C2 and D2, likely due to decreased infiltration from the river and an increased influence from a deeper groundwater source. Well A1 shows a smoother signal, with high values year-round and a gradual increase in summer, likely due to the decreasing snowmelt contribution in the outwash plain. During winter, groundwater EC in well A1 increases, rapidly reaching 180 μS cm^{-1}.

3.4.2 Groundwater dynamics in the outwash plain

From the groundwater head observations in the outwash plain, we computed the daily averaged lateral (perpendicular to the stream) and longitudinal (parallel to the stream) aquifer gradients (Fig. 3.6). During the summer, the lateral upstream gradient (well D1–D2) is mostly comprised between 0 % and 0.5 %. The EC at well D2 is similar to tributary 2, which suggests a hillslope recharge from tributary 2 or a constant deeper bedrock exfiltration which maintains a mild lateral gradient towards the stream. The lateral downstream gradient (wells B1–B2) shows a stronger slope of about 1 % in the direction of the stream, which gradually decreases to values close to 0 % by September. This gradient seems closely related to the snowmelt-fed tributary 3. Indeed, well B2 shows a low EC in the early melt season, similar to tributary 3, which only increases in mid-August, when this tributary runs dry (Fig. 3.5).

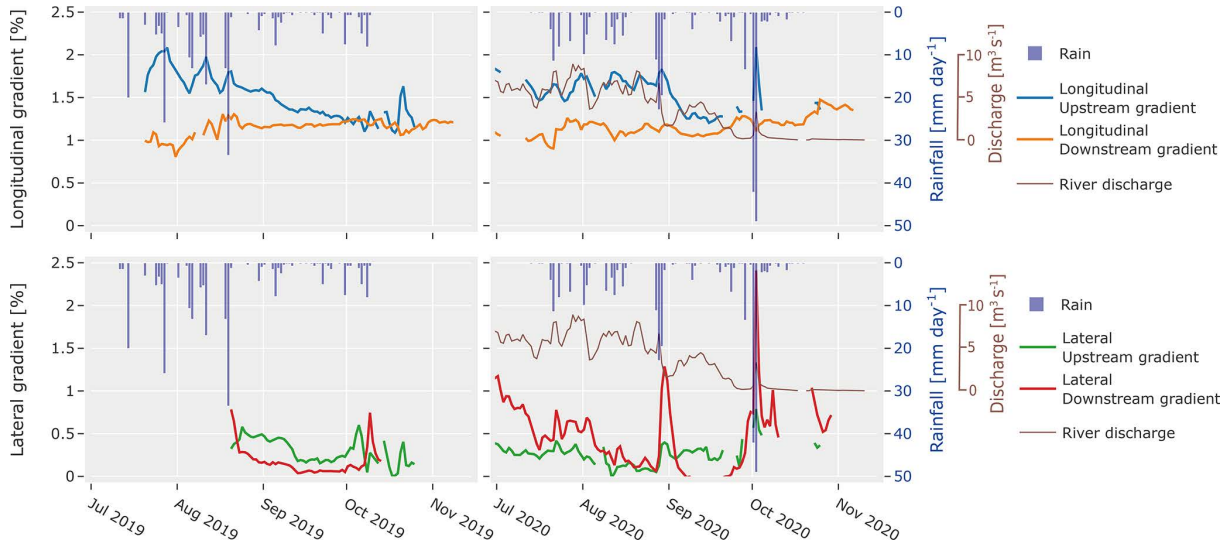

Figure 3.6: Groundwater gradients in the outwash plain for summers 2019 and 2020. The upstream longitudinal gradients are estimated between wells D1 and C1, the downstream gradient between C1 and B1. The lateral gradients are estimated between D wells upstream and B wells downstream, and their slope is directed towards the main river. In 2020, the mean daily discharge at the glacier outlet (GS1) is shown in brown and was scaled between 1 % and 2 % slope for easier comparison with the gradients. Daily measured rainfall at the glacier snout (weather station) are shown by inverted blue bars.

The longitudinal gradient seems to maintain a larger slope of about 1 % to 2 % during the summer. Interestingly, the daily discharge in 2020 shows a similar weekly dynamic to the upstream gradient, although the gradient tends to react with a delay of 1 to 2 d. This suggests a strong influence of the stream discharge magnitude on the upstream gradient, which starts decreasing only in early September, i.e., at the moment when discharge peaks decrease.

River stages at the well transects could not be measured continuously due to the high discharge and unstable sediments; a few isolated measurements show that, in the upper part of the floodplain (B, C, and D transects), the river stage is always 10 to 40 cm higher than the groundwater level in the wells closest to the river, indicating a lateral gradient from the stream to the well and thus a losing stream reach. Higher discharge therefore leads to a higher river stage, which increases the hydraulic gradient through the riverbed and therefore promotes higher stream infiltration.

Based on the hydraulic gradients, it appears that groundwater flows in the same direction as the terrain's main slope are recharged in its upstream part by the stream and re-emerge at the end of the outwash plain. This re-emergence results from the underlying bedrock with much lower hydraulic conductivity, which forces water to exfiltrate in the river as the sediment thickness decreases towards the end of the plain. This groundwater upwelling is also supported by the EC in well A1 (Fig. 3.5), which shows the highest EC in the floodplain, although it is located at 5 m from the river, indicating long flowpaths and no direct contact with the river at this location.

3.4.3 Hydraulic conductivity in the outwash plain

3.4.3.1 Pressure wave diffusion

We identified aquifer thickness using ERT and illustrate the results for well transects D1–D2 (Fig. 3.7). A thin layer of dry sediments can be identified at the top, following a lower layer where resistivity is in a range between 1000 and 3000 $\Omega\,m^{-1}$. Near the stream, resistivity is slightly higher, likely due to lower groundwater EC close to the stream than the hillslope. The bedrock is located at a depth of about 10 to 15 m, with resistivity higher than 5000 $\Omega\,m^{-1}$.

Using the diffusion model (Sect. 3.3.1), we modeled the diffusion of stream stage fluctuations in the aquifer, estimated diffusivity and obtained hydraulic conductivity using an aquifer thickness (15 m) and porosity,

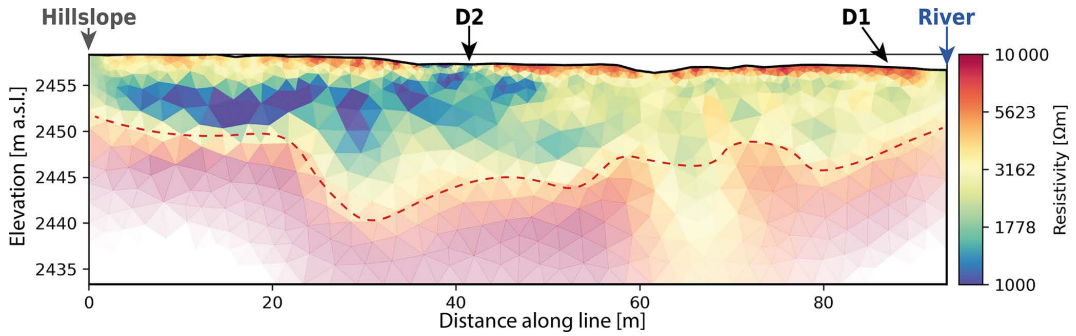

Figure 3.7: Results of one ERT profile perpendicular to the stream at the location of groundwater wells D1 and D2 (see Fig. 3.2). The electrode array consists of 48 electrodes with 2 m spacing. Robust inversion was performed for the dipole–dipole scheme using a regularization coefficient lambda of 10. Location of groundwater wells as well as the hillslope and river sides are also highlighted. The red dashed line shows the limit between water-filled sediments and the underlying bedrock.

Table 3.1: Estimated saturated hydraulic conductivity of the outwash plain for high-flow and low-flow conditions during the summer period along two transects based on the pressure wave diffusion model.

	High flow K_s [m s^{-1}]	Low flow K_s [m s^{-1}]
Upstream transect (D1 and D2)	2.5×10^{-3}	0.96×10^{-3}
Downstream transect (B1, B2 and B3)	7.6×10^{-3}	5.6×10^{-3}

with an average value of 0.25. Unlike in the work of Magnusson et al. (2014), satisfying results were obtained using a unique K_s value to simulate the fluctuations of all wells along the same transect (Figs. A1 and A2). The results are summarized in Table 3.1. Only the estimated lower value for well transect D in September 2019 appears more uncertain, as the simulated head variations for well D1 at 5 m from the river do not match the observed results well (Fig. A2b).

3.4.3.2 Salt tracer injection

The passage of the salt plume was identified by a change in resistivity (of more than an order of magnitude) in a well-constrained zone of the ERT line (plume radius of about 1 m), with the maximum change occurring 10.5 to 11.5 h after injection. Using a travel distance of 9.38 m, we obtain an average pore velocity v_p of 2.4×10^{-4} m s^{-1}. The corresponding aquifer gradient between three groundwater wells (one 1 m upstream of the injection point and two along the ERT line) has a maximum slope of 1.7 %. Based on these values, we obtain an estimated hydraulic conductivity of 3.5×10^{-3} m s^{-1}. A detailed illustration of the time-lapse ERT is available on Zenodo (Müller, 2022c). The surface hydraulic conductivity estimated with this second approach is close to the mean of the K_s values estimated with the diffusion model (4.2×10^{-3} m s^{-1}).

3.4.4 Landform-based groundwater storage dynamics

In order to disentangle the relative contribution of different superficial landforms, we suggest comparing the recession constant ($1/\alpha$), which provides a way to compare how fast each aquifer compartment releases water and what their significance is for maintaining flow during dry periods. We reviewed studies focusing on specific landforms in glaciated catchments where hydraulic conductivity (K_s) was estimated in Table 3.2.

We then estimated the storage and response time of each unit in the Otemma catchment using the landform-based model (Sect. 3.3.5) based on K_s values from Table 3.2, including maximum and minimal K_s values to account for uncertainty. We also defined aquifer properties realistic for our catchment (Table 3.3). For lateral moraines (Caballero et al., 2002; Rogger et al., 2017), we selected K_s to be smaller than for flatter deposits (Kobierska et al., 2015a), which probably reflects the lesser degree of compaction at the valley bottom. We separated talus slopes from lateral moraine as talus slope material is coarser and lay

Table 3.2: Calculation of the recession constant $1/\alpha$ for different landforms based on a typical aquifer structure (h_L/L, ϕ, and L) and a review of hydraulic conductivity values (K_s) reported in proglacial studies. Maximum and minimum values of K_s are given where applicable. Values of $1/\alpha$ for studies which estimated this parameter based on discharge recession analysis independently of K_s were also reported.

Author	Landform	Method	Aquifer slope [%]	Porosity [-]	Aquifer length [m]	Slope parameter b [-]	Reported K_s [m s^{-1}]		Reported recession constant $1/\alpha$ in study [days]	Calculated recession constant $1/\alpha$ [days]	
							min.	max.		min.	max.
Clow et al. (2003)	Talus slopes	Recession analysis	25	0.30	200	1	6.50E-03	9.40E-03	-	0.3	0.4
Caballero et al. (2002)	Talus slopes	Kinematic wave propagation	25	0.30	200	1	6.90E-04	2.50E-03	-	1.1	4.1
Muir et al. (2011)	Talus slopes	Wave & tracer	25	0.30	200	1	1.00E-02	3.00E-02	1	0.1	0.3
Kurylyk and Hayashi (2017)	Talus slopes	Kinematic wave propagation	25	0.30	200	1	2.00E-03	2.00E-02	-	0.1	1.4
Caballero et al. (2002)	Lateral glacial deposits	Kinematic wave propagation	25	0.25	200	1	2.90E-04		-	8	
Rogger et al. (2017)	Lateral glacial deposits	Grain size analysis	25	0.25	200	1	2.22E-04		-	11	
Langston et al. (2013)	Glacial deposits	Mass balance	8	0.25	1000	1.5	3.00E-04	3.00E-03	-	12	121
Magnusson et al. (2012)	Glacial deposits	Slug test	8	0.25	1000	1.5	6.94E-05	4.86E-04	-	74	521
Kobierska et al. (2015a)	Glacial deposits	Tracer propagation (salt)	8	0.25	1000	1.5	5.15E-04	1.35E-03	0.27 (fast resevoir) 29 (slow reservoir)	27	70
Winkler et al. (2016)	Rock glacier	Tracer propagation	15	0.30	500	1	7.00E-05	4.60E-02	21 (early recession) 125 (20-80 days) 500 (late recession)	0.3	167
Rogger et al. (2017)	Rock glacier	Grain size analysis	15	0.30	500	1	5.56E-03		-	2	
Harrington et al. (2018)	Rock glacier (summer melt)	Kinematic wave propagation	15	0.30	200	1	5.00E-03	1.00E-02	3 to 4	0.5	1
Harrington et al. (2018)	Rock glacier (baseflow)	Darcy's law	15	0.30	200	1	6.00E-05	2.00E-04	14 to 50	23	78
Robinson et al. (2008)	Outwash plain (sandur)	Grain size analysis	2	0.25	1000	1.5	1.16E-04	1.74E-03	-	83	1250
Ó Dochartaigh et al. (2019)	Outwash plain (sandur)	Pumping tests	2	0.25	1000	1.5	2.89E-04	4.63E-04	-	313	500
Käser and Hunkeler (2016)	Outwash plain	Pumping test	2	0.25	1000	1.5	6.00E-04	5.00E-03	-	29	241
This study	Outwash plain	Pressure wave diffusion	2	0.25	1000	1.5	9.60E-04	7.60E-03	-	19	151

above the LIA line. For the outwash plain, we used our own estimate of the hydraulic conductivity, and for mildly sloping glacial deposits, comprised between a slope of 8 to 22°, we used a mean slope of 10° as the majority of those deposits were rather flat.

Supported by a simple degree-day model for snow accumulation and melt, we estimated the catchment-scale average rainfall and snowmelt during the year 2020. Rainfall amounts to a total of 204 mm and

Table 3.3: Estimated recession constant ($1/\alpha$) based on aquifer characteristics of the entire Otemma catchment for the main landform compartments. c stands for the slope coefficient of Eq. 3.4 and was defined to be 1 when aquifer slope is larger than 10°.

	Landform area (A_i) [km^2]	Slope [°]	Porostiy [-]	Aquifer length [m]	c [-]	K_s [m s^{-1}]			$1/\alpha$ [days]		
						min.	mean	max.	min.	mean	max.
Talus slope	1.58	27	0.30	250	1	7E-4	2E-3	1E-2	0.19	1	2.8
Lateral moraine	4.99	27	0.25	250	1	1E-4	3E-4	5E-4	3.2	5.4	16.2
Glacial deposits	2.16	10	0.25	500	0.5	3E-4	6.5E-4	1E-3	8.6	13.3	28.8
Outwash plain	0.14	1.15	0.25	1000	0.5	1E-3	4E-3	7E-3	20.7	36.2	144.7

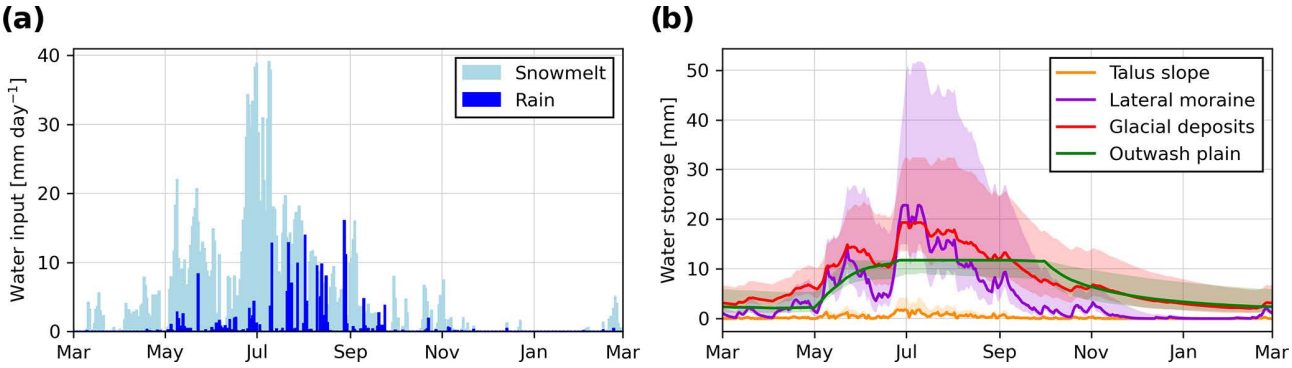

Figure 3.8: **(a)** Measured precipitation input at the glacier snout (mm d^{-1}) and mean snowmelt input simulated with a simple degree-day approach (mm d^{-1}). **(b)** Evolution of the groundwater storage of the four main geomorphological landforms (outwash plain; flat glacial deposits < 22°; lateral moraines > 22°; talus slopes > 22°) based on the landform model described in Eqs. (3.12) to (3.14). Storage volumes in cubic meters are divided by the entire catchment area in square meters to provide comparable estimates in millimeters.

snowmelt to 1732 mm of water equivalent (see Fig. 3.8a). Figure 3.8b shows the resulting estimated maximum storage for each landform.

The resulting maximum baseflow storage in the flat glacial deposits is 19 mm (with an uncertainty margin from 13.5 to 32.5 mm) or a maximum aquifer thickness of 1.1 m (0.8 to 1.8 m) during peak snowmelt. The storage in the outwash plain gradually increases due to constant recharge from the river and rapidly reaches its maximum storage of 11.3 mm (or an aquifer thickness of 10 m). The lateral moraines show a very flashy storage response linked to their short recession constant. Their storage reaches 23 mm (15 to 52 mm) during snowmelt, corresponding to an aquifer thickness of 0.55 m (0.35 to 1.25 m). Due to their very low retention capacity, talus slopes only transmit water, and their storage is low, with only 1.8 mm (1 to 4.5 mm) and a maximum aquifer thickness of 0.11 m (0.06 to 0.27 m). After peak snowmelt, storage decreases quickly in the lateral moraines and somewhat more slowly in the flatter glacial deposits, while maximum storage is maintained in the outwash plain due to the stream recharge. During fall, lower discharge leads to a storage decrease in the outwash plain too, so that by early December the total remaining storage becomes very limited, with only 8.8 mm (5 to 20 mm) remaining from the outwash plain and flat moraine deposits.

3.4.5 Catchment-scale winter river recession analysis

Discharge recession was analyzed from 2006 to 2017 at the catchment outlet by calculating the averaged relationship between recession rates (dQ/dt) and river discharge (Q) (Fig. 3.9). A change in slope occurs for discharge higher than 0.33 mm d^{-1}, probably due to the transition between discharge dominated by ice melt to discharge fed by groundwater. Due to this slope change, we assume that the recession starts when baseflow discharge is smaller than 0.33 mm d^{-1}, and higher values are excluded for the linear regression shown in Fig. 3.9.

The estimated regression has a slope of $b = 1.56$, leading to a quadratic relationship between storage and discharge (Eq. 3.6). Due to the low values computed in Fig. 3.9, a change in the smoothing process of the raw discharge data may have an impact on the recession. We have tested different processing parameters

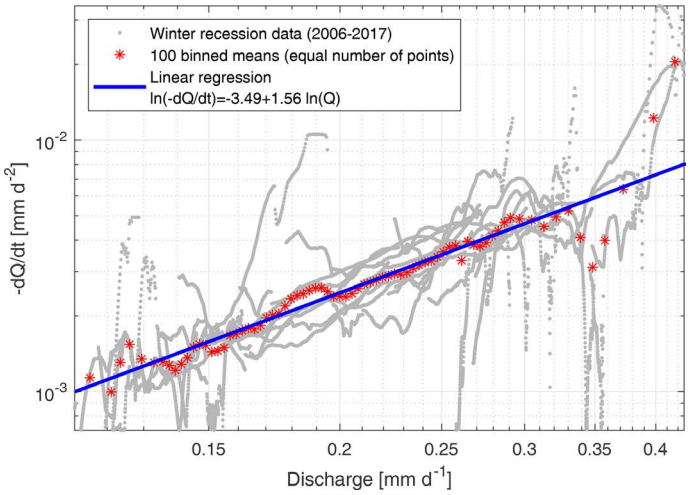

Figure 3.9: Plot of the smoothed discharge recessions ($-\mathrm{d}Q/\mathrm{d}t$) against discharge (Q) for all recession periods from 2006 to 2017 (in grey) at the catchment outlet (GS3). Binned averages are shown in red, each bin comprising 1 % of the data points. A linear regression (in the logarithmic space) to all binned values smaller than 0.33 mm d^{-1} is plotted in blue. Axes are in logarithmic scale.

and assessed the impact on the linear regression; overall, the slope varies between 1.45 and 1.65.

Using the same recession periods, the recession trends of each individual year are assessed (Fig. 3.10) using a quadratic relationship (Eq. 3.8) and fitting the maximum baseflow discharge (Q_0) and the recession coefficient (e). The corresponding calculated recession constant ($1/\alpha$) seems to decrease in recent years, but the trend is unclear due to the overall short time period, while the temporal evolution of Q_0 and S_0 does not show any trend, suggesting no clear increase in groundwater storage over the 12-year period (Fig. 3.11).

Overall, we obtain a similar estimation of the baseflow storage in the Otemma catchment during each winter, with a mean maximum baseflow discharge of 0.34 mm d^{-1}, a mean maximum storage of 42.5 mm and a recession constant ($1/\alpha$) comprised between 90 and 155 d. Finally, at the end of the recession periods in late winter, discharge has decreased by a factor of 3, which indicates that the baseflow storage does not completely empty and still retains on average 58 % of the maximum baseflow storage of early December.

Those results are in contradiction with the landform-based model (Fig. 3.8), where a maximum baseflow storage during early December was estimated to only 8.5 mm. Accordingly, the landform-based analysis seems to miss a relatively important storage compartment.

3.5 Discussion

3.5.1 Groundwater storage and release functions of the main geomorphological features

Our analysis has shown that the landform- as well as catchment-scale hydrological responses critically depend on (i) the sediment structure defining K_s and (ii) the landform characteristics in terms of slope and aquifer flowpath length. These key properties can then be combined to estimate an averaged response time ($1/\alpha$) of each landform, although the storage–release behavior may be more complicated when considering more complex aquifer geometries (Berne et al., 2005), heterogeneous landforms with varying physical properties for K_s and ϕ, preferential flowpaths (Harman et al., 2009) or non-stationary processes (Benettin et al., 2017). In this study, we focused on characterizing the "slow" groundwater compartment, which is relevant for baseflow only, but an initial part of the water release may also occur in a faster superficial layer, as suggested in other studies (e.g., Kobierska et al., 2015b; Stewart, 2015; Winkler et al., 2016). Our approach, while simple, relies on physical properties of the aquifer. The calculated values for $1/\alpha$ were similar to studies which estimated this parameter based on direct observations of discharge recession. This supports the validity of our approach for analyzing the storage–release behavior and the relative importance of different landform units in a glaciated catchment.

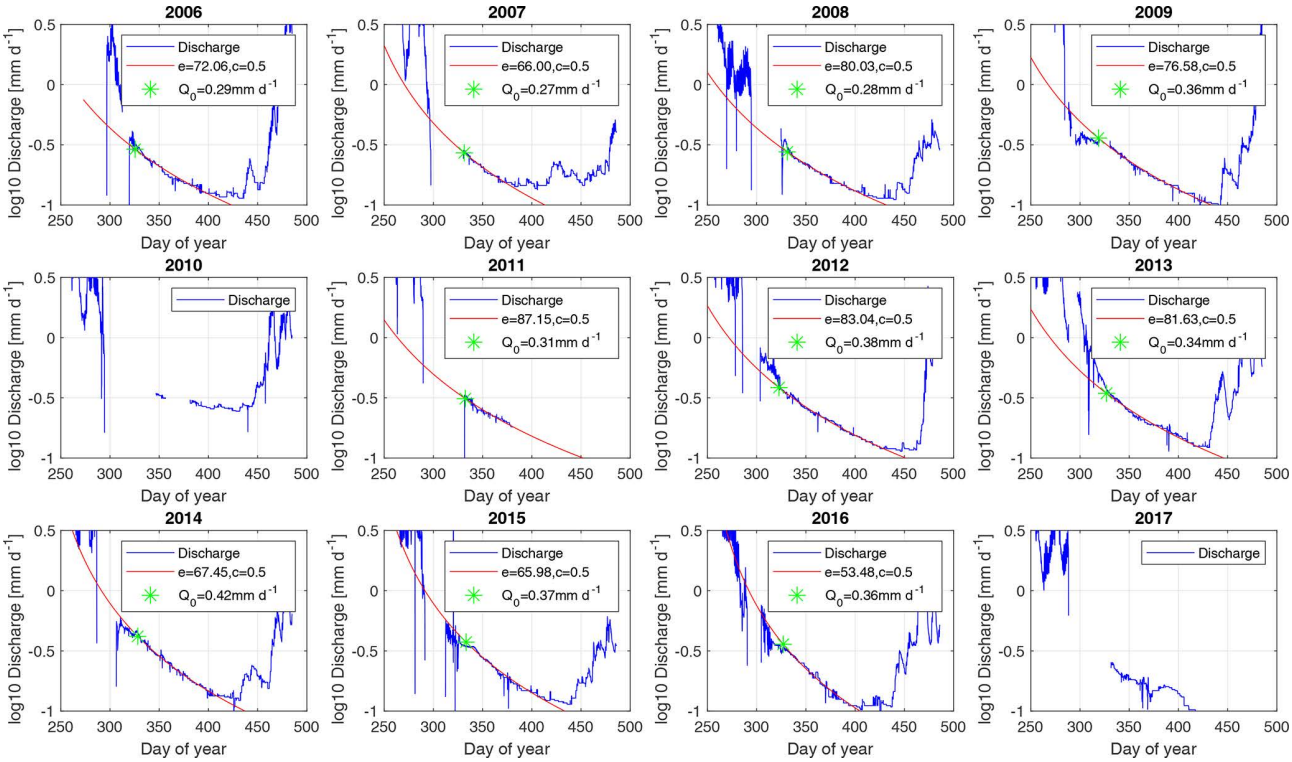

Figure 3.10: Annual recession analysis at the catchment outlet (GS3). The measured discharge is presented in blue (logarithmic scale), and the best fit of the power-law regression ($Q_t = Q_0(1 + \frac{1}{e} Q_0^{0.5} t)^{-2}$) is shown in red, along with the estimated fitted parameters Q_0 and e. Day of year larger than 365 indicates a recession spanning over the following year. The years 2010 and 2017 show large data gaps, so that no fit was calculated.

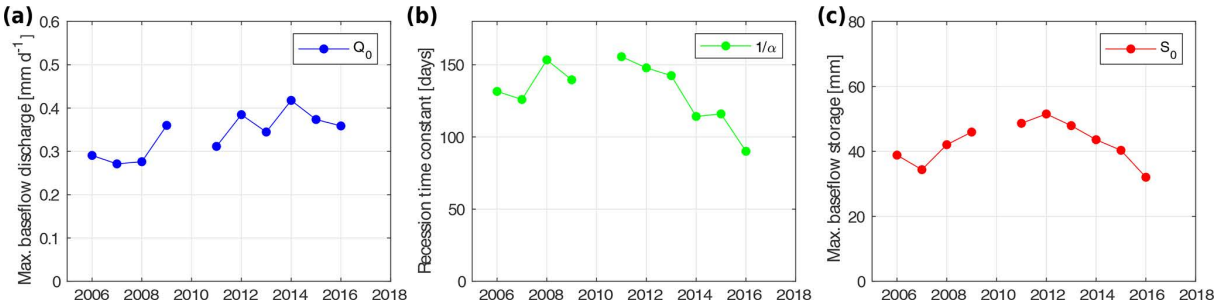

Figure 3.11: Temporal evolution of the recession characteristics obtained from the annual recession analysis of the Otemma catchment, showing the results of the best-fitted parameters for **(a)** maximum baseflow (Q_0), **(b)** recession constant ($1/\alpha$), and **(c)** maximum baseflow storage (S_0).

With this analysis, we have shown that only flat aquifers release water at timescales longer than weeks. In addition to K_s, the bedrock slope plays an important role, as it changes the relationship between storage and discharge, illustrated in our landform-based model by the slope coefficient c. Indeed, steeper slopes promote stronger advective fluxes (Harman and Sivapalan, 2009a) and modify the recession equation (Eqs. 3.7 and 3.10), so that a sloping aquifer ($c = 1$) would lose 50 % of its storage 1.4 times faster and 99 % 4.5 times faster than a flat aquifer ($c = 0.5$).

The seasonal landform-based analysis of superficial storage proposes an example of the groundwater dynamics in a glaciated catchment. The estimated storage amounts are likely not accurate due to a strong simplification of the recharge processes and the absence of superficial overland flow; it nevertheless illustrates (i) the strong relationship between recharge and storage, (ii) the importance of the timing of the water input and (iii) the relative speed at which different reservoirs may empty. Accordingly, we can establish a sound perceptual model (see Sect. 3.5.3).

Prior to introducing this model, we first discuss and summarize hereafter what new insights we gain from

our case study on the hydrological functioning of the main classes of geomorphological landforms.

3.5.1.1 Talus slopes

In the Otemma catchment, talus slopes have only a marginal extent, so that the estimated storage is very low. In other less glaciated catchments, talus slopes may cover a much larger area, but, due to their coarse aquifer structure, their recession constant is only on the order of a day (Table 3.2), leading to a rapid transmission of water and little storage capacity. This is illustrated in our landform-based model by a maximal aquifer thickness of 11 cm. Therefore, groundwater storage is likely discontinuous and may only occur in pockets due to bedrock depressions at the base of the talus (fill and spill mechanism; Muir et al., 2011; Tromp-Van Meerveld and McDonnell, 2006). If a less conductive layer exists at the bottom of the talus, most studies have only reported a few centimeters of water saturation with relatively high conductivity (Kurylyk and Hayashi, 2017; Muir et al., 2011). Some studies have however shown different results, mainly the study by Clow et al. (2003), who estimated an aquifer thickness of a few meters and concluded that talus slopes contributed up to 75 % of winter baseflow. We want to stress here that this study is based on an erroneous calculation of the storage–discharge relationship where the authors wrongly included the time. This mistake may have influenced the conclusions made by others, and we insist here that talus slopes do not have the capacity to store water; they only transmit it from and to other landforms or the underlying fractured bedrock, as also suggested by others (e.g., Harrington et al., 2018; McClymont et al., 2011).

3.5.1.2 Steep lateral moraines

Steep lateral moraines may present glacial deposits on the order of tens of meters (Rogger et al., 2017) and have a lower hydraulic conductivity than talus slopes. Even though their structure is steep, they may retain water at a timescale of around 1 week. Their response remains relatively flashy, and the amount of potential storage is mainly driven by the rate of snowmelt in the early summer season. This is illustrated in our field observations in early September 2020, where the EC in tributary 2 recovers rapidly after a heavy rain event (Fig. 3.5) and where the lateral downstream gradient decreases on the same timescale (Fig. 3.6). Additionally, EC difference between the bedrock outcrop and tributary 2 is marginal, indicating limited chemical weathering and thus fast subsurface flow.

In our landform-based model, we assumed a homogeneous recharge, which is unlikely in the late midsummer season, when snowmelt mainly occurs in the upper part of the catchment or in hanging valleys and when both surface and subsurface meltwater responsible for its recharge are likely concentrated in gullies or other zones of flow convergence due to the bedrock topography. The amount of recharge of steep lateral moraines is thus likely dependent on the frequency of flow convergence upslope; the more concentrated the upslope flow is, the less recharge occurs. In Otemma, these concentrated flows seem rather superficial, with limited infiltration into deeper parts of the moraine, which is likely due to more cemented grains and early soil development. Part of the water does nonetheless infiltrate and re-emerge at the foot of the hillslope as in tributary 2. Thus, the estimated storage of such landforms due to snowmelt is likely not as large as estimated here (23 mm), as only a fraction of this landform is located above zones of snowmelt-induced recharge. They have however the potential to store significant amounts of rainwater, at least in the Otemma catchment, as they cover a significant part of the whole catchment (about 20 %). Finally, as suggested in other mountainous areas (Baraer et al., 2015), it is also possible that some water may reach the bottom of the moraine with lower hydraulic conductivity and directly exfiltrates into the outwash plain underground, making direct observations not possible. This phenomenon may explain the increase in EC observed in wells C2 and D2 during the cold spell, which is likely due to older groundwater from the slopes (Fig. 3.5). Based on our landform-based model, such groundwater flow should still be relatively fast due to the steep slopes, so that this older water may also come from bedrock exfiltrations transmitted through the moraine to the outwash plain.

3.5.1.3 Flatter glacial deposits

Flatter glacial deposits, such as alluvial fans or melt-out till moraines, have a similar structure to steeper moraines but are usually less cemented and may present an eluviation of fine sediments, leading to a some-

what greater hydraulic conductivity (Ballantyne, 2002; Langston et al., 2011). In Otemma, those mildly sloping structures are dominated by moraine deposits, and their recession constant was estimated to be 2 to 3 times larger than for steeper moraines. Their water release is also slower due to a weaker advective flux and more diffusion, which we illustrated using a quadratic form of recession ($c = 0.5$; see Eq. 3.6). An aquifer slope of 10° is however at the upper limit of such a recession equation, so that the actual drainage is probably faster, more similar to steeper lateral moraines. Their capacity to sustain baseflow depends on the amount and timing of water recharge during the snowmelt period. Where glacial deposits are connected to a more constant source of water such as ice melt, storage may remain high throughout the summer (Kobierska et al., 2015b), and they will function similarly to an outwash plain as described hereafter. In the case of the Otemma catchment, the usual thickness of these sediments is on the order of tens of meters, making direct groundwater observation at their base not possible. No clear changes in EC were observed in summer beyond the outwash plain (between GS2 and GS3), a section where morainic material is present, which could indicate a marginal contribution from this area, but the signal is likely dampened by additional ice melt with low EC from hanging glaciers. In winter, a slight increase between GS2 and GS3 is observed, suggesting some groundwater contributions, which could be attributed to the morainic deposits or bedrock exfiltration.

3.5.1.4 Outwash plains

Outwash plains show strong surface water–groundwater interactions, which maintain near-saturation conditions far after the peak of snowmelt as long as glacier melt maintains stream discharge. Our field observations show that stream infiltration is the main source of recharge in the upstream part and reaches far from the stream in summer, as illustrated by the higher EC near the hillslopes and in the well A1 near the lower end of the plain. Such behavior was also shown by others in older outwash plains or sandurs (Mackay et al., 2020; Ward et al., 1999).

In winter, groundwater EC increases largely in A1, but this increase is also partially due to an increase in EC in the source water, i.e., the upstream river at GS1 (Fig. 3.4a). In fact, the difference in EC between A1 and the stream at GS1 does not change much between summer (about 70 μS cm^{-1}) and winter (about 80 μS cm^{-1}), which indicates a strong connection year-round, a limited change in EC with depth in the aquifer and a groundwater transit time which only increases slightly in winter. Nonetheless, the EC difference in the stream before (GS1) and after the outwash plain (GS2) increases in winter, indicating that the outwash plain seems to contribute to some extent to baseflow but also that an upstream groundwater source above GS1 drives the EC increase in the stream before it enters the outwash plain.

Our landform-based model, based on our estimation of K_s, validates these observations, as it was shown that the outwash plain provides some baseflow in winter due to its longer recession constant (about 35 d). Compared to older alluvial systems (Käser and Hunkeler, 2016; Ó Dochartaigh et al., 2019), our estimates of K_s are slightly larger, maybe due to a less consolidated aquifer and the absence of vegetation. If the current role of outwash plains in maintaining baseflow is clearly limited due to their small areal extent in Alpine catchments, future glacier retreat may extend their area, especially where bedrock overdeepenings can be filled with sediments. Finally, together with earlier snowmelt in a warming climate, their role in providing baseflow during drought conditions is likely to become increasingly important in the future.

3.5.1.5 Missing storage

From the above comments and the landform-based model (Fig. 3.8), it appears that the current capacity of the superficial geomorphological landforms to store water is limited to the melt period, with the exception of the outwash plain and maybe some flatter glacial deposits, with only about 8.5 mm of storage remaining in early December (i.e., at the start of the winter recession). Nonetheless, on the basis of the baseflow recession analysis at the catchment scale, we estimated a potential groundwater storage on the order of 40 mm. This value was estimated using a simple mathematical relationship between storage and discharge, which has been shown to be sensitive to the choice of the recession periods, which may include processes which are not directly linked to aquifer drainage (Staudinger et al., 2017). For instance, in our study, the recession analysis may be biased if substantial basal ice melt provides water during winter, which we cannot

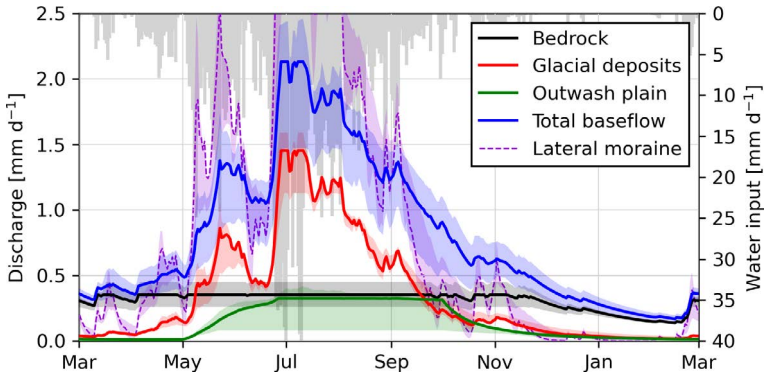

Figure 3.12: Evolution of modeled groundwater baseflow discharge of different hydrogeomorphological landforms. Total baseflow represents the sum of the outwash plain, flat glacial deposits, and bedrock discharge; steep lateral moraines are also plotted but are not considered in the sum of baseflow due to their fast response. Simulated total water input (snowmelt and rain) is plotted in grey.

exclude. Nevertheless, even if the estimated value may not fully represent the real storage in the catchment, the catchment-scale recession timescales of about 100 d cannot be explained by the superficial landforms present in the catchment, and stream EC at the glacier outlet (GS1) does show a strong increase in winter, supporting the presence of an unidentified compartment, which was not included in the landform-based model. Finally, the measured cumulated winter discharge (December to the end of March) at GS3 is on the order of 20 to 25 mm each year, further supporting the presence of a missing storage compartment, which slowly drains during the whole winter.

We propose here some hypotheses concerning its nature. The first hypothesis is that the remaining baseflow recession in winter is actually not due to a storage unit but rather to some residual snowmelt or permafrost losses or due to basal melt at the glacier bed. Snowmelt and permafrost losses are not very likely during the cold season, as mean air temperature at the weather station is around −5 to −10 °C. Basal melt may however occur during the whole winter due to the overburden pressure of the ice mass (Flowers, 2015). The second hypothesis is the contribution from a groundwater reservoir underneath the glacier itself, which is recharged in summer, without winter basal ice melt. Previous studies have however predicted a rather rocky or mixed glacial bed in this area (Maisch et al., 1999), with a discontinued till thickness on the order of tens of centimeters (Harbor, 1997). A large enough reservoir (4 times the current outwash plain) could exist in a large glacial overdeepening, but it is unclear whether sufficient sediments would accumulate in such a pocket based on the sediment export capacity of the glacier. The smooth increase in EC at GS1 during winter could better be explained by a combination of the first two hypotheses, where a smaller subglacial reservoir is recharged by decreasing basal melt which slowly empties during winter and acquires solutes by the weathering of bedrock or sediment.

The third hypothesis is that the storage occurs mainly in the bedrock and that sufficiently short flowpaths allow this storage to drain during the winter. This hypothesis is likely since large fractures may occur due to glacier debuttressing (Bovis, 1990; Grämiger et al., 2017) and groundwater seepage through deep fractures probably occurs underneath other landforms and cannot be measured directly. Moreover, some studies have reported similar catchment-scale storage in elevated catchments, although it is usually not clearly associated with a distinct hydrological unit. In particular, in a similar highly glaciated catchment, the work of Hood and Hayashi (2015) reported a peak catchment-scale storage in spring of 60 to 100 mm. Moreover, the work of Oestreicher et al. (2021) modeled an estimated catchment-scale storage change of 70 mm in a Swiss glaciated catchment of similar glacier coverage, which they could relate to a deep borehole water head change (Hugentobler et al., 2020). Such estimates represent the peak spring storage, accounting for all storage units, and not only the winter storage estimated in our study. Based on the rough estimates of Fig. 3.8, the peak summer storage estimated is 30 mm for flat glacial deposits and the outwash plain and 23 mm for the steep lateral moraines, which, combined with a bedrock storage of 40 mm, would result in similar numbers. Finally, during a cold spell in Otemma, some evidence of the contribution of deeper, older groundwater was observed as depicted by a fast increase in EC in wells C2 and D2 (Fig. 3.5), which could be

due to older water exfiltrating from the bedrock.

Based on the above discussion, we suggest allocating the missing storage to bedrock storage with a maximum of 40 mm, which we can then add to our previous landform-based model (Eq. 3.12) with a recession constant ($1/\alpha$) of 115 d to reflect the baseflow recession analysis. The resulting baseflow of each landform is shown in Fig. 3.12.

3.5.2 Landform hydrological connectivity

While our approach identifies the relative size and seasonal hydrological response of proglacial landforms, we use a simplistic recharge model. In reality, hydrological connectivity from the water sources and between landforms will ultimately drive the amount of actual recharge. Due to the coarse and barren nature of the sediments in such environments and the limited presence of soils, it can be expected that any water input will infiltrate into the sediments (Maier et al., 2021). It has also been shown that groundwater flow is driven by the bedrock topography underneath the landform, where a strong change in hydraulic conductivity drives the water downslope (Hayashi, 2020; Vincent et al., 2019). We can therefore assume that recharge occurs directly at the location of the water input, percolates until the bedrock and is then directed downslope. In the case of snowmelt, this recharge will gradually move upslope with the snow line during summer, a zone where talus slopes and bedrock are frequent. Water will rapidly be directed downslope at the bedrock interface and directed in zones of bedrock depression, concentrating the flow and thus providing little recharge to other downhill-sloping deposits. Water may also reach a flatter zone in hanging valleys, where flatter morainic material may be present in rock overdeepenings, which likely act as an immobile storage, where groundwater only overflows above the bedrock, similarly to a fill-and-spill mechanism (Tromp-Van Meerveld and McDonnell, 2006). The concentrated groundwater flow eventually reaches either the main stream or a flat glacial deposit (moraine or outwash plain) and acts as point recharge, so that only areas located below a zone of bedrock convergence will receive recharge. Similarly, glacier melt recharge will mostly occur along the reach of the glacial stream at the valley bottom and will maintain high groundwater storage in outwash plains or flat moraines exclusively.

3.5.3 A sound perceptual model for the hydrological functioning of a glaciated catchment

We summarize here the gained insights into a perceptual model (Fig. 3.13) of the hydrological functioning of the Otemma catchment, augmented with an additional "missing" storage which we tentatively allocate to bedrock (Sect. 3.5.1.5). In this representation, the partitioning between the different sources of water recharging each landform are taken from the results of our landform-based model of the Otemma catchment (Fig. 3.8). We also provide a comparison of the discharge amounts provided by each landform proportional to the results of Fig. 3.12.

The perceptual model illustrates well how steep lateral moraines may provide large water amounts during peak snowmelt or strong rain events in mid-summer but drain very rapidly in fall. Talus slopes were not included in the perceptual model, as they play a marginal role in the Otemma catchment and have even faster drainage than steep moraines. In contrast to steep slopes, the baseflow provided by the bedrock aquifer appears more stable, although its storage decreases by half during winter. In a perspective of future early snowmelt, the model shows that most landforms may become dry much more quickly, with the exception of (i) the outwash plain, which receives water from the glacial stream, and (ii) the bedrock, which drains slowly, highlighting the future increasing importance of such aquifers for providing wetness and maintaining favorable ecological conditions.

In this representation we also neglected the impact of permafrost melt, although it is likely present at high elevation and in north-sloping moraines (Boeckli et al., 2012) and may provide some future additional meltwater in glaciated catchments, as shown in the work of Rogger et al. (2017). Rock glaciers were also not included as their presence is marginal currently in Otemma, but their role in storing and releasing water may become increasingly important since they have a capacity to store water on timescales of months, as shown in Table 3.2 and as discussed in more deglaciated catchments in Austria (Wagner et al., 2021).

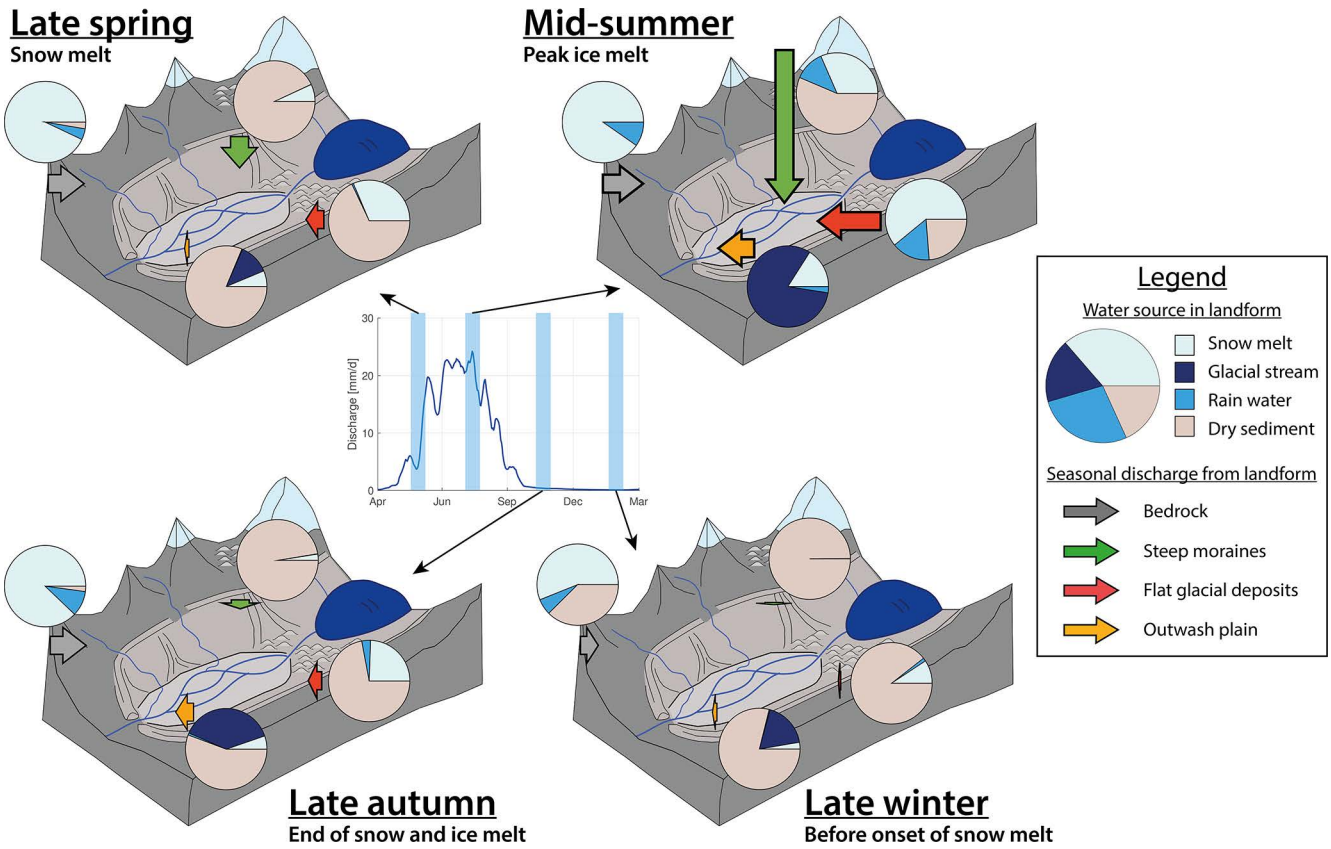

Figure 3.13: Perceptual model of groundwater dynamics in the Otemma catchment during four key hydrological periods. The central hydrograph represents the mean daily catchment-scale river discharge for the year 2015. The pie charts represent the seasonal partitioning of the three water sources (rainwater, snowmelt, glacial stream) calculated based on recharge and outflow (Sect. 3.3.5) for the three main superficial landforms as well as a bedrock aquifer. The source "Glacial stream" represents the mixed discharge leaving the glacier outlet and is an undefined mix of ice melt and snowmelt as well as of any liquid rain transiting through the glacier. The share of dry sediments represents the percentage of aquifer storage drained compared to the calculated maximum storage (Sect. 3.4.4), which is 40 mm for bedrock (missing storage), 23 mm for the steep lateral moraines, 19 mm for flatter glacial deposits, and 11 mm for the outwash plain. The length of the arrows represents the relative magnitude of the baseflow discharge estimated in Fig. 3.12 for each landform.

3.6 Conclusions

This study attempted to bridge the gap between the catchment-scale response of a high-elevation glaciated catchment and the hydrological behavior of its landforms, using the case study of a large glacier in the Swiss Alps. The quantitative analyses are simple and are based on a rough estimation of the hydrogeological response of different landforms. Nevertheless, the analysis framework identified the order of magnitude and the timing of the contribution of the different landforms and is readily transposable to other case studies. The resulting perceptual model provides a realistic representation of the main drivers of the groundwater dynamics of the deglaciated zones of a typical glaciated catchment, which can serve as a blueprint for future experimental works as well as for hydrological model development. One clear uncertainty lies in the estimated hydraulic conductivities per landform, in particular their variability in space and depth. In addition, we had to attribute a large part of the groundwater storage to an unidentified compartment, which is likely partially due to a bedrock compartment but could also be due to a combination of meltwater and a subglacial compartment. Future research is needed to specify the very nature of this groundwater storage.

We have shown that superficial geomorphological landforms have a relatively limited capacity to store or release water at timescales longer than a few days, partly because of steep slopes but also due to the generally high hydraulic conductivity. In the future, two main changes can be expected. Firstly, with increasing glacier retreat, the extent of flatter landforms at the valley bottom will increase and may accumulate sufficient sediments to create new outwash plains or flat hummocky moraines that would increase the overall

groundwater storage. It remains unclear how many sediments are produced with decreasing glacier volumes and whether they will be deposited or transported downstream (Carrivick and Heckmann, 2017; Lane et al., 2017). Secondly, with increasing vegetation growth, the formation of soils with enhanced organic matter content and finer soil texture are expected, which will promote water retention and modify the surface hydraulic conductivity (Hartmann et al., 2020). Recent studies on the evolution of morainic structures have shown that limited changes occurred on timescales smaller than a millennium, with a slight decrease in hydraulic conductivity (Maier et al., 2020, 2021). Thus, the impact of soil–vegetation development on the hydraulic conductivity and the rate of aquifer drainage is likely limited. Nonetheless, early soil development and biofilm growth may start to modify the water retention locally (Roncoroni et al., 2019), promoting more superficial soil moisture but limiting water infiltration and promoting surface runoffs, which will likely modify groundwater recharge. Finally, the ecological feedback of vegetation development on bank stabilization may also play a role in limiting sediment export and slow geomorphological changes (Miller and Lane, 2018), which may preserve the current geomorphological landforms.

The framework used to analyze the hydrological behavior of selected landforms based on groundwater levels and electric conductivity recordings is readily transferable at relatively low costs to other glaciated catchments. Our EC data underline a large variability between the landforms and spatially across the outwash plain, in addition to strong variations with changing groundwater heads. This observation shows that simple mixing models based on few observations of groundwater electrical conductivity in selected sources are likely not representative of the contribution of each landform and may provide very erroneous estimates of groundwater contribution.

More sophisticated tracer work could complement these analyses in the future. In particular, analysis of stable water isotopes could provide interesting insights into the relative share of subsurface recharge resulting from snow and rain over the season. The use of other geochemical tracers (Gordon et al., 2015; Hindshaw et al., 2011) or even noble gases (Schilling et al., 2021) could provide further insights into the potential contribution from deeper bedrock exfiltrations as well as better constrain the length or travel time of certain groundwater flowpaths.

A Appendix

A.1 Diffusion model analysis

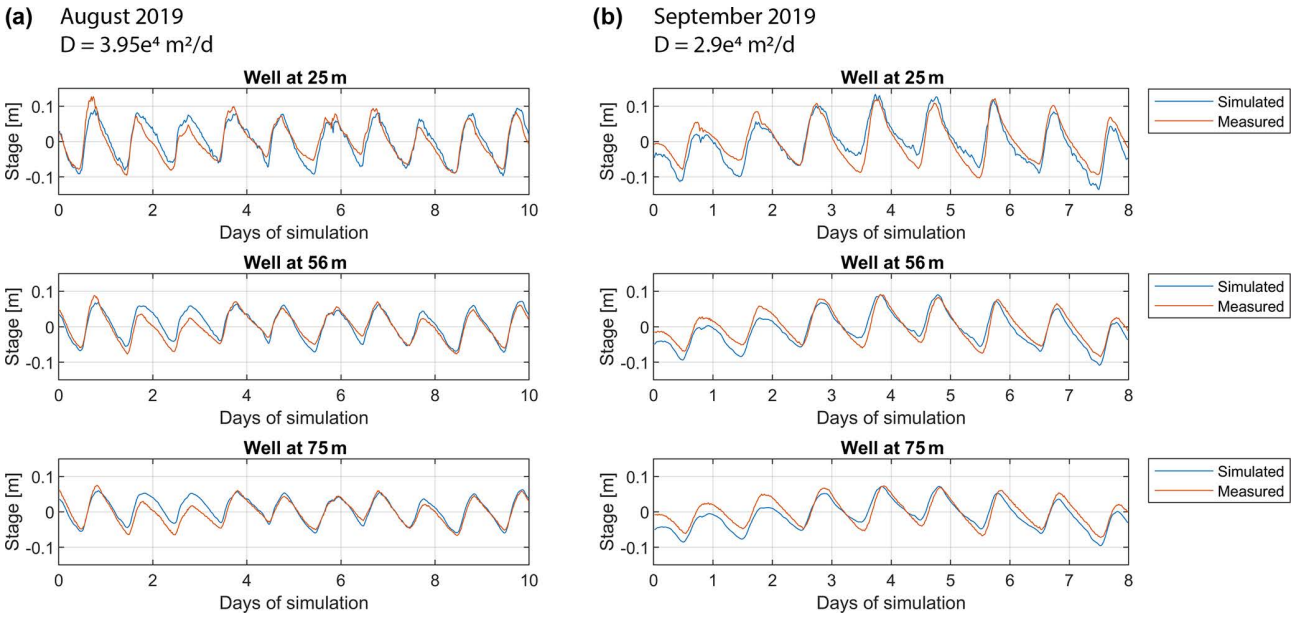

Figure A1: Measured and simulated water head variations for piezometers along the downstream transect "*B*" for the best calibration of the diffusion parameter *D* and for **(a)** the high-flow condition in August 2019 and **(b)** lower-flow condition in September 2019.

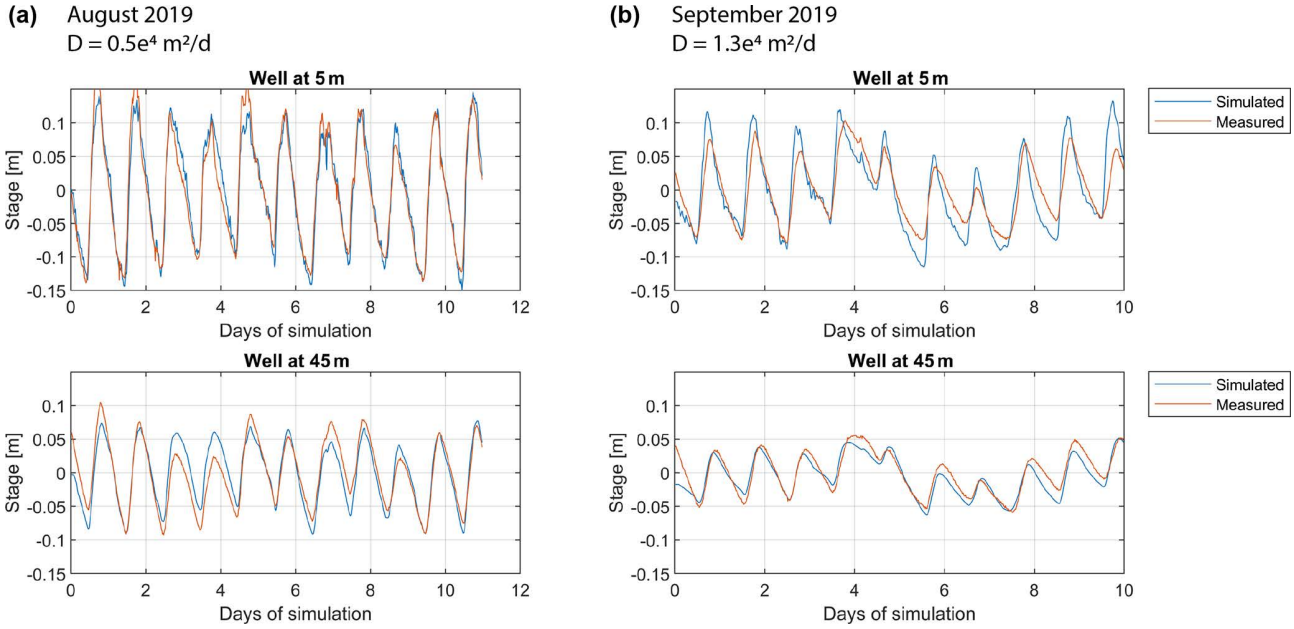

Figure A2: Measured and simulated water head variations for piezometers along the upstream transect "*D*" for the best calibration of the diffusion parameter *D* and for **(a)** the high-flow condition in August 2019 and **(b)** the lower-flow condition in September 2019.

Code data availability Weather data are available under 10.5281/zenodo.6106778 (Müller, 2022a), piezometer data under 10.5281/zenodo.6355474 (Müller, 2022b), river data under 10.5281/zenodo.6202732 (Müller and Miesen, 2022) and ERT data under 10.5281/zenodo.6342767 (Müller, 2022c).

The code to reproduce the recession analysis (see Sect. 3.4.5) was written in MATLAB using the published data. The codes for the simple storage–discharge model as well as the snow mass balance model (see Sect. 3.4.4) were written in python using Jupyter Notebook. Both codes are available in the Supplement.

Author contribution TM conducted all the data collection and data analysis, produced all the figures and wrote the manuscript draft, including the literature review. BS proposed the general research topic and acquired the funding. SNL and his team organized all fieldwork logistics. BS and SNL jointly supervised the research and edited the manuscript draft version. All the authors have read and agreed to the current version of the paper.

Competing interests At least one of the (co-)authors is a member of the editorial board of *Hydrology and Earth System Sciences*. The peer-review process was guided by an independent editor, and the authors also have no other competing interests to declare.

Acknowledgements The authors also thank Christophe Lambiel and James Irving (University of Lausanne) for lending the ERT device as well as Emily Voytek (University of Lausanne) for acquiring the first ERT data in the Otemma forefield in 2019. Tom Müller thanks all students and PhD students from the Alp-WISE group at the University of Lausanne, and in particular Floreana Miesen, who participated in field data collection at the Otemma glacier forefield. The authors also thank the two anonymous reviewers for their constructive comments to improve this work.

Financial support This research has been supported by the Schweizerischer Nationalfonds zur Förderung der Wissenschaftlichen Forschung (grant no. 200021_182065).

Review statement This paper was edited by Insa Neuweiler and reviewed by two anonymous referees.

Figure 3.3: Picture of the outwash plain of the Otemma glacier during a typical afternoon high flow.

4

Research paper 2

Current and future role of meltwater-groundwater dynamics in a proglacial Alpine outwash plain

Tom Müller[1,2], Matteo Roncoroni[1], Davide Mancini[1], Stuart N. Lane[1] and Bettina Schaefli[1,2,3]

[1]Institute of Earth Surface Dynamics, Lausanne, University of Lausanne, Switzerland
[2]Institute of Geography (GIUB), University of Bern, 3012 Bern, Switzerland
[3]Oeschger Centre for Climate Change Research (OCCR), University of Bern, 3012 Bern, Switzerland

Received: 24 December 2022 – Discussion started: 7 February 2023
Currently in review.

Hydrology and Earth System Sciences (HESS)
https://doi.org/10.5194/egusphere-2022-1503

Based on the outcome of the first paper, this chapter focuses on the aquifer formed by the outwash plain, the interactions with the glacial stream and its importance to maintain baseflow. For this purpose, a 3D model (MODFLOW) was built to simulate the aquifer behavior during two years and was calibrated based on different field observations using an automated parameter estimation model (PEST). On the basis of this model, we show the currently limited dynamic storage of such aquifer. We finally attempt to identify future potential new emerging outwash plains due to glacier retreat and discuss their combined cascading effect on river discharge.

Abstract

Glaciated alpine catchments are rapidly evolving due to glacier retreat and consequent geomorphological and ecological changes. As more terrain becomes ice free, the interactions between surface and subsurface waters become gradually more significant, leading to potential changes in water storage and release, which in turn may impact ecological, geomorphological and hydrological processes. In this study, we aim to understand the current and future hydrological functioning of a typical outwash plain in a Swiss Alpine catchment. Such outwash plains constitute a fluvial aquifer which appears as a focal point for water storage and alpine ecology and their dynamics have only rarely been studied. Based on geophysical investigations as well as year-round stream and groundwater observations, we developed a simplified physically-based 3D MODFLOW model and performed an optimized automatic calibration using PEST HP. By comparing the model results to field observations, we highlight the strong interactions between the upstream river and the aquifer, with stream infiltration being the dominant process of recharge. Groundwater exfiltration occurs in the lower half part of the outwash plain, balancing out the amount of river infiltration at a daily time scale. We show that hillslope contributions from rain and snow-melt have little impact on groundwater levels. We also show that the outwash plain aquifer can maintain groundwater levels close to the surface even during long dry periods. From a hydrological perspective, we finally explore how new outwash plains may form in the future in this catchment due to glacier recession and discuss what cascading impact the presence of multiple outwash plains may have. For this case study, we estimate the total dynamic storage of future outwash plains to be about 20 mm and we demonstrate their limited capacity to produce more stream water than what they infiltrate upstream, except for very low river flows (< 150 to 200 L s^{-1}). Below this limit, they can provide limited baseflow on timescales of weeks, thus maintaining some moisture conditions potentially beneficial for proglacial ecosystems. Their role in attenuating floods also appears limited, as less than 0.5 m^3 s^{-1} of river water can be infiltrated. The studied outwash plain appears therefore to play an important role for alpine ecosystems but has a marginal hydrological effect on downstream river discharge.

4.1 Introduction

Alpine glaciated catchments are rapidly evolving under the effect of rising temperatures and rapid glacier melt. Previously ice-covered glacial forefields may be impacted by significant sediment release from the glacier and deglaciated hillslopes (Mancini and Lane, 2020) as well as reworking by glacier meltwater (Carrivick and Heckmann, 2017), leading to rapid geomorphological and ecological changes. In addition, seasonal water supply is changing, with more winter liquid precipitation, earlier snow-melt and ice-melt, more intense diurnal discharge cycles and reduced snow-melt supply in the later summer months (Berghuijs et al., 2014; Lane and Nienow, 2019; Milner et al., 2017). These combined climatic, hydrological and geomorphological processes are strongly modifying the hydrology of glaciated catchments, which may have strong implications for high-elevation hydropower production (Schaefli et al., 2019), water-related hazards, proglacial and regional ecology (Brighenti et al., 2019b) and downstream water availability.

In this context, research has focused on characterizing the influence of glacier retreat on the geomorphological processes influencing sediment transport (Lane et al., 2017) and on the evolution of seasonal streamflow volumes (e.g. Huss and Hock (2018); Huss et al. (2008)). However, assessment of the role of groundwater storage and release is usually oversimplified (Vincent et al., 2019), even if it may play an important role especially during extreme drought events (Buytaert et al., 2017). Due to the complexity of landforms in glacial forefields and their susceptibility to rapid reworking, groundwater storage is likely contained in different compartments such as superficial landforms or bedrock fractures with different water storage potential and retention time scales (Hayashi, 2020; Müller et al., 2022a). For this reason, a sound understanding of future water availability and storage in alpine glaciated catchments can only be achieved by acquiring detailed knowledge of the hydrological functioning of different landforms and their associated water storage potential as well as of spatial groundwater recharge and exfiltration patterns (Müller et al., 2022a). Some recent studies started to address this issue (Glas et al., 2018; Hayashi, 2020) by characterising and mapping geomorphological landforms such as talus slopes (Kurylyk and Hayashi, 2017; Muir et al., 2011), lateral deposits (Baraer et al., 2015), moraines (Kobierska et al., 2015a; Langston et al., 2013; McClymont et al., 2011) or rock glaciers (Harrington et al., 2018; Wagner et al., 2021; Winkler et al., 2016). For a detailed review, the reader is referred to the work of Hayashi (2020).

Outwash plains have been less studied and so here we characterize the hydrological behavior of an alpine proglacial outwash plain, a type of newly-formed fluvial aquifer composed of gravelly-sandy sediments deposited in front of a glacier after subglacial erosion. The ecological importance of older Quaternary fluvial deposits has been studied, showing that their location in flat valley bottoms allows them to accumulate water, sediments and organic matter from different sources leading to a patchwork of environmental habitats essential for endemic species (Crossman et al., 2011; Hauer et al., 2016; Miller and Lane, 2018). Studies have shown the strong surface water-groundwater interactions, with infiltrated stream water extending hundreds of meters laterally beyond the stream network (Hauer et al., 2016; Ó Dochartaigh et al., 2019) and with a dominant longitudinal groundwater gradient, which leads to groundwater upwelling in downstream river sections (Ward et al., 1999). Whilst the behavior of such larger aquifers is well known, the emergence of new small alluvial floodplains after the Little Ice Age in the Alps has not been studied from a hydrological perspective, with the exception of a series of studies in Val Roseg in the Swiss Alps (Malard et al., 1999; Ward et al., 1999).

The importance of further research in this field is emphasised by the fact that proglacial outwash plains will likely provide the only viable habitat for cold-water species (Brighenti et al., 2019b) and may store relatively large amounts of water. Four questions arise: (i) what is their future spatial extent and hydrological significance in deglaciated terrain?; (ii) are their groundwater dynamics similar to larger Quaternary floodplains in terms of their potential to maintain shallow groundwater seasonally?; (iii) how will they respond to early-season and reduced ice- and snowmelt?; and (iv) how will vegetation feedbacks influence their stability and water and sediment storage (Roncoroni et al., 2019).

We address the first three questions by providing a detailed analysis of a selected case study in the Swiss Alps, the Otemma glacier forefield, where a large outwash plain system has been monitored for sediment, ecological and hydrological processes since 2019 (Müller et al., 2022a). Based on two years of groundwater well observations and of discharge and electrical conductivity measurements, we build a 3D MODFLOW model

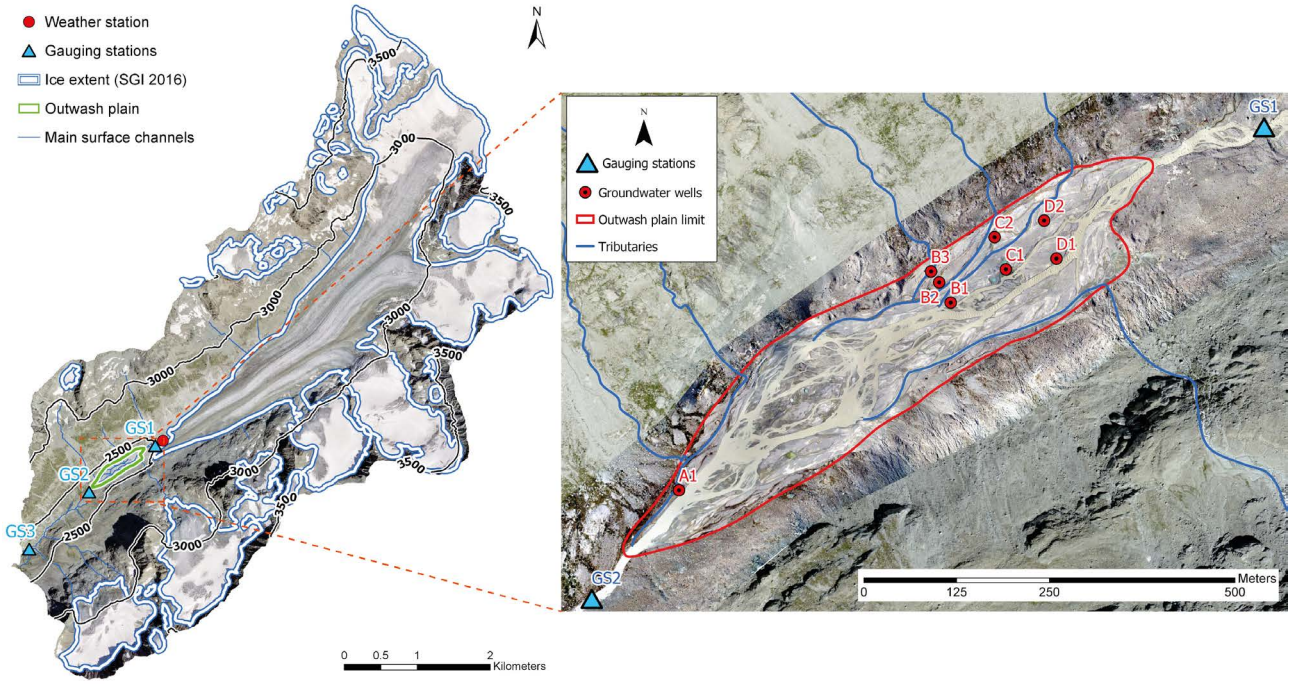

Figure 4.1: Overview of the Otemma catchment and the outwash plain, gauging and weather stations. The window on the right shows the braided outwash plain with the 8 groundwater wells and the main hillslope tributaries.

to characterize the groundwater dynamics and the rate of stream water infiltration and groundwater exfiltration. This allows us to characterize the surface water-groundwater dynamics of a typical outwash plain, which is likely similar to other those of other alpine environments. Finally, we apply the developed model to a hypothetical future scenario where new outwash plains are formed due to glacier retreat in deglaciated bedrock overdeepenings and demonstrate their overall hydrological significance.

4.2 Study site and experimental methods

The Otemma glacier is located in the Western Swiss Alps (45°56'03"N,7°24'42"E) with a catchment area of 30.3 km^2, a mean elevation of 3005 masl (2350 masl to 3780 masl) and about 45 % glacier cover in 2020 (Linsbauer et al., 2021). The glacier is characterized by a relatively flat tongue which is rapidly retreating. The outwash plain studied here was gradually uncovered between 1988 and 2020 over a length of about 1250 m in 32 years, or a glacier retreat rate of almost 40 m year^{-1} (GLAMOS (1881-2020)).

The underlying bedrock consists of orthogneiss and metagranodiorites (Burri et al., 1999), overlain by coarse superficial sediment deposits with limited vegetation development and shallow, young soils. The outwash plain is composed of non-consolidated sandy-gravelly material forming a mosaic of bars and terraces. It covers a surface of 118'000 m^2 or 0.4 % of the total catchment area. The main stream network is braided in the lower part of the plain, with rapid channel modifications due to periodic high discharge, and more constrained in the upper part, where the stream is usually limited to one channel, although large channel erosion (>5 m per hours laterally) was also observed during large flood events (once a year). There is a general downslope gradient from coarser to finer sandy-silty material, typical of outwash plains (Maizels, 2002; Zielinski and Van Loon, 2003). The melt-out of buried ice is also observed, leading to the formation of "kettle holes" (Maizels, 1977). The outwash plain has a longitudinal length of about 900 m and a slope between 1 % in its lower part to 2 % upstream and a mean slope of 1.4 %. The lateral relief is variable between 2 and 3 m and associated with terraces.

4.2.1 Meteorological data

Since 2019, a meteorological station was installed near the glacier terminus at an elevation of 2450 masl and continuously measured liquid precipitation with a Davis tipping rain gauge and air temperature, relative

humidity and pressure with a Decagon VP-4.

Additionally, winter solid precipitation was measured using the closest SwissMetNet weather station, either in Otemma (2357 masl) or in Arolla (2005 masl) for time steps where the Otemma station showed missing values (the two stations are 1.5 km and 11.5 km from the outwash plain). Data and their description are available on Zenodo (Müller, 2022a).

4.2.2 Surface water data

Two gauging stations were installed in the main stream, upstream (GS1, Fig. 4.1) and downstream (GS2, Fig. 4.1) of the outwash plain in bedrock-constrained river sections. Stream temperature, water electrical conductivity (EC) and river stage were measured continuously at 10 minute intervals using an automatic sensor (Keller DCX-22AA-CTD). Sensor measurements were checked against bi-monthly manual measurements. Discharge was estimated at both sites by building a stage-discharge rating curve. Point discharge measurements were performed by dilution gauging using fluorescence dye tracing (Rhodamine WT 20 %). The dye concentration was measured with a Fluorometer (Albillia GGUN-FL30) recording at 5 second intervals following dye injection. For flows smaller than 1 $m^3\ s^{-1}$, discharge was measured using salt dilution gauging instead of dye. Dissolved salt concentration was measured using EC and a local EC to salt concentration curve was built. In total, 27 discharge measurements were performed for GS1 and 21 for GS2 in 2020, and 15 and 13 respectively in 2021. For each gauging station, we covered a wide range of discharge values, from low winter baseflow (100 $L\ s^{-1}$) to summer high flow (10 $m^3\ s^{-1}$). The estimated mean discharge uncertainty (95 % confidence) is 0.55 $m^3\ s^{-1}$. More detailed description of the data is available in the work of Müller and Miesen (2022).

Along stream gauging was also attempted to quantify rates of surface water-groundwater interactions. This was however only successful during the autumn period when stream flow is low and less turbulent and thus streamflow measurements via salt gauging were more precise. This was the only period when the discharge measurement error was smaller than water exchange rates. On 17 September 2021, we gauged the stream at three locations : above the start of the outwash plain (GS1), at the location of well B1 and at the end of the outwash plain (100 m above GS2). At that time, all surface tributaries were visually dry so that lateral water inputs are negligible.

In addition to the main stream, small hillslope tributaries were also manually monitored for EC and water temperature. All manual measurements in this study were performed with the same device (WTW Multi 3510 IDS logger with a IDS TetraCon® 925 water conductivity probe).

4.2.3 Groundwater measurements

Between 2019 and 2022 we installed eight fully-screened groundwater observation wells in stable terraces of the outwash plain, consisting of three lateral transects (transect B,C,D) in the upstream part of the plain and one single well (A1) in the downstream part (Fig. 4.1). The wells reached a depth of about 2 m below the ground surface. Groundwater levels were measured using autonomous loggers (Seeeduino Stalker V3.1) equipped with SparkFun MS5803-14BA pressure sensors measuring with a 10 minute interval. The sensor resolution was 1 mm with an accuracy of ±2 cm and sensor bias was manually checked bi-monthly using manual groundwater stage measurements. The sensors functioned year-round, but groundwater stage usually fell below the sensor in winter and sometimes the sensors were damaged by winter snow accumulation. More detailed description of the data is available in the work of Müller (2022b). Periodic point measurements of groundwater EC and temperature was also performed. Prior to measurement, groundwater wells were flushed by pumping 3 times their water volumes.

4.2.4 Electrical resistivity tomography

Electrical resistivity tomography (ERT) was performed in the outwash plain in order to map sediment depth and bedrock with a Syscal Pro Switch 48 from Iris Instruments. The array consisted of 48 electrodes with a spacing between 1.5 m and 4 m and we performed both dipole-dipole (DD) and Wenner-Schlumberger (WS) schemes for each measurement site. The location of each electrode was measured with a GNSS GPS (Trim-

ble R10 GNSS) and we performed data inversion using the Open-Source pyGIMLi python library (Rücker et al., 2017). We included topography and used a robust inversion scheme (L1-norm) with a set of regularization parameters in order to assess the results sensitivity to over-fitting.

A total of 21 different electrical resistivity tomography profiles were obtained between 2019 and 2021. The depth of the sediments was identified based on a sharp transition from water-saturated sediments with resistivity values between 500 and 2000 Ωm to a lower layer with resistivity of between 4000 and 7000 Ωm. The depth obtained with both electrodes setups (DD and WS) were systematically compared to assess any differences in the obtained depth profiles.

Some more resistive patches were identified, with values larger than 10000 Ωm, which we attributed to the presence of buried ice (Bosson et al., 2015). More detailed description of the data is available in the work of Müller (2022c).

4.3 Methods

4.3.1 3D MODFLOW model

We set-up a 3D MODFLOW model of the outwash plain aquifer using the python package Flopy (Bakker et al., 2016) with the latest MODFLOW 6.3 version (Langevin et al., 2022). The model was first initialized with a pre-defined set of parameters and, in a second phase, we calibrated the model parameters (Sect. 4.3.2.3) using the optimisation algorithm PEST HP, a PEST version (Doherty, 2015) optimized for Highly Parallelized (HP) environments.

The calibrated model was then used to analyse the aquifer behavior during a whole year. The main packages used to build the MODFLOW model are described in the following sections and the main parameter values are summarized in Table 4.1.

4.3.1.1 Temporal Discretization (TDIS)

The model is defined with an hourly time step. The time period for the calibration phase is from 15 August 2020 to 18 November 2020. This time period was considered adequate to cover both summer high flows and the autumn recession period.

4.3.1.2 Structured Discretization (DIS), Node Property Flow (NPF), Storage (STO)

The model lateral boundary corresponds to the limit of the outwash plain, which was manually digitized (Fig. 4.1). The surface topography was determined using Surface-from-Motion Multi-View Stereo (SfM-MVS) photogrammetry, using imagery acquired with a Dji Phantom Drone, resulting in a final DEM with a 0.25 m resolution and a ± 0.02 m precision. A detailed description of the procedure is provided in Roncoroni et al. (2022).

The DEM was then resampled to a model grid of 10 by 10 m. In order to estimate the elevation of the water bodies precisely, we isolated the zones in the DEM corresponding to the stream network and performed a separate resampling of these zones only. Due to the typically larger noise in the DEM of the water bodies, we then applied a smoothing filter algorithm (Savitzky–Golay) along the stream network.

The depth of the model is defined using data from the electrical resistivity tomography (ERT) measurements. We only simulated the coarse-grained sediment aquifer and defined the underlying bedrock as the model boundary. We neglected any infiltration into the bedrock because its hydraulic conductivity is likely 3 to 4 order of magnitudes smaller (Masset and Loew, 2010) and thus negligible for the times-scales and purpose of our model. From the ERT transects, we manually drew lines of equal depth and then performed a spatial interpolation (Topo to Raster function from ArcGIS) to create the bedrock topography of the whole domain (Fig. 4.2). The model domain is further split into 4 aquifer layers where hydraulic conductivity and porosity (specific yield) are allowed to vary independently. Those parameters were calibrated in a second step using PEST HP (Sect. 4.3.2). The top layer includes the first 2 meters below the measured elevation of the water body to the top of the DEM. The next lower layer extends from - 2 m to - 6 m, and subsequent

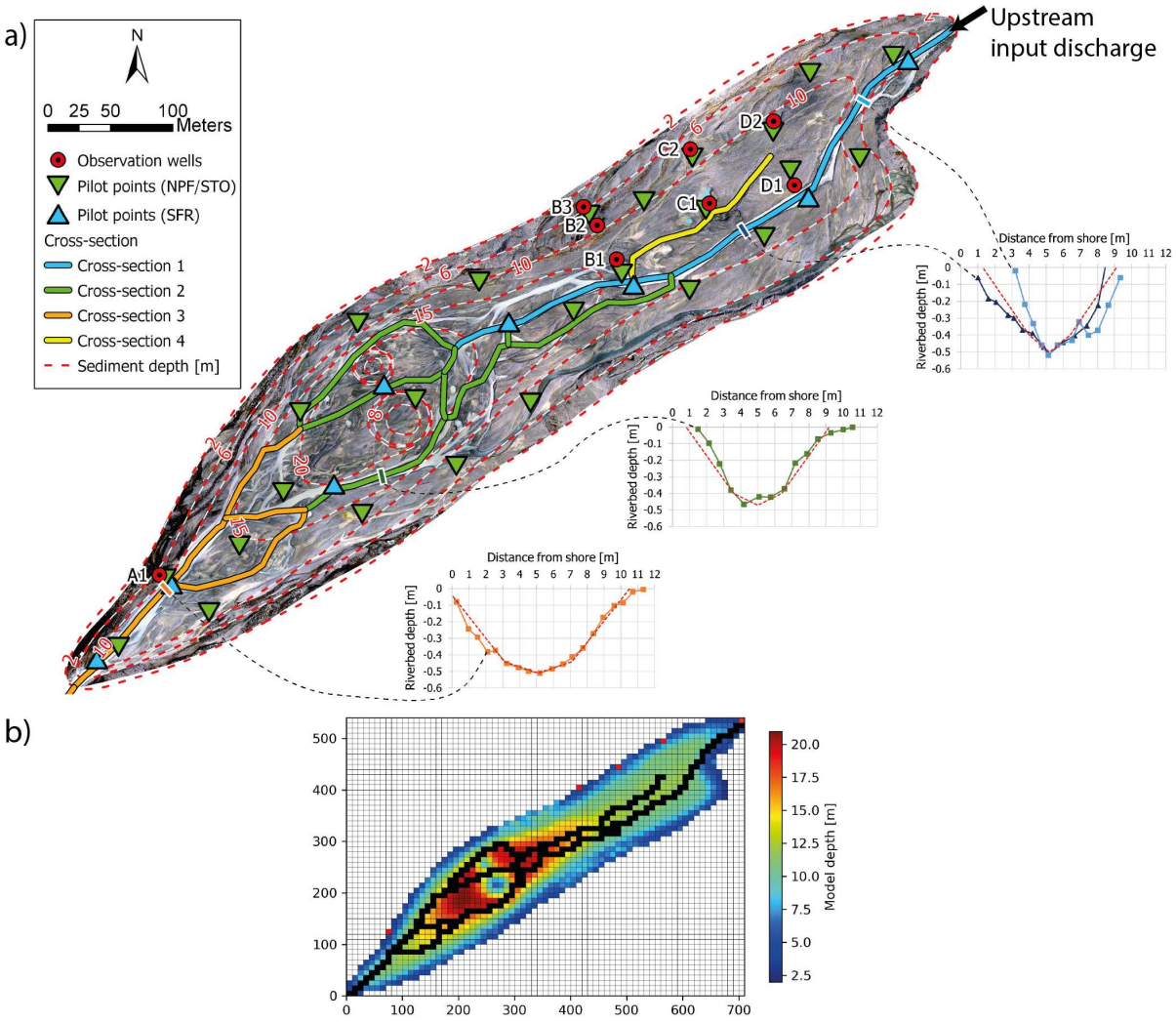

Figure 4.2: **a)** Overview of outwash plain model parameters. Six pilots points are used for streamflow (SFR) and 15 for hydraulic conductivity (NPF) and storage (STO). Observation wells are used for history-matching. Sediment depth was drawn manually based on ERT profiles and the two anomalies in the largest part of the floodplain are due to buried ice (see Sect.4.4.1). River cross-sections are separated in 4 classes, two bathymertrics profiles are shown for Cross-section 1 (light/dark blue), one for cross-section 2 (green) and cross-section 3 (orange). The dashed red line in the graphs represents the corresponding simplified cross-section used as model input. **b)** Corresponding MODFLOW grid. The colorscale represents the maximal model depth. The stream network is shown in black and the red squares represent the location of recharge and input discharge.

layers of 4 m depth are defined until bedrock is reached.

The model uses the Newton-Raphson formulation which allows for a precise computation of unconfined groundwater flow.

4.3.1.3 Streamflow Routing (SFR)

The stream network was manually identified using the orthophoto from 18 August 2020 (Fig. 4.2). Only the main larger permanent channels were identified and were assumed not to change during the modelling period.

We use the SFR package from MODFLOW which allows for an estimation of surface water-groundwater exchanges and an estimation of river stage and width based on Manning's equation, river discharge and riverbed cross-section. For each river grid cell, the riverbed elevation was estimated using the calculated elevation from the surface DEM and an average depth for each stream segment based on a bathymetric survey performed on the 18 August 2020, where river cross-section was measured with a differential GPS

Trimble R10 and a spacing between points of about 0.5 m.

We also defined a simplified cross-section for each segment consisting of a trapezoidal section. Four different cross-section categories were defined (Fig. 4.2). The upstream river segments (category 1) have slightly steeper channel slopes and narrower bottom width than the downstream parts (category 3); category 2 makes a transition between the upstream and downstream parts; category 4 represents a stream segment which was usually disconnected from the upstream river, but where groundwater exfiltration maintained some baseflow in summer. This segment was defined with a rectangular cross-section with a width of 2 m. MODLFOW first estimates discharge for each river cell and then calculates river stage and width based on the cross-section so that the wetted perimeter available for water exchanges varies with time. The Manning's roughness coefficient was defined as a calibration parameter in the model.

4.3.1.4 Hillslope recharge

In addition to the river discharge defined for the streamflow, hillslope recharge was also specified in the model. We specified four points of groundwater recharge on the side of the modelling domain (red squares in Fig. 4.2b) where a time-varying water input was applied in the first groundwater layer. The amount of recharge was estimated by building an enhanced temperature-index melt model (Gabbi et al., 2014), which computes snow accumulation and melt as well as rain for the four selected hillslope subcatchments based on averaged hourly air temperature, incoming radiation and precipitation measured at the weather station. Precipitation was provided in summer by the weather station at the glacier tongue and winter precipitation from the closest available SwissMetNet station. The model was established at the catchment scale by defining model grid cells of 200 m, where mean elevation, slope and aspect were computed based on a 2m resolution digital elevation model (DEM) from SwissTopo (2019). Snow redistribution on steep slopes was defined by limiting precipitation above a calibrated slope threshold. The incoming radiation was corrected for slope and aspect using a correction function defined by two calibration parameters. Model calibration was performed automatically using PEST-HP (see Sect. 4.3.2), by minimizing the error on calculated and measured snow water equivalent (SWE). SWE was estimated based on snow depth measurements performed manually at 5 locations on 26 June 2020 and 92 locations on 29 May 2021 on the whole glacier main lobe (from 2500 to 3000 m. asl). Snow density was estimated by measuring the average density of the whole snow pack with a snow sampler in the centre of the glacier main lobe in 2020 and at two locations in 2021 on the same dates as snow depth. Additionally, a second objective function was defined in PEST to minimize the error between modelled and observed presence/absence of snow in each cell. Seasonal snow cover was based on daily 3m resolution Planet images (Planet Team, 2017), where snow was identified using a K-Means unsupervised learning algorithm from Google Earth Engine (ee.Clusterer.wekaKMeans (Arthur and Vassilvitskii, 2007)). On average, one clear sky day image was available every week in the summer. Finally, for the hillslope subcatchments, the same model was applied with the established parameter calibration but we used 50 m elevation bands instead of grid cells as those subcatchments where too small for such grid cells. A simple routing to convey water from each elevation bands to the subcatchment outlet was defined using a gamma distribution function, where the peak of the distribution matches the estimated transit time in the hillslope. The averaged transit time for a steep hillslope was estimated using a kinematic subsurface saturated flow equation (MacDonald et al., 2012), with a mean slope of 45 °, an aquifer porosity of 0.3 and a hydraulic conductivity of 5 x 10^{-2} m s^{-1}, typical for coarse talus slopes (Muir et al., 2011). The model codes and calibrated parameters are available in the supporting material.

Water input from the hanging glacier located on the southern hillslope (Fig. 4.1), either via hillslope recharge or directly via its tributary to the main network (near the end of the outwash plain) was neglected due to a lack of measurements in this part of the outwash plain. The implications of this simplification are detailed in the discussion.

4.3.2 PEST HP

PEST HP is a model-independent algorithm for parameter estimation using inverse methods; model parameters are iteratively modified such as to minimize the variance of the error between the model outputs and corresponding field observations (Doherty, 2015). PEST HP was used for calibration.

Table 4.1: Summary of the main MODFLOW parameters by packages. Ranges in red indicate bounds for parameters calibrated during the calibration phase.

MODFLOW parameters	**Value**
Packages TDIS/DIS	
Time step	1 hour
Simulation length	95 days
Cell size	10 meters
Number of groundwater layers	4
Top elevation	From DEM
Bottom elevation	From DEM and ERT
Packages NPF/STO	
Layer hydraulic conductivity	500 m per day (10 - 2000)
Layer specific yield	0.25 (0.2 - 0.3)
Layer specific storage	1e-05
Package SFR	
Manning's coefficient	0.035 s $m^{-1/3}$ (0.01 - 0.05)
Streambed thickness	0.5 m
Streambed hydraulic conductivity	5 m per day (0.1 - 20)
Stream gradient	From DEM
Reach width	max. 20 m
Reach length	From orthophoto
Reach bottom elevation	From DEM and bathymetry
Reach cross-section	Trapezoid from bathymetry

4.3.2.1 Calibration parameters and pilot points

The MODFLOW parameters selected for calibration are groundwater hydraulic conductivity (K_{gw}), groundwater specific yield (S_y), streambed hydraulic conductivity (K_{rb}) and the Manning's roughness coefficient (n). Groundwater parameters govern the rate of groundwater flow in the subsurface and are typically used for model calibration against observations of hydraulic head (Brunner et al., 2017). River-bed hydraulic conductivity was also estimated as it was shown to have a strong impact on the rate of water exchanges between surface water and groundwater (Schilling et al., 2017). Manning's roughness coefficient was also calibrated as it is recognised as an effective parameter (Lane, 2014) designed to represent a set processes not directly included especially with the hydraulic formulation in MODFLOW used here.

Parameter estimation of the whole model domain was carried out by defining a subset of pilot points for calibration on which automatic kriging was applied. For K_{gw} and S_y, we place 25 pilot points separated by approximately equivalent distance over the domain for each 4 groundwater layers. For the stream parameter K_{rb}, we use 8 pilot points along the stream (Fig. 4.2).

4.3.2.2 Parameter regularisation and initial values

To avoid unrealistically high spatial heterogeneity and overfitting in the parameter estimation, we used Tikhonov preferred value regularisation (Park et al., 2018), which adds a penalization term to the least-squares problem so as to dampen the influence of non-desired solutions. Preferred initial calibration parameter values are summarized in Table 4.1. For K_{gw}, the estimation was based on groundwater salt tracing and diffusive wave propagation was performed in the outwash plain in a previous work (Müller et al., 2022a); there, we estimated saturated hydraulic conductivity values in the groundwater ranging from 85 to 660 m per day. We, therefore, defined here an initial value of 500 m per day with a range between 10 and 2000 m per day for K_{gw}. A similar value was also used in the work of (Schilling et al., 2017) for a Quaternary alluvial aquifer. S_y was also measured in the field with a mean porosity of 0.25. Riverbed hydraulic conductivity could not be measured in the field directly so that an initial value was estimated by manually running the model without automatic calibration, and was set to 5 m per day. Finally, Manning's roughness coefficient was set to a value 0.035 s $m^{-1/3}$, adequate for natural unvegetated gravelly streams (Phillips and Tadayon, 2006), but with a calibration range of 0.01 to 0.05.

4.3.2.3 Objective function and model calibration

We use the time period from 15 August 2020 to 18 November 2020 for model calibration. Five different reference data sets were used to build a set of objective functions to calibrate the model with PEST: i) daily averaged water heads data from all 8 wells; we excluded the three first days of data from the calibration period in order to initialize the model; ii) daily head differences, iii) the daily time of maximal head; iv) rate of daily head change and v) surface water-groundwater exchange fluxes along the main stream.

The transformed datasets ii) and iii) were obtained from head measurements and contained additional information compared to the raw groundwater heads. It has indeed been shown that diel head fluctuations in fluvial aquifers are due to stream level variations that propagate as a diffusive wave into the aquifer (Magnusson et al., 2014), and that depend directly on the hydraulic diffusivity (D) of the aquifer, which combines K_{gw}, S_y and aquifer depth (b) following the relationship $D = K_{gw}b/S_y$. The amplitude and timing of diel fluctuations were therefore useful estimators of the aquifer properties variation with depth. The rate of daily head changes (dataset iv) were used to put more weight onto the recession that occurs in autumn, so that the rate of the aquifer drainage was well represented. Surface-groundwater exchange fluxes (resulting from surface water infiltration and groundwater exfiltration) were obtained from streamflow measurements along the main stream and corresponding differences between upstream and downstream section ends (see Sect. 4.2.2 in study site). Although the measurement was performed in 2021, we observed similar flow conditions (similar discharge at GS1 and groundwater heads) the year before so that this observation of stream-groundwater exchanges gave a first-order estimate of the fluxes during low flows and contributed to a better estimation of K_{rb}.

In total, we thus had 5 reference data sets for defining a calibration objective function corresponding to a non-linear weighted least squares function. The calibration was then obtained with PEST by running the model 50 times until algorithm convergence. For all other algorithmic parameters of the PEST algorithm, the suggested default values were used and and are accessible in the Supporting Material.

Following the calibration procedure, we ran the model for the entire period for which we have data, i.e. from 27 June 2020 to 15 September 2021 (445 days), which yields us additional 350 days to evaluate the model performance outside the calibration period.

4.3.3 Future of outwash plain storage and subglacial overdeepening mapping

Outwash plains are formed through successions of sediment aggradation and deposition which depend on sediment load, accommodation space, slope and discharge magnitude and intensity of variation (Maizels, 2002; Miall, 1977). In glaciated alpine catchments, valley bottoms are usually steep, so that suitable locations for the formation of outwash plains are restricted to areas where the bedrock topography is wide and flat. This mostly occurs where overdeepenings in the bedrock occur due to glacier erosion (Otto, 2019). If sediment supply fills such depressions, a new outwash plain may form. We therefore identified potential future outwash plains by locating bedrock overdeepenings below the current Otemma glacier. The latest estimate of ice thickness distribution and corresponding bedrock topography for Switzerland was produced by Grab et al. (2021), where they used a mixed approach consisting of airborne Ground Penetrating Radar (GPR) profiles combined with glaciological modeling. Based on the digital elevation model (DEM) of bedrock topography with a resolution of 10 m, we automatically identify bedrock overdeepenings (ArcGIS Fill tool). We then manually defined a plane connecting the lower and upper edge of the identified overdeepenings, which would correspond to a theoretical outwash plain surface. We finally calculated the depth and volume of each future outwash plain by subtracting the elevation of the surface outwash plain DEM and the bedrock DEM.

Based on these results, we made the hypothesis of the emergence of additional outwash plains of similar volumes to the existing one and created a scenario where outwash plain aquifers would connect to each other and analyzed the cascading effect on river discharge and aquifer storage. The aim here was to approximate the order of magnitude of the impact of outwash plain groundwater storage and release on stream flow in the future rather than building a realistic and precise future scenario. This was obtained by applying the developed MODFLOW model sequentially to all identified outwash plains, where streamflow outflow from the

upstream plain was used as streamflow input to the downstream plain. Lateral inflow from hillslopes was here excluded from the model in order to only analyze the impact of the floodplain on the cascading discharge. We analyzed the impact both for high discharge and severe drought situations where water supply rapidly decreases to zero.

4.4 Results

4.4.1 Bedrock topography

We present here the results of three ERT lines (of a total of 21 lines) collected in 2020, which cover different parts of the outwash plain (Fig. 4.3). The inversion results obtained are stable regardless of the chosen regularization parameter (lambda); lambda values around 1 show coarser results, likely due to over-fitting; a mild regularization (lambda values of 10 to 50) leads to smoother images. The relative root mean square error (rRMSE) of most inversions is below 20 %, indicating low model misfit (Jordi et al., 2018).

We compared the results from both Wenner-Schlumberger and dipole-dipole schemes as well as intersecting ERT lines to assess the robustness of the bedrock depth estimation. The corresponding results agree well in most cases, in general with less than 10 % difference. Sediment depth increases smoothly from the hillslope edges of the outwash plain (with a depth of 2 to 5 m) towards its center. Maximum sediment depth in the lower part of the outwash plain reaches 20 to 25 m (line 03 in Fig. 4.3) and 10 to 15 m in the upper part (line 02 in Fig. 4.3). Bedrock is also shallower at the upstream and downstream end of the outwash plain, with sediment depth of only 2 to 5 m. The outwash plain appears therefore as a large bedrock overdeepening filled with sediments and showing a surface slope of 1 % downstream to 2 % upstream.

Some blocks of buried ice were also detected (Fig. 4.3). In line 02, two more resistant areas of 1 to 2 m diameter can be identified in the middle of the sediment layer. These blocks were repeatedly measured for 3 years, with a size and resistance slowly decreasing over the years. Since they are exactly located below kettle holes, which also became larger each year, these spots are attributed to slowly melting ice blocks , with a melting rate of less than 1 m in diameter per year. The ERT profile of line 03 also shows two more resistive (>10 000 Ωm) areas, which are much wider and deeper, reaching a width of 20 and 40 m. Their elliptic shape and highly resistant nature indicate the presence of large zones of buried dead ice which fill a large part of the outwash plain. The presence of such large zones was only observed at this location, although daily imagery reveals kettle hole formation throughout the braidplain.

4.4.2 Surface water observations and electrical conductivity

River discharge at the glacier outlet was estimated continuously from July 2020 to September 2021 (Fig. 4.4a). The early melt season is characterized by high discharge but small diel variations, which can be explained by the incapacity of the distributed subglacial drainage system to rapidly evacuate large snowmelt water inputs. By August, diel fluctuations are larger as snow-line recession reduces buffering by the snow pack and the subglacial channel network has extended up most of the glacier Lane and Nienow (2019). Discharge starts to decrease in September, but a steeper recession starts in October. By early December, no more diel fluctuations are recognisable; discharge keeps decreasing slowly, with a minimum discharge of about 70 L s^{-1}, until March, when the first melt events occur.

Discharge at GS2 remains slightly larger than GS1, likely due to the ungauged glacial catchment, but the difference usually falls in the uncertainty margin of the discharge estimation. Water electrical conductivity (EC) in the stream is inversely correlated with discharge (Pearson correlation of -0.84). In summer, EC varies between 10 and 25 $\mu S\,cm^{-1}$ at the glacier outlet (GS1) and is about 5 to 10 $\mu S\,cm^{-1}$ larger at the end of the outwash plain (GS2). During discharge recession, EC increases sharply, reaching values of 115 $\mu S\,cm^{-1}$ for GS1 and 160 $\mu S\,cm^{-1}$ for GS2 (Fig. 4.4b). This suggests that some stream water is provided to the outwash plain also during the cold winter months and is characterized by a steadily increasing EC. The origin of this stream water is not clear and may be due to some basal ice melt or a groundwater reservoir in the bedrock as suggested in the work of Müller et al. (2022a). The stream EC at the end of the outwash plain in winter shows higher values, which is likely due to ground water contributions from the outwash plain area. This is

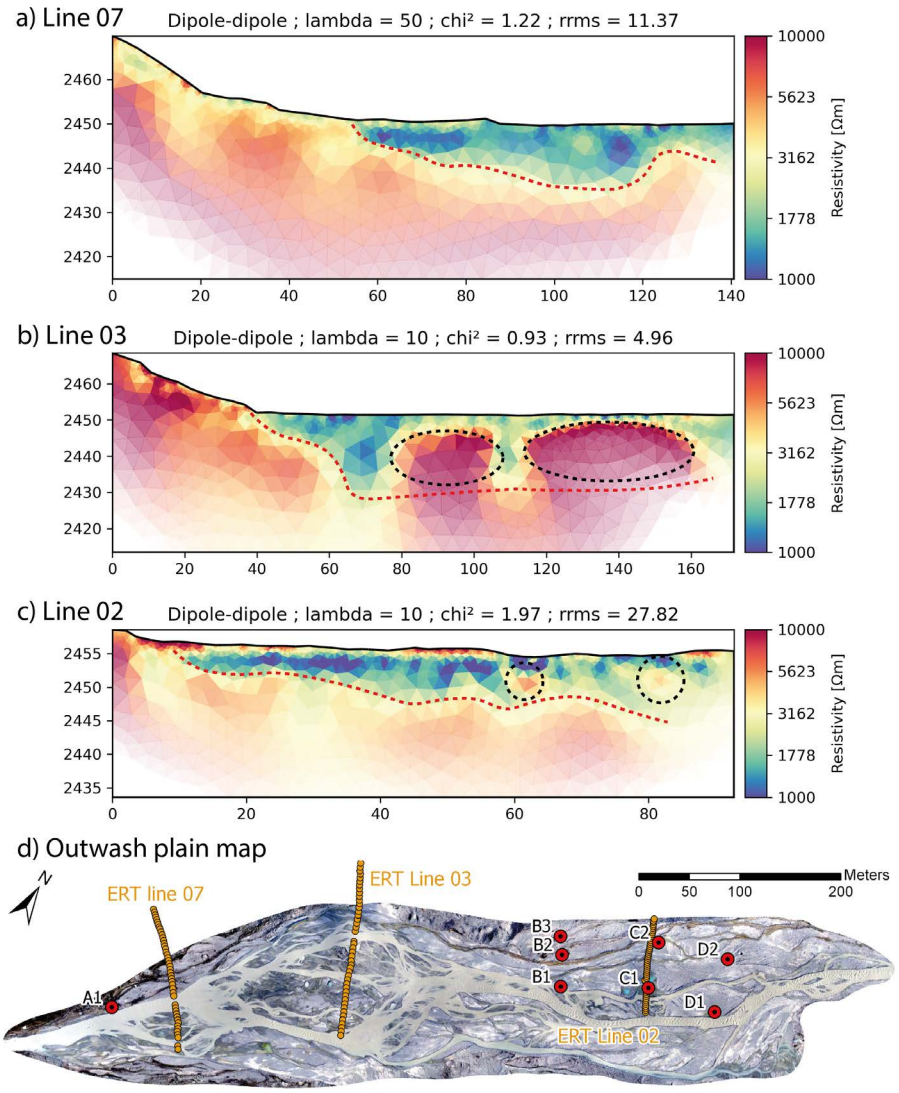

Figure 4.3: ERT profiles of **a)** line 07 (electrode spacing of 3 m), **b)** line 03 (electrode spacing of 4 m), **c)** line 02 (electrode spacing of 2 m) and **d)** corresponding locations of the ERT lines in the outwash plain. All lines are oriented from the hillslope to the center of the outwash plain. Red dashed lines correspond to the bedrock limit where resistivity became larger than 2000 Ωm and black dotted circles highlight the location of buried dead ice with very high resistivity (>10 $k\Omega m$). Regularisation parameter (lambda) and model performance are also indicated.

further detailed in the discussion.

The wells close to the stream (D1,C1,B1) tend to have low EC during summer, slightly larger than the stream EC, with a gradual increase in EC from the upstream well D1 to the more downstream well B1 (Fig. 4.4c,d). Well A1, also located near the stream but at the lower end of the outwash plain, has much higher EC values. The low EC in upstream wells (D1,C1,B1) indicates a strong influence from the nearby stream and the EC increase from upstream to downstream suggests that groundwater tends to become older with greater distance from the upstream part of the outwash plain. In particular, the high EC values of well A1 indicate that we find here the longest groundwater flowpaths, with no direct exchanges with the nearby stream.

The wells closer to the hillslopes (D2,C2,B3) show higher EC than the wells located at the same transect near the stream. Here, high EC may be due to either (1) long groundwater flow paths from the stream reach or (2) lateral hillslope recharge from a source characterized by higher EC than the stream.

Wells B2 and B3 show very low EC values in the early melt season (Fig. 4.4c), which is due to a connection with an ephemeral hillslope tributary characterized by low EC values (10 to 20 $\mu S\,cm^{-1}$) related to snowmelt input via surface runoff. This recharge seems to be only dominant during the early snow melt at this specific location.

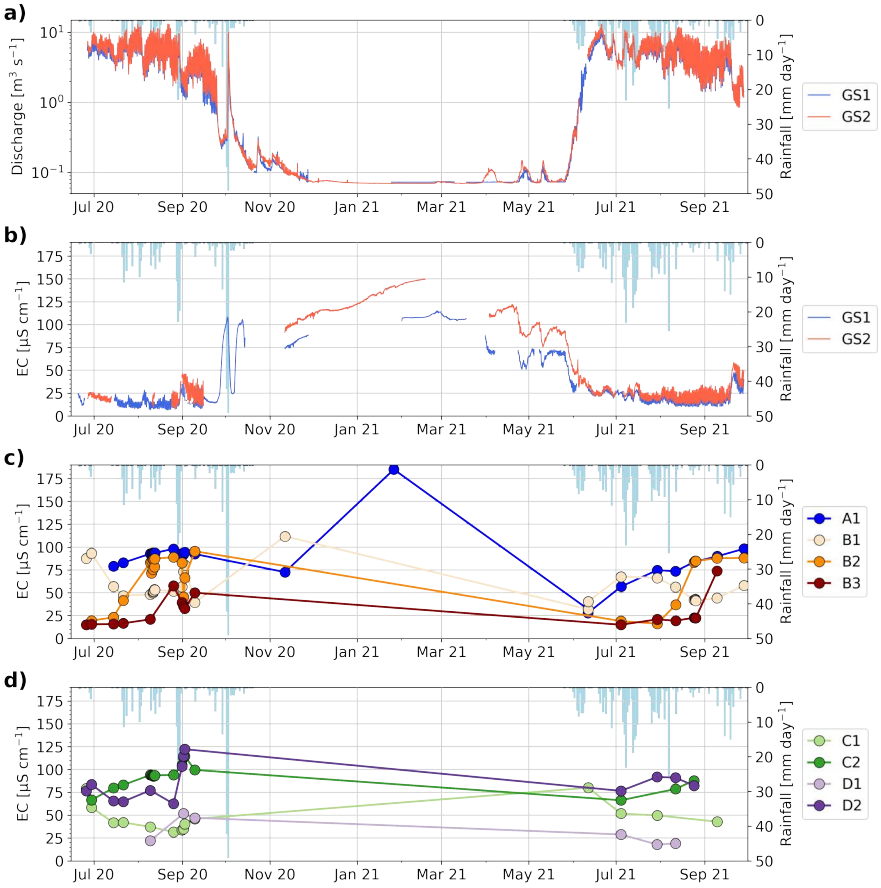

Figure 4.4: **a)** Discharge measurements in the main stream at the glacier outlet (GS1) and at the end of the outwash plain (GS2); the y-axis is in logarithmic scale.**b)** Electrical conductivity observations in the main stream and in observation wells (**c**),**d**). Measured daily rainfall amounts are also shown in light blue in all plots.

In summary, EC in wells is highly spatially and temporally variable due to a combination of different water sources with varying EC composition and varying degrees of connectivity with the stream. In general, EC in the wells seem to be correlated with their distance to the upstream part of the outwash plain, with well D1 showing EC very similar to the stream EC, suggesting a strong river infiltration from the upstream stream reaches. The contribution from lateral hillslope groundwater will be further assessed based on modelling results.

4.4.3 MODFLOW model calibration

The average calibration result obtained with PEST-HP for K_{rb}, K_{gw}, S_y and n are shown in Fig. 4.5; corresponding initial parameter values and calibration ranges are summarized in Table 4.1. K_{gw} of each layer shows some spatial variability, with zones of higher conductivity in the upper layers (400 to 1200 m per day), leading to somewhat larger average values for the top layer (Fig. 4.5a). Aquifer porosity (S_y) shows local variability in the top two layers, while the initial values were retained for the third and last layers (Fig. 4.5b). The riverbed hydraulic conductivity (K_{rb}) was estimated to have values between 3.5 and 15 m per day, with a tendency to increase in the lower half part of the braidplain (Fig. 4.5c). Although the Manning's roughness coefficient was on average close to the initial value of 0.035 s $m^{-1/3}$, it varied systematically and spatially between higher (up to 0.05) and lower (0.02) values. The modelled groundwater levels matched well the observations and the timing of the daily peaks have an average RMSE of 1.56 hours (Fig. 4.6). The median relative error of diel head amplitudes and diel head changes for each well (absolute residuals divided by the observed value) are shown in Fig. 4.6; they show satisfying results, with diel head amplitudes error smaller than 20 % and modelled head changes showing similar trends as the measured ones.

Groundwater infiltration on 17 November in the upstream part of the catchment (until well B1) is some-

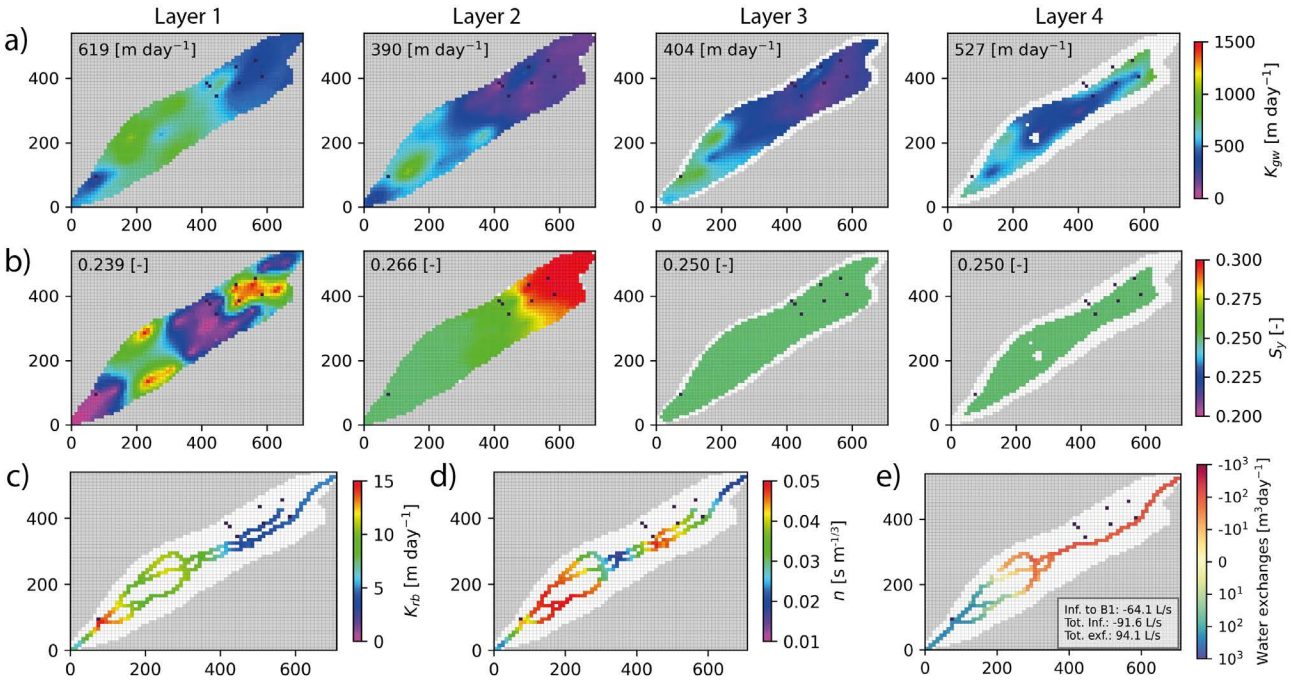

Figure 4.5: Results of parameter estimation using PEST-HP. **(a)** Groundwater hydraulic conductivity (K_{gw}) and **(b)** aquifer porosity (S_y) for the 4 groundwater layers. The parameter numbers correspond to the average value in the whole domain. **(c)** Parameter estimation for the riverbed hydraulic conductivity (K_{rb}). **(d)** Parameter estimation for Manning's roughness coefficient (n). **(e)** Corresponding modelled surface-groundwater exchanges on 17 November with text indicating modelled infiltration (until well B1 and total) and total exfiltration. Black dots correspond to locations of observation wells. Grey shaded areas are outside of the model domain and white indicates the area where the layer does not exist. X-Y values correspond to model grid coordinates in meters.

what overestimated, with 64.1 L s^{-1} compared to the observed 30 L s^{-1}; net streamflow difference between upstream and downstream discharge is underestimated, with a net water gain to the stream of 2.5 L s^{-1} compared to an observed water gain of 8.3 L s^{-1} (Fig. 4.5d).

4.4.4 MODFLOW model validation

For the additional 12 months simulated for model evaluation, the model performance for diel head amplitudes and for the timing of diel peaks is similar to the calibration period. The daily averaged heads for three observation wells are shown for illustration purposes in Fig. 4.7. In addition, we also show results of a model run where all tributaries are removed so that upstream discharge is the sole water input.

Over both summers, groundwater levels appear well simulated, during both high and low flow conditions. For well D1, there is a slightly larger offset between observed and modelled heads in 2021 and the decrease in head occurring in late August to September 2020 and 2021 does not seem to be well modelled, although the head catches up again in October 2020. This latter phenomenon is likely due to some changes in the structure of the river channel which was not incorporated in the model. For both summers, wells B2 and A1 appear to match closely the observations.

During winter, the slight groundwater recession in well A1 is not fully well represented. This may be due to the lower bedrock edge of the outwash plain which may be somewhat deeper than modelled, constraining groundwater exfiltration in this lower part. For well B2, the simulated groundwater level in mid-February 2021 matches the observation, supporting the good performance of the model to simulate groundwater drainage during low winter flow. The first initial recharge event in late February is also well modelled but the next two short peaks (April and May 2021) are underestimated. This is likely due to an underestimation of the lateral hillslope recharge or due to direct snow-pack melt on the outwash plain, which was not included in the modelling framework.

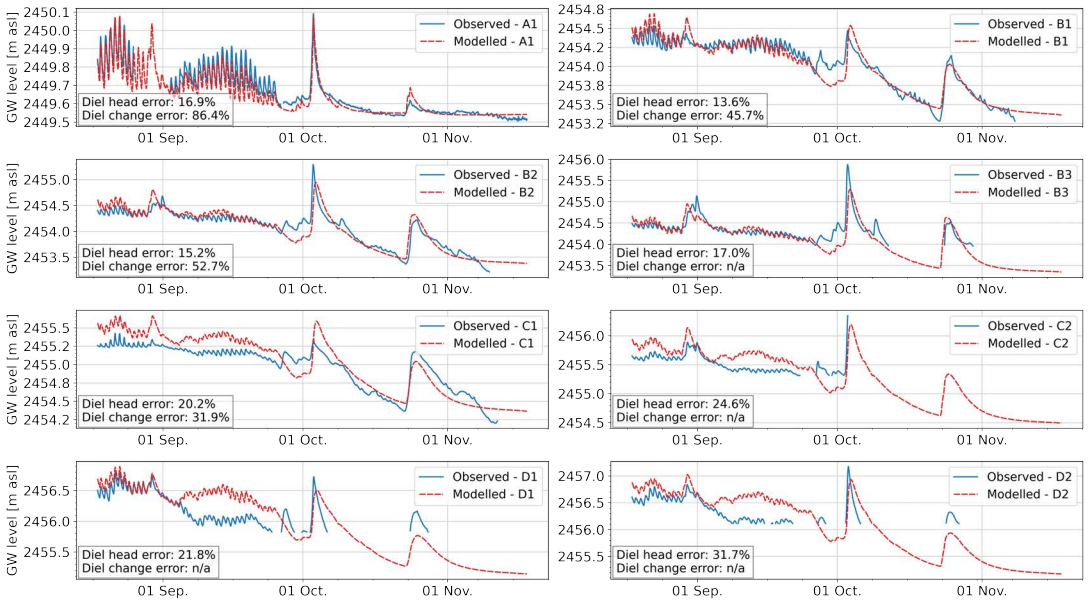

Figure 4.6: Observed (blue) versus modelled (dashed-red) groundwater heads for each well (A1 to D2). Mean absolute relative errors for the diel head amplitudes and diel head changes are also shown in the lower left box. No error is estimated (n/a) for the rate of change of wells where the autumn recession could not be measured.

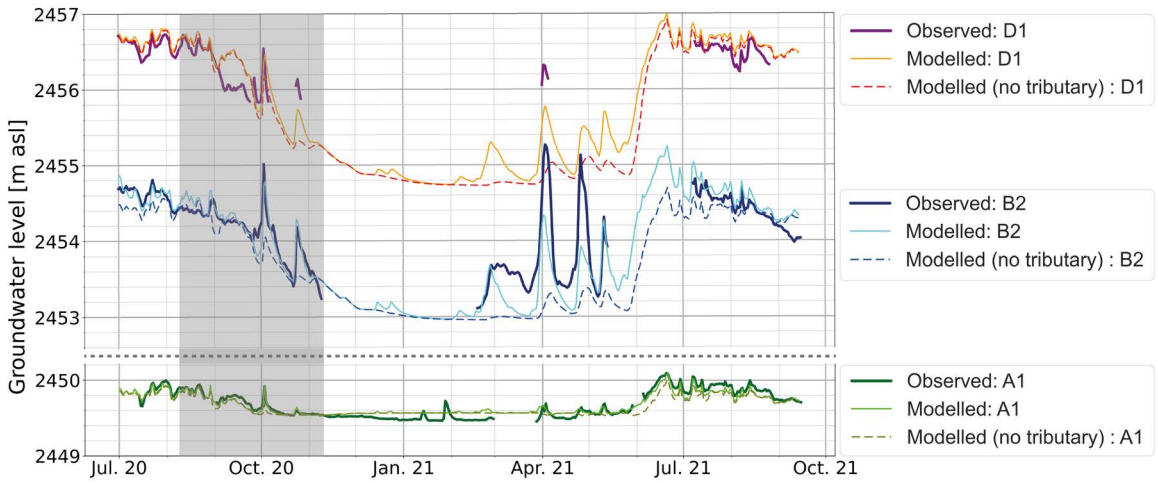

Figure 4.7: Observed versus modelled groundwater levels for three selected wells during a 14 months period. The dashed lines represent model results when all hillslope water input is set to zero during the entire simulation. The shaded area represents the calibration period. Note that the y-axis is cropped between well A1 and B2, but the scale is the same.

4.4.5 Groundwater storage and surface water-groundwater exchanges

Infiltration of stream water to groundwater occurs preferentially in the upper half of the floodplain and exfiltration of groundwater to the stream occurs in the lower half (Fig. 4.5d) of the plain. Summer infiltration is proportional to discharge, with a maximum infiltration rate of about 400 L s^{-1} and a minimal rate of 60 L s^{-1}. Some hysteresis is visible: for similar discharge, more infiltration occurs in the late morning (10:00 to 14:00) when groundwater levels are low, than in the night, when groundwater levels are high (Fig. 4.8a). Exfiltration of groundwater is also correlated with stream water infiltration: lowest exfiltration rates occur in periods with increasing infiltration rates and discharge and highest exfiltration rates occur during periods of decreasing infiltration and when groundwater levels are high (Fig. 4.8c).

During discharge recession in winter, discharge decreases sharply and infiltration is reduced proportionally. The decrease in infiltration is mainly due to a change in the wetted perimeter of the stream reach, limiting

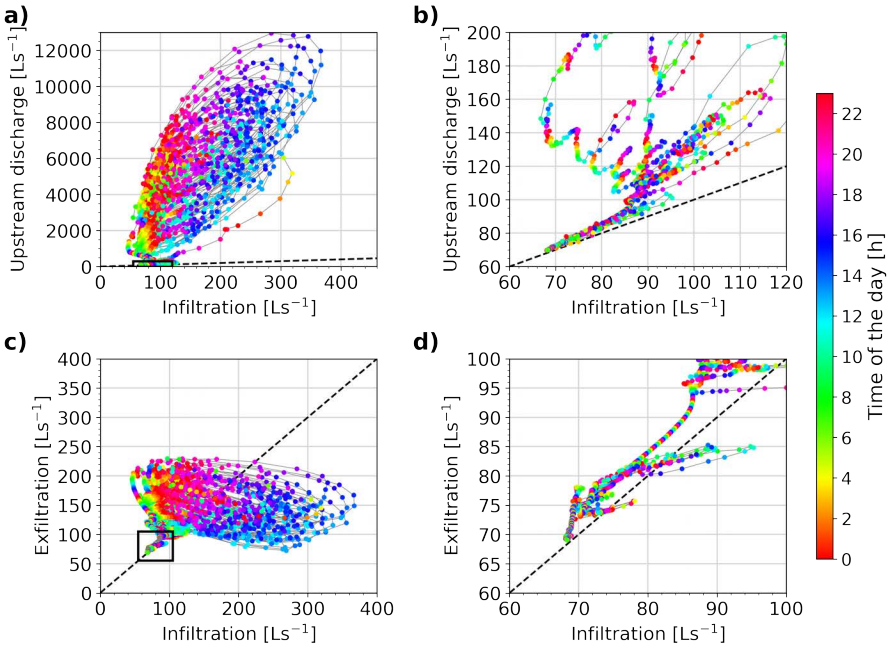

Figure 4.8: Surface water - groundwater exchanges. **(a)** Relationship between river reach infiltration and incoming upstream river discharge. **(c)** Relationship between river reach infiltration and groundwater exfiltration into the stream. The black rectangles indicate the zone of the zoom-in windows of the graph on the right **(b)** and **(d)**. The colorscale corresponds to the hour of the day for each point. The straight dashed lines show the line of equal values.

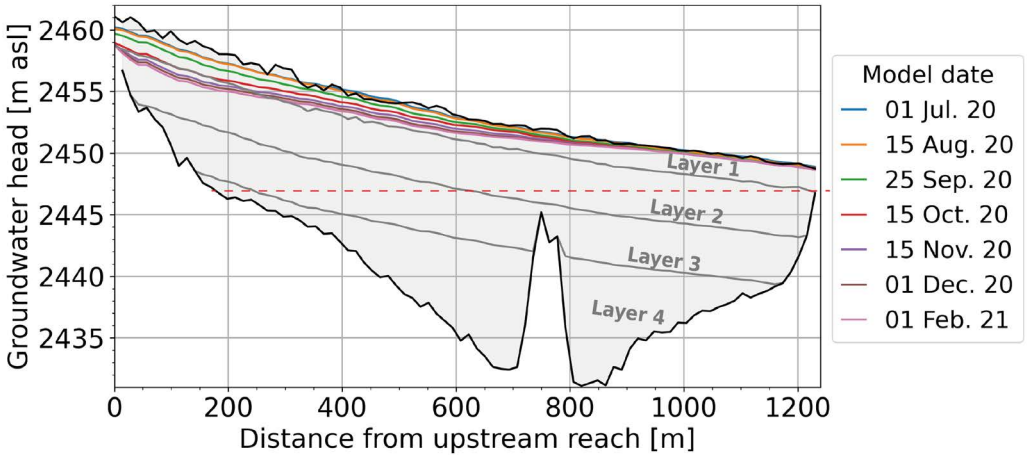

Figure 4.9: Modelled groundwater levels at different time steps (dates) along a vertical cross-section of the outwash plain, from the top right corner (upstream reach), to the bottom left corner (downstream reach) of the model domain. The grey area represents the whole aquifer with the 4 groundwater layers and the black lines represent the bedrock and surface limit of the model. The steep jump between a distance of 700 m to 800 m represents the location of the buried ice from ERT (Fig. 4.3), which is defined as bedrock in the model. The dashed red line indicates the lower limit of the dynamic storage, below which groundwater heads cannot drop.

the surface area for water exchanges. This change is more marked for upstream stream reaches, whose channel banks are steeper than downstream sections (Fig. 4.2).

When discharge decreases below than 85 L s^{-1}, most stream water infiltrates in the upper half of the outwash plain (Fig. 4.8b) so that the main stream retains little surface water in the central part of the outwash plain. However, at low discharge, exfiltration in the lower half part is slightly higher than infiltration (Fig. 4.8d), leading to more stream discharge at the end of the outwash plain than upstream.

In summer, it appears therefore that the outwash plain is only capable of infiltrating small amounts of water from the stream; infiltration happens preferentially in the morning. The aquifer exfiltrates a similar amount of water with a peak during the night, so that the average daily groundwater level remains relatively con-

Table 4.2: Estimated volumes of the five glacier overdeepenings (OD) from the lowest (#1) to the highest (#5) along the glacier main lobe of the Otemma glacier. The volume in m^3 represents the total "empty" space, the volume in mm corresponds to the total potential groundwater storage relative to the catchment scale (30.4 km^2) assuming a porosity of 0.25; the active storage represents the groundwater storage above the horizontal line (Fig. 4.10).

	Area [m^2]	**Volume** [m^3]	**Volume** [mm]	**Active storage** [mm]
OD 1	114 000	746 354	6.1	4.8
OD 2	148 300	1 899 117	15.6	7.8
OD 3	34 200	286 527	2.4	0.8
OD 4	403 400	16 837 733	138.5	66.9
OD 5	410 600	14 527 905	119.5	16.1

stant. In winter, most of the upstream river discharge infiltrates from the stream to the aquifer, but a slightly larger amount exfiltrates from the aquifer, leading to a gradual decline of the aquifer level. The aquifer therefore sustains a higher discharge at the downstream end of the outwash plain than at the upstream end. The observed slow rate of aquifer recession throughout the winter is due to a small but constant upstream water input, i.e. to upstream discharge recession.

The rate of decline is illustrated in Fig. 4.9. In summer, groundwater is maintained close to the surface in the entire plain, with a distance of about 0.5 to 1 m from the surface in the upstream part and of 0.1 to 0.5 m in the downstream part. The total water storage in the outwash plain in summer equals 3.0x10^5 m^3, which is equivalent to 10.0 mm with respect to the entire catchment area (30.4 km^2). It appears clearly in Fig. 4.9 that a large part of the aquifer volume is located below the lowest edge of the bedrock, so that this volume cannot empty. The water amount which can exfiltrate from the groundwater to maintain river discharge is hereafter defined as the dynamic storage (Staudinger et al., 2017) and corresponds to 6.7 mm (relative to the catchment area) or 67 % of the maximal total storage. In winter, the groundwater level gradually declines from the upstream end of the outwash plain, but remains close to the surface in the lower part, where groundwater flow is constrained by bedrock and forced to exfiltrate. At the time of lowest discharge (1 February 2021), the total dynamic storage amounts to 5.4 mm, so that the aquifer has lost 1.2 mm during the recession period.

4.4.6 Future hydrological role of outwash plains

We identified five bedrock overdeepenings below the Otemma glacier main lobe (Fig 4.10) and quantified their dynamic storage by calculating the volume included between the sloping aquifer and the horizontal line at the lower edge of the overdeepening and using a porosity of 0.25 (Table 4.2). The lowest two overdeepenings show similar areas and volumes as the current outwash plain. The third one is limited to a smaller volume of sediments having a storage potential of about 10 mm. The two upper ones are characterized by much deeper depths and larger volumes.

Based on the hypothesis of the future emergence of 2 new outwash plains, we analyzed the cascading effects of a chain of 3 outwash plain aquifers. The results depicted in Fig. 4.11a) show that for high flows, a slight reduction of the peak discharge occurs. In the first outwash plain, river infiltration amounts to about 350 L s^{-1} of stream water when peak discharge reaches 13 m^3 s^{-1}; the aquifer simultaneously releases about 180 L s^{-1}, leading to a decrease of total discharge of about 170 L s^{-1}. At the end of the third plain, the total peak flow reduction due to infiltration is about 400 L s^{-1}. The peak is also slightly delayed and attenuated due to flood routing along the braided river system, leading to a total decrease of about 600 L s^{-1}, i.e. slightly less than 5 % of the upstream water input.

For the drought scenario (Fig. 4.11b), after the first outwash plain, higher downstream river discharge is only maintained when the input discharge decreases below 180 L s^{-1} (or about 0.5 mm per day) on day 10. The rate of discharge recession is fast, with the discharge decreasing by half in about 4 days and decreasing 10 times in about 25 days, leading to an emptying of 85 % of the total dynamic storage. In the case where 3 outwash plains are interconnected, river discharge remains similar than with only one outwash pain before day 10. When the discharge decreases below 180 L s^{-1}, the discharge recession rate becomes slower, leading

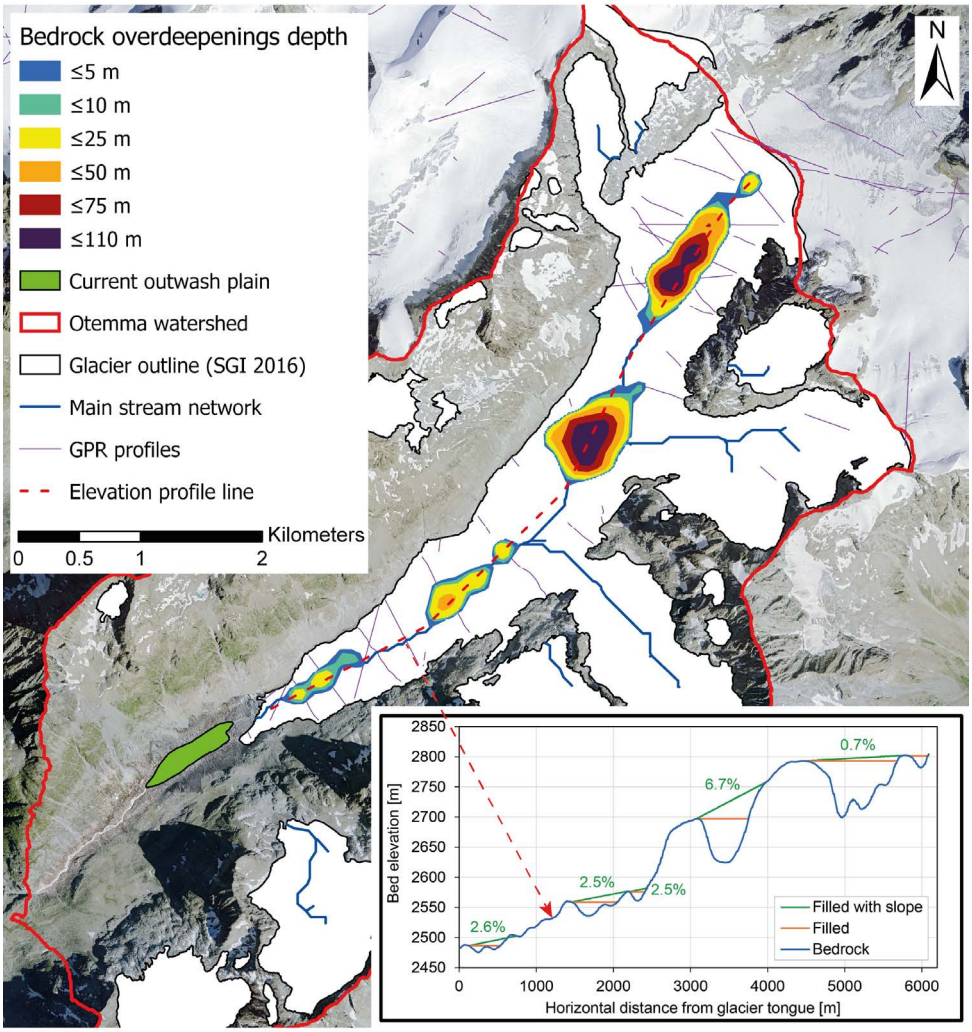

Figure 4.10: Mapping of the Otemma glacier overdeepenings estimate from based on the bedrock topography provided by Grab et al. (2021) with depth below a gently sloping plane connecting the lower and upper edge of the overdeepening. An elevation profile of the bedrock along the glacier main lobe is also highlighted with the dashed red line and the profile is illustrated in the bottom right graph in blue. In the graph, the green line shows the slope of the planes used to fill the bedrock overdeepenings, while the orange line represents the horizontal limit from the lower edge of the overdeepening. Airborne GPR profiles from the work of Grab et al. (2021) from which topography is estimated is also shown in violet. The main stream network was calculated using flow accumulation (Arcgis pro v2.3) based on the bedrock topography map. The current outwash plain is shown in green outside the glacier area (white area).

to discharge decreasing by half in 8 days and by 10 times in 54 days. Thus, slightly more discharge can be expected during droughts with a chain of outwash plains, with a discharge recession rate about twice slower.

4.5 Discussion

We first discuss below the limitations related to the simplifications and assumptions used here to set up the MODFLOW model. We then review the insights gained on the hydrogeological behavior of the outwash plain in Otemma and compare field observations with results from the numerical model. Finally, we discuss what future hydrological changes may be expected in the Otemma catchment when considering potential future outwash plain and in particular in the case of future droughts or high flow events. We conclude with some more general implications from both an ecological and a more methodological perspective.

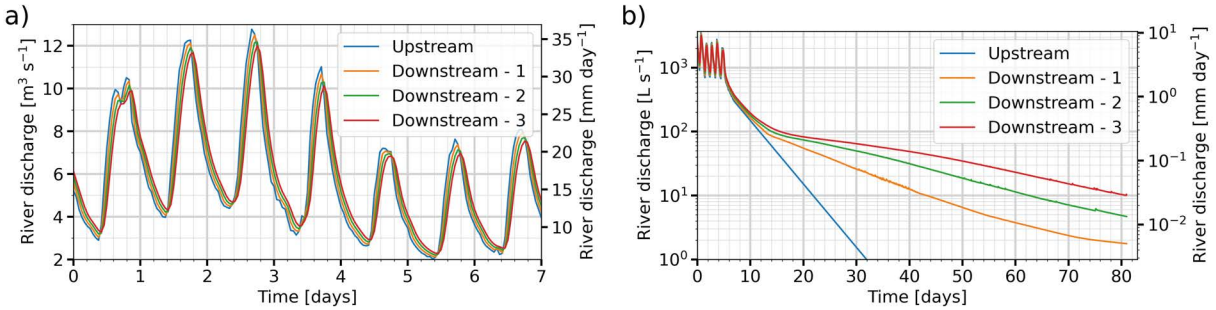

Figure 4.11: Simulated impact on stream discharge for a hypothetical chain of three outwash plains. **a)** Discharge estimation for high discharge and **b)** baseflow estimation, resulting from a theoretical input discharge (blue), and modelled outflow discharge from a first outwash plain (orange) to a second plain (green) and a third one (red). In **b)**, the y-axis is in logarithmic scale. The secondary y-axis indicates the corresponding discharge in [mm per day] at the catchment scale (30.4 km^2).

4.5.1 MODFLOW model limitations

We used ERT to constrain the depth to the bedrock at specific locations. Although inversion results lead to a clear transition between water-filled sediments and bedrock, an error of a few meters cannot be excluded. The bedrock depth was interpolated between the ERT profiles which leads to a larger uncertainty in areas distant from those lines. We only defined 4 aquifer layers with vertically constant parameters, while lenses of silt and sand are distributed at much smaller scales, as observed in sediment facies (Maizels, 2002). The spatial parameter interpolation between pilot points in each layer does also not allow to form specific flow paths as we used no particular training image, i.e. we did not impose any specific patterns (Mariethoz et al., 2010; Orsi et al., 2016). This leads to a clear oversimplification of the heterogeneity of such a fluvial aquifer. As a result, our parameter estimation does not allow for the formation of preferential flow paths, which may increase drainage and groundwater levels in specific parts of the outwash plain (Cozzetto et al., 2013). These limitations are at least partly mitigated by performing a calibration designed to not only fit groundwater levels, but rather a set of aquifer behaviors. As such, even though our groundwater wells are shallow (about 2 m deep), K_{gw} could be better constrained with depth by matching the amplitude of diel groundwater variations, which leads to a reliable estimate of the depth averaged value of K_{gw}. Even if preferential flow paths exist, the rate of groundwater drainage is constrained in the calibration by the rate of groundwater recession in Autumn and the measured rate of groundwater exfiltration in the lower part.

Geomorphological changes in the outwash plain were also not taken into account. Strong cycles of sediment deposition and aggradation modify on a daily and seasonal timescales the shape of the riverbed and the number of stream branches. Indeed, on a daily basis, some transient channels will appear during high discharge and disappear during low flow, which influences the total wetted area and thus modifies the rate of stream infiltration and groundwater exfiltration. This phenomenon appears especially important in the lower half part of the braidplain, as clearly visible in the orthoimage (Fig. 4.2), where we only defined three permanent channels. Using Manning's equation and a v-shapped cross-section, we estimated that a hypothetical addition of 10 ephemeral branches, would lead to an increase of 200 % of the total wetted area and a decrease of 20 % of the river stage. Such changes are not negligible but can be at least partially compensated by the calibration procedure, by adapting the riverbed hydraulic conductivity (K_{rb}) and the Manning's coefficient (n). The calibration procedure seems indeed to lead to such compensation, as both K_{rb} and n were estimated to be larger in the lower half of the plain (Fig. 4.5c,d), which allows for larger exchange rates between river and groundwater. Higher n values in the lower part are also expected from a geomorphological perspective due to a more irregular, meandering and larger, flatter channels (Phillips and Tadayon, 2006). n also appears lower in straighter parts of the river network and higher in zones of flow convergence where more flow turbulence may increase flow resistance and decrease velocity. The local variations in the estimation of n may however also arise more artificially from the calibration procedure which attempts to match the diel amplitude and the timing of the groundwater fluctuations. The higher estimated n value near well B1 is likely due to increased diel stream variations which have a direct impact on the nearby well and thus locally compensate for some uncertainties in the simplified river morphology.

The estimated K_{rb} for the upstream reaches is between 3 and 15 m per day, similar to another study of a Quaternary glaciofluvial aquifer where the retained K_{rb} value was 2.4 m per day (Schilling et al., 2017). In the lower half part of the plain however, the estimated K_{rb} values were larger, which is likely due to the calibration procedure attempting to balance the lack of some secondary channels and somewhat artificially increasing the exfiltration rate.

Despite the overall good performance, there are some notable differences between observations and modelled groundwater heads. For instance, during September and October 2020, wells D1 and D2 have a modelled water head about 0.5 m higher than measured (Fig. 4.6). This is due to a change in the stream reach at this location, which moved further away from the wells and eroded vertically, leading to a decrease in the head. This illustrates that our model fails to locally reproduce the exact depth of the groundwater and this issue is likely more important where no groundwater observations are available.

Our estimation of groundwater - surface water exchanges relies on stream-flow observations at only two locations on a single day, which might in particular lead to uncertain exchange fluxes during low flows, which may reduce the capacity of our model to accurately reproduce exchanges during very dry periods.

Finally, we also neglected the contribution from the small hanging glacier on the upper south side of the outwash plain, although it clearly provides additional recharge. This choice is due to the lack of groundwater and discharge observations in this area and thus no means to quantify the input discharge. As discussed before, we have shown that the main behavior of the aquifer can be explained by the incoming upstream discharge and that any additional lateral water input likely only affects the local groundwater levels, but does not modify the seasonal-scale dynamics.

Overall, the calibration procedure allowed the model to reproduce the aquifer behavior of the study site reliably and in particular the aquifer levels throughout the year, the aquifer drainage rates and rates of infiltration and exfiltration. In particular, even with a static definition of the geomorphology, the long model run over 14 months (Fig. 4.7) show that the average level of all groundwater wells could be satisfyingly reproduced.

4.5.2 Outwash plain groundwater dynamics

The outwash plain appears to recharge rapidly in the early melt-season, from the hillslopes and from the main stream. Hillslope recharge provides significant recharge especially in the early melt period (March to June in Fig. 4.7), but is rapidly drained when less melt occurs. Groundwater levels increase synchronously with stream discharge in early June and maintain a high level, even when hillslope recharge is largely reduced in later summer. Thus, although hillslope tributaries maintain locally higher groundwater heads (up to about 1 m for well B2 in Fig. 4.7), it is the moderate but constant river infiltration from the stream which maintains groundwater levels close to the sediment surface during the snow-free season (Fig. 4.7) and which drives the seasonal groundwater dynamics.

This behavior was validated by EC observations made in the groundwater wells. Wells close to the hillslope (B3, C2, D2) tend to show a gradual increase in EC from June to September (Fig. 4.4), which correlates with a gradual decline of hillslope discharge and a lowering of groundwater levels (Fig. 4.7). This suggests a transition from groundwater recharge by snow melt with low EC from hillslope tributaries towards more upstream river recharge with higher EC due to longer groundwater travel time.

The increase in EC after peak snow melt could also be explained by a hillslope recharge from an older groundwater source such as bedrock seepage. Indeed, some other studies in similar proglacial catchments have highlighted the presence of deeper, more perennial, baseflow from the hillslopes (Crossman et al., 2011). In early September 2020, a cold spell occurred, leading to a rapid decrease of stream discharge. During this event, EC in wells C2 and especially in D2 increased while the groundwater levels dropped rapidly. The increase in EC could be explained by a reduced contribution from the stream reach infiltration and an increased contribution from an older hillslope seepage. Such contribution is however difficult to prove without further geochemical analysis and is beyond the purpose of this work.

Regardless of the presence of deeper more perennial lateral recharge, the modelling results indicate that the measured seasonal groundwater levels can be largely explained by upstream river reach infiltration.

During periods of high snow melt, lateral hillslope recharge via surface runoffs locally modify the groundwater stage, but this additional water recharge is rather superimposed on the groundwater originating from upstream river infiltration. Here we suggest that hillslope water does likely not fully mix with deeper groundwater at the outwash plain edges. Groundwater may therefore be dominated by lateral infiltration in its first meter of depth, leading to an apparent water composition in shallow sampling wells resembling water from hillslope tributaries, as observed in wells B2 and B3 for instance. It is however the upstream river infiltration that maintains the groundwater levels close to but still below the surface so that deeper groundwater in the outwash plain may present a different geochemical composition.

At the daily scale, diel groundwater fluctuations were observed. These are due to the combined snow- and ice-melt signal which leads to strong diel river discharge variations that propagate in the aquifer laterally. Those groundwater variations are due to the diffusion of a pressure wave which is much faster than the actual groundwater flow velocity and does involve any actual transport (Magnusson et al., 2014). In fact, running the model by smoothing out these daily stream variations lead to similar daily total infiltration and exfiltration rates, with the difference that hourly rates are averaged through the day so that peak rates are reduced. The role of stream variations on the number of stream branches as well as potential preferential flow paths may to some extent modify this statement but could not be modelled in the present study.

The seasonal groundwater recharge can therefore be explained by stream water that enters the aquifer in the upstream half of the outwash plain. The groundwater flow follows flowpaths parallel to the stream, sinking deeper in the central part of the plain and re-emerging in the lower half where groundwater exfiltration occurs. Using the particle tracking module for MODFLOW (MODPATH v7), a median groundwater transit time of 15 to 20 days during high flow and 20 to 25 days during low winter flow can be estimated. This difference is mainly due to a decrease in the aquifer gradient due to the lowering of the groundwater head upstream (Fig. 4.9). In both high and low flows, the distribution is skewed towards a few longer flow paths lasting 80 to 100 days. Similar time scales were also found for a Quaternary aquifer based on radioactive natural tracers and modelling in the work of Popp et al. (2021b); Schilling et al. (2017). Such groundwater flow paths is reflected in the groundwater wells (Fig. 4.4), with the most upstream well D1 showing an EC very close to stream water, and a gradual increase in EC in the wells more downstream (C1, B1, A1). In particular, in the downstream part, well A1 shows the highest EC although it is close to the stream, which indicates no direct contact with the nearby reach, long groundwater flow paths and thus groundwater upwelling. Such upwelling has also been discussed for other Quaternary glacio-fluvial deposits (Ward et al., 1999). During winter, EC increases significantly in well A1 but so does the EC of the upstream river (GS1, Fig. 4.4b), so that the difference in EC between A1 and the stream is about 85 μS cm^{-1} in winter, hardly higher than in summer (70 to 80 μS cm^{-1}). This suggests that groundwater travel time changes only slightly with the lowering of the groundwater level as the change in EC remains similar and fits with our modelled median transit time. Winter groundwater EC increases therefore due to an increase of the source stream water EC which increases prior to entering the outwash plain and does not indicate arrival of deeper groundwater as also discussed in the work of (Käser and Hunkeler, 2016). For winter recharge, as also reported in another similar proglacial glaciofluvial aquifer (Malard et al., 1999), we have shown that the increasing groundwater EC in the lower part of the floodplain is dominated by an upstream change in stream water composition and that the lower groundwater levels result from the reduced rate of river infiltration due to a smaller stream wetted area.

Using the stream EC at GS1 and GS2 and EC of well A1 for groundwater (Fig. 4.4), a typical two components mixing model (e.g. (Kobierska et al., 2015b)) can be established to estimate the percent contribution from groundwater at the lower end of the floodplain (GS2). During summer, for daily peak flow at around 18:00, groundwater contribution amounts to about 3 to 4 %, or an equivalent groundwater exfiltration of 300 to 350 L s^{-1}. For daily low flows at about 10:00, groundwater contribution increases up to 8 to 10 % or a groundwater discharge of about 200 L s^{-1}. Those estimations for groundwater exfiltration are similar to the modelled exfiltration rates in Fig. 4.8c with an estimated exfiltration of about 200 to 250 L s^{-1}. For winter, performing the same analysis leads to a groundwater contribution of about 50 % or an exfiltration tate of 35 L s^{-1} which is about half of the modelled minimum exfiltration (Fig. 4.8d). This suggests that half of the stream water in winter at GS2 comes from groundwater, but also that half of the discharge comes from surface river flowing from GS1. For early summer, the analysis cannot be performed as too much snow melt

contribution from hillslopes likely affects the stream EC as well as locally the groundwater EC at well A1.

Based on the above comments, the outwash plain aquifer has a limited capacity to maintain higher baseflow as a similar amount of water infiltrates upstream and is exfiltrated downstream, acting more like a buffer which collects water from different sources. Constant river recharge allows groundwater levels to be maintained close to but below the surface at average depths varying between 0.2 and 0.5 m during the whole year in its downstream part, while hillslope contributions locally superimpose a higher enriched groundwater layer. This conclusion needs some caution however as the river in the downstream part tends to erode vertically in late summer which would cause further groundwater drawdown.

4.5.3 Future hydrological changes from outwash plains

Two future glacier overdeepenings were identified where sediment filling was hypothesized. Using an estimation based on passive seismometry of current stream bedload transport at the glacier outlet for 2021 of 72000 tonnes per year (personal communication from Davide Mancini) and assuming a similar amount of suspended load (Carrivick and Heckmann, 2017), we can calculate a filling time of 10 and 25 years for the two first overdeepenings. Such overdeepenings appear therefore likely to fill in the future, although basal sediment production may decrease with recessing glacier length and volume. However, in addition to the amount of bedload transport, sediments may also be delivered following from debuttressing of unstable slopes (Mancini and Lane, 2020), by subglacial melt-out at the glacier front (Evans et al., 2006) and supraglacial sediment accumulation. It was visually observed that the Otemma glacier is characterized by a more than 5 meters thick debris-rich basal ice layer containing large volumes of coarse sediments and boulders, likely due to basal till regelation at the glacier bed (Bennett, 2009). In addition, from historical aerial imagery, the glacier front appears to accumulate sediments near its tongue which can lead to the burying of dead ice as identified by ERT in the center of the current floodplain (Fig. 4.3). With a depth of 20 m, these large buried dead-ice zones seem to sit on the bedrock which suggests that the current outwash plain was not filled with a thick layer of subglacial till prior to its melt.

Those observations indicate a rapid filling of the overdeepening with non-sorted, loose sediments from melt-out and fluvial deposition as well as potential dead-ice bodies. This suggests that the largest part of the outwash plain sediments are deposited by a similar process, should show similar hydraulic properties and do not sit on older less permeable subglacial till and also supports the hypothesis of the formation of new outwash plains of similar volumes in the future, even if reduced sediment production takes place.

In terms of groundwater storage from outwash plains, the current one has an estimated dynamic storage of 6.7 mm. The two future ones have a total dynamic storage of 12.5 mm, leading to a total future storage of about 20 mm. The potential burial of ice blocks may occur at the glacier bed but will likely remain in the non-active storage zone, as it is the case for the current one (Fig. 4.9). The simulation of the cascading effect of a chain of three outwash plain has shown that during high flows, the outwash plain has little effect on the total streamflow. In the case of a large flood (>13 $m^3\ s^{-1}$), it seems that no more than 0.5 $m^3\ s^{-1}$ can be temporally infiltrated in the outwash plains. We have also shown that attenuation of the flood along the river network due to increased storage and riverbed friction may have a similar or even larger effect than the limited increased storage in the aquifers. In fact, in the case of large floods, outwash plains may be fully underwater (which was not simulated in our model), significantly increasing surface storage and likely leading to more flow attenuation. In the case of significant drought, outwash plains do not provide significantly higher baseflow discharge, as exfiltration is only slightly higher than infiltration. Nonetheless, outwash plains still maintained a minimum baseflow discharge, when upstream discharge drops below 150 to 200 $L\ s^{-1}$ or 0.5 mm per day. The duration of the aquifer drainage is here largely affected by the number of outwash plains, so that baseflow is reduced by half in about 4 days with one aquifer, while recession is twice slower with three aquifers. For this analysis we excluded hillslope recharge in order to assess the impact of the cascading outwash plains on discharge exclusively. In a more realistic case however, some hillslope drainage may recharge the outwash plain aquifer in addition to the stream and thus increase downstream discharge.

4.6 Conclusion

We have studied in this work a small fluvial aquifer in a recently deglaciated proglacial margin. Although representing only 0.4 % of the entire catchment, we have shown its potential to store about 7 mm of groundwater. Its recharge is dominated by upstream river infiltration while hillslope recharge only maintains locally higher groundwater levels and perched surface water. In its lower half, groundwater tends to flow upwards and exfiltrate to the stream so that daily surface water-groundwater exchanges are balanced, which maintains a high groundwater level through the melt season. We have shown that the rate of river infiltration was not larger than about 0.4 $m^3\ s^{-1}$ or about 1 mm per day. This suggests that changes in the seasonality of snow-melt will have limited impact on the recharge of such aquifers as long as a limited ice-melt recharge maintains an upstream river discharge of 1 mm per day. Due to this limited river infiltration capacity, such outwash plain aquifers have a limited impact on stream discharge during peak flow, providing little potential to attenuate future floods. In case of severe droughts, where flow recharge falls below 150 $L\ s^{-1}$, the outwash plain in Otemma has the potential to maintain a minimum baseflow during a one month period. Such low flows are however only to be expected during the cold season as long as summer glacier melt provides ice-melt downstream.

In the future, new outwash plains are expected to form as glaciers retreat and as will likely be the case at Otemma. A total future active groundwater storage of 20 mm is estimated from those outwash plains. This volume remains smaller than the current winter catchment-scale groundwater storage which was estimated to be in the order of 40 mm (Müller et al., 2022a). Indeed, the observed increase in stream EC in winter at GS1 before entering the outwash plain indicate that other sources of groundwater maintain the winter baseflow, rather than the outwash plain by alone. The source of this water remains unclear but may be due to subglacial melt or exfiltration from deeper bedrock fractures. Further geochemical or natural tracers analysis could here potentially provide further details on the larger catchment-scale dynamics.

Compared to older Quaternary fluvial aquifers, the groundwater parameterization of the Otemma outwash plain aquifer was in the same range (Mackay et al., 2020; Schilling et al., 2017) and a similar groundwater dynamics was also observed based on natural tracers (Malard et al., 1999; Ward et al., 1999). Although slow colonization from surface vegetation may build shallow soils, change sediment granulometry (Maier et al., 2020) and improve channel stability (Roncoroni et al., 2019), deeper aquifer characteristics seem to evolve on time-scales of thousands of years (Maier et al., 2021), making the hydrological conclusions applicable to other fluvial systems. It seems therefore that new small outwash plains behave similarly to older Quaternary floodplains, with a somewhat faster average hydraulic conductivity and smaller aquifer volumes. While hydraulic parameters may remain in a similar range for outwash plains aquifers in other locations, groundwater dynamics will likely depend on the local aquifer characteristics such as surface topography, aquifer length to depth ratio or riverbed permeability.

From a more technical perspective, large heterogeneities in groundwater EC were observed both in time and in space, horizontally as a function of distance to river infiltration and vertically with potential partial mixing of hillslope waters. This suggests that any groundwater quantification based on mixing models should be only performed with a prior good understanding of groundwater flowpaths and adequate sampling locations and depths.

Finally, in addition to the impact of those fluvial aquifers on downstream river discharge, outwash plains have a central ecological role for alpine landscapes. Although the modelled groundwater depth may not be fully accurate due to a lack of model adaptation to changes in the geomorphology, it appears from our model that groundwater is usually located a depth greater than a few tens of centimeters, leading to relatively dry sediments at the surface. From an ecological perspective, access to moisture is likely not promoted by the local outwash plain aquifer, but rather from other sources of surface runoff from hillslope tributaries. The origin of such sources of water may be diverse, coming either from glaciers and snow melt, rock glaciers and permafrost thaw or more perennial bedrock exfiltrations. Such water sources appear therefore key to provide moisture, nutrients and DOC Fellman et al. (2015); Hood et al. (2015) for the onset of biofilm and vegetation development (Miller and Lane, 2018; Roncoroni et al., 2019) or to provide cold water environments for alpine species (Brighenti et al., 2019a). While the local groundwater outwash plain aquifer may not be key for early vegetation succession and pioneer species, it will however play a future role in main-

taining a complex mosaic of habitats essential for more complex vegetation as well as aquatic and terrestrial species (Hauer et al., 2016).

Code data availability Weather data are available under (Müller, 2022a), piezometer data under (Müller, 2022b), river data (Müller and Miesen, 2022) and ERT data under (Müller, 2022c).

The code to build the MODFLOW model was written in Python using Jupyter Notebook and and is available the in the Supplementary Material. The calibration procedure using PEST-HP can be run in command line and is also provided in the Supplementary Material. The codes to reproduce the hillslope drainage is also provided.

Author contribution T.M. conducted the data collection of ERT, surface and groundwater data, data analysis and model development, produced all the figures and wrote the manuscript draft. M.R. collected the orthoimages and produced the DEM. D.M. collected the bathymetric profiles and estimated river depth. B.S. proposed the general research topic and acquired the funding. S.L. and his team organised all field work logistics. B.S. and S.L. jointly supervised the research and edited the manuscript draft version. All authors have read and agreed to the current version of the manuscript.

Competing interests At least one of the (co-)authors is a member of the editorial board of *Hydrology and Earth System Sciences*. The peer-review process was guided by an independent editor, and the authors also have no other competing interests to declare.

Acknowledgements The authors also thank Prof. Christophe Lambiel and Prof. James Irving (University of Lausanne) for lending the ERT device as well as Dr. Emily Voytek (University of Lausanne) for acquiring the first ERT data in the Otemma forefield in 2019. T.M. thanks all students and PhD students from the AlpWISE group at University of Lausanne and in particular Floreana Miesen who participated in field data collection at the Otemma glacier forefield.

Financial support This research has been supported by the Schweizerischer Nationalfonds zur Förderung der Wissenschaftlichen Forschung (grant no. 200021_182065).

Figure 4.12: Picture of the Otemma glacier front shortly after a large ice collapse of a part of the main subglacial channel.

5

Research paper 3

Evolution of the stable isotope compositions of snow and ice melt waters and their impact on improving glacio-hydrological models in highly glaciated catchments

Tom Müller[1,2], Mauro Fischer[2], Stuart N. Lane[1], and Bettina Schaefli[1,2,3]

[1]Institute of Earth Surface Dynamics, Lausanne, University of Lausanne, Switzerland

[2]Institute of Geography (GIUB), University of Bern, 3012 Bern, Switzerland

[3]Oeschger Centre for Climate Change Research (OCCR), University of Bern, 3012 Bern, Switzerland

In preparation for publication.

This research article builds on the extensive isotopic data obtained at the glacier outlet and for snow and ice to discuss the use of water stable isotopes to separate snow and ice-melt in such a highly glaciated catchment. For this purpose, we developed a simplified glacio-hydrological model which simulates all water fluxes as well as the isotopic composition of snowmelt, icemelt and rain. The model is calibrated based on snow and ice mass balance measurements obtained between 2020 and 2021 and snow cover maps from satellite imagery. The model ultimately allows us to simulate the integrated isotopic composition of snowmelt, icemelt and rain at the catchment outlet which we compare with the measured isotopic composition of the river to estimate their contribution. We finally show the significant uncertainty linked to this isotopic approach which we compare with results from the glacio-hydrological model.

5.1 Introduction

Highly glaciated catchments are rapidly evolving with climate change worldwide, with changes in annual glacier runoff of up to -30 % in the Andes and central Asia (Huss and Hock, 2018). Such changes, combined with more liquid precipitation, earlier snow melt and consequently less snow melt resources during the melt season, will significantly affect water resource availability (Beniston et al., 2018; Berghuijs et al., 2014). Those changes will have a serious impacts on downstream ecosystems (Milner et al., 2017), water usage for irrigation (Shokory et al., 2023; Viviroli et al., 2020) or other domestic water uses (Immerzeel et al., 2020), both in densely populated lowlands (Biemans et al., 2019; Pritchard, 2019) or in small communities at high elevated areas (Buytaert et al., 2017). In this context, glacio-hydrological models have been developed to assess current or future changes in discharge (van Tiel et al., 2020b). Models usually rely on different sources of information, the most common being discharge, followed by ice and snow-related products (van Tiel et al., 2020b). Predictions are therefore mainly based on a statistically correct estimation of the calibration or validation dataset, even if the underlying physical processes responsible for runoff may be simplified (Schaefli et al., 2011). In addition, observations in high-elevation catchments, where access is difficult and environmental conditions are harsh, are usually sparse and subject to large spatio-temporal variations. While the main drivers of annual mass-balance are well documented, non-stationary processes like vegetation adaptation to new climatic conditions appear challenging to correctly represent (Duethmann et al., 2020). Moreover, the lack of direct observations below the surface or below the ice also leads to simplifications, such as for e.g. the effect of debris transport and debris-cover (Ayala et al., 2016; Jouvet et al., 2011), lateral subsurface flow (Carroll et al., 2019), permafrost melt (Rogger et al., 2017) or superficial and deep groundwater recharge and exfiltration (Hood and Hayashi, 2015; Penna et al., 2017).

Additional streamflow information such as natural tracers appear as a possible way to assess the main sources of water at the catchment-scale and have been used to identify the sources of water or the mechanisms involved in their release (e.g. Baraer et al., 2015; Jasechko, 2019). Ideally, in order to provide correct estimations of water shares, natural tracers need to be conservative, have clearly defined end-members values with limited spatio-temporal variations. Most commonly, water stable isotopes are used in combination with a hydrochemical tracer to separate snowmelt, groundwater and rain (e.g. Carroll et al., 2018; Klaus and McDonnell, 2013). In glaciated catchments, the additional icemelt contribution would require a third tracer, which remains difficult to identify, so that most studies neglect one component. However, a number of challenges were discussed in recent studies. First, direct groundwater measurements are usually difficult to acquire and water from springs may show large differences based on the nature of the water sources and geology (Carroll et al., 2018; Müller et al., 2022a). The use of geochemical tracers may also not be conservative due to soil flushing or weathering (Carroll et al., 2018; Sharp et al., 1995) and this is usually not accounted in uncertainty quantification. Spatial variations in the ice and snow-melt isotopic signature may also be large and a limited number of samples may lead to biases (Engel et al., 2016; Schmieder et al., 2018; Zuecco et al., 2019). Finally, the temporal evolution of their isotopic signal remains usually unclear and the choices of selected values lead to a significant tradeoff between snow and ice contributions (Penna et al., 2017). Due to such large uncertainties, these methods seem to provide only limited additional information regarding the catchment-scale processes. As an alternative, a limited number of studies used isotopes for glacio-hydrological model validation (Hindshaw et al., 2011) or calibration (He et al., 2019; Nan et al., 2022). These studies showed promising results with a reduction of uncertainties in both parameter and mixing estimation when additionally using isotopes for calibration. Nonetheless, the mechanisms involved in the temporal isotopic enrichment of the snowmelt signal due to fractionation relies on a rough extrapolation which could be improved. The complex isotopic snow processes (see review by Beria et al. (2018)) have however been largely studied experimentally (e.g. Carroll et al., 2022; Taylor et al., 2001) and equations characterizing the main processes of isotopic enrichment have been

proposed (Ala-aho et al., 2017; Feng et al., 2002).

In this study, we propose to build on the parsimonious model proposed by Ala-aho et al. (2017) and to extend it to the case of glaciated catchments, in order to assess the potential of such approach to better estimate water contributions of ice and snow-melt in particular. Our main goal is to propose a combined isotopic and glacio-hydrological model to precisely estimate the temporal enrichment of snowmelt based on physical processes (rain on snow, sublimation, melt-out) and limit uncertainties due to the spatial variations of snow sampling. Since data collection is challenging in such environments, this parsimonious method is mainly based on meteorological and mass-balance observations with a reasonable number of isotopic samples and can be easily applied to other basins. Based on the estimated snowmelt isotopic signal and two-years of isotopes samples in various locations of the catchment and in particular at sub-daily-scale at the glacial stream outlet, we propose guidelines for a more robust definition of end-members. Finally, we compare results obtained from an end-member mixing model based on isotopes and on the results from the glacio-hydrological model.

5.2 Study site and experimental methods

5.2.1 The Otemma glacier

The Otemma glacier is located in the Western Swiss Alps (45°56'03"N,7°24'42"E) and is amongst the 15 largest (in terms of surface area) Swiss glaciers (GLAMOS (1881-2020)). It is characterized by a long flat main tongue and a small accumulation zone, with an equilibrium line altitude (ELA) located at around 3200 m asl (estimated for 2020 and 2021 in this study). Due to the limited area at high elevation, it is retreating rapidly since the Little Ice Age (LIA) in 1850, with a total length recession of about 2500 m or about 40 m per year since the 1970s (GLAMOS (1881-2020)). The glacier main tongue was projected to completely melt by 2060 under current climate change (Gabbi et al., 2012). The glacier possesses two medial moraines, which deliver supraglacial and englacial sediments to the glacier tongue, especially in its more shaded southern part which gradually becomes heavily debris-covered. Except for this area, the glacier mostly consists of relatively clean ice with an average debris cover of about 10 % (estimated from Linsbauer et al., 2021). The catchment boundary was defined by the glacier outlet, where a gauging station was installed. It has an area of 20.8 km^2, a mean elevation of 3080 m asl (2470 m to 3730 m) and a glacier coverage of 56 % in 2019 (adapted from Linsbauer et al., 2021). The underlying bedrock consists of orthogneiss and metagranodiorites (Burri et al., 1999), overlain by coarse superficial sediment deposits with limited vegetation development.

5.2.2 Weather observations

A weather station was installed 200 m from the glacier terminus at an elevation of 2450 m asl in September 2019 and measured data continuously until October 2021 with a 5 minutes resolution. Liquid precipitation was measured with a Davis tipping rain gauge, air temperature, relative humidity and pressure with a Decagon VP-4 and incoming short-wave radiation with a SP-110-SS from Apogee Instruments. Solid winter precipitation was measured at the nearby SwisMetNet stations: at Otemma (~5 km away, at 2357 m asl) for the winter 2019-2020 and at Arolla for the winter 2020-2021 (~10 km away, at 2005 m asl). All data published (Müller, 2022a).

5.2.3 Stream discharge

Starting in July 2020, a stream gauging station was installed 50 m below the glacier tongue, in a bedrock-constrained river section to insure the collection of all upstream flow. Stream discharge was estimated using a stage-discharge relationship (Müller et al., 2022a). River stage was measured continuously at 10 minute intervals with a Keller DCX-22AA-CTD datalogger. Discharge was

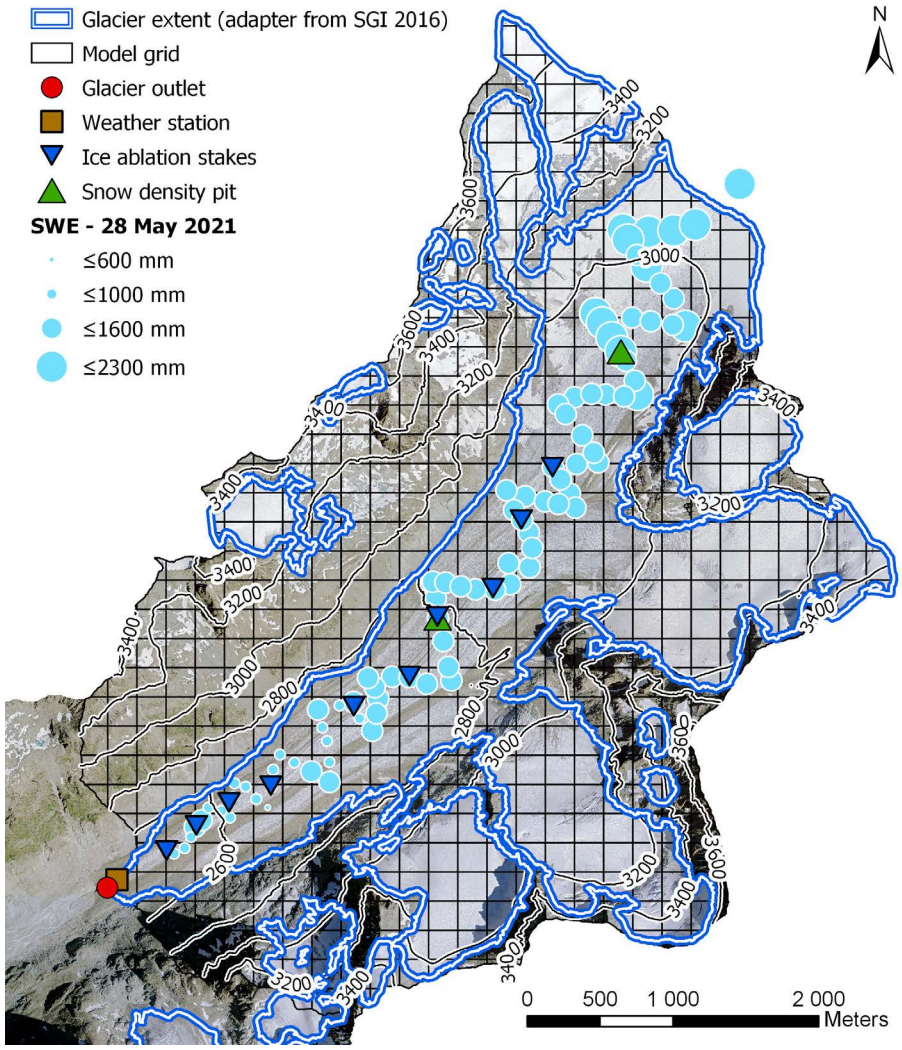

Figure 5.1: Glaciated catchment overview with locations of the gauging station (glacier outlet), weather station. We also highlighted the location of the 10 ablations stakes used for ice ablation measurements, the 2 snow pits for density estimation and isotope sampling and finally the results of the SWE measurements performed on 28 May 2021. The black grid represents the size of each model cell where mass-balance and snow isotopic composition was measured. Orthoimage provided by SwissTopo (2019)

estimated by dilution gauging using Rhodamine WT 20 % dye. The fluorescent dye concentration was measured with a Fluorometer (Albillia GGUN-FL30). Based on 21 gaugings in 2020 and 15 in 2021, the estimated mean discharge uncertainty (95 % confidence) was ±0.55 $m^3\ s^{-1}$, but tends to increase for peak discharge with an error of ±2 $m^3\ s^{-1}$ for a river discharge of 13.5 $m^3\ s^{-1}$.

5.2.4 Snow and ice mass-balance observations

Snow depth measurements were performed manually at 5 locations on 26 June 2020 and 92 locations on 28 May 2021 on the whole glacier main lobe (from 2560 to 3020 m asl). Snow density was estimated by measuring the average density of the whole snow pack with a snow sampler in the centre of the glacier main lobe in 2020 and at two locations in 2021 on the same dates as snow depth. Snow water equivalent (SWE) was calculated by multiplying the snow depth with its density. In 2021, snow density estimations at both sampling locations yielded to the same value of 442 $g\ L^{-1}$.

In July 2020, nine ablation stakes covering the glacier main tongue from an elevation of 2590 m asl to 2890 m asl were installed using an eight meters deep Kovacs ice drill. Ice ablation was measured three times in summer 2020 and 7 times in 2021. A density of 900 $g\ L^{-1}$ was used to estimate the

equivalent water volumes.

Dye tracing experiments were also carried out by injecting Sulforhodamine WT on the glacier surface into moulins and recording the transit time to the glacier outlet to characterize the water drainage velocity.

5.2.5 Water sampling for stable isotope measurements

Water samples were collected manually for snow and ice. The snowpack was sampled by extracting a layer of snow at a certain depth and letting it fully melt in a sealed plastic bag. Similarly, ice cores were extracted using a manual ice screw for shallow samples and a Kovacs Ice Auger for deeper samples and were also completely melted in a bag. Once melted, the samples were directly transferred in the field in 12 mL amber glass vials with an air-tight screw cap containing a silicone rubber septa. All other liquid samples were directly sampled in similar glass vials, which were previously flushed with the sample water to avoid contamination. Melted snow leaking from the snowpack was collected at a few locations where possible. Ice melt from small supraglacial gullies was also sampled on the glacier, at least one kilometer away from the snowline to avoid potential mixing with snowmelt. Stream water at the glacier outlet was sampled automatically two to three times a day during low and high flows, using an ISCO 6712 full-size portable water sampler with 24 bottles of 1 L capacity, which were half filled. Water bottles were transferred to 12 mL glass vials every one to two weeks. We left the 1L ISCO bottles open as limited evaporative fractionation should occur during such short timescales and due to the cold air temperature (average summer air temperature of 7 °C between July and September at the weather station in 2021) and the shaded, protected location of the sampler. Indeed, von Freyberg et al. (2020) showed a deuterium difference of about 1 ‰ for a two to three weeks period at such temperatures. Our results also showed no deviation of the samples from the local meteoric water line which indicates limited evaporative losses. Finally, rain water was sampled using a simple PVC funnel, which diverted rain into a plastic bag through a 2 mm plastic tube. Rain water was then transferred to 12 mL vials after each rain event, so that the rain samples correspond to the isotopic composition of the bulk of each rain event.

All water vials were brought to the laboratory and kept in a cold chamber until analysis. Water stable isotopes were measured using a Wavelength-Scanned Cavity Ring Down Spectrometer (Picarro 2140i, Santa Clara, California, USA). We systematically performed 8 injections and only kept the mean of the three last injections to avoid memory effects between samples. The median analytical error (one standard deviation) of all samples was 0.04 ‰ and 0.25 ‰ (maximum error of 0.11 ‰ and 0.65 ‰) for $\delta^{18}O$ and $\delta^{2}H$, respectively. A reference sample was analyzed after every 7 samples to assess potential systematic deviation during the measurement sequence. Finally, all raw values are expressed relative to the international Vienna Standard Mean Ocean Water (VSMOW) standards (Coplen, 1994) based on a calibration curve with three internal standards, measured at the beginning and the end of each measurement sequence.

5.2.6 Water sampling location and frequency

Snow for stable isotope analyses was sampled during two periods: from the glacier snout to the highest ablation stakes between 24 and 30 June 2020 and on the whole glacier main lobe on 28 May 2021 (see Fig. 5.1). For 2020, 4 snow depths and one snow density measurements were performed on 29 June. For 2021, 92 snow depths and 2 snow density measurements were performed on 28 May (Fig. 5.1). Outside of these two periods, snow was sampled on the glacier in mid July at a few locations. After July, snow was only located on inaccessible parts of the catchment. Snow was mainly sampled either by extracting the first 5 to 10 centimeters of the snowpack, which we define as *Snow surface*, or alternatively by sampling a lower snow layer comprised between 10 and 20 cm, called *Snow 10cm*. In early summer 2021, we also sampled snow in three snow pits where snow density was measured by extracting snow at specific layers in the snowpack (see Fig. 5.1). Finally,

we sampled snowmelt leaking from late snowpacks at a few locations when possible.

Ice samples for isotope measurements were collected from to 2019 to 2021 at various random locations on the glacier surface during two to four sampling campaigns, each year from late June to late August. On 30 June 2021, two ice cores of 8 m and 5 m deep were sampled at the location of the 5th and 8th ice ablation stakes from the glacier snout and ice was sampled by taking a bulk sample of the ice core every meter.

From 2019 to 2021, we collected 39 liquid precipitation samples near the weather station at the glacier snout. All samples represent a single rain event and were usually collected the day after the end of the rain. We identified rain events by rain periods separated by at least one day without rain. In winter, we also sampled fresh snow during directly after a few snow events. Due to air temperature below 0 °, we assume that little snow transformation or fractionation occurred so that those samples represent the isotopic composition of the solid precipitation event.

5.3 Numerical modelling

We propose here a framework to model the share of snow melt, ice melt and rain at the outlet of the Otemma glacier based on a glacio-hydrological model, which integrates a snow isotopic module. The model is separated in three main modules, which were calibrated individually (Fig. 5.2). The first module corresponds to the mass-balance model which simulates snow and ice melt. Here, our purpose is to assess the current year's shares in water sources. Since we do not aim to simulate future mass-balance states, we do not validate the model on other years but rather on the observed discharge of the same year. The second module estimates the isotopic composition of each water source based on the mass-balance calculation, and the third module implements a hydrological routing routine to convey water simulated at each cell to the glacier outlet. For each module, a separate calibration was performed. All abbreviations, parameters and variables of the model are summarized in Table B1. Please refer to this table for variables and parameter units.

5.3.1 Model discretization

The model domain corresponds to the watershed limits calculated from the glacier outlet, which collects all water drained in the glacier area. We discretized the area using a square grid with a width of 200 m, leading to a total of 586 grid cells (see Fig. 5.1). For each cell, the mean elevation, slope and aspect are estimated using a 2 m resolution DEM from SwissTopo (2019).

5.3.2 Snow and ice mass-balance model

5.3.2.1 Model definition

Snow accumulation and melt was estimated at an hourly time step using an enhanced temperature-index (Eq. 5.1) melt model (Gabbi et al., 2014) from October 2019 to October 2021. Ice melt was estimated using the same equation with different parameter values.

$$M = \begin{cases} f_{\text{melt,T}}\, T_j + (1-\alpha_{\text{snow}})\, I_{\text{corr}} & \text{if } T_j > T_{\text{melt}} \\ 0 & \text{if } T_j \leq T_{\text{melt}}, \end{cases} \tag{5.1}$$

where I_{corr} is the corrected incoming shortwave radiation (see also Eq. 5.9) and T_j the air temperature for the cell j. The albedo (α_{snow}) was estimated as suggested in the work of Gabbi et al. (2014). The threshold temperature (T_{melt}) distinguishing between melt and no melt is a calibration parameter. The temperature melt factor ($f_{\text{melt,T}}$) as well as the shortwave radiation factor ($f_{\text{melt,rad}}$) were calibrated for snow and ice.

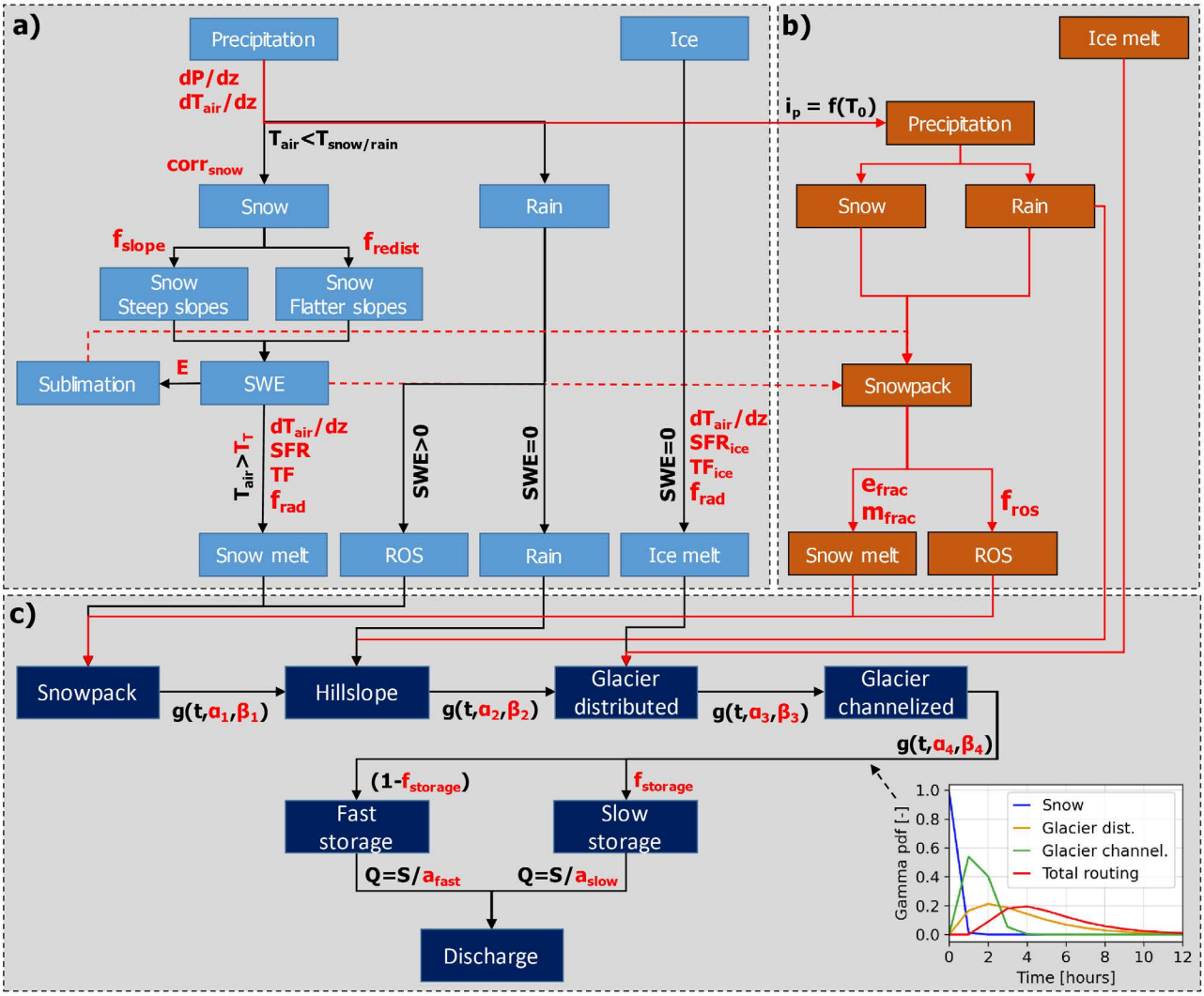

Figure 5.2: Schematic representation of the main modelling blocks of the combined isotope and glacio-hydrological model, separated by the independently calibrated main sub-modules. **a)** Snow and ice mass-balance model estimates amounts of snowmelt, rain on snow (ROS), rain and ice melt for each model cell. Main calibration parameters are highlighted in red. **b)** Isotopic model uses a calibration curve with air temperature (T_0) to estimate δ^2H of precipitation, while ice melt is defined based on direct measurements. **c)** Hydrological routing is based on convolution with gamma distribution ($g(t,\alpha,\beta)$) based on the mean estimated travel time of water through the main land-cover types in our catchment and is finally routed through a "glacial" fast and slow reservoir. The bottom right figure illustrates the Gamma distributions for one specific cell.

The temperature separating snowfall and rainfall was set to a lower threshold of 1 °C (only snow) and an upper threshold of 2 °C (only rain), with a linear fraction in between.

Air temperature (T_j) and precipitation (P_j) are estimated in each cell j based on the cell elevation z_j and on the measured air temperature (T_0) and precipitation (P_0) at the glacier weather station (elevation 2450 m asl.) following Eqs. 5.2 & 5.3. The temperature lapse rate (Δ_T) and precipitation lapse rate (Δ_P) are included as calibration parameters.

$$T_j = T_0 - \Delta_T \frac{z_j - 2450}{100} \tag{5.2}$$

$$P_j = P_0 \left(1 + \Delta_P \frac{z_j - 2450}{100}\right) \tag{5.3}$$

We allow the temperature lapse rate to change seasonally as it was previously shown that higher

lapse rates occur in summer than in winter in alpine and glaciated regions (Marshall et al., 2007; Rolland, 2003). The lapse rate (Δ_T) was defined by a normal distribution function as a function of the day of the year (DOY) which we then rescaled (Eqs. 5.4 & 5.5). The parameters of the probability density function (μ_{Δ_T}, σ_{Δ_T}) and the scaling parameters ($f_{\Delta_T,\text{range}}$,$f_{\Delta_T,\text{inc}}$) are calibrated for each year. An illustration of the resulting function is provided in Fig. B4c.

$$\text{pdf(DOY)} = \frac{1}{\sigma_{\Delta_T}\sqrt{2\pi}} e^{-\frac{1}{2}(\frac{\text{DOY}-\mu_{\Delta_T}}{\sigma_{\Delta_T}})^2} \tag{5.4}$$

$$\Delta_T(\text{DOY}) = \frac{\text{pdf}}{\max(\text{pdf})} f_{\Delta_T,\text{range}} + f_{\Delta_T,\text{inc}} \tag{5.5}$$

Since winter precipitation was measured at the nearby weather station (Otemma or Arolla) at a different elevation, a fixed snow correction factor ($f_{\text{corr,snow}}$) for the whole winter is calibrated for each year.

A simple snow sublimation module is included which is necessary for the isotopic model. Snow sublimation (E_{sp}) is calculated following the work of Ala-Aho et al. (2017) and Hock (1999). An estimation of snow temperature (T_{sp}) is required to calculate E_{sp}. Since no energy calculation is established here, we used a very simple estimation of $snowtemp$ based on air temperature and snow melt. Since, during winter, condensation tends to increase the snow temperature and during summer, melt tends to decrease it, we simply used air temperature (T_j) with a strong smoothing (simple moving average with a window of 7 days) and accounted for cooling due to snow melt (M_{snow}) based on a calibration factor (f_E) following Eq. 5.6.

$$T_{\text{sp}} = \text{smooth}(\frac{T_j}{2} - f_E M_{\text{snow}}\ ;\ 7\ \text{days}) \tag{5.6}$$

We account for snow redistribution based on terrain slope (θ in degree) by defining a calibrated slope threshold ($\theta_{\text{accum,thresh}}$) above which snow mass loss occurs (Eq. 5.7). Above this threshold, we decrease the amount of solid precipitation received by a certain factor (f_θ). To account for this mass loss on steep slopes, the total amount is then redistributed on all other cells. We defined a simple redistribution function which calculates an increase factor (f_{redist}) for solid precipitation for each cell based on its elevation (Eq. 5.8).

$$P_{\text{sf}} = P_{\text{sf}}(1 - f_\theta(\tan(\theta - \theta_{\text{accum,thresh}}))) \qquad \text{if } \theta > \theta_{\text{accum,thresh}} \tag{5.7}$$

$$P_{\text{sf}} = P_{\text{sf}} f_{\text{redist}} \qquad \text{if } \theta < \theta_{\text{accum,thresh}} \tag{5.8}$$

The redistribution is not dependant on the topography but only depends on elevation and was calibrated by defining a calibration objective function where the total monthly amount of solid precipitation removed from steep slopes equals the monthly total amount redistributed on all other cells. This method respects the total mass-balance of solid precipitation in a simple way without a complex estimation of curvature of connected cells and compensates for local anomalies between observed and modelled SWE. An illustration of the resulting functions is provided in Fig. B4a & b.

We also correct the measured incoming shortwave radiation (I_0) by taking into account the terrain slope (θ in degree) and aspect (γ in degree) (Eq. 5.9). First, the radiation is increased with slope by a certain factor ($f_{\text{rad,slope}}$) until a maximum slope threshold ($\theta_{\text{max,rad}}$) is reached (Eq. 5.10). Then, a factor ($\gamma_{\text{max,rad}}$) is subtracted to account for aspect: the factor corresponds to 0 when aspect corresponds to 180 ° (south facing slopes) and increased linearly with terrain aspect facing north

until a calibrated factor ($\gamma_{\text{max,rad}}$). Moreover, the slope is also taken into account so that steep north slopes are reduced more than mildly north facing slopes (Eq. 5.11). An illustration of the resulting function is provided in Fig. B4d.

$$I_{\text{corr}} = I_0(f_{\text{rad,slope}} - f_{\text{rad,aspect}}) \tag{5.9}$$

$$f_{\text{rad,slope}} = 1 + \cos\Big(\frac{90}{\theta_{\text{max,rad}}}(\theta - \theta_{\text{max,rad}})\Big) f_{\text{rad,slope}} \tag{5.10}$$

$$f_{\text{rad,aspect}} = \gamma_{\text{max,rad}} \frac{|\gamma - 180|}{180} \sin(\theta) \tag{5.11}$$

In order to define more realistic initial values of SWE and of isotopes, we ran the model a first time will null values for SWE and isotopes and initial model parameter values for a year and then used the final SWE and isotope results as new initial values for the start of the model calibration.

5.3.2.2 Mass-balance model calibration

We calibrated all model parameters using PEST. This model-independent algorithm iteratively minimizes the variance of the error between model outputs and corresponding field observations via inverse estimation (Doherty, 2015). We defined three sets of field observations. The first set of observations corresponds to estimated snow water equivalent (SWE) acquired on the glacier main lobe. The second dataset corresponds to the annual ice ablation measured at the ablation stakes for each year (Fig. 5.1). The third set of observations correspond to maps of the snow cover during the whole ablation periods. We used daily 3 m resolution Planet satellite imagery (PlanetScope Scene (Planet Team, 2017)) and manually identified clear sky days during the whole summers of 2020 and 2021. We then automatically identified snow cover using a K-Means unsupervised learning algorithm from Google Earth Engine (Arthur and Vassilvitskii, 2007) and created maps of snow presence/absence for our discretised model with an approximately two weeks return period for the whole snow melt seasons. We set PEST to minimize the error of modelled and observed snow presence/absence at the dates of all snow maps for each pixel. This procedure allows better determination of the evolution of the snow line (Barandun et al., 2018) and significantly improves the modelled SWE estimation especially in zones where no direct SWE observations are possible. All calibration parameters were calibrated separately for each hydrological year (starting 1st October) but the calibration procedure was performed on both years directly, so that initial SWE and snow cover at the end of the first year also impact results of the second year.

Table B1 summarizes the results of the calibration procedure.

5.3.3 Snow isotopic module

5.3.3.1 Basic model formulation

Due to the strong correlation between water stable isotopes of oxygen (δ^{18}O) and deuterium (δ^{2}H), we chose to base the rest of this study on the isotopic composition of δ^{2}H only.

Using the estimated SWE from the mass-balance model, we estimated the mean snowpack isotopic composition (i_{sp}) from each cell. The same approach proposed in the work of Ala-Aho et al. (2017) is used to estimate the isotopic evolution of the snow pack and of snowmelt using an amount weighted approach based on a precipitation input in the form of rain (P_{r}) or snowfall ($snowfall$), snow sublimation (E) and snow melt (M_{snow}). A simple fractionation routine is used for snow melt (i_{sm}) and snow evaporation (i_{E}) using two calibration parameters ($f_{\text{frac,sp}}$, $f_{\text{frac,E}}$) and n_{melt}, the number of days since the beginning of snowmelt.

$$i_{\mathrm{sm}} = i_{\mathrm{sp}} - \frac{f_{\mathrm{frac,sp}}}{n_{\mathrm{melt}}} \tag{5.12}$$

$$i_{\mathrm{E}} = i_{\mathrm{sp}} - f_{\mathrm{frac,E}} \tag{5.13}$$

$$i_{\mathrm{r}} = a_r + b_r T_0 \tag{5.14}$$

$$i_{\mathrm{ROS}} = i_{\mathrm{sp}} f_{\mathrm{ROS}} + i_{\mathrm{r}}(1 - f_{\mathrm{ROS}}) \tag{5.15}$$

$$i_{\mathrm{sp}}^{t} = \frac{i_{\mathrm{sp}}^{t-1} h_{\mathrm{SWE}}^{t-1} + i_{\mathrm{r}}^{t} f_{\mathrm{ROS}} P_{\mathrm{r}}^{t} + i_{\mathrm{sf}}^{t} P_{\mathrm{sf}}^{t} - i_{\mathrm{E}}^{t} E_{\mathrm{sp}}^{t} - i_{\mathrm{sm}}^{t} M_{\mathrm{snow}}^{t}}{h_{\mathrm{SWE}}^{t-1} + f_{\mathrm{ROS}} P_{\mathrm{r}}^{t} + P_{\mathrm{sf}}^{t} - E_{\mathrm{sp}}^{t} - M_{\mathrm{snow}}^{t}} \tag{5.16}$$

The isotopic composition of the precipitation during the whole year as rain (i_{r}), or snowfall (i_{sf}) was determined by computing a linear regression curve between measured air temperature at the weather station (T_0) and the isotopic composition of precipitation events (see Sect. 5.3.3.2).

Rain on snow (ROS) incorporation and water release is a complex process, which may have a strong impact on the snowpack isotopic composition, depending on whether rain water leaks through the snowpack, is stored or refreezes in the snowpack (Beria et al., 2018; Juras et al., 2017). The proposed isotopic model from Ala-Aho et al. (2017) assumed a complete incorporation of the rain in the snowpack, which they assume to be characteristic of ripened isothermal snowpack typical of the main melt season. Nonetheless, as shown in the experimental work of Juras et al. (2017), they acknowledge potential bias due to rapid waterflow movements in non-ripe cold snow where preferential flow is more likely, leading to a 5 times faster infiltration velocity of the rain and only partial mixing with the snowpack. In an artificial ROS experiment of a ripe snowpack, Juras et al. (2017) showed that more than 50 % of rainwater was not released from the snowpack and remained stored. An other in-situ study by Rücker et al. (2019a) showed that interactions between rainwater and snowpack were mostly influenced by the residence time of the rainwater in the snowpack, which mostly depended on snow depth and rainfall amounts. To account for ROS, we here introduce a factor (f_{ROS}) in Eq. 5.16 which defines the fraction of rainwater which is incorporated in the snowpack and contributes to modifying its isotopic composition. As observed in Juras et al. (2017), we assume that the same amount of ROS event water is released from the snowpack, but part of this release (equivalent to $f_{\mathrm{ROS}} P_{\mathrm{ROS}}$) is composed of previously stored snowmelt pushed out of the snowpack via piston flow, so that the isotopic composition of the rainwater leaving the snowpack (i_{ROS}) is composed of a mix of snowmelt and rainwater (Eq. 5.15). We defined a simple calibration function between SWE and f_{ROS}, where f_{ROS} increases with thinner SWE. This relationship is based on the assumption that deeper snowpacks are less ripe (due to less melt) and water infiltration is faster because of more preferential flow paths, so that the incorporation of rain is only partial. In thinner snowpacks, we assume that snow is ripe which leads to more rain trapped and mixed with the snow.

No isotopic lapse rate was used since no clear trend could be observed from 8 simultaneous rain samples at 2450 m and 2800 m. This choice is discussed in Sect. 5.5.1.3.

The three isotope parameters ($f_{\mathrm{frac,E}}$, $f_{\mathrm{frac,sp}}$, f_{ROS}) were calibrated manually following simple rules. First, the resulting snowmelt δ^2H value should remain below the measured stream δ^2H during the early melt season since snowmelt is isotopically lighter than icemelt (snowmelt is the end-member with the most negative values). Secondly, in June, snowmelt δ^2H should be close to stream δ^2H since snowmelt is the major contributor at that time. Then, the modelled snowpack δ^2H at a grid cell should also be similar to the depth-averaged isotopic composition of the corresponding snowpit. Finally, during the mid-melt season, we observed that daily isotopic variations in the stream showed a minimum (more depleted) in the morning. This is likely due to an increased icemelt contribution in the afternoon compared to snowmelt, with icemelt showing a less depleted δ^2H value than snowmelt. During the late season, the stream isotopic minimum occurs in the afternoon, indicating here that the snowmelt isotopic composition has become more enriched than icemelt,

due to snow fractionation and rain on snow. The moment when the stream δ^2H signal switches from a minimum in the morning to a minimum in the afternoon indicates when snowmelt δ^2H becomes isotopically heavier than icemelt.

5.3.3.2 Air temperature and precipitation stable isotopes relationship

In order to estimate the snowpack isotopic composition, we relate the isotopic composition of each precipitation event to air temperature. For each precipitation sample, the corresponding air temperature of the event was estimated by calculating a 10 minutes precipitation weighted average temperature for any precipitation in the last day. In order to assess the uncertainty, we defined a normally distributed error for both the isotopic composition of precipitation and air temperature. We defined a Gaussian distribution with a standard deviation (σ) of 1 °C for air temperature and 5 ‰ for δ^2H. We then performed 5000 iterations where we randomly picked values in the respective distributions of air temperature and isotopic composition of all points and calculated the best linear fit each time. Finally, we use the two regressions with the smallest and largest slope coefficients as the limit of the uncertainty of the relationship. We use the mean and two extreme cases as parameters to estimate i_{sf} and i_{r} from measured air temperature (T_0) in our isotopic model (see Eq. 5.14).

5.3.4 Hydrological routing module

A simple hydrological routing scheme is used to transport water with its isotopic composition from its input cell to the catchment outlet. In this model, we do not consider any interactions between hydrologically connected cells but only use the hydrological path length from each cell to the catchment outlet. We divided the path in four different categories: (1) flow through the snowpack; (2) flow through the hillslope sediments; (3) flow through the glacier distributed system; (4) flow through the glacier channelized system. The total flow path from each cell to the glacier outlet was calculated using the Flow Distance tool (ArcGIS pro v2.3) based on 2m DEM (SwissTopo, 2019). For each category, we apply a convolution between the water input at time t and a Gamma distribution probability density function ($g(t, \alpha_g, \beta_g)$) as described in Eqs. 5.17 & 5.18. In this approach, the Gamma function is used to reproduce a realistic transit time distribution (TTD) of the water input (McGuire and McDonnell, 2006). The convolution of each TTD provides the total TTD of the water from each cell to the glacier outlet (Fig. 5.2).

$$\delta_{out}(t) = \int_0^\infty g(\tau)\delta_{in}(t-\tau)d_\tau = g(t) * \delta_{in}(t), \tag{5.17}$$

$$g(t, \alpha_g, \beta_g) = \frac{\beta_g^{\alpha_g} t^{(\alpha_g - 1)} e^{-\beta_g t}}{\Gamma(\alpha_g)}, \tag{5.18}$$

where ($\delta_{in}(t)$) is any given input flux at time t and ($\delta_{out}(t)$) is the output flux.

In order to estimate the TTD, the parameters of the Gamma distribution needs to be defined. For each of the four compartments, we estimate the mean transit time (t_{MTT}) of the water based on physical properties of each compartment and use this delay to define the mode of the Gamma distribution ($t_{\mathrm{MTT}} = \frac{\alpha_g - 1}{\beta_g}$). The dispersion of the flow for the Gamma distribution is defined by a dispersion factor (D=α_g-1).

5.3.4.1 Hillslope routing

Here we consider that the landcover is mainly composed either of hillslope sediments or ice. This is a reasonable assumption for this steep sediment-covered area where only sediment and apparent bedrock dominate the hillslope. For the hillslopes, the average transit time (t_{MTT}) from

each grid cell to the glacier surface was calculated using an estimated groundwater pore velocity (Eq. 5.19). Pore velocity is defined for kinematic subsurface saturated flow (MacDonald et al., 2012) as a function of slope (θ), aquifer distance (L_a), aquifer porosity (ϕ) and hydraulic conductivity (K_s). We selected a porosity of 0.3 and a hydraulic conductivity for talus slopes of 5x10^{-2} m s^{-1} based on previous research (Müller et al., 2022a).

$$t_{\mathrm{MTT}} = \frac{L_a}{v_p} = \frac{L_a \phi}{K_s \sin(\theta)} \tag{5.19}$$

5.3.4.2 Snowpack routing

In the case of snowmelt or rain on snow (ROS) events, a TTD through the snowpack is used. Here we calibrated an average pore velocity in the snowpack with an initial velocity of 1200 mm h^{-1} based on the experimental work of Juras et al. (2017). As previously, the average transit time (t_{MTT}) through the snowpack is used to define the mode of the Gamma distribution. Since SWE evolves with time, the TTD through the snowpack changes with time and was recalculated for each day.

5.3.4.3 Glacier routing

Once the flowpath reaches ice, we defined two different compartments. The glacier drainage system was considered to be either distributed or channelized. During the winter, due to ice movement, less melt and creep closure (Flowers, 2015), subglacial channels tend to close, leading to an inefficient distributed drainage system characterized by slow water flow. During summer, larger conduit-like subglacial channels tend to develop and extend up-glacier with the recession of the snowline (Nienow et al., 1998). Therefore, based on the snow cover estimated with the mass-balance model, we calculated the mean distance between the glacier outlet and the first 5 cells on the glacier with snow cover to define the length of the channelized flow. We do not assume supraglacial flow here. However, the calibration may compensate this simplification by artificially increasing the subglacial velocity. The length of the channelized flow and their corresponding TTD for each cell changes through time since it is based on the snow cover evolution. The length of the distributed flow is computed as the difference between the total length on the glacier and the channelized flow length.

For the summer channelized system, an average velocity of 0.8 m s^{-1} was defined based on dye tracing. For the snow-covered distributed subglacial system, the mean velocity could not be measured directly. Here an initial value of 0.1 m s^{-1} was used based on Nienow et al. (1998).

5.3.4.4 Total routing

The convolution of the combined Gamma distributions (snow, hillslope, distributed glacier system, channelized glacier system) with rainfall ($P_{\mathrm{r},j}$), ROS, ($P_{\mathrm{ROS},j}$), snowmelt ($M_{\mathrm{snow},j}$), or icemelt ($M_{\mathrm{ice},j}$) time series obtained from the mass-balance model for each cell j with an area (A_j) provides the estimated discharge at the catchment outlet per water source and per cell. The sum over all cells corresponds to the total discharge from each water source. The case for snowmelt is illustrated in Eqs. 5.20 & 5.21.

$$Q_{\mathrm{sm,tot}} = \sum_{cell=1}^{cell=n} \Big(g_j(t, \alpha_g, \beta_g) * (M_{\mathrm{snow},j} A_j) \Big) \tag{5.20}$$

where $Q_{\mathrm{sm,tot}}$ is the total discharge from snowmelt at the outlet. The same approach can be applied to estimate the mean isotopic composition of each water source by applying the same convolution on the multiplication of the precipitation or melt time series and the isotopic signal (i_{sm}, i_{ROS} and

i_r). This assumes that the isotopic composition of a water input is transported and redistributed at the catchment outlet following the same TTDs. The sum of each cell divided by the total discharge corresponds to the amount-weighted average isotopic composition of the compartment ($i_{sm,tot}$).

$$i_{sm,tot} = \frac{\sum_{j=1}^{j=n}\left(g_j(t,\alpha_g,\beta_g) * (i_{sm,j} M_{snow,j} A_j)\right)}{Q_{sm,tot}} \tag{5.21}$$

5.3.4.5 Fast and slow glacier storage

This approach assumes that the groundwater flow is mainly driven by advective flux and not by diffusion. In the case of diffusion dominated flow, the discharge response at the catchment outlet would be dominated by "old" water being pushed out of the aquifer due to the pressure gradient so that the isotopic signal would not be proportional to the particle transit time distribution. This typical old/new water paradox is widely discussed in the literature (e.g. Kirchner, 2003). In the specific case of Otemma, talus slopes are characterized by a swift hydrological response due to their coarse nature and steepness (Müller et al., 2022a), leading to subsurface flow dominated by advection (Harman and Sivapalan, 2009a) so that a weighted average isotopic estimation is physically plausible. However, it is likely that part of the water is stored in some part of the subglacial and englacial glacier network. To account for this, we ultimately define two reservoirs which represent a fast and slow linear storage. The integrated discharge of each water sources after the convolution with the Gamma distributions is then separated between both reservoirs based on a calibrated fraction ($f_{reservoir}$), which assigns how much goes into the slow reservoir. The outflow discharge of each reservoir finally depends on a calibrated response time constant (k). For the fast reservoir, this results in (Eq. 5.22).

$$Q_{fast} = \frac{S_{fast}}{k_{fast}}, \tag{5.22}$$

where S_{fast} is the filling of the reservoir. The slow reservoir response is computed in analogy to above equation. The isotopic composition of each reservoir is separated between each water sources and is assumed to be fully mixed at each time step.

5.3.4.6 Hydrological routing calibration

The calibration of the hydrological routing was also performed using PEST-HP, as already proposed in other glacio-hydrological studies (Immerzeel et al., 2012). We set three objective functions. The first function minimizes the error on observed and simulated discharge at the catchment outlet at an hourly time step. The second function optimizes the amplitude of diel flow variations, which is a typical feature of glaciated streams and which tends to increase in the late melt season (Lane and Nienow, 2019; Nienow et al., 1998). Finally, the last objective function aims to minimize the observed and modelled stream water stable isotopes. Stream water isotopes were modelled by multiplying the discharge fraction of each water source based on the routing model with their simulated isotopic composition. We finally tested the differences in model performance by using only the discharge data or by adding the water isotopes. The calibration was performed by only including data for the summer 2020 (26 June to 15 September) and from 8 June to 20 June 2021. The first two weeks of June 2021 were included as they were not recorded in 2020 and represent the initial increase in streamflow after winter. The period from 20 June 2021 to 15 September 2021 were then used to evaluate the model performance.

5.3.5 Mixing model for water sources

In order to estimate the contribution from rain, snow and ice melt, a three components mixing model needs to rely on two independent tracers. Here, since we only rely on water stable isotopes,

we propose estimating the shares of rain (ρ_{rain}) and rain on snow (ρ_{ROS}) using the output discharge of the routing model divided by the total modelled discharge at the glacier outlet. Then, we only use isotopes to estimate the share of snow, ρ_{snow} and of ice melt, ρ_{ice} following Eq. 5.23. The isotopic composition of rain (i_{r}) and snow (i_{sm}) is estimated using the isotopic model. The isotopic composition of ice melt (i_{ice}) is defined as constant through the year based on our measurements.

$$\rho_{\text{ice}} = \frac{i_{\text{stream}} - i_{\text{sm}} - (i_{\text{r}} - i_{\text{sm}})\rho_{\text{rain}} - (i_{\text{ROS}} - i_{\text{sm}})\rho_{\text{ROS}}}{i_{\text{ice}} - i_{\text{sm}}} \tag{5.23}$$

Additionally, thanks to the routing of rain and ROS, the integrated isotopic composition of specific rain events (i_{event}) can be better approximated than in typical mixing models which simply use bulk rain samples to define i_{event}. In this approach, event water is defined as the mixing of rain and ROS weighted by their respective discharge (Eq. 5.24). Since i_{ROS} mostly inherits the signature of the snowpack (Eq. 5.15), and Q_{ROS} is somewhat delayed by the routing through the snowpack, the event isotopic signature can be seen as a mix of rain water on dry cells, mixed with a delayed release of snowmelt released from ROS. The fraction of event water in the total discharge (ρ_{event}) can then be estimated by a simple two-component mixing model (Eq. 5.25) where we estimate the isotopic composition of the baseflow (i_{baseflow}) using a simple interpolation of the stream isotopic composition between pre-event and post-event composition.

$$i_{\text{event}} = \frac{i_{\text{r}} Q_{\text{r}} + i_{\text{ROS}} Q_{\text{ROS}}}{Q_{\text{r}} + Q_{\text{ROS}}} \tag{5.24}$$

$$i_{\text{stream}} = (1 - \rho_{\text{event}})\, i_{\text{baseflow}} + \rho_{\text{event}}\, i_{\text{event}} \tag{5.25}$$

5.4 Results

5.4.1 Field isotopic measurements

From July 2019 to October 2021, we measured the water δ^2H as well as the water electrical conductivity (EC) at different locations within the catchment. We summarize all results in Fig. 5.3. The rain water EC has a median value of 26 μS cm^{-1}. Snow and ice samples have lower values usually below 10 μS cm^{-1}, likely due to the preferential elution of solutes in the snowpack (Costa et al., 2020). Interestingly, the stream EC shows systematically higher EC than the snow and ice samples, even during the peak snow and ice melt period. Regarding water stable isotopes, only rain is significantly different. The surface snow and ice samples have similar ranges and show a large variability, which completely overlaps with the stream signal. As suggested in other studies (Beria et al., 2018), the composition of the snow- and icemelt samples show less variability than the surface snow samples. Figure 5.4 shows the spatial variability of the isotopic composition of snow on a single day and Fig. 5.5 shows the spatial variability of the isotopic composition of ice for the two years of sampling. Surface samples show a large variability with no clear tendency with elevation. Snow samples at the same locations but at a depth of 10 to 20 cm have completely different values and the median of all samples also differ significantly (-88.2 ‰ and -103.7 ‰ for surface snow samples and at 10 cm depth). Snow samples were also collected with depth in three snow pits. The snowpack δ^2H appears stratified with a tendency for more isotopically depleted snow with depth, reflecting the colder air temperature of the snowfall in the early winter season, which was conserved in the snowpack. The two upper snow profiles have a depth-weighted mean δ^2H of -125 ‰ for the central profile and -117 ‰ for the upper profile, lighter than the other samples. The snow profile at lower elevation shows less variability likely due to a more ripe snowpack and more mixing. At this location, snowmelt at the bottom of the snowpack was also sampled and reflected the average composition of the snowpack (-108 ‰).

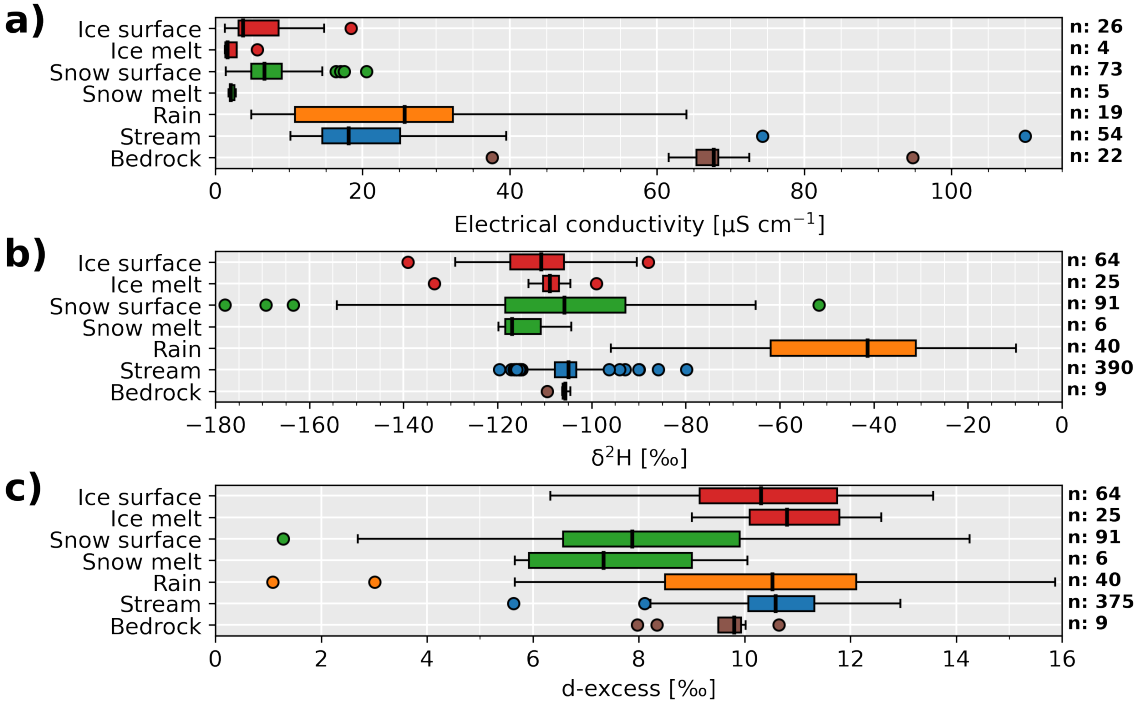

Figure 5.3: Boxplots of all water sources collected between July 2019 and October 2021. Water exfiltrations from the bedrock sidewalls are also shown. We show results of the water electrical conductivity **(a)**, δ^2H for water stable isotopes **(b)** and corresponding d-excess **(c)**. The total number of samples (n) is also indicated on the right.

The isotopic composition of the surface ice shows a strong spatial variability, with a slightly smaller range than surface snow. Ice melt sampled as superficial melt water on the glacier has a much smaller variability which likely corresponds to a more integrated average value of the glacier ice. Two samples in the first 8 and 5 meters in depth of the glacier were also analyzed. No clear trend with depth can be observed but their average value is similar to the ice melt samples. In general no trends with elevation are observed.

In addition to the snow samples presented in Fig. 5.4, the additional samples collected during the snowmelt season suggest no significant temporal trend (Fig. B2). It was expected that the snowpack will become gradually more enriched in heavier isotopes due to mechanisms such as rain on snow (Juras et al., 2017) and fractionation from snow sublimation and melt (Beria et al., 2018). Such behavior appears difficult to observe for surface snow samples since the spatial variance of their isotopic composition appears to be large and not representative of the whole snowpack evolution.

5.4.2 Air temperature and relationship to isotopic composition of precipitation

The relationship between air temperature and precipitation δ^2H appears to be linear with a coefficient of determination (R^2) of 0.85 (Fig. 5.6. However most of our samples cover the summer season, which shows a larger variability and the trend is strongly influenced by the limited number of winter precipitation samples. For this reason, we based our isotopic model on the regression curve obtained by the mean slope and intercept (dashed green curve in Fig. 5.6). Additionally, we also highlighted the two cases with the maximal and minimal regression slopes from the sensitivity analysis (red curve in Fig. 5.6).

5.4.3 Mass-balance model calibration results

The mass-balance model was calibrated against SWE, ice melt and snow cover for both years separately (Table B1). The temperature lapse rate shows a maximum around mid-May with a mean

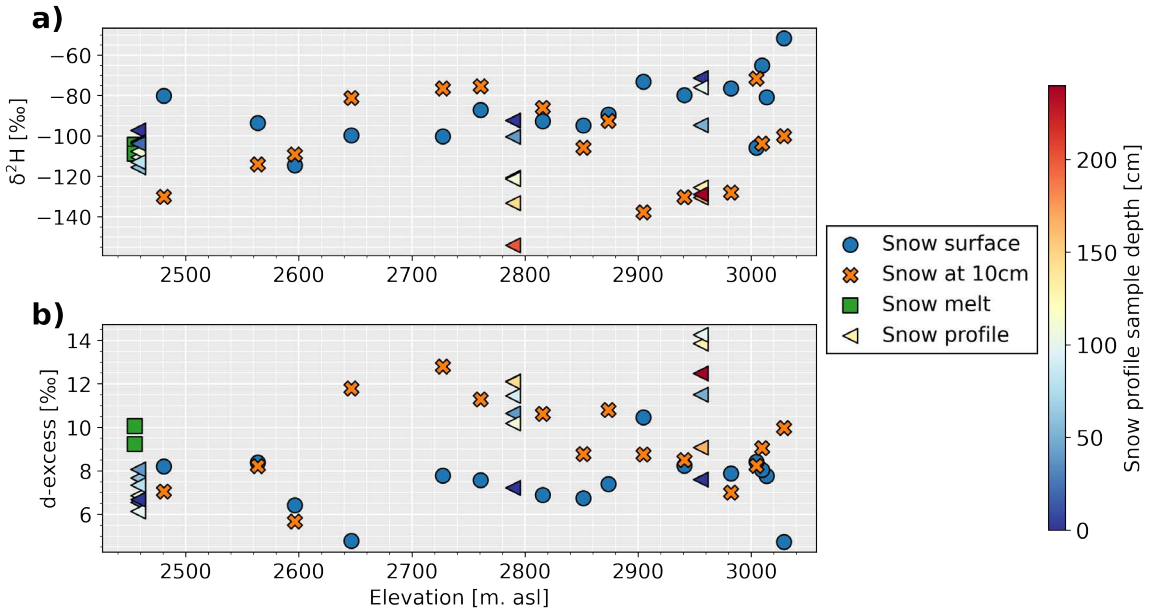

Figure 5.4: Isotopic composition of snow samples with elevation collected on 28 May 2021 on the glacier main lobe. The total number of samples is 16 for snow surface, 15 for snow at 10 cm, 19 for the three snow profiles and 2 for snow melt. The depth of the snow profiles (0 to 250 cm) is indicated by the colorbar.

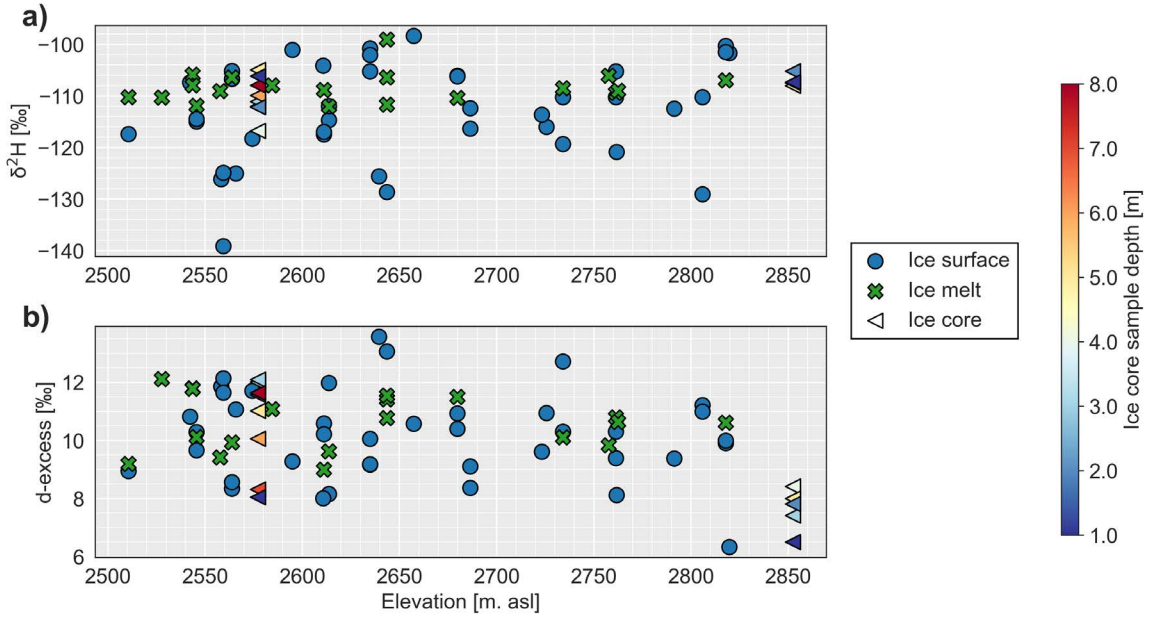

Figure 5.5: Isotopic composition of ice samples with elevation collected between 2020 and 2021 on the glacier main lobe. The total number of samples is 40 for ice surface, 19 for ice melt and 13 for ice cores. The depth of the ice core (0 to 8 m) is indicated by the colorbar.

value of 0.41 °C and 0.5 °C per 100 m for 2020 and 2021 and a maximal seasonal variation of about ±0.1 °C per 100 m around the mean (Fig. B4c). Regarding snow redistribution, both calibration years lead to the same slope correction factor, with a slope threshold of 32 ° above which snow redistribution occurs towards gentler slopes (Fig. B4a). The calibration of the snow redistribution appears also relatively similar for both years, with some redistribution near the glacier tongue (lower elevation) and above an elevation of 3000 m asl (Fig. B4b). An important snow redistribution also occurs for year 2021 at high elevations (3400 to 3600 m asl), which mainly corresponds to small high elevated hanging glaciers, where snow redistribution from the nearby steep bedrock slopes is likely. Such elevated zones have a limited total area (3 %) so that the impact on the total mass-balance is limited. Finally, the radiation correction factor is mainly comprised between 1 for

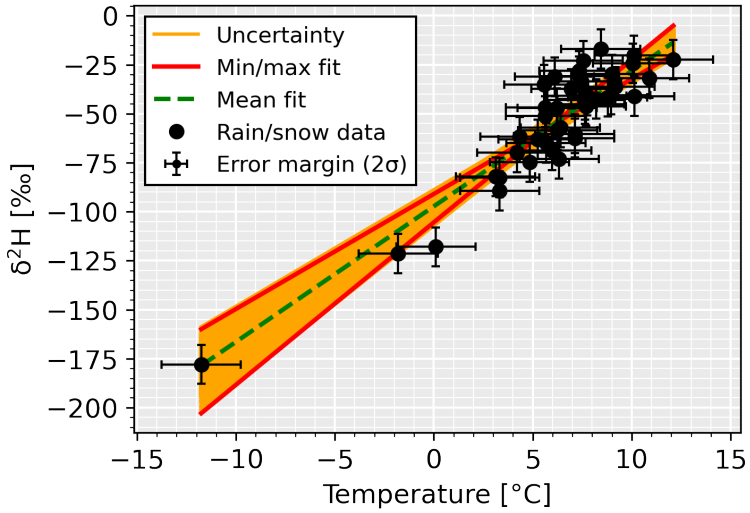

Figure 5.6: Relationship between air temperature measured at the weather station and the isotopic composition of 39 precipitation events between 2019 and 2021. For each point we defined a normally distributed error margin of two standard deviations (σ). The uncertainty margin (orange area) represents the linear regressions obtained from 5000 random realizations from all measurements points when including the error margin. The green dashed line correspond to the mean regression and the red curves show the two most extreme fits.

flat slopes and 2 for north facing slopes around 40 ° (Fig. B4d). A mild precipitation lapse rate of 1.7 and 3 % for 2020 and 2021 was also estimated.

Overall the model shows good performance for SWE, although the model results appear smoother with elevation than the point SWE measurements which are more spatially variable (Fig. B6). The root mean square errors (RMSE) for SWE are 99.2 mm and 86.2 mm for 2020 and 2021 respectively. The RMSE for ice ablation are 237.7 mm (in water equivalent, hereafter w.e.) for 2020 and 268.0 mm w.e. for 2021. The mean error of all mass-balance calculations is close to 0 mm. The snow cover is well represented during the whole season, showing similar patterns of melt, with earlier snow disappearance on north facing steep slopes (Fig. B7 to B10). In 2020, one summer snow event seems underestimated, leading to a constant bias in the snow cover fraction after July 2020 (Fig. B11). In 2021, the snow cover evolution fits well the observations during the whole season, with a somewhat earlier snow disappearance in the upper part of the catchment, potentially due to precipitation underestimation in this zone.

Catchment-scale average snow melt over the hydrological years (starting in October) is 1824 mm and 1550 mm for 2020 and 2021, 225 mm and 343 mm for liquid precipitation, 1230 mm and 924 mm for ice-melt and 61 mm and 92 mm for snow sublimation. Although sublimation losses were simulated with a simple routine, such amounts are in a reasonable range compared to other studies in elevated catchments (e.g. Stigter et al., 2018; Strasser et al., 2008).

Finally, the results of the total mass-balance (rainfall, snowmelt, icemelt) at a daily timescale appears to match well the measured discharge at the glacier outlet (Fig. B5). In particular, the cumulative mass-balance follows well the cumulative measured discharge, except for the month of September 2020, where the total mass-balance overestimates the measured discharge.

5.4.4 Hydrological routing model results

The calibration of the hydrological routing parameters was performed in a second separate step following the mass-balance calibration and parameters are summarized in Table B1.

Hillslope parameters calibration leads to a lower K_s value than initialized, which significantly smoothes out the response from the hillslope water inputs. The channelized glacier routing shows a similar velocity ($v_{\text{channelised}}$) as measured, with limited dispersion ($D_{\text{channelised}}$) (dispersion de-

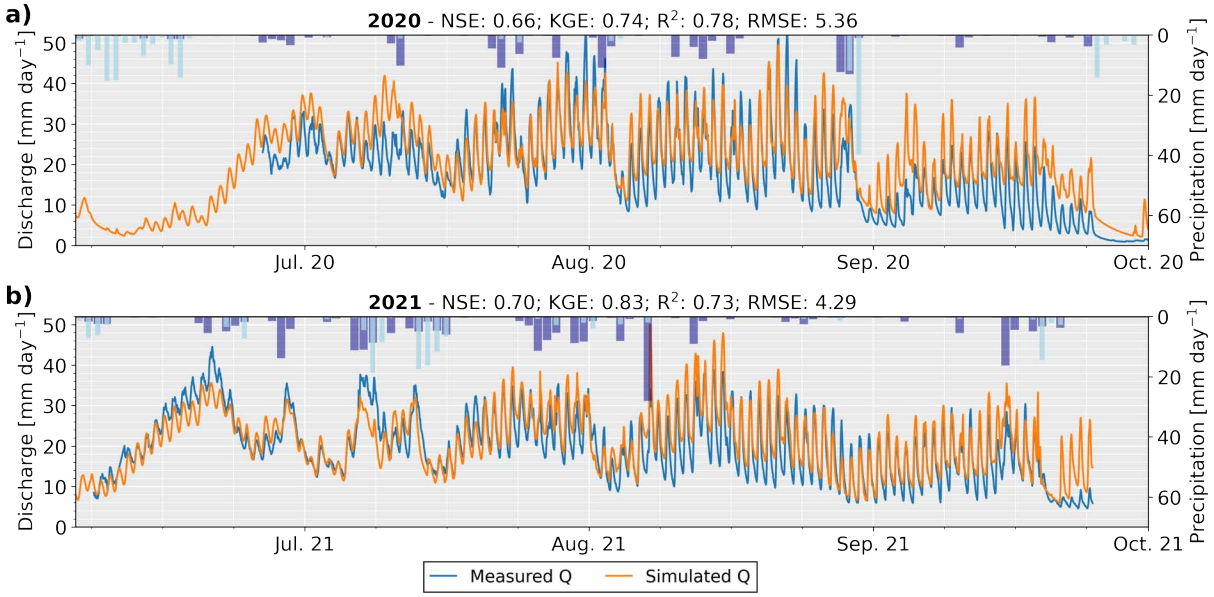

Figure 5.7: Comparison between measured discharge (Q) at the glacier outlet and simulated discharge by the combined mass-balance and routing model for the melt season of 2020 (a) and 2021 (b). For each year, we show the Nash-Sutcliffe efficiency (NSE) and Kling-Gupta efficiency (KGE), as well as the root mean square error (RMSE) and coefficient of determination (R^2). Daily mean solid (light blue) and liquid (dark blue) precipitations are shown as inverted bars.

creases with increasing value), so that water is conveyed rapidly fast in this compartment. The distributed glacier routing shows lower velocity ($v_{\text{distributed}}$), with a somewhat longer dispersion ($D_{\text{distributed}}$), which successfully allowed representation of the changes in discharge variations during the early and late melt season. The rain and snowmelt infiltration (v_{ROS},v_{sp}) through the snowpack are relatively similar, with a transit time of less than an hour for all model cells. The parameter estimation of the fast reservoirs indicates that it has a response time constant (k_{fast}) of 1 hour and that 57 % of all water is instantaneously released from this storage. The rest of the inflow is stored in a slower reservoir where a response time (k_{slow}) of 96 hours is estimated.

The final discharge results are presented in Fig. 5.7. Diel fluctuations are well represented with an increase in magnitude towards the late melt season as discussed in the work of Lane and Nienow (2019). Discharge recession during short cold spells are also well simulated. The hydrological routing model was only calibrated against data for 2020, but the model performance appears as good for 2021. This behaviour is confirmed by the Nash-Sutcliffe efficiency (NSE) and Kling-Gupta efficiency (KGE) criterion (see Gupta et al. (2009) for references) of 0.66 for NSE and 0.74 for KGE in 2020 and 0.70 and 0.83 in 2021. Since KGE applies by definition a more equal weighting between correlation, bias and variability (Knoben et al., 2019), the higher KGE values obtained compared to NSE indicate a limited bias and a good representation of the flow variability, while the correlation appears somewhat lower.

5.4.5 Isotopic model results

Based on stream δ^2H measurements and mean δ^2H of supraglacial icemelt samples, the icemelt δ^2H was set to a fixed value of -109 ‰ which reflected the minimum stream δ^2H in late summer, when snow cover is lowest. The snowmelt δ^2H was calibrated manually. Parameter M_{frac} was set to 8 ‰ for δ^2H but had little impact on the results as also shown by Ala-aho et al. (2017). The sublimation parameter E_{frac} was set to a value of 16 and 2 ‰ for δ^2H for 2020 and 2021. This represents a rather mild fractionation compared to Ala-aho et al. (2017). Parameter f_{ROS} had a similar impact on snowmelt as E_{frac} but led to a slower enrichment in early July 2020 than sublimation, which better fitted with the measured δ^2H of the stream. f_{ROS} was set to 1, similarly to Ala-aho

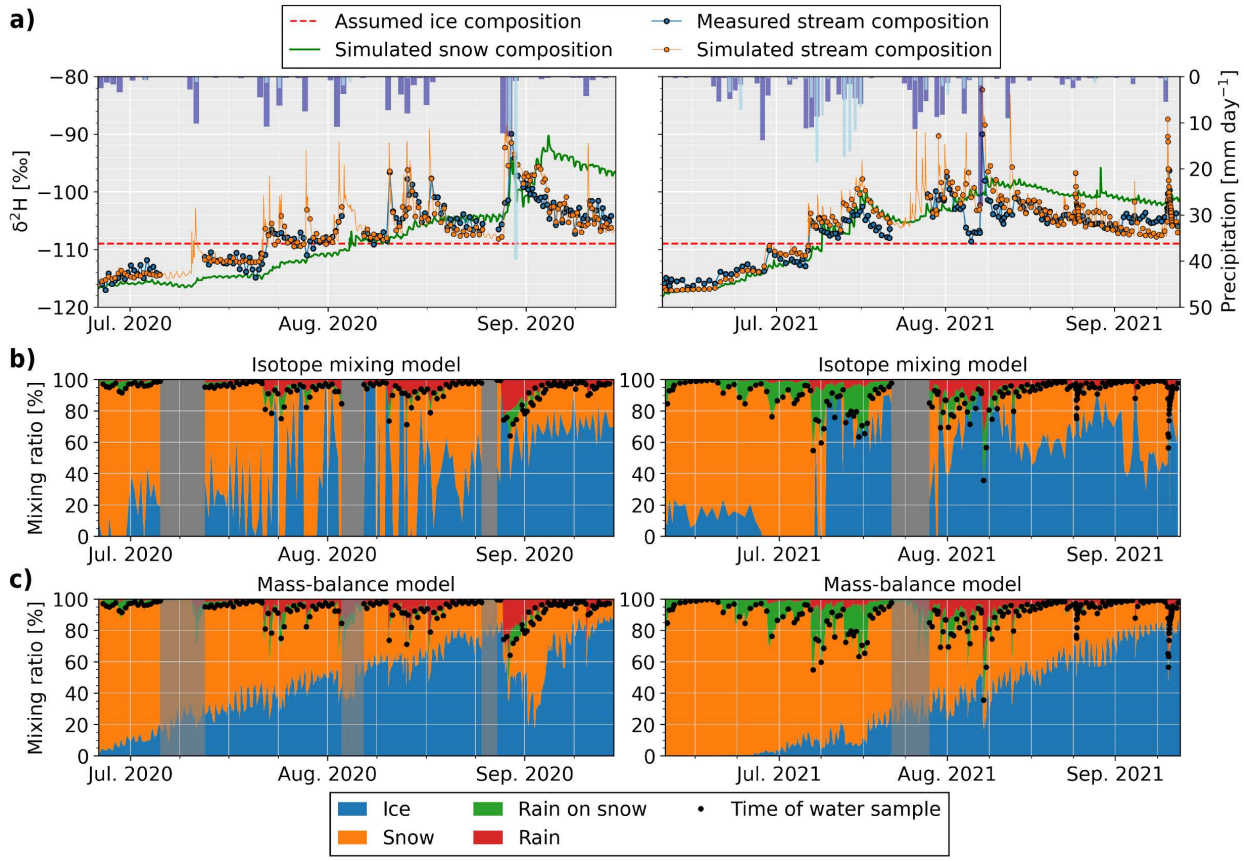

Figure 5.8: Results of the isotopic model. **a)** Measured and simulated stream δ^2H at the glacier outlet as well as the value used for the ice composition and the modelled evolution of the snowmelt composition. Daily mean solid (light blue) and liquid (dark blue) precipitations are shown as inverted bars. **b)** Estimated mixing ratios between ice melt, snow melt, rain and rain on snow based on the measured stream δ^2H and the estimated δ^2H of the water sources. The shares of rain and ROS were estimated by the routing model. The black dots indicate the dates of each stream water sample used to estimate the mixing ratios. Grey areas represent periods when no samples were available for more than a day. **c)** Mixing ratios estimated from the combined mass-balance and routing model only. The mean value of the precipitation events are shown as inverted bars.

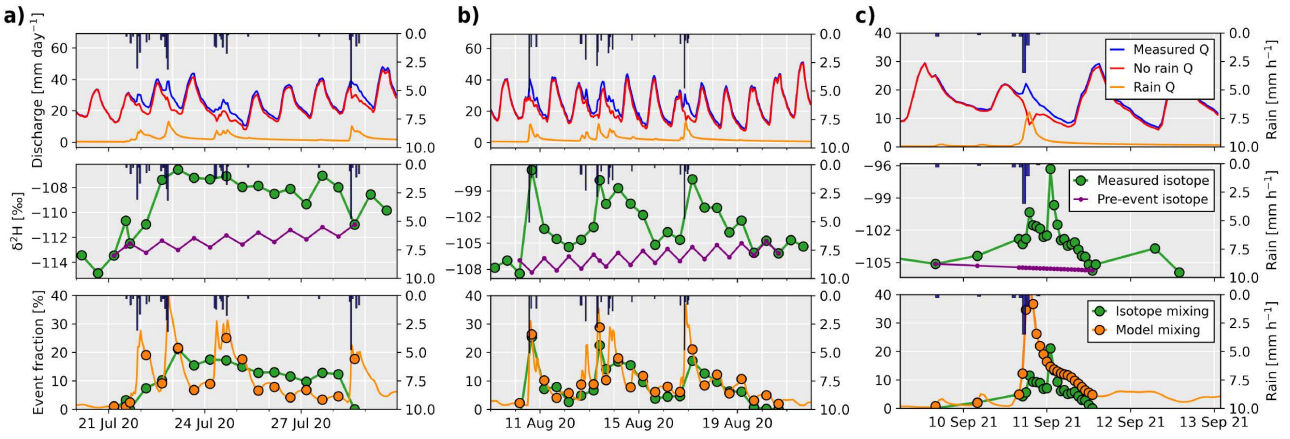

Figure 5.9: Comparison of the estimated fraction from the total discharge originating from rain events during the early **(a)**, mid **(b)** and late melt season **(c)**. The upper figures show the measured discharge (blue curve) and the sum of rain and ROS discharge (event discharge) estimated from the model (orange). The red curve shows the measured discharge without the simulated event water. The central figures show the measured stream δ^2H (green) and an estimation of the pre-event δ^2H based on a simple interpolation between the pre- and post-event stream compositions. We added small diel variations based on the behavior of the previous days. Lower figures show the fraction of event water estimated either based on the modelled event discharge (see upper figures) or based on isotopes (see central figures).

et al. (2017), but only when SWE was lower than 1000 mm and to 0.5 when SWE was larger than 2000 mm, with a linear increase in between. This indicates that thicker snowpack (>2000 mm w.e.), which underwent less melt, transmits part of the rain signal while rain is completely integrated in the snowpack when SWE becomes thinner (and likely isothermal) due to more melt. The resulting snowmelt δ^2H is shown in Fig. 5.8a. The modelled snowpack δ^2H at the snowpits was -119.5 ‰ compared to two mean measured snowpits δ^2H of -125 ‰ and -117 ‰. Snowmelt δ^2H is slightly smaller than stream δ^2H in the early melt season. The resulting simulated stream δ^2H based on the water ratios from the routing model and the δ^2H of the water sources appear to fit well the stream observations.

For the second half of July 2020, stream δ^2H is overestimated during some rain events. Interestingly, the hydrograph response to those rain events is very fast (within an hour) with a rapid recession (about half a day) (Fig. 5.9a). However, the isotopic signal appears more dampened, with a smaller peak and a much longer return to the baseline value about 5 days later. This highlights the typical old water paradox (Kirchner, 2003), where hydrograph response is swift but the water composition is composed of more pre-event water. This phenomenon may be due to a larger subglacial or englacial water storage in the early melt season when the drainage system is less developed. The latter responds rapidly to an increased water input (increased pressure) by releasing older water. In the later summer, in mid-August 2020 (Fig. 5.9b), the response to rain events seems better represented by our model, which may be linked to a more efficient drainage system and thus a smaller storage. Finally, during September (Fig. 5.9c), the isotopic signal shows a fast recession of about one day, with a first peak rapidly after the rain event and a second one about 6 hours later, while no increase in discharge is observed. Interestingly, this second peak seems to come from snowmelt given that d-excess during this peak significantly decreased to 5 ‰, while it returns to its baseline value of 10 ‰ within the next 3 hours, synchronous with the end of the isotope peak.

5.4.6 Estimation of mixing ratios

We propose to compare the estimated mixing ratios between the four different water sources, either only based on the estimated discharge from the mass-balance and routing model or based on the simulated isotopic compositions of the water sources. As discussed in Sect. 5.3.5, since we only use water isotopes as tracer, only two components can be separated (snow and icemelt), while we use the results of the mass-balance and routing model to estimate the water fractions from rain and ROS events. The results of the mass-balance model (Fig. 5.8c), show a gradual transition from a snow-dominated discharge towards more icemelt in the late season. The estimated contributions of rain and ROS remain usually below 20 %, except for large events (>15 mm) where the peak contribution reaches up to 50 %. The results of the mixing model based on isotopes (Fig. 5.8b) are more variable. For both years, mixing ratios for the early and late melt seasons are in a similar range as those from the mass-balance model. During the mid-season, the estimated ratios of snow and ice melt appear much more variable and difficult to interpret. There are two main causes for such large uncertainties. First, the mid-season is characterized by frequent rain events. As discussed previously, it is likely that mechanisms responsible for the release of older water during rain events are not well represented in our model, so that the ratio of rain is subject to some uncertainty, which impacts the separation between snow and icemelt. Secondly, during the mid-season, the isotopic composition of snowmelt gradually increases and becomes relatively similar to icemelt. Since the ratio of ice and snowmelt depends on the difference between both compositions (see Eq. 5.23), the uncertainty becomes larger when their δ^2H values are close.

5.4.7 Sensitivity of snowmelt isotopic composition

A sound estimation of mixing ratios between snow and ice melt appears therefore very sensitive to their estimated δ^2H values. The results of the simulated snowmelt δ^2H in our model relies on a

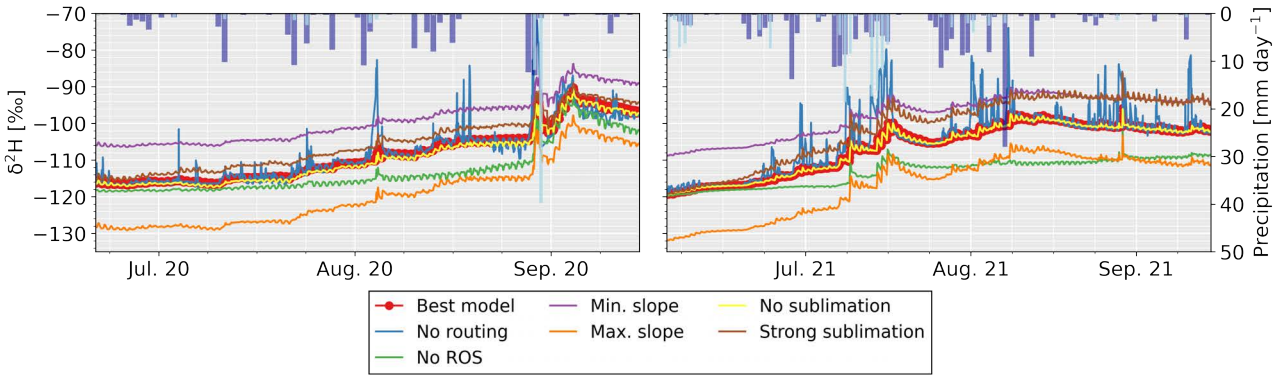

Figure 5.10: Sensitivity analysis of the modelled snowmelt δ^2H at the glacier outlet. The curves shown are : Best calibrated model (Best model); model without flow routing (No routing); model without ROS infiltration (No ROS, f_{ROS} = 0); extreme fits of the air temperature - precipitation isotopes (Min. slope, Max. slope); extreme values of the isotopic fractionation (No sublimation with $f_{frac,E}$=0 ‰, Strong sublimation with $f_{frac,E}$ = 80 ‰). Daily mean solid (light blue) and liquid (dark blue) precipitations are shown as inverted bars.

linear regression with air temperature and three calibration parameters (f_{ROS}, $f_{frac,E}$, $f_{frac,sp}$). We review the effects of those different parameters in Fig. 5.10. For the regression with air temperature, we use the results for the lower and upper bounds highlighted in Fig. 5.6. The impact on the snow δ^2H value appears to be very large, with a consistent bias of about 10 ‰. Neglecting the incorporation of rain on snow (f_{ROS} = 0) leads to a much slower enrichment of the snow in heavy isotopes during the melt season. Only new, relatively warm, summer snow events modify significantly the snowmelt δ^2H, as it can be observed for late August 2020 or mid-July 2021. Based on our calibration, we used a mild sublimation fractionation factor ($f_{frac,E}$) compared to Ala-aho et al. (2017), so that the differences with no sublimation are limited. Using a stronger factor leads to a faster enrichment of the snowpack during the melt season. The impact of the liquid fractionation factor ($f_{frac,sp}$) leads to only very limited changes (less than 1 ‰) and is not shown on Fig. 5.10. For the early melt season (early June), it appears therefore that the calibration parameters have little effects on the estimated δ^2H value of snowmelt, which mainly depends on the relationship between air temperature and the δ^2H value of precipitation. During the melt season, $f_{frac,E}$ and f_{ROS} have a stronger impact and both contribute to an enrichment of the snowpack. Nonetheless, based on the stream δ^2H measurements, the stream isotopic composition increased only slightly in July 2020, a period when limited rain occurred. It seems therefore that a strong sublimation factor would lead to a too early enrichment of the snowpack during this period so that ROS events appear to be the more dominant process of snow enrichment in our catchment.

Finally, we show the isotopic composition of snowmelt if we simply take the average value of all snowmelt cells without the routing model (blue curve in Fig. 5.10). In this case, the signal shows more variability and small peaks mainly due to the effect of warm summer snowfall or ROS on the older snowpack. The hydrological routing appears therefore to mainly act as a type a of low-pass filter, smoothing out short term variations while the signal remains similar when no precipitation occurs.

5.5 Discussion

5.5.1 Model choices, limitations and parameter estimation

5.5.1.1 Mass-balance model

We constructed a simple mass-balance model relying on air temperature and incoming solar radiation. Seasonal temperature and precipitation lapse rates could not be measured in the field as only one weather station at the glacier snout is available. Extrapolating trends from meteorolog-

ical stations in nearby, non-glaciated catchments was not used as surface energy balance and air flow dynamics over glacier may be different than the surroundings, especially in summer when katabatic winds may occur (Greuell and Böhm, 1998). The calibrated temperature lapse rate led to steeper gradients in summer similarly to other studies (e.g. Marshall et al., 2007; Rolland, 2003). Interestingly, at higher elevation, the colder summer temperatures obtained with a varying lapse rate compared to a constant lapse rate led to less melt, which in turn influenced the calibration of the precipitation lapse rate. Precipitation lapse rate decreased indeed from about 10 % per 100m with a constant temperature lapse rate to about 2 to 3 % which is closer to studies for other glaciers (Schaefli et al., 2011). The snow loss function on steep slopes, combined with the radiation correction function based on slope and aspect was essential to represent correctly the timing of the presence/absence of snow on north and south-facing slopes. The benefit of fine-scale daily images from Planet Team (2017) allowed for weekly snow maps which strongly constrained those parameters. Finally, we developed a rough snow redistribution function which allowed to respect mass-balance and correct for local anomalies while avoiding overfitting due to the simplicity of the relationship with elevation.

Based on the current limited cover of debris (~10 %), the model does not include modification of melt for debris-covered glacier areas (Ferguson and Vieli, 2021). The model also did not include the potential melt induced by warm rain events. This phenomenon, while likely not representing a large fraction of the annual mass balance (Mazurkiewicz et al., 2008), may play a role during ROS events, by modifying the isotopic composition of the event water. For instance, Juras et al. (2017) showed that up to 25 % more water was released from a snow-dripping experiment in a isothermal snowpack. However, some studies showed limited melt during ROS flood events and attributed the flashy discharge response to ground heat flux induced-melt of fresh snow, increased overland flow (Pomeroy et al., 2016) and faster snow infiltration due to snowpack saturated conditions (Singh et al., 1997). It remains therefore unclear to what extent higher melt is induced, rather than the "normal" melt expected from the weather conditions. Some studies also reported a rain induced icemelt (Saberi et al., 2019). This phenomenon was not studied further in this work.

During the winter period, we measured a discharge recession reaching a minimum of about 0.24 mm day^{-1}. Our model was not designed to account for such low flows, so that discharge results cannot be compared for the winter months. There are two main hypothesis regarding the nature of this storage. Basal melt in winter could provide such limited flow, creating a thin water film (Flowers and Clarke, 2002), slowly draining through subglacial till or at the contact with bedrock and acquiring solutes. Alternatively, groundwater contribution from a deeper aquifer could provide such baseflow and is discussed in Sect. 5.5.3.

As illustrated in Fig. B5c & d, seasonal mass-balance results match unexpectedly well the observed discharge. This seems to further support the conclusion that groundwater, basal melt or rain-induced snowmelt represent only a marginal water input in summer. It is also possible that such additional water inputs are compensated in our model by a stronger icemelt in sediment-covered regions.

Including snow cover as an objective function improved the results significantly. Interestingly, for year 2020, we put 5 times more weight on the snow cover objective function than the snow mass balance one, which led to better discharge and snow cover results. The limited number of SWE observations for that year may not have been representative of the overall catchment and the calibration results led to a stronger gradient in SWE than observed, while the ice ablation results seemed better matched (Fig. B6c).

5.5.1.2 Routing model

We simulated routing based on an estimation of the mean transit time of the water through different compartments using gamma distributions. While this approach is somewhat different from more typical bucket-type approaches (Schaefli et al., 2005), it leads to relatively similar results, as

the spread of the gamma distribution can be related to a storage recession time constant. It allows however for a better definition of the transit time based on realistic estimations of flow velocities. One noticeable limitations is that routing does not depend on previous conditions such as antecedent wetness or the amount of storage in a reservoir. Since little to no soils are present in this area, we hypothesize that soil water retention is limited so that previous moisture conditions should not be a major driver in such area. A phenomena of water retention in the snowpack is however likely, which leads to variable infiltration speed, with faster release when the snowpack is saturated (Singh et al., 1997). In the early melt season, the discharge response to rain events was relatively well modelled, but was composed of more older pre-event water and new rain water was released smoothly during the next few days (Fig. 5.9a). This indicates that older water was preferentially released from a reservoir in response to additional rain water. It is likely that water is only partially mixed in a glacial reservoir so that our simple fully mixed reservoir was here not adequate. Moreover, since the shares of event water appear better represented for the mid-season (Fig. 5.9b), it is possible that the time constant of the reservoir should be adapted, similarly to the ratio of channelized and distributed routing. Interestingly, even during the mid-season, the event response based on isotopes shows a smooth recession, while our model estimates a smaller share of event water during daily peak melt, since at that time the rain event discharge is more diluted. This indicates that when melt increases, glacial storage increases which results in the release of more previously stored rain water. To account for such behavior, the glacier storage cannot be considered fully mixed and a mechanism of partial mixing should be more adequate.

We tested both routing parameter calibration with or without including stream δ^2H as an objective function. Overall, discharge NSE and KGE were similar for both calibration. Parameter estimation was not particularly different except for hillslope parameters which led to a faster transmission with a faster recession when isotope were not used. The slower response of hillslopes when isotopes are included is likely due to the dampened stream isotopic response during rain events illustrated in Fig. 5.9a. As a result, including isotopes modifies the internal mechanisms of the hydrological routing model, but it remains unclear if such changes reflect more realistic processes or a simple trade-off due to the inability of the model structure to represent the preferential release of older water.

5.5.1.3 Isotopic model

We chose a constant ice melt δ^2H based on supraglacial measurements and the shape of the stream δ^2H values. Changes in catchment-scale ice-melt δ^2H should mainly occur due to the melting of ice with significant age differences. Different spatio-temporal studies on ice melt isotopes show conflicting temporal results, with ice becoming either enriched (Penna et al., 2017), depleted (Schmieder et al., 2018) or showing no trends (Maurya et al., 2011). For the Swiss Alps, Jenk et al. (2009) analyzed a 80 m deep ice core and showed some δ^2H variations but no particular trends with depth, except for a shift at the ice base. Since the ice surface likely represents ice of different age, the bulk melt signal is likely similar to the mean of an ice core and does not significantly vary on Alpine glaciers where ice is relatively young. This statement may not be valid for larger ice sheets where ice may originate from older glaciations. Using the end of summer stream δ^2H seems a reasonable method to estimate the ice melt δ^2H, but residual high elevation snow patches may still contribute to discharge as illustrated in our case by the 20 % snow contribution in September before the first snowfall.

Interestingly, during the early season, stream δ^2H shows short diel variations, with a peak around 18:00 (Fig. 5.8a). Such variations are also observed in the later season, but with inverted fluctuations, so that lowest δ^2H values are then observed in the morning. In the early season, snowmelt δ^2H is lower than icemelt and has likely smoother discharge variations than icemelt due to the longer travel times and water retention in the snowpack. As a result, peak discharge is dominated by icemelt and therefore stream δ^2H points more towards the δ^2H of icemelt. In the late sea-

son, due to snow enrichment, snowmelt becomes isotopically heavier than icemelt so that, during peak discharge, the stream δ^2H still points towards icemelt, but in the other direction. Therefore, the moment of the inversion of these fluctuations indicates when snowmelt δ^2H becomes heavier than icemelt.

Several assumptions were made concerning the isotopic composition of the snowpack. For instance, we neglected any precipitation isotopic lapse rate since it could not be observed. This is supported by some studies reporting complex air flow above a high topography leading the air parcels to stagnate or even reverse, which modifies condensation and thus invalidates a direct relationship between elevation and a depletion of heavy isotopes in the water vapor (Galewsky, 2009). Such an absence of isotopic lapse rate trend, was also observed from precipitation data in Switzerland at high elevation especially in Winter (Kern et al., 2014). Nonetheless, at least one recent study by Carroll et al. (2022) provided a detailed description of multiple snow profiles with elevation. While they measured an isotopic precipitation lapse rate of -0.16 ‰ per 100m for δ^2H, they show no statistical differences with elevation in the snowpack bulk isotopic composition at peak snow accumulation. They attribute this behavior to the persistence of warm, enriched early winter snow at high elevation and different rates of snow accumulation and sublimation in winter.

Moreover, it seems that a trade-off exists between the isotopic lapse rate and the rate of enrichment due to vapor losses. Indeed, and as reported in other studies (Stigter et al., 2018), sublimation may increase at high elevation and lead to more snow enrichment, which counterbalance the lapse rate. In our model, best performance was found with a very limited sublimation factor (E_{frac}). This behavior is likely due to the choice of not using an isotopic lapse rate. Summer liquid precipitation isotopic lapse rate may also differ from winter and therefore closer to 0 in our case. Similarly, the precipitation lapse rate for summer rainfall amounts in summer is assumed to be similar to winter which may be erroneous. Some studies reported flat or even inverse lapse rates in the Swiss Alps above 2500 m asl (Schäppi, 2013). These uncertainties may introduce a bias in the estimation of the summer snowpack during ROS events. This is likely illustrated in our model in mid-July 2021 (Fig. 5.8a), where stream δ^2H appears slightly overestimated following a period of heavy snow and rain events.

In our model, the major snowpack enrichment mechanism is due to enriched summer snow fall, ROS and sublimation. Nonetheless, multiple studies (e.g. Taylor et al., 2001) have also reported liquid fractionation during melt as an important driver of isotopic enrichment. This process defined by Eq. 5.13 seems to play a minor role due to the rapid increase of the number of melt days (d_{melt}). While, we retained the original model from Ala-aho et al. (2017), the validity of this model could be further explored. In any case, all calibration parameters for liquid and vapor fractionation and for ROS point towards an enrichment of the snowpack, making accurate calibration difficult (Fig. 5.10).

We created a simple regression curve between air temperature and δ^2H of the precipitation to create an homogeneous snowpack. Due to the large spatial variability of δ^2H of surface snow, we cannot compare the performance of this approach, except from the observations of two snow pits. Carroll et al. (2022), provided a much more in-depth analysis using a similar approach and showed that, at peak snow accumulation, snowpack conserved well the δ^2H value corresponding to the air temperature of the precipitation and that the mean bulk snowpack δ^2H could be reasonably well estimated with a simple regression with air temperature.

5.5.2 Towards a better estimation of the isotopic composition of the snow

From the above discussion, it appears that reconstructing snowpack based on meteorological data and a mass-balance model is possible but large variations may arise from the definition of parameters as shown in Fig. 5.10. We suggest that bulk snow samples, estimating the average δ^2H of the snowpack is one prerequisite to validate this approach. At peak snow accumulation, Carroll et al.

(2022) showed relatively limited bulk δ^2H differences for about 13 snowpack profiles repeated during 4 years. This suggests that a limited number of bulk snow samples may be sufficient to calibrate or validate the winter isotopic model. Ideally, simple snow lysimeter could also be installed (Rücker et al., 2019b).

The behavior during the melt period remains likely more challenging, mainly because of the complex processes involved during ROS events. In our case, we relied on high resolution stream δ^2H data, which helped to constrain the snowmelt evolution by setting simple rules: snowmelt δ^2H should always be lower than stream δ^2H in the early melt season if there are strong evidence that snow is the more depleted end-member. For the late season stream δ^2H was less useful as snowmelt δ^2H was more enriched than icemelt. Additional bulk snow samples could better calibrate the model but snowpack sampling at high elevation may be compromised by difficult access.

From the results of the routing model, the delay between snowmelt and its arrival at the catchment outlet was usually lower than a day for the largest part of the flow, so that there was no clear differences in the estimated snowmelt δ^2H at catchment outlet whether using complex or simple routing based on the daily melt amount-weighted mean snowmelt δ^2H of all cells at the catchment-scale (Fig. 5.10). During rain events, routing allows improved smoothing of the signal, but relatively similar results could likely be obtained by applying a low-pass filter to the weighted mean snowmelt δ^2H data.

Therefore it seems possible to estimate the temporal evolution of the outlet snowmelt δ^2H based on mass-balance modeling (with necessary meteorological data) and snow observations only, without relying on discharge data which are required to create a routing model and usually difficult to acquire in such an elevated catchment.

5.5.3 The role of groundwater

The contribution from groundwater sources was not included in the model. To some extent, delayed lateral subsurface flow (Carroll et al., 2019) from elevated snowmelt transmitted through the hillslope is estimated by the routing model, but deeper bedrock exfiltration was not considered. Bedrock contributions may not be completely negligible as such storage has recently been discussed in Swiss Alpine glaciers (e.g. Müller et al., 2022a; Oestreicher et al., 2021). It is possible that a part of early snowmelt contributed to recharge the highly fractured bedrock and was redistributed towards the late melt season when snow cover is limited. Such recharge was discussed by Hood and Hayashi (2015), who estimated about 60 to 100 mm of storage, while Müller et al. (2022a) estimated a winter bedrock storage of about 40 mm with an unknown faster seasonal storage, potentially similar to Oestreicher et al. (2021), who estimated at total storage of 70 mm based on modelling and bedrock well observations. Potentially, such limited storage could be visible in Fig. B5d where the cumulative simulated discharge in the early season is about 50 mm larger than measured (Fig. B5d, cumulative discharge from 0 to 500 mm), which could be due to some snowmelt infiltrating in the bedrock and not routed to the glacier outlet. Later in the season, groundwater bedrock drainage leads to higher measured discharge as observed in Fig. B5d (cumulative discharge from 1000 to 1500 mm). This amount of storage falls however in the same range as the RMSE of the differences between observed and modelled SWE in 2021 (Fig. B6b), although the mean error is close to 0. This storage remains therefore in the statistical error margin of the model but could validate other independent analysis made in the catchment in a previous study (Müller et al., 2022a).

Stream EC was always larger than ice and snow melt EC and largely increased in winter, which also highlights the potential contribution of a groundwater reservoir. However, as clearly highlighted in some studies (e.g. Hindshaw et al., 2011; Sharp et al., 1995), subglacial weathering at the contact with the bedrock or sediments leads to an increase of solutes in the meltwater. Since EC is clearly not a conservative tracer, groundwater estimation with such a method may lead to much larger

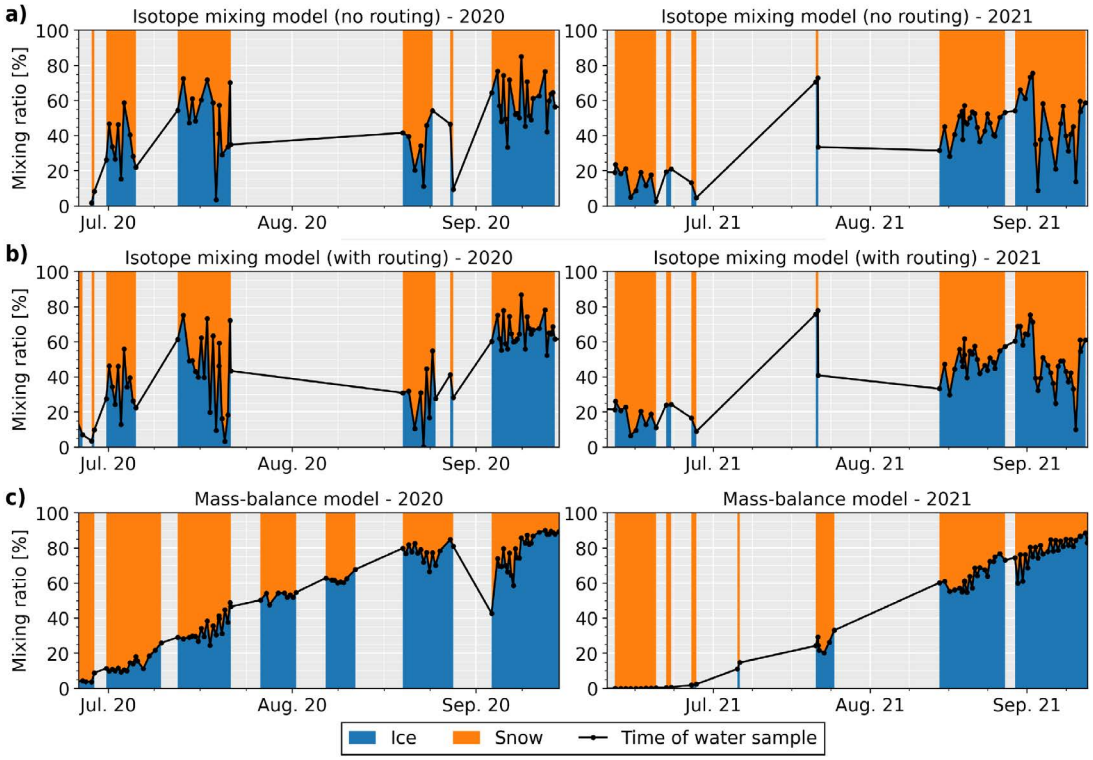

Figure 5.11: Mixing ratio between snow and ice melt when rain contribution is less than 5 %. **a)** Results based on snowmelt δ^2H estimated by a simple weighted-average of all model cell (without routing). **b)** Results when snowmelt δ^2H is routed to glacier snout. **c)** Results from the mass-balance and routing model without isotopes. Black points show when samples were taken.

uncertainty than what some studies may suggest, as weathering cannot be quantified easily. In any case, groundwater contribution should not largely impact the stream δ^2H, as bedrock leakages were found to be similar to icemelt (Fig. 5.3).

5.5.4 Mixing model limitations

In this research, we have proposed a way to better characterize the temporal evolution of snowmelt δ^2H. This method, especially if validated with more snowpack or snowmelt observations should contribute to limit uncertainties due to the spatio-temporal variability of the snow δ^2H. Nonetheless, even with such an approach, mixing results based on isotopes (Fig. 5.8b) appear very challenging. When rain is further involved, our results become unrealistic. We therefore provide an estimate of the ice and snow melt shares when we estimated a rain fraction of less than 5 % in Fig. 5.11. In that case, isotope results appear more coherent, but mid-season results still deviate significantly from the mass-balance results. No significant mixing differences can be observed with or without routing for snowmelt, which illustrates again that routing may not be necessary to estimate the snowmelt δ^2H.

It appears therefore that during the major part of the melt season, ice and snowmelt δ^2H values become similar in our catchment, so that uncertainties in the estimation of their δ^2H lead to large uncertainties in their shares. We suggest that separating ice and snowmelt with isotopes remains a very difficult task and a simple mass-balance approach likely leads to better results on a weekly-scale. Nonetheless, the stream δ^2H signal provides interesting insights in some of the internal mechanisms which modulate the glacio-hydrological response on a sub-daily scale and may contribute to develop more sound physically-based models. Outside of the main melt season, discharge becomes lower and other marginal sources of water, such as groundwater, may become more important and should not be neglected. We suggest however that using EC in highly

glacierized catchments results to an overestimation of its share if weathering rates are not taken into account in the subglacial drainage system.

5.6 Conclusion

This research aimed to address the challenging use of isotopes in glaciated catchments. As other studies highlighted the strong spatio-temporal variability in the water sources (e.g. Penna et al., 2017; Schmieder et al., 2016, 2018; Zuecco et al., 2019), we attempted to limit such uncertainties by developing a modeling framework building on the previous work of Ala-aho et al. (2017) and applying it to a case where snow and icemelt are the main sources. Our field results illustrate the large spatial variability in surface snowpack δ^2H, and we strongly suggest basing future work on bulk samples of the whole snowpack. We have proposed a complete methodology which allows to estimate the temporal evolution of snowmelt δ^2H by taking into account the main isotopic enrichment mechanisms. This approach needs to rely on a mass-balance approach, which requires additional data but can also benefit greatly from new satellite products. Certainly, one major challenge is the construction of an adequate regression curve between precipitation δ^2H and air temperature, since seasonal precipitation δ^2H samples are required. Snowmelt δ^2H estimation remains challenging in our case, due to a lack of validation of bulk snowpack δ^2H values but appears promising. In the case of glaciated catchments, snow enrichment leads to a snowmelt signal close to icemelt, making hydrograph separation using isotopes only very challenging and may not be advisable. We therefore lack other natural tracers for snow which are clearly conservative. The use of d-excess may offer additional information to separate snowmelt from other sources, especially for late more evaporated snowpack as suggested in the work of Michelon et al. (2023). Alternatively, mixing models based on hydrochemical analysis have been for example proposed (e.g. Baraer et al., 2015; Guido et al., 2016; Saberi et al., 2019), but the conservative nature of such tracers is questionable (subglacial weathering, elution of solutes). In none-glaciated catchments, the proposed approach may provide a way to limit uncertainties in mixing models. Finally, our glacio-hydrological model combined with stream δ^2H may provide interesting insights into the physical mechanisms of water routing and release. For instance, we showed that during rapid rain events, older pre-event water was preferentially released during the early hydrograph response, with a slower release of event water than observed in the hydrograph, suggesting the presence of a temporary storage which decreased over the season.

Finally, PEST-HP allowed detailed snow cover maps as calibration objective functions with similar weights as the SWE or ice ablation objective functions. Inclusion of such functions was found to be efficient in calibrating a simplified mass-balance model, even without calibration against stream discharge.

B Appendix

B.1 List of glacio-hydrological model parameters

Table B1: Glacio-hydrological model parameters with initial and calibrated values for years 2020 and 2021.

Model parameters	**Units**	**Initial value**	**Calib. 2020**	**Calib. 2021**
Mass-balance model parameters				
Temperature lapse rate (μ_{Δ_T})	[days]	150	144.8	128.4
Temperature lapse rate (σ_{Δ_T})	[days]	75	74.8	66.8
Temperature lapse rate ($f_{\Delta_T,\text{range}}$)	[°C per 100 m]	0.200	0.175	0.217
Temperature lapse rate ($f_{\Delta_T,\text{inc}}$)	[°C per 100 m]	0.350	0.323	0.370
Precipitation lapse rate (Δ_P)	[% per 100 m]	2.00	1.68	2.97
Snow precipitation factor ($f_{\text{corr,snow}}$)	[-]	2.0	1.94	2.36
Temperature melt threshold (T_{melt})	[°C]	1.0	1.05	0.98
Temperature factor ($f_{\text{melt,T,snow}}$)	[mm h^{-1} °C^{-1}]	0.130	0.113	0.114
Shortwave radiation factor ($f_{\text{melt,rad,snow}}$)	[mm m^2 h^{-1} W^{-1}]	3.5E-03	3.55E-03	3.65E-03
Temperature factor ($f_{\text{melt,T,ice}}$)	[mm h^{-1} °C^{-1}]	0.300	0.336	0.324
Shortwave radiation factor ($f_{\text{melt,rad,ice}}$)	[mm m^2 h^{-1} W^{-1}]	1.0E-03	3.05E-04	1.43E-04
Sublimation factor (E_{sp})	[°C h mm^{-1}]	8.00	7.73	11.81
Slope factor (f_θ)	[-]	1.25	1.31	1.33
Slope threshold ($\theta_{\text{accum,thresh}}$)	[°]	30.0	32.2	32.0
Radiation slope factor ($f_{\text{rad,slope}}$)	[-]	1.5	1.67	1.58
Radiation slope threshold ($\theta_{\text{max,rad}}$)	[°]	60.0	68.9	61.4
Radiation aspect factor ($\gamma_{\text{max,rad}}$)	[-]	3.00	1.243	2.667
Isotope model parameters				
Snowpack melt fractionation factor ($f_{\text{frac,sp}}$)	[‰]	8	8	8
Snowpack sublimation fractionation factor ($f_{\text{frac,E}}$)	[‰]	40	16	2
Rain on snow incorporation factor (f_{ROS})	[-]	1	0.5 to 1	0.5 to 1
Routing model parameters				
Hillslope dispersion coefficient ($D_{\text{hillslope}}$)	[-]	1	0.49	0.49
Hillslope hydraulic conductivity (K_s)	[m s^{-1}]	0.05	0.01	0.01
Channelised system dispersion coefficient ($D_{\text{channelised}}$)	[-]	1	5.72	5.72
Channelised system velocity ($v_{\text{channelised}}$)	[m s^{-1}]	0.80	0.85	0.85
Distributed system dispersion coefficient ($D_{\text{distributed}}$)	[-]	0.5	1.14	1.14
Distributed system velocity ($v_{\text{distributed}}$)	[m s^{-1}]	0.10	0.26	0.26
Snowpack dispersion coefficient (D_{sp})	[-]	1	2.39	2.39
Snowpack infiltration velocity (v_{sp})	[mm h^{-1}]	1200	5044	5044
Rain on snow dispersion coefficient (D_{ROS})	[-]	1	1.54	1.54
Rain on snow infiltration velocity (v_{ROS})	[mm h^{-1}]	1200	3847	3847
Slow reservoir response time constant (k_{slow})	[h]	40.0	96.0	96.0
Fast reservoir response time constant(k_{fast})	[h]	2.0	1.0	1.0
Slow reservoir fraction ($f_{\text{reservoir}}$)	[-]	0.5	0.43	0.43

B.2 Stream data

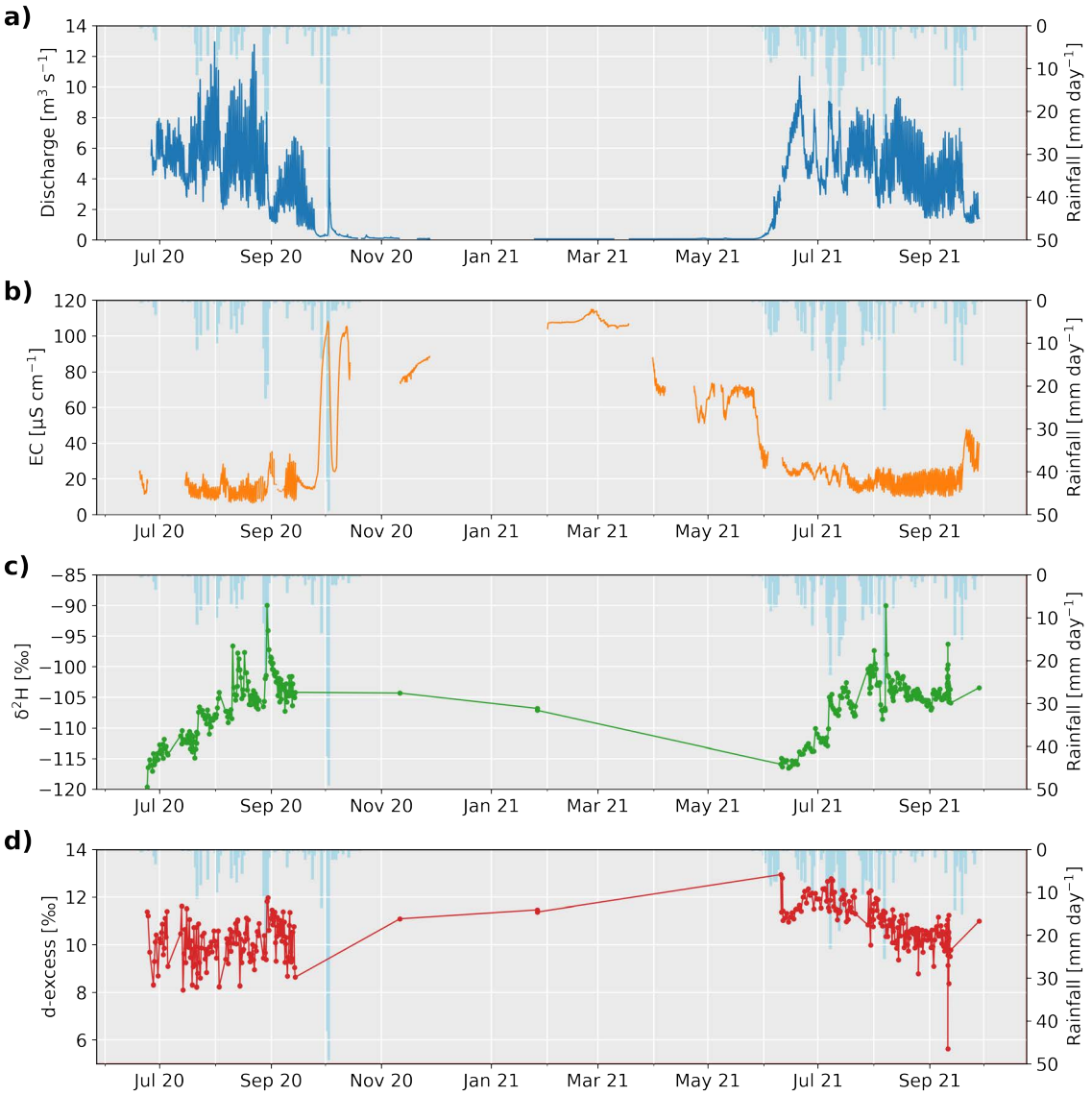

Figure B1: Observations performed from late June 2020 to mid-September 2021 in the glacial stream directly at the glacier outlet. **a)** Estimated discharge data based on stream stage and a discharge rating curve. **b)** Water electrical conductivity (EC). **c)** Water stable isotopes (δ^2H) observations with dots representing the date of the sampling (usually twice a day in summer). **d)** Corresponding isotopic d-excess. The inverted blue bars show the measured rainfall events measured at the weather station.

B.3 Snow and ice isotopes over time

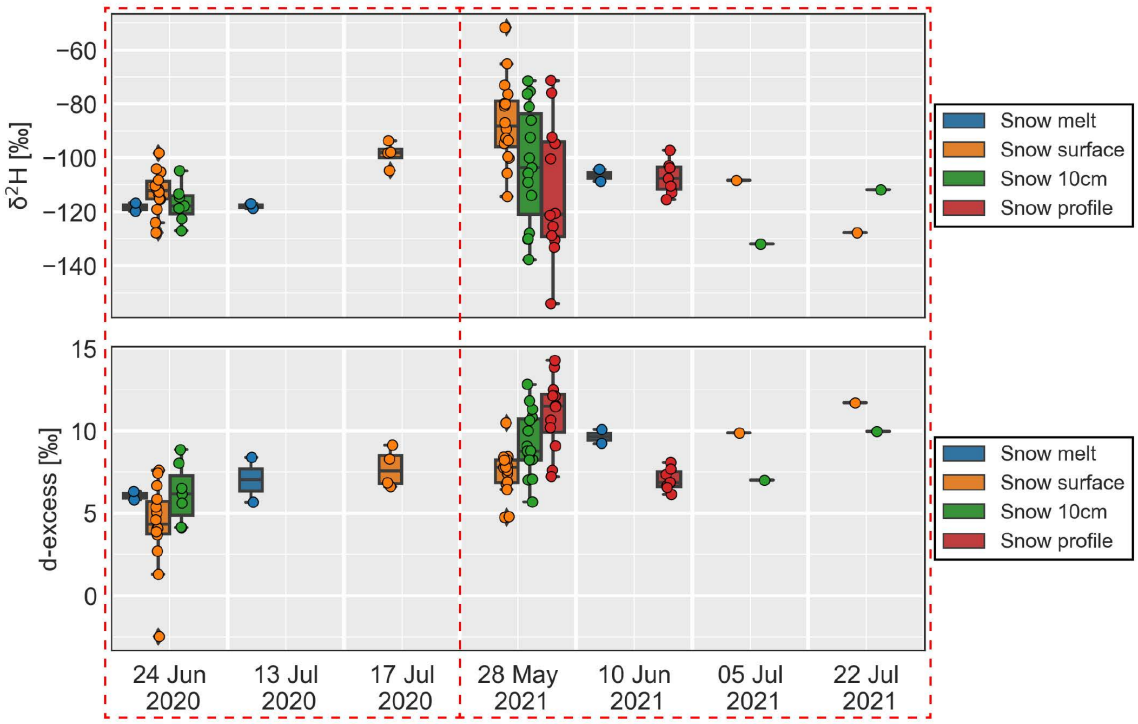

Figure B2: Temporal isotopic (δ^2H) and d-excess evolution of snow samples. Boxplots show each dates where the different types of snow samples were collected and dots show their distribution. The red dashed square separates each year of data.

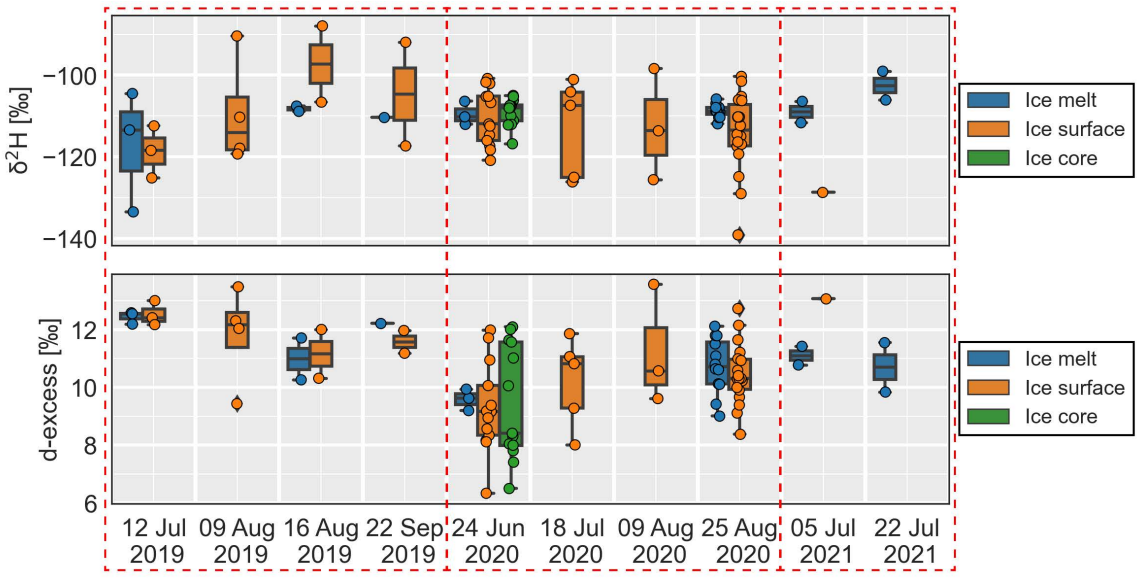

Figure B3: Temporal isotopic (δ^2H) and d-excess evolution of ice samples. Boxplots show each dates where the different types of ice samples were collected and dots show their distribution. The red dashed square separates each year of data.

B.4 Calibrated snow mass balance functions

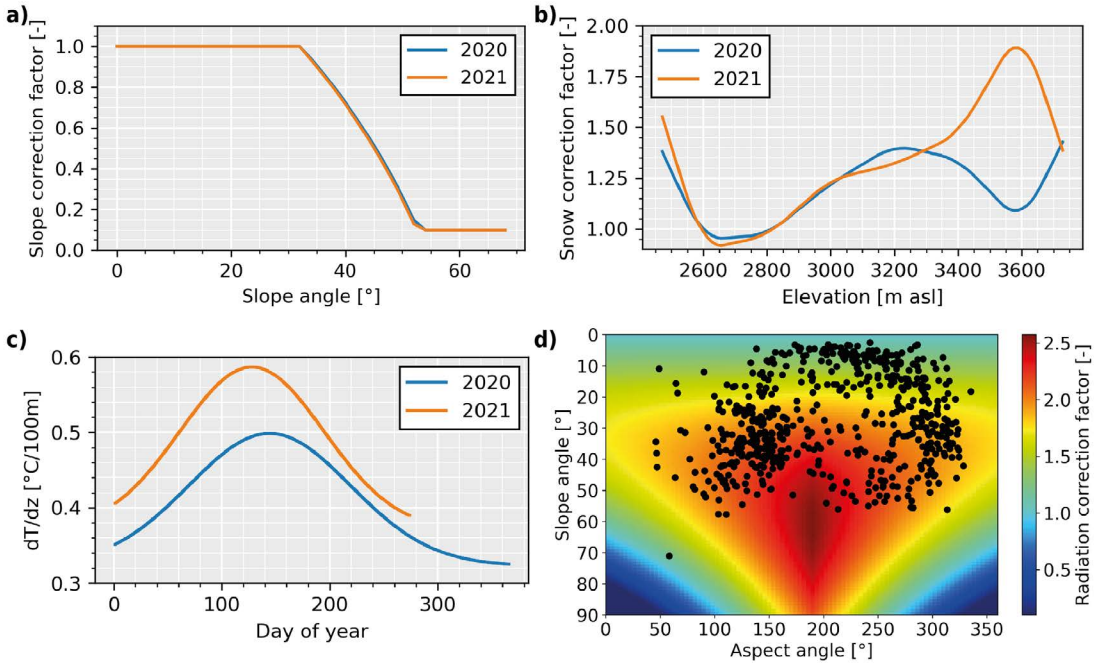

Figure B4: Results of the calibrated snow mass balance functions for year 2020 and year 2021 by PEST-HP. **(a)** Slope correction factor where snow reduction occurs when the terrain slope angle is higher than $L_{slope} \approx 32$ ° with a reduction rate $f_{slope} \approx 1.3$. **(b)** Corresponding snow correction function when slope is smaller than L_{slope}. Snow redistribution is estimated based on a simple relationship with terrain elevation. **(c)** Temperature lapse rate (dT/dz) calibration for both years. **(d)** Radiation correction factor based on terrain slope and aspect for year 2021. Black dots correspond to each cells of the model discretisation.

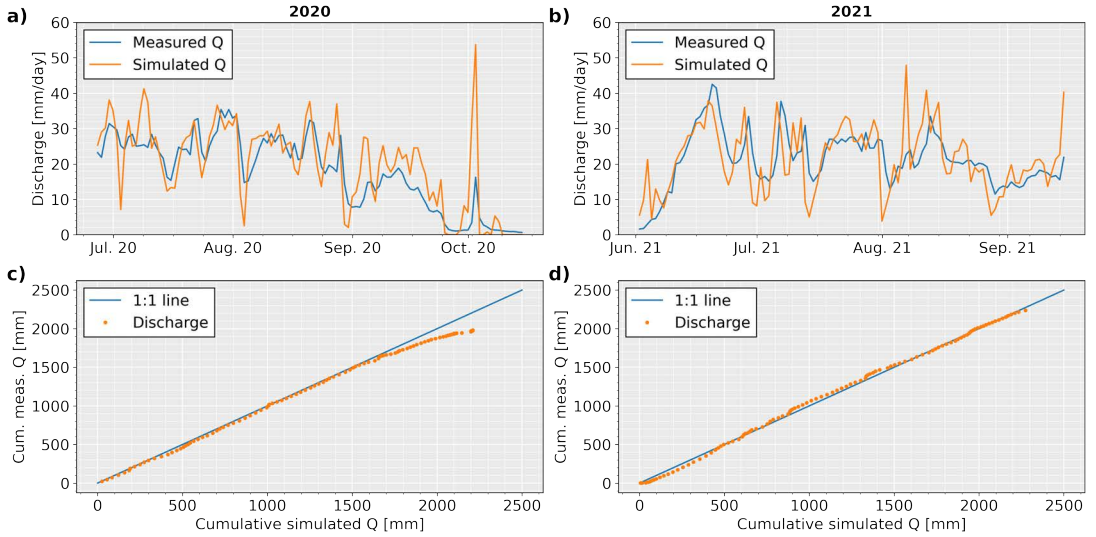

Figure B5: Simulated and measured total daily mass balance (rainfall, snowmelt, icemelt) for year 2020 **(a),(c)** and year 2021 **(b),(d)**. **(a),(b)** Daily total mass balance (simulated discharge) during both melt seasons and corresponding measured discharge at the glacier outlet. **(c),(d)** Comparison of the cumulative total mass balance (simulated discharge) and measured discharge at the glacier outlet. Q stands for discharge.

B.5 Simulated and measured snow and ice mass balance

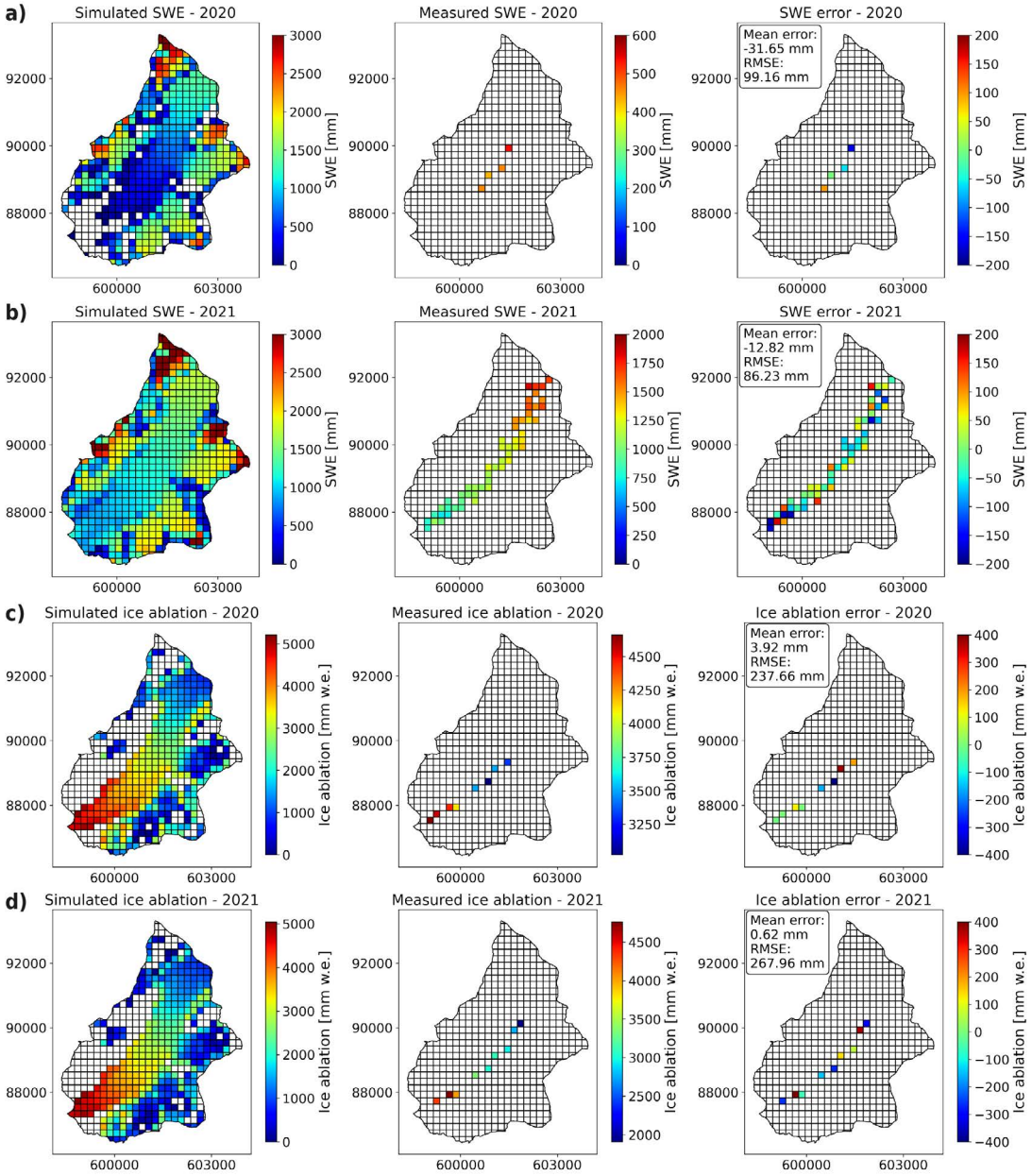

Figure B6: Simulated and measured snow mass balance for year 2020 **(a)** and year 2021 **(b)** and ice mass balance for 2020 **(c)** and 2021 **(d)**. Right figure shows the simulated mass balance with the corresponding year. The middle figure row shows the measured point mass balances. The third figure row shows the difference between measured and simulated mass balance. The corresponding mean total error and root mean square error for each map is also highlighted. Year 2020 correspond to the measurement date of the 29.06.2020 and year 2021 to the 28.05.2021.

B.6 Simulated and measured snow cover map

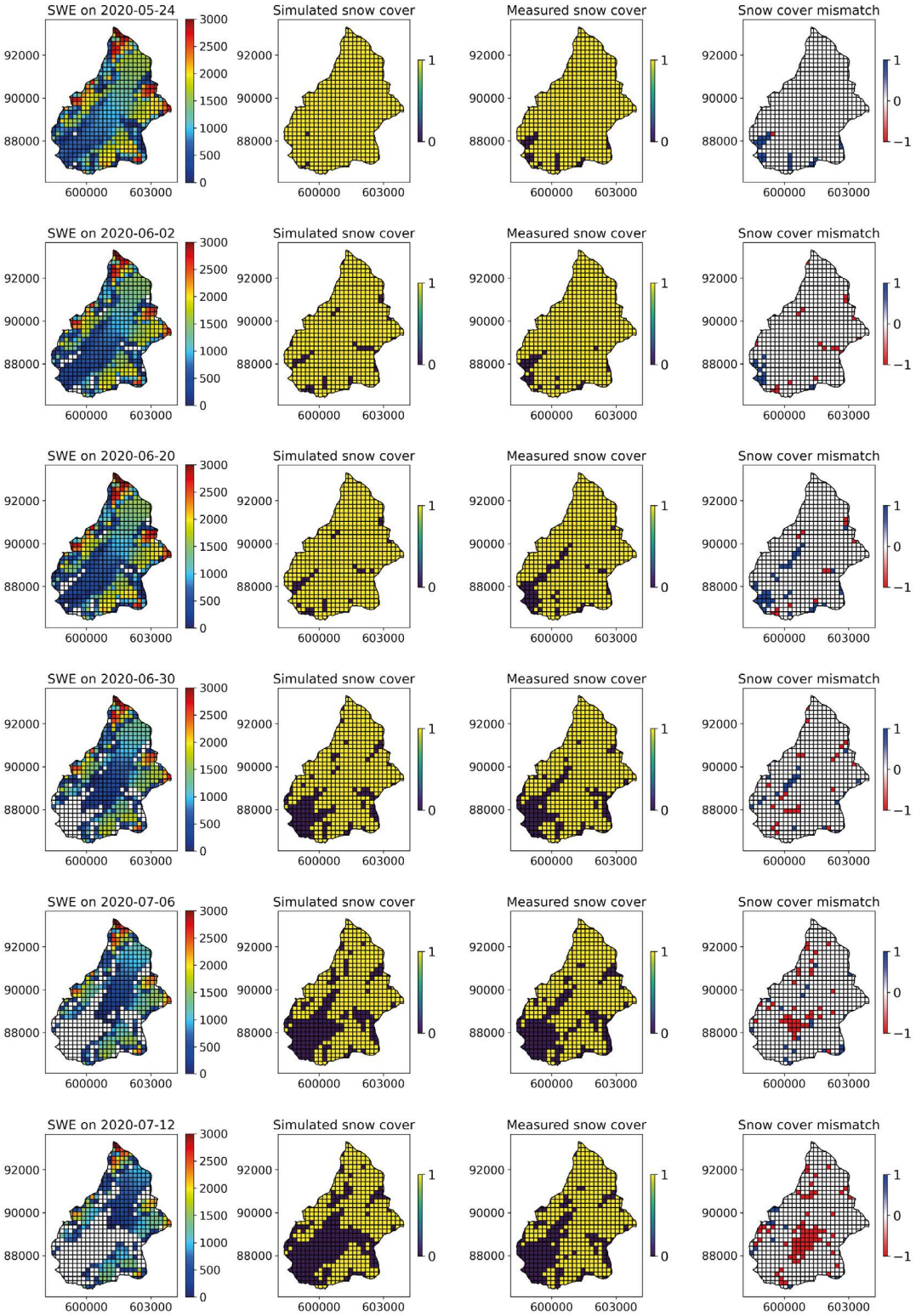

Figure B7: Simulated and measured snow cover map 2020 (part 1). Right figure shows the simulated SWE with the corresponding date. The second figure row shows the simulated snow presence (1) or absence (0) maps. The third figure row shows the measured snow presence (1) or absence (0) maps based on Planet satellite imagery. The last row shows the mismatch between measured and simulated snow presence and absence (1 for wrong simulated snow cover presence, -1 for wrong simulated snow cover absence). The figure lines show different dates as indicated on the SWE map titles.

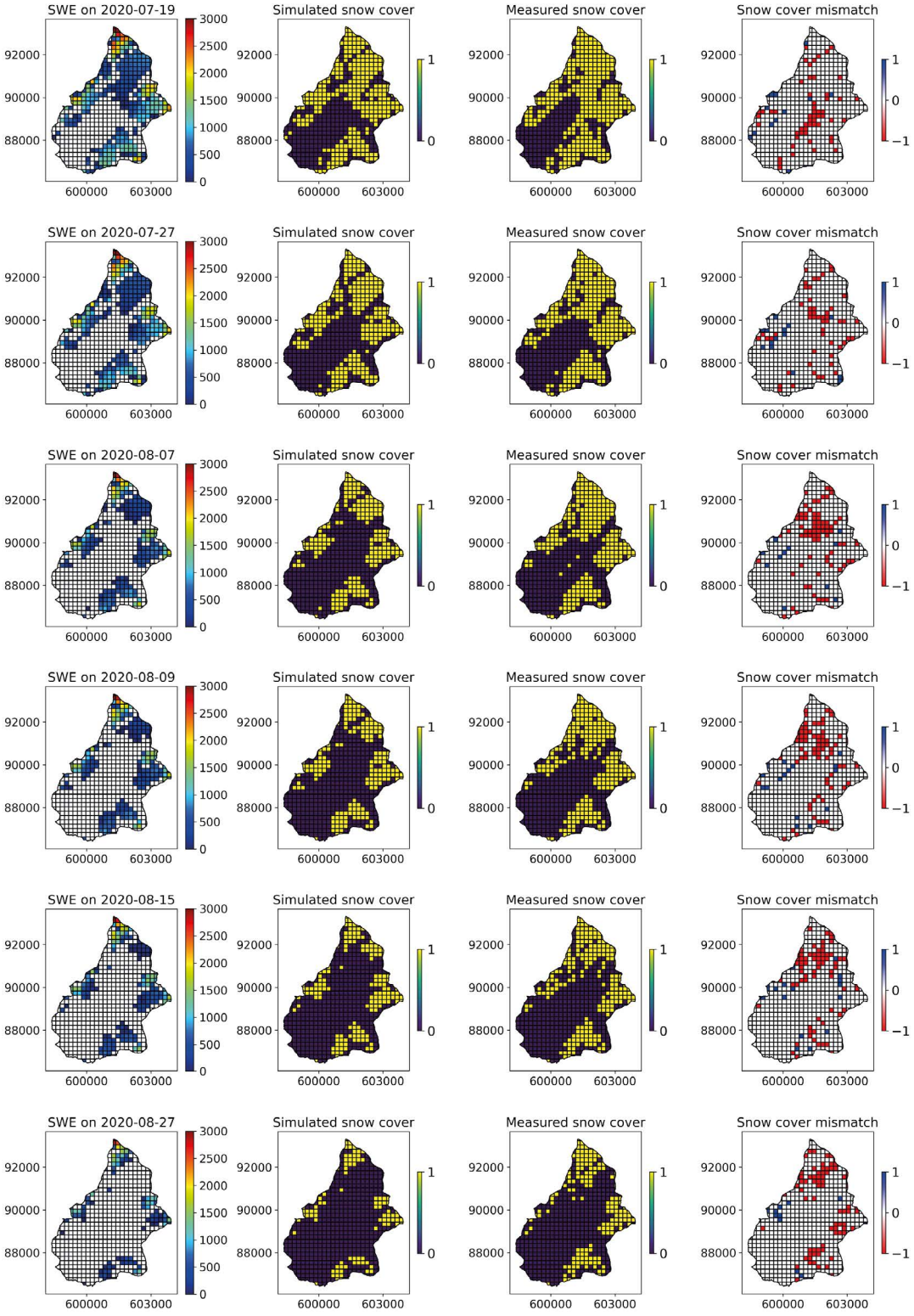

Figure B8: Simulated and measured snow cover map 2020 (part 2). Right figure shows the simulated SWE with the corresponding date. The second figure row shows the simulated snow presence (1) or absence (0) maps. The third figure row shows the measured snow presence (1) or absence (0) maps based on Planet satellite imagery. The last row shows the mismatch between measured and simulated snow presence and absence (1 for wrong simulated snow cover presence, -1 for wrong simulated snow cover absence). The figure lines show different dates as indicated on the SWE map titles.

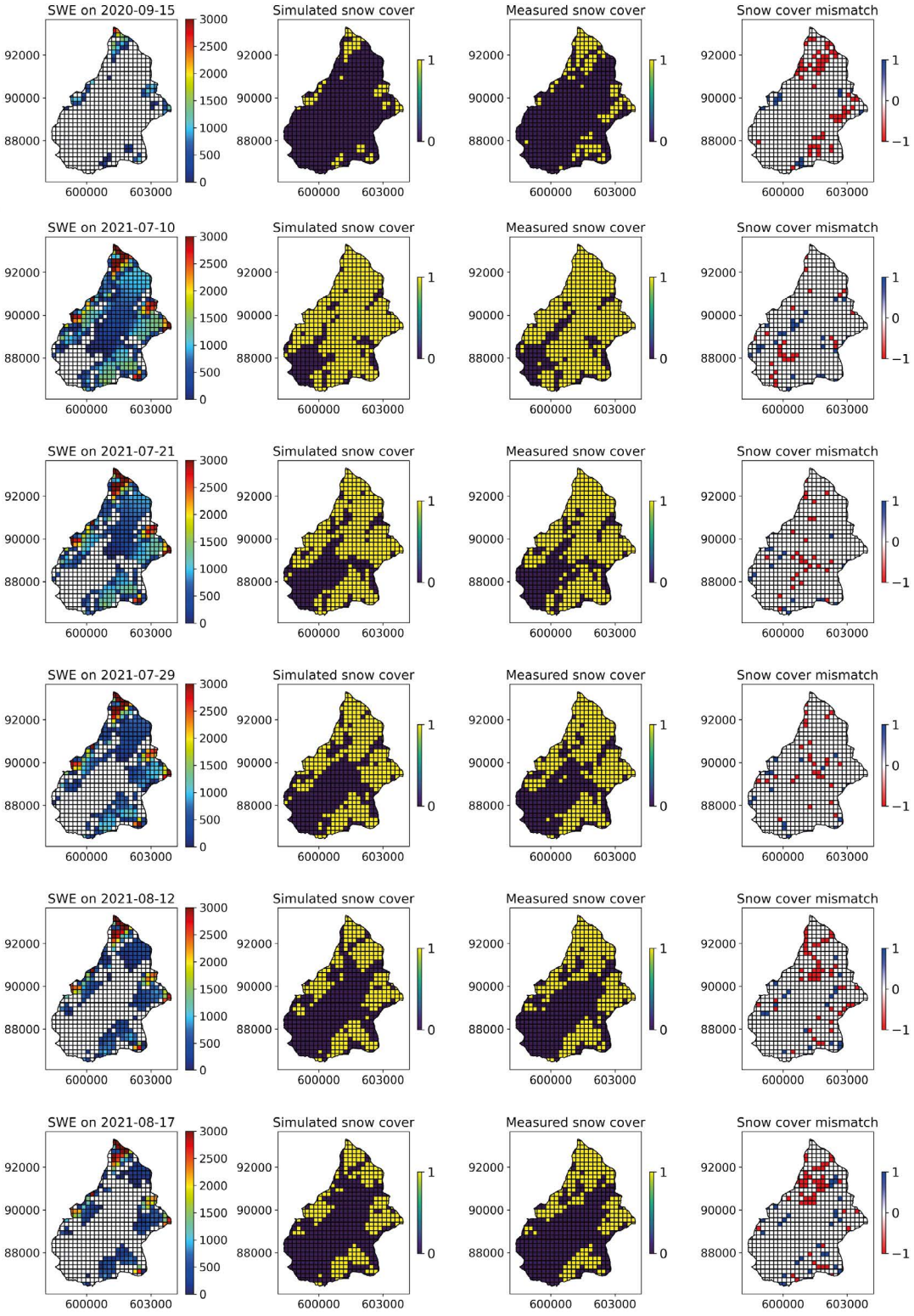

Figure B9: Simulated and measured snow cover map 2021 (part 1). Right figure shows the simulated SWE with the corresponding date. The second figure row shows the simulated snow presence (1) or absence (0) maps. The third figure row shows the measured snow presence (1) or absence (0) maps based on Planet satellite imagery. The last row shows the mismatch between measured and simulated snow presence and absence (1 for wrong simulated snow cover presence, -1 for wrong simulated snow cover absence). The figure lines show different dates as indicated on the SWE map titles.

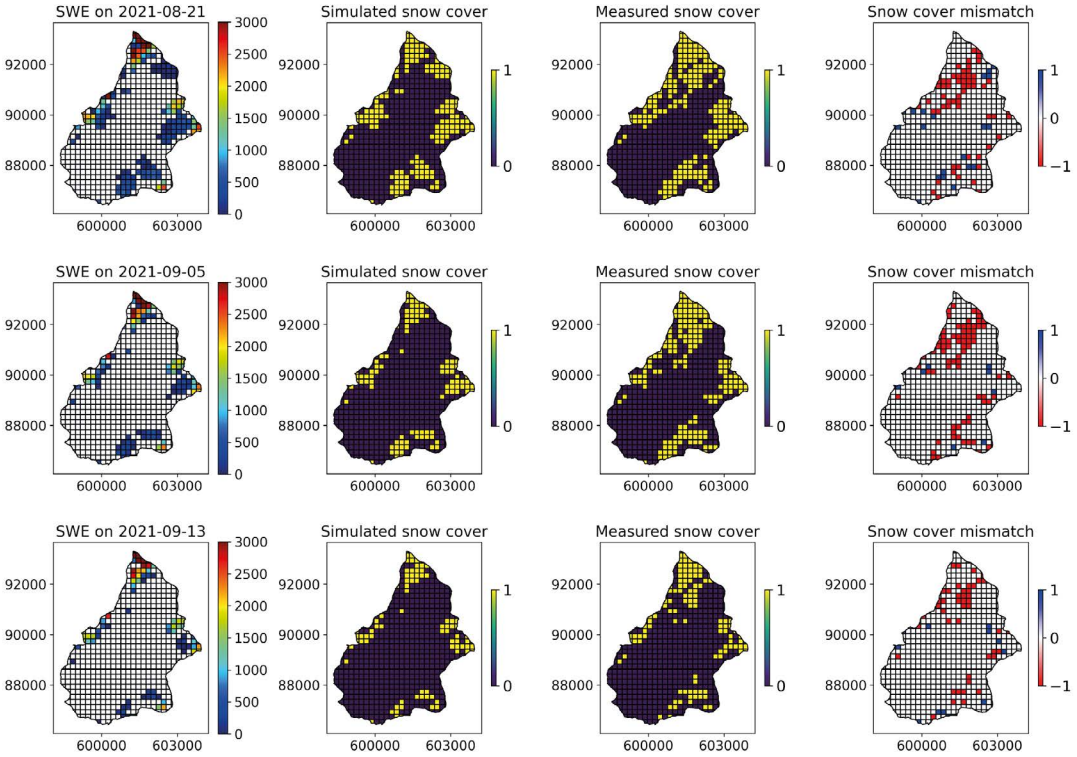

Figure B10: Simulated and measured snow cover map 2021 (part 2). Right figure shows the simulated SWE with the corresponding date. The second figure row shows the simulated snow presence (1) or absence (0) maps. The third figure row shows the measured snow presence (1) or absence (0) maps based on Planet satellite imagery. The last row shows the mismatch between measured and simulated snow presence and absence (1 for wrong simulated snow cover presence, -1 for wrong simulated snow cover absence). The figure lines show different dates as indicated on the SWE map titles.

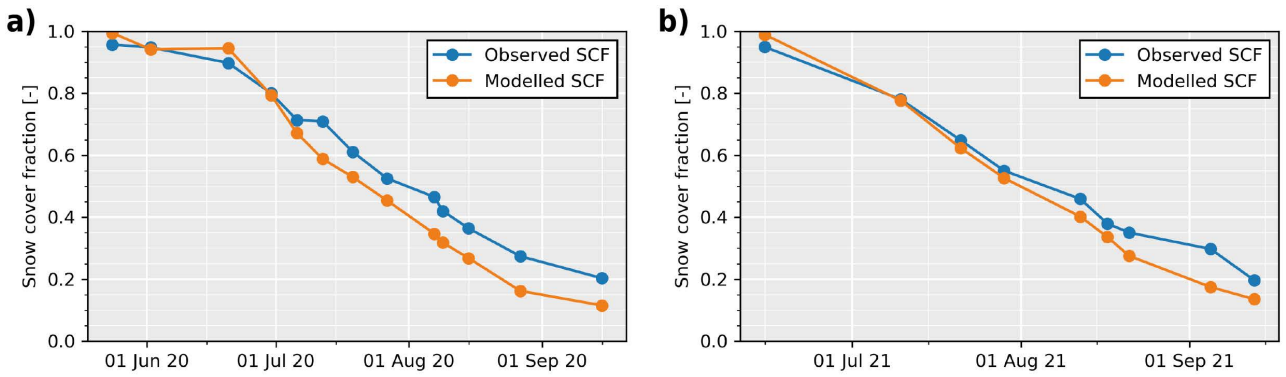

Figure B11: Simulated and measured snow cover fraction for **(a)** 2020 and for **(b)** 2021 based on observed snow cover from planet satellite imagery and as simulated by the mass balance model

Code data availability All isotopes data are available on Zenodo under (Müller, 2023). The codes for the glacio-horological model was written in python using Jupyter Notebook and are provided in the Supplement.

Author contribution T.M. conducted all the data collection and data analysis, produced all the figures and wrote the manuscript draft. B.S. proposed the general research topic and acquired the funding. S.L. and his team organised field work logistics. M.F. organized all mass-balance related field and first estimates of mass-balance. B.S. and S.L. jointly supervised the research. B.S., S.L. and M.F. edited the manuscript draft version. All authors have read and agreed to the current version of the manuscript.

Competing interests The authors declare that there is no conflict of interest. One co-author is a member of the editorial board of Hydrology and Earth System Sciences.

Acknowledgements T.M. and M.F. thank Vera Girod who was in charge of the field work in 2020 and Valentin Tanniger who carried out the dye tracing work. T.M. also thanks all bachelor, master and PhD students from the University of Lausanne who helped in data collection and in particular Floreana Miesen who organised field logistics and participated in field data collection on the Otemma glacier.

Financial support This research has been supported by the Schweizerischer Nationalfonds zur Förderung der Wissenschaftlichen Forschung (grant no. 200021_182065).

Figure 5.12: Picture of the bedrock outcrop above the outwash plain of the Otemma glacier at the top of the south-facing hillslope.

6

Research paper 4

Assessment of subglacial and proglacial groundwater connectivity using a multi natural tracers analysis in a highly glaciated catchment

Tom Müller[1,2], Anna Tassaux[1], Stephanie Grand[1], Stuart N. Lane[1], and Bettina Schaefli[1,2,3]

[1]Institute of Earth Surface Dynamics, Lausanne, University of Lausanne, Switzerland

[2]Institute of Geography (GIUB), University of Bern, 3012 Bern, Switzerland

[3]Oeschger Centre for Climate Change Research (OCCR), University of Bern, 3012 Bern, Switzerland

In preparation for publication.

This chapter explores groundwater connectivity in the proglacial and subglacial zone of the Otemma catchment. For this purpose, we mainly compare observations from three different types of natural tracers : i) water stable isotopes; ii) geochemical and EC data and iii) noble gases. Based on the previous chapters, we show that the nature of the most significant groundwater storage at a seasonal scale remains unclear. Moreover, while the modelling work highlighted the seasonal groundwater dynamics of the outwash plain, the relative contribution from hillslope recharge could be better estimated based on natural tracers. We therefore combine different natural tracers approaches to identify the signature of different groundwater compartments and assess how they affect groundwater storage in the outwash plain or in the stream composition at the glacier outlet. While each method shows clear limitations, their combined interpretation, compared with results from the previous work, allows to propose a perceptual model of a coupled bedrock-subglacial groundwater system. This last chapter finally allows to evaluate the results from the previous works with a more direct approach and contributes to a more integrated understanding of the current hydrogeological functioning of a typical highly glaciated catchments.

6.1 Introduction

Water hydrogeochemical composition has been widely used in Alpine environments to trace water flowpaths (Carroll et al., 2019; Ward et al., 1999), to develop mixing models (Baraer et al., 2015; Carroll et al., 2018) or as an indicator of early-stage biogeochemical interactions, rock weathering and soil development (Malard et al., 1999; Tockner et al., 2002). However, due to complex geologies and landforms, sources of groundwater are usually highly heterogeneous in an Alpine context, which makes end-member definition challenging and may lead to significant uncertainty in the results interpretation (Kiewiet et al., 2019; Zuecco et al., 2019). Some studies have assumed that geochemical tracers are conservative in some Alpine environments due to the crystalline nature of many areas and due to limited biological processes, which leads to relatively slow chemical weathering, especially compared to carbonate rock environments (e.g. Engel et al., 2016; Penna et al., 2017). This assumption has, however, been disproved by several studies that have documented a rapid increase in major ions due to the high suspended sediment load in glacial streams (Mitchell et al., 2001; Sharp et al., 1995) and due to the strength of abrasive processes subglacially (Łukasz Stachnik et al., 2022).

Secondly, recent work on noble gases have shown its potential to quantify the sources of groundwater recharge, especially for floodplains (Popp et al., 2019, 2021b). While laboratory analysis of such gases is complex, new portable mass spectrometers have been developed to provide continuous and direct measurements in the field (Brennwald et al., 2016; Popp et al., 2021a). Recently, such a system was successfully applied to a Quaternary alpine floodplain in Canada to assess groundwater recharge from snow melt (Schilling et al., 2021). In 2021, we deployed such a portable mass spectrometer in three groundwater wells in the outwash plain of the Otemma glacier (South-Western Switzerland) and present here preliminary results.

In this context, the main objectives of this work are : i) a detailed analysis of groundwater flowpaths and connectivity between landforms based on multiple tracers and previous observational and modelling work in the catchment (Müller et al., 2023; Müller et al., 2022a); ii) a synthesis of the complementary of the studied tracer in similar environments. The natural tracers studied here can be separated in three main groups : i) stable isotope compositions of water; ii) hydrogeochemical analysis of major ions and trace elements; iii) noble gases. We first provide an overview of the water composition in various landforms of the Otemma catchment and attempt to identify potential suitable tracers in order to better constrain the origin and amount of groundwater recharge in different parts of the catchment. More specifically, the analysis focuses in more detail on the groundwater connectivity of the outwash plain with the glacial stream and with the hillslopes and underlying bedrock; we furthermore embed these results in our previous model-based results Müller et al. (2023). Secondly, we attempt to provide a more complete perceptual model of subglacial groundwater storage and conductivity compared to the first version proposed in the work of Müller et al. (2022a), where we identified a missing groundwater storage in winter of the order of 40 mm, possibly due to bedrock or subglacial storage.

6.2 Methods

6.2.1 Location of water samples

Samples were collected from July 2020 to October 2021; the sampled water belongs to four categories: i) stream water at the discharge gauging station 1 (GS1) near the glacier snout and GS2 at the downstream end of the outwash plain; ii) 9 groundwater wells in the outwash plain (A2 is right next to Trib4); iii) 5 tributaries which drain hillslope water on the southern slope; iv) water exfiltrating from the bedrock outcrop in a small bedrock cavity (Fig. 6.1).

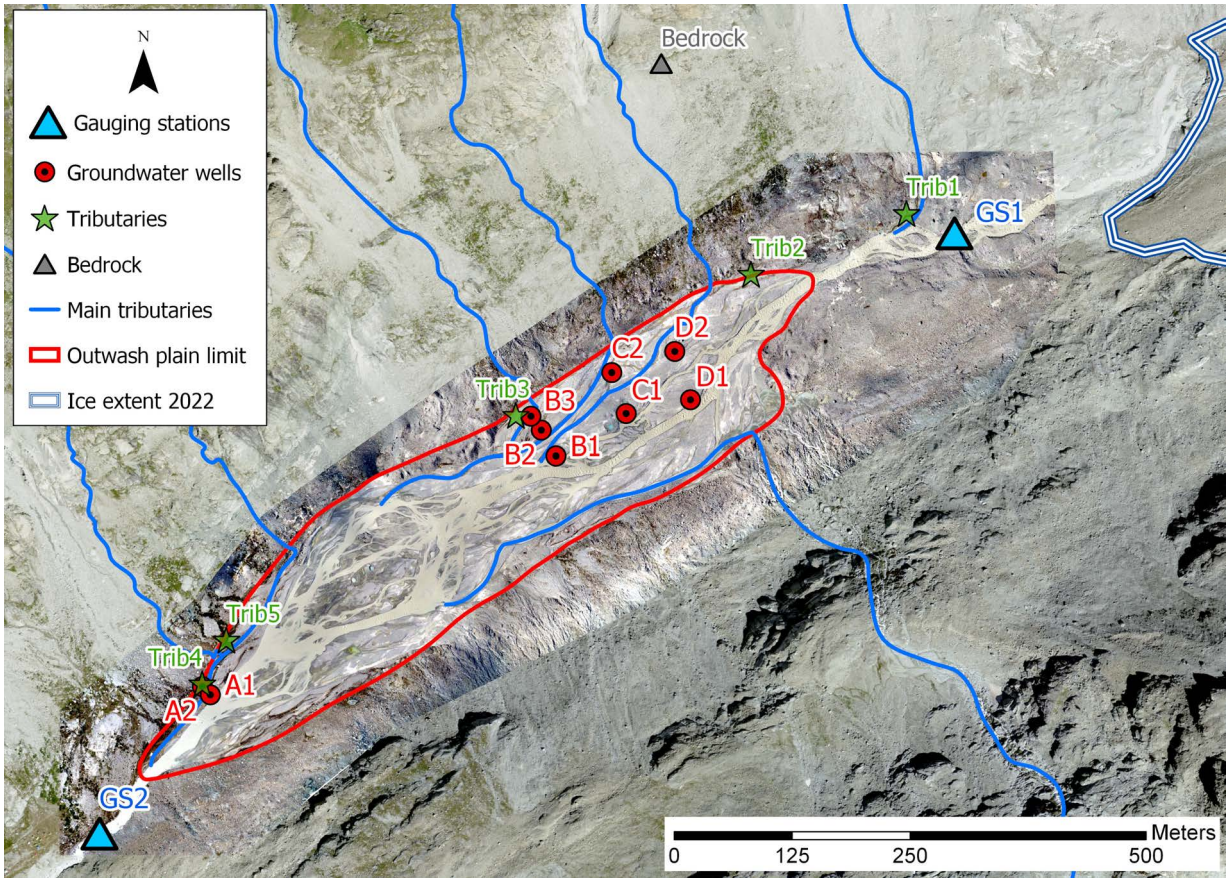

Figure 6.1: Overview of the sampling locations in the Otemma glacier forefield. Shown are also the main seasonal tributaries and the edge of the glacier snout. The background orthoimage was provided by SwissTopo (2020a).

6.2.2 Electrical conductivity and water stable isotopes

Water electrical conductivity (EC) and water stable isotopes (δ^2H) were measured on water sampled following the same approach as discussed in Chapt. 5. In 2020, hillslope tributaries were sampled every day around 18:00. Outwash plain groundwater was sampled about once a week. In 2020, most values of d-excess appear to vary randomly to a much larger degree than in 2021. This is especially visible for stream samples (Fig. C2). These variations in d-excess are likely due to a slight vapor loss which caused some fractionation in the vials during storage, which affected the d-excess values. D-excess data of 2020 are therefore not interpreted. This slight vapor loss did however likely not affect δ^2H values significantly, as, for example, the δ^2H values along three stream gauging station appear always very similar.

6.2.3 Hydrogeochemical analysis

Hydrogeochemical samples were collected around once a month in 2020 and twice a month in 2021 at similar locations as EC and δ^2H. Samples were collected in plastic bottles and directly filtered with 0.45 μm cellulose acetate filters and then maintained near 0 °C until transport in the lab, usually about one or two days later. Major ions were measured with an ion chromatography (IC Metrohm) at a precision of 0.1 ppm. Trace elements were measured with an ICP-MS Quadrupole spectrometer (Agilent 7700), with a precision of 0.01 ppm. Finally in 2021, we also measured total organic carbon (TOC) and inorganic carbon IC using a TOC analyzer (TOC-L Shimadzu). More details about the procedure can be found in the master thesis of Tassaux (2022) who collected and analyzed the samples in 2021.

In 2020, due to other standards and machine calibration, the precision of the analysis was about an order of magnitude weaker than in 2021. Due to the low concentrations in glacial water, many

$$\text{Plagioclase weathering}: Na_{0.4}Ca_{0.6}Al_{1.32}Si_{2.68}O_8 + 1.32H_2CO_3 + 0.66H_2O \longrightarrow 0.4Na^+ + 0.6Ca^{2+} + 1.32HCO_3^- + 1.36SiO_2 + 0.66Al_2Si_2O_5(OH)_4 \quad (6.1)$$

$$\text{Carbonate weathering (calcite)}: CaCO_3 + CO_2 + H_2O \longrightarrow Ca^{2+} + 2HCO_3^- \quad (6.2)$$

$$\text{Sulfide oxidation (pyrite)}: FeS_2 + 3.75O_2 + 2H_2O \longrightarrow 4H^+ + 2SO_4^{2-} + 0.5Fe_2O_3 \quad (6.3)$$

trace elements were therefore below the limit and could not be measured. In 2021, some data are not reliable due to some confusion during the analysis in the laboratory. Data are presented here as it is and appear most of the time logical, although some samples show exceptionally high or low values while other locations showed no specific behavior. The data from 2021 should therefore be interpreted with care, keeping in mind some potential analytical errors resulting in wrong values.

The Otemma catchment is mainly characterized by silicate rocks with a mix of orthogneiss, metagranodiorite and metagabbro. The average mineralogy was measured by (Tassaux, 2022) and shows a large dominance of quartz, plagioclase, K-feldspar, Mg-Fe hornblende, biotite and amphibole in varying proportions based on the moraine deposits. Pyrite was also observed through a binocular microscope. Metagabbro was composed of 8 % of calcite.

Based on the methodology of the Master thesis research of (Tassaux, 2022) and the work of (Anderson et al., 2000), three main types of water-rock weathering processes are responsible for the dissolution of solutes. In alpine environments, due to cold temperature, silicate weathering is limited (Anderson, 2007) but typically involves the incongruent dissolution of plagioclase feldspar. Equation 6.1 was adapted from Anderson (2007) to represent the plagioclase composition of the Otemma catchment (40 % albite, 60 % anorthite). The Otemma catchment lithologies are dominated by silicate rocks, but traces of carbonates may rapidly lead to a dominant dissolution of calcite in the meltwater (Eq. 6.2) as reported in other alpine studies (Anderson et al., 2000; Mitchell et al., 2006). Finally, sulfide oxidation of pyrite (Eq. 6.3) was also shown to occur and is especially enhanced by the physical weathering of mineral grains in subglacial sediments (Łukasz Stachnik et al., 2022). Pyrite oxidation leads to a decrease of the pH, which has been shown to also enhance calcite dissolution (Shukla et al., 2018).

It should be noted that weathering of plagioclase feldspar (anorthite) is likely the major source of calcium in the Otemma glacier forefield, as suggested in others silicate-dominated catchments (Anderson et al., 2000). However, other minerals may also lead to silicate weathering of other feldspars such as potassium silicates (K-feldspar), which releases $K^+$and finally biotite and hornblende, which may be a source of Mg^{2+}, F^-or SO_4^{2-}.

Based on all samples collected between 2020 and 2021, we performed a standard principal component analysis (PCA) (Mitchell et al., 2006). Following this analysis, we identified groups of similar ions and then focused our analysis on these solutes only, as they represent the main weathering processes contributing to solutes dissolution.

6.2.4 Noble gases

We installed in August 2021, a gas-equilibrium membrane-inlet portable mass spectrometer (GE-MIMS) (Brennwald et al., 2016) in groundwater wells B1, B2 and B3. The instrument measured dissolved noble gases (He, Ne, ^{40}Ar, Xn, ^{84}Kr) in water and air, as well as N_2, CO_2, O_2, H_2. The GE-MIMS was connected to three Geopump^{TM} Peristaltic Pumps with 10 mm silicon tubes, which ensured no air exchange before analysis. The whole system was powered by a solar system to ensure continuous recording day and night. Each well was sampled around every one to two hours. Due to several technical difficulties, the GE-MIMS only ran properly from 23 August to 11 September 2021.

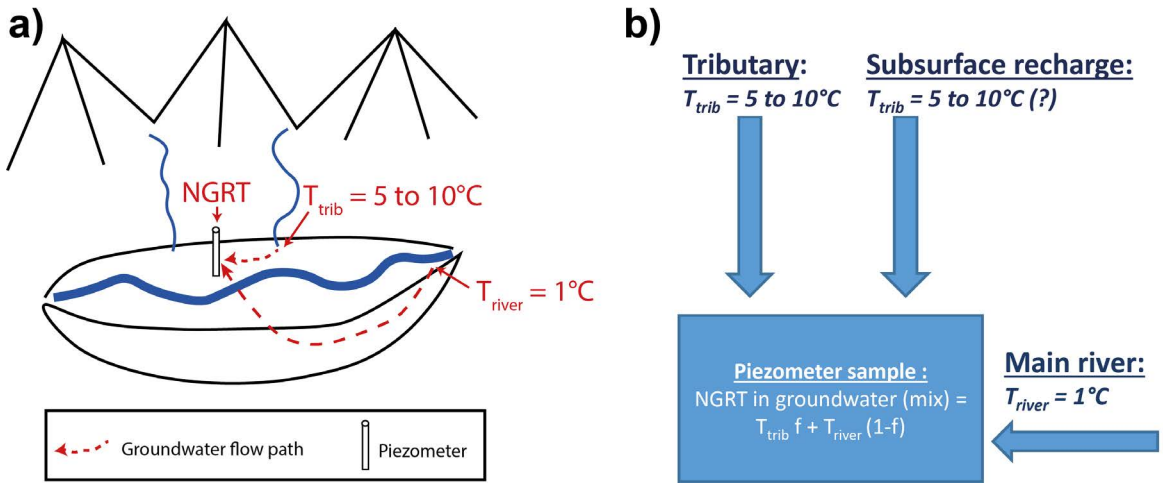

Figure 6.2: Illustration of the NGRT methodology. **a)** Simple illustration of the outwash plain with two different flow-paths, either from the hillslope or from stream infiltration. **b)** Simple two components mixing model based on water temperaturs at their respective point of infiltration in the aquifer. f represents the fraction of hillslope recharge.

Similarly to the work of (Schilling et al., 2021), we attempted to estimate hillslope recharge in the outwash plain by estimating the Noble Gas Recharge Temperature (NGRT). This method assumes that noble gases dissolved in a water body in contact with air are at equilibrium and their concentration can be estimated with suitable conservative natural tracers. This estimation relies on Henry's law, where the Henry coefficient relates linearly the concentration of dissolved gases in water to the partial pressure in the air. This coefficient mainly depends on water temperature and atmospheric pressure so that the concentration of noble gas air-saturated water (ASW) can be estimated at the point of infiltration and percolation into the groundwater (Schilling et al., 2021), assuming that there is no further gas exchange thereafter. By comparing the relative concentrations of pairs of noble gases, a theoretical line corresponding their ASW concentrations at different recharge temperatures can be drawn. Higher gas concentration may however occur if air bubbles become entrapped in the groundwater during recharge or due to variations in groundwater levels. To account for such excess air, we followed the same methodology as in the work of Schilling et al. (2021) and used the simple model for unfractionated excess air (UA) (Kipfer et al., 2002).

In the case of the outwash plain aquifer in the Otemma glacier forefield, recharge mainly occurs from either upstream water infiltration or from surface or subsurface hillslope runoff. The NGRT in this fluvial aquifer should thus represent a mix of the recharge water temperature of these two sources. It is therefore possible to establish a simple two component mixing model to estimated the fraction of hillslope recharge compared to stream water infiltration (Fig. 6.2).

In addition to the above water source tracing based on recharge temperatures, noble gases can be used for dating. The isotopes of Helium (^{4}He and ^{3}He) are produced by the radioactive decay of ^{3}H, U or Th (Popp et al., 2019). The ratio of ^{3}H/^{3}He has been typically used to date relatively young water (>50 years), but laboratory analyses are complex and costly (Kipfer et al., 2002). Recent work has shown that ^{4}He, which can be measured in-situ with the GE-MIMS, is strongly correlated with ^{3}H/^{3}He and thus with water age (Moeck et al., 2021). This would allow to estimate spatio-temporal water age variations more easily with the GE-MIMS than previously with lab analyses. The correlation is, however, site-specific and accordingly, reference analyses of ^{3}H/^{3}He are required. In the context of this work, we measured ^{4}He in the field, but we do not have concomitant laboratory analyses and can thus not proceed to water age dating. Nevertheless, an increase of the ^{4}He concentration compared to the estimated ASW concentration would indicate a significant contribution from an older groundwater.

6.2.5 Mixing model of subglacial EC variations

Based on the observations based on the geochemical analyses, we propose to build a simple mixing model based on 3 reservoirs and EC in order to estimate the discharge from the baseflow component Q_{base}. The first reservoir corresponds to the subglacial till contribution. Since no direct EC measurements of subglacial till water are possible, we used the maximum measured stream EC in winter at GS1 as an approximation. The second component is the subglacial water transiting through the distributed part of the glacier system. There, water flows slower than in the channelized part and EC increases to some extent due to weathering (Sharp et al., 1995). The third reservoir represents fast channelized flow where only limited weathering occurs. To estimate the relative discharge from the distributed (Q_{dist}) and from the channelized (Q_{chann}) subglacial components, we use the early-summer maximum and minimum daily discharge (Q_{init}) as an estimate of the the contribution from the distributed system and assume no discharge from the channelized system during this period.

Then, we estimated the fraction of the channelized system (f_{chann}) by using the length of the channelized network divided by the total glacier length (d_{glacier}) based on the previous results of the glacio-hydrological model of Chapt. 5. There we used the (modelled) mean snowline distance from the glacier terminus (d_{snowline}) as a proxy for the channelized system evolution (Eq. 6.4). We use this fraction to estimate the decrease of the distributed discharge during the melt season (Eq. 6.5). Similarly, we defined the end-of-the-season maximum and minimum daily discharge (Q_{end}) as the discharge of the channelized system (Eq. 6.5) and multiply it with f_{chann} (Eq. 6.6). Finally, we calculate stream EC based on the three discharge components and their respective EC values (Eq. 6.7). The EC of the distributed and channelised system as well as of the baseflow are calibrated manually in order to match the observed stream EC. EC is assumed to be constant during both low flow and high flow. The equations below were applied both for high flow and low flow for Q.

$$f_{\text{chann}} = \frac{d_{\text{snowline}}}{d_{\text{glacier}}} \tag{6.4}$$

$$Q_{\text{dist}} = (1 - f_{\text{chann}}) Q_{\text{init}} \tag{6.5}$$

$$Q_{\text{chann}} = f_{\text{chann}} Q_{\text{end}} \tag{6.6}$$

$$EC_{\text{stream}} = \frac{Q_{\text{chann}} EC_{\text{chann}} + Q_{\text{dist}} EC_{\text{dist}} + Q_{\text{base}} EC_{\text{base}}}{Q_{\text{chann}} + Q_{\text{dist}} + Q_{\text{base}}} \tag{6.7}$$

6.3 Results

6.3.1 Electrical conductivity and stable isotope compositions of water

Boxplots of all EC, δ^2H and d-excess measurements are provided in Fig. C1. Overall, δ^2H values of all samples in the catchment are within the range of the values for snowmelt. Only rain samples show significantly different values. EC shows large variations, especially in the piezometers in the outwash plain. Ice and river samples have a higher median d-excess, around 11, likely due to significant condensation or refreezing at the contact with ice, which leads to an isotopic depletion of heavy isotopes of the residual water (Beria et al., 2018). Snow melt shows the opposite behavior, with a d-excess closer to 8, due to evaporative or melt-related fractionation. The temporal evolution of corresponding data for stream water is illustrated in Fig. C2.

Based on the results of the EC and δ^2H analysis from the hillslope tributaries (Fig.6.3), three main classes of runoff can be identified. The first class consists of bedrock-fed tributaries and includes Tributary 2 and 5. They are characterized by relatively constant EC and δ^2H values during the whole snow-free season, with only slight increases of δ^2H (and synchronous decreases in EC) in

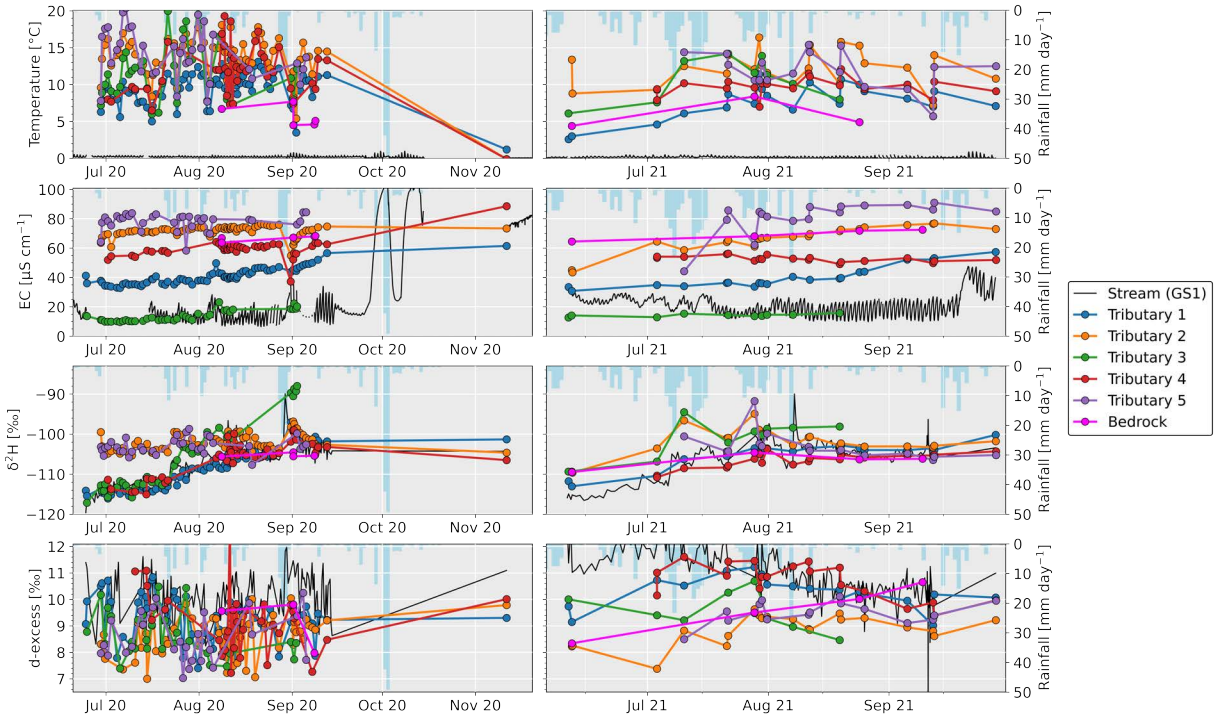

Figure 6.3: Evolution of hillslope tributaries temperature, EC, δ^2H and d-excess for year 2020 and 2021. The signal of the bedrock leakages as well as the stream at GS1 are also provided for comparison. The inverted blue bars represent measured daily rain amounts.

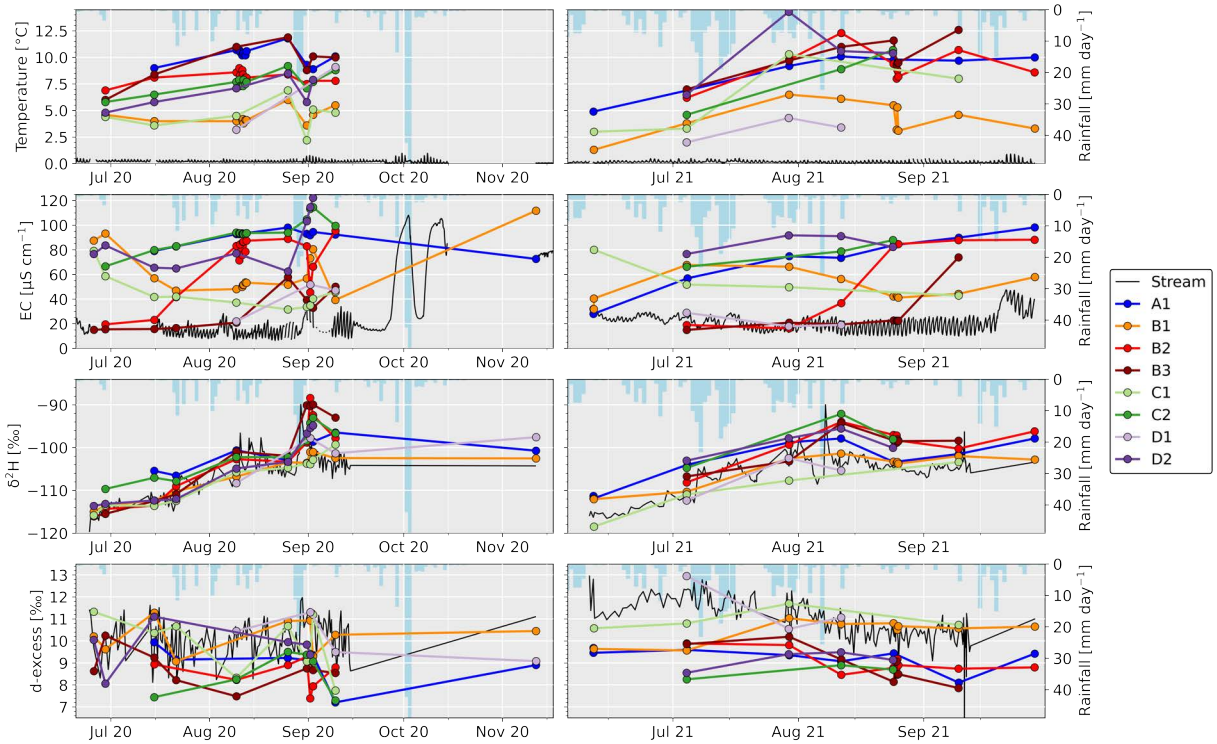

Figure 6.4: Evolution of outwash plain groundwater temperature, EC, δ^2H and d-excess for year 2020 and 2021. The signal of the stream at GS1 is also provided for comparison. The inverted blue bars represent measured daily rain amounts, in mm.

response to rain events. These tributaries appear to have very similar values to those of the samples from the bedrock outcrop, which also showed little change over time. The lack of seasonal variability of the bedrock water (median δ^2H of -105.5 ‰ and EC of 68 μS cm^{-1}) indicates a sig-

nificantly long storage inside bedrock fractures, which significantly dampened yearly variations in EC and δ^2H. Only in June 2021, bedrock δ^2H and EC was slightly lower, and d-excess also increased during the melt season in 2021, which seems to indicate a larger influence of snowmelt in the early season and slightly more rain recharge in the late summer season. Stream flow, although limited to a few liters per second, was relatively constant for both tributaries. Both tributaries emerged from the morainic sediments at the base of the outwash plain. Accordingly, we might a priori assume that they are recharged by water stored in the talus slopes or in the lateral moraines. However, due to i) their limited increase in EC compared to bedrock and ii) constant discharge, they seem much more likely to be recharged by bedrock exfiltrations that rapidly re-infiltrated into the sediments and re-emerged near the outwash plain.

This is confirmed by a salt tracing experiment where we injected salt near the bedrock sampling location and measured the arrival time near Tributary 2 (Fig. C4). We obtain a fast travel time with two peaks in EC, likely representing two flowpaths with an estimated hydraulic conductivity of 9.5 x 10^{-2} m s^{-1} and 2.7 x 10^{-2} m s^{-1}, similarly to other studies of talus slopes (Muir et al., 2011).

The second class of tributaries include Tributary 1 and 4. These tributaries are characterized by higher EC values than the bedrock water and show a δ^2H evolution very similar to that of the main stream. They are likely recharged from snowmelt at high elevation in small hanging valleys. Those small valleys also likely contain permafrost and potentially some relict ice buried in the sediments, which may provide additional water input. They probably inherit some dissolved material in the elevated part of the catchment where water infiltrates through thick moraines.

The third class represents Tributary 3, which in the study period ran dry in mid-August. This source has a very low EC and is directly recharged by snowmelt as illustrated by the fast δ^2H enrichment when most snow has melted. This tributary also directly infiltrates in the outwash plain near well B3 and maintains there a much lower groundwater EC than in the other wells. As soon as this tributaries dries in mid-August, EC starts to increase in this well. The impact seems to also reach well B2 where EC also stays low at the start of the melting season, but EC values start to increase earlier in the season than in B3.

Regarding the outwash plain, upstream wells close to the stream (B1,C1,D1) show δ^2H values similar to those of the stream (Fig.6.4); the well are likely recharged by stream infiltration as discussed in the work of Müller et al. (2023). Piezometers closer to the hillslope (C2, D2) and well A1 show a similar rate of ^{2}H enrichment than the stream, but the their δ^2H values remain slightly heavier than in the stream. It is likely that those wells are preferentially recharged by bedrock exfiltrations, which have a more constant and heavier δ^2H signal, either from the surface (similarly to Tributary 2) or from below the ground. The higher EC values for piezometers close to the hillslope could also be due to such contributions from the bedrock.

6.3.2 Hydrogeochemical analysis

Results of the geochemical analysis suggests that the weathering of different rocks appears in different proportions depending on the water flowpaths. The geological context of Otemma seems rather typical of high Alpine regions with relatively similar weathering processes as the much more studied glacier d'Arolla (e.g. Mitchell et al., 2006; Sharp et al., 1995).

Following the solute mass-balance model described in the work of Anderson et al. (2000) and adapted in Eqs. 6.1 to 6.3, Tassaux (2022) showed that, in summer, slightly more than 50 % of the HCO_3^- flux is explained by carbonate weathering, about 40 % by plagioclase weathering and 10 % by biotite weathering. This suggests that although the lithology in the Otemma catchment is dominated by silicate rocks, traces of carbonates appear indeed to largely influence the solute budget. Results from the PCA analysis (Fig. 6.5) indicate the clustering of three main groups of solutes. Ca^{2+}, Na^+, Sr, Si and $HCO_3^-$are strongly correlated and are likely linked to carbonate and plagioclase weathering. $SO_4^{2-}$and $Na^+$are slightly less correlated with the latter solutes, likely in-

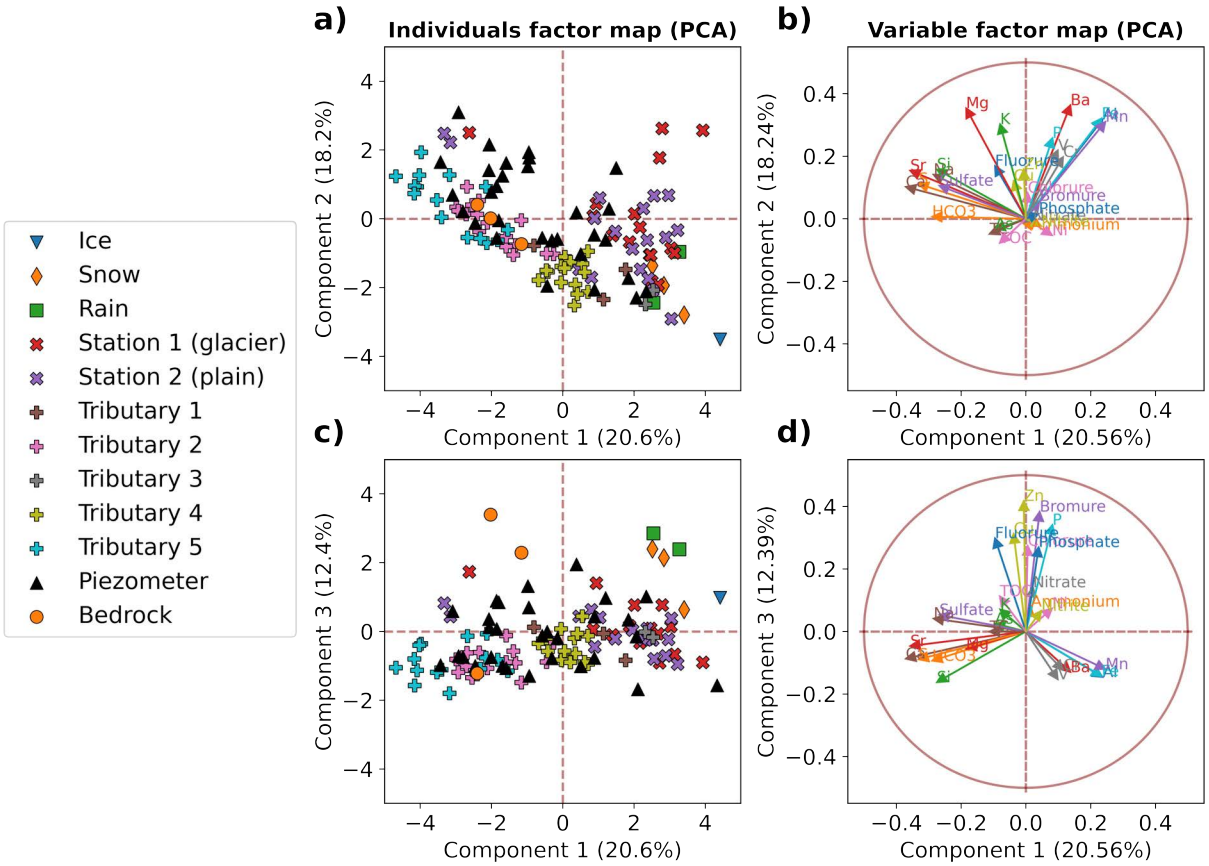

Figure 6.5: Principal component analysis (PCA) of major and trace elements from all water samples collected in the Otemma catchment for the three first PCA dimensions (component 1 and 2 for **a)** and **b)**, component 1 and 3 for **c)** and **d)**). **a)** and **c)** Individual factor maps showing the location of each sample. **b)** and **d)** variable factor map showing the correlation between solutes and their location relative to the PCA components.

dicating that plagioclase weathering and pyrite oxidation may in some cases happen differently than carbonate weathering. Mg^{2+}, $K^{+}$and F^{-}appear also correlated and are likely due to alteration of other feldspars (K-feldspar, biotite, hornblende). Some other trace elements such as Ba, Mn, Al and Fe are also strongly correlated. Finally, most other solutes do not show any significant response and are not further discussed. The correlation matrix of all solutes as well as boxplots of the main solutes are presented in Fig. C5 & C7. The temporal evolution of the main solutes in the stream (GS1 and GS2) shows a strong increase in winter with the exception of Fe (Fig. 6.6). In general, winter increase is larger at GS2 than GS1, except for Na^{+}. In summer, a clear trend is difficult to observe. In early August 2021, a strong rainfall event led to a strong increase in TOC in all tributaries, but also to an increase at GS1 at the glacier outlet. Soil flushing was shown previously to be a strong contributor of annual $Na^{+}$and Si fluxes in alpine catchments (Clow and Mast, 2010), however, during this rain event other solutes do not increase, which likely refutes the soil flushing mechanism. Since TOC also increases at the glacier outlet, it is likely that TOC increases are rather due to the flushing of snow, which shows the highest TOC values in the catchment over the study period.

To assess the dilution effect of increasing discharge on solute concentrations, we plotted their concentration against discharge in log space (Fig. 6.7). In the case of complete dilution without weathering and negligible concentration in the meltwater, the slope should be -1, since the concentration (C) would be inversely proportional to discharge (Q) following the equation $C = kQ^{-1}$ so that, log(C) = -log(Q)+log(k), where k is a certain constant. With the exception of SO_4^{2-}, all slopes are above -1, which indicates that concentrations decrease more slowly than discharge. This suggests that either increased weathering occurs with increasing discharge or that a source of more

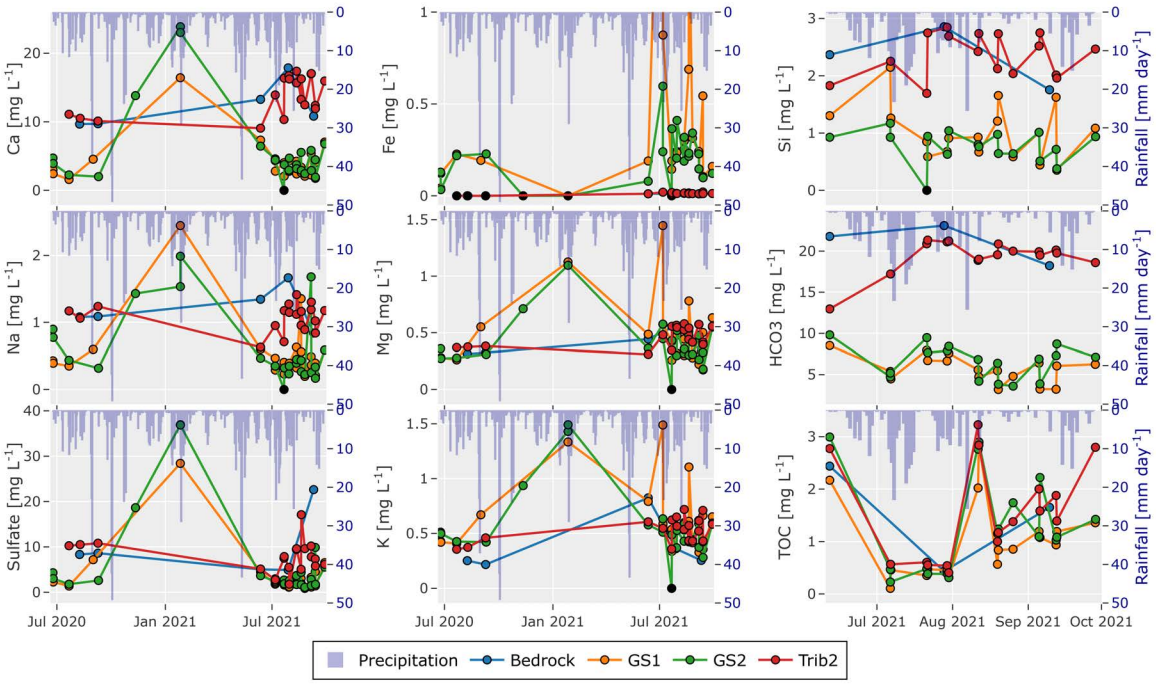

Figure 6.6: Temporal evolution of the main dissolved solutes in the stream (GS1 and GS2), in one tributary (Trib2) and in the bedrock. Note that for the last column, data were only available in 2021. The inverted blue bars represent measured daily rain amounts in mm.

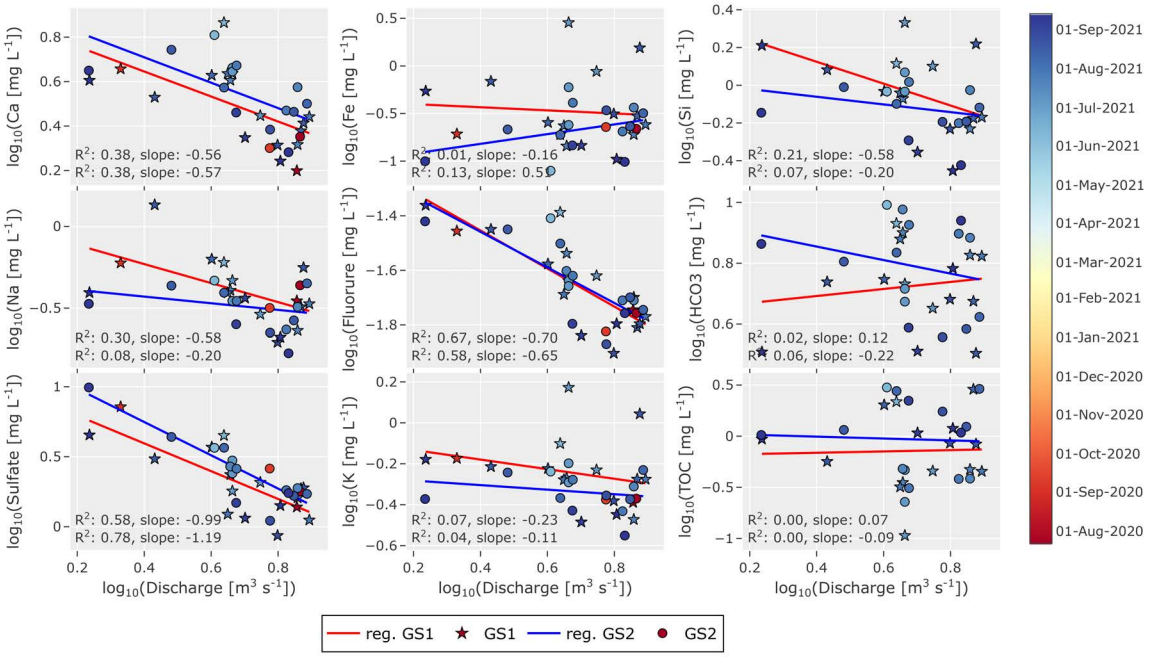

Figure 6.7: Main solute concentrations against river discharge at GS1 and GS2 in logarithmic scale for all samples. Colorbar shows the date of the sampling. Regression lines are also provided, with the coefficient of correlation (R^2) and slope of the regression for GS1 (upper equation) and GS2 (lower equation).

enriched water contributes more during high flow. This could happen if the internal glacier storage increases. Surprisingly, Fe shows a completely different behavior than SO_4^{2-}, while pyrite oxidation is likely the main weathering process for both solutes. Moreover, Fe shows a chemostatic behavior with no clear change in concentration with increasing discharge. Such a behavior was previously also shown to be due to soil flushing and to the release of older water during storm events (Clow and Mast, 2010; Godsey et al., 2009), but is likely not dominant in a glaciated catchment.

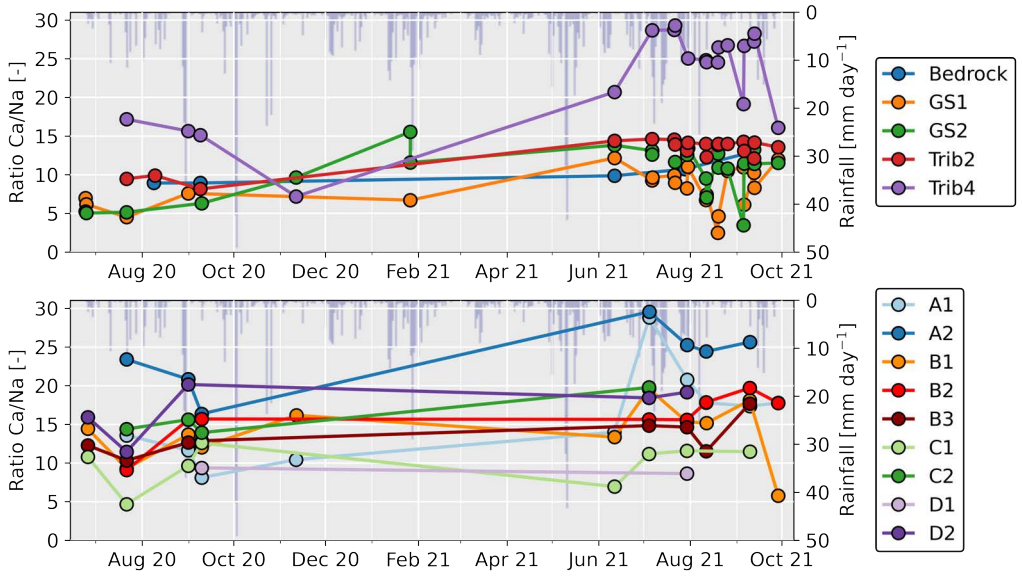

Figure 6.8: Solutes ratio between calcium and sodium from July 2020 to October 2021. The top plot show samples in the stream, the bedrock and two tributaries. The lower plot shows the ratio in the groundwater. Inverted blue bars represent measured daily rain amounts.

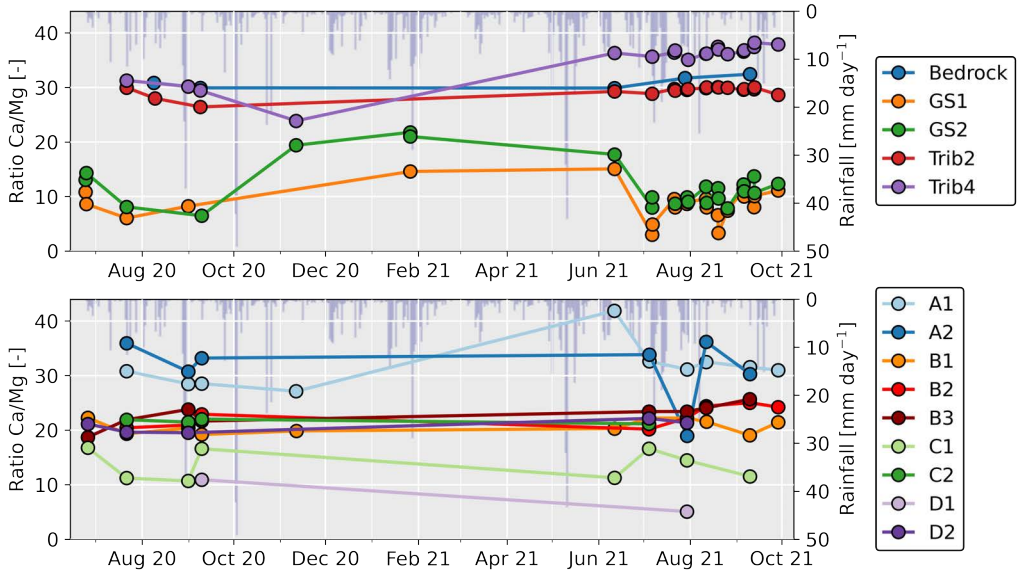

Figure 6.9: As Fig. 6.8 but for solutes ratio between calcium and magnesium.

Łukasz Stachnik et al. (2022) has shown that the Fe concentration increases especially in subglacial streams due to strong subglacial abrasive processes. However, Mitchell and Brown (2007) also showed that Fe, Al, Ba and Mn are rapidly reaching oversaturation levels so that a fraction of the dissolved load rapidly precipitates on the suglacially transported suspended sediments. In addition, they showed that an increase in discharge usually leads to an increase in the suspended sediments concentration, which further increases Fe adsorption on sediments and maintains a relatively constant dissolved concentration in the stream.

$Mg^{2+}$and K^{+}, contrary to Fe, were not oversaturated (Mitchell and Brown, 2007), so that in this case, the flat slope of the discharge-concentration regression observed in this study seems to indicate a largely increasing weathering with discharge. The same observation seems valid for $Ca^{2+}$and Na^{+}, although they appear more diluted with increasing discharge.

In the outwash plain groundwater, solutes appear to be more dissolved near the stream than near

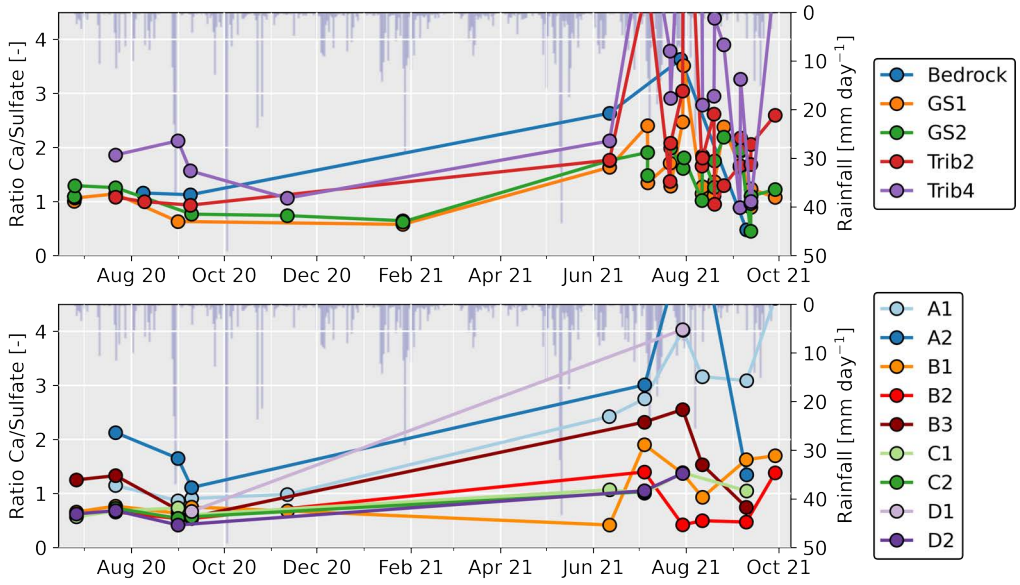

Figure 6.10: As Fig. 6.8 but for solutes ratio between calcium and sulfate.

the bedrock, as previously discussed for EC. At this stage, the ratio of certain solutes may provide further information regarding the weathering processes and sources of water. In Fig. 6.8, 6.9 & 6.10, we compare the ratio of Ca^{2+} (from calcite and plagioclase weathering) to Na^{+} (from plagioclase (albite)), to Mg^{2+} (from biotite or hornblende) and to SO_4^{2-} (from pyrite). A change in those ratios indicates a change in the relative proportion of weathering rates of different minerals, which may be due to different rock-water interactions.

The ratio of Ca^{2+}/Na^{+} appears to be relatively constant for all sampling locations. A value of 10 in the stream indicates a substantial proportion of carbonate weathering (Anderson et al., 2000). This is higher than values reported in a study in the Morteratsch proglacial area, where a value between 1 and 5 was obtained (Mavris et al., 2010), but lower than for the Arolla proglacial system, where a value of 20 was estimated (Mitchell et al., 2006). Typical ratios for plagioclase weathering are around 0.5 (Anderson et al., 2000). Tributary 4 shows the highest ratio, which seems to indicate more carbonate weathering and a similar ratio appears visible in the neighbouring groundwater wells (A1 and A2), suggesting a strong connection to that tributary.

The ratio Ca^{2+}/Mg^{2+} appears to be high in the bedrock and in the tributary and low during the summer in the stream, especially at GS1. A low ratio at GS1 in summer indicates a larger weathering rate of Mg-bearing rocks such as biotite and hornblende (Mavris et al., 2010). Stream water temperature changes should have a marginal effect on dissolution rates as water temperatures are comprised between 0 and 2 °C during a year at GS1. The same trend can also be observed for K^{+}. The fact that the stream ratio becomes larger in summer may indicate that biotite weathering is enhanced, especially in the fast drainage part of the subglacial system. This is likely an indicator of water transiting quickly through a channelized system. This observation is different than what has been shown in the work of Hindshaw et al. (2011); they showed no significant trend in the Ca^{2+}/Mg^{2+} ratio, likely highlighting the site-specific lithologies. Most of the groundwater wells have a Ca^{2+}/Mg^{2+} ratio near 20, which, based on a simple mixing model between bedrock and stream, would lead to a ratio of around 50 % recharge from both sources. Well C1 and D1 show values that are much more similar to those of the stream, and A1 and A2 show values closer to those of the tributary. It should be kept in mind, however, that weathering processes in the groundwater may also modify this ratio, leading towards an unknown bias.

Finally, the ratio of Ca^{2+}/SO_4^{2-} is relatively high in the bedrock and in tributaries, indicating limited sulfide oxidation. In the stream, values are higher in summer and about twice lower in winter. This

suggests that sulfide oxidation is more dominant in a slow storage below the glacier, likely representing a larger contribution from a distributed system with longer flowpaths. For instance, Łukasz Stachnik et al. (2022) showed that pyrite oxidation occurred predominately in recently eroded sediments (<60 years), which would explain why bedrock exfiltrations (where long flowpaths are expected) show a much higher ratio due to a more limited pyrite oxidation compared to plagioclase weathering. Interestingly, here $SO_4^{2-}$is the only solute which shows an inversely proportional dilution effect with discharge (slope near -1 in Fig. 6.7), suggesting that limited sulfide oxidation occurs in the fast channelized subglacial system. Similar results were also obtained at the Glacier d'Arolla (Mitchell et al., 2006). The Ca^{2+}/SO_4^{2-}ratio in tributaries appears to be very variable in 2021 due to the dilution effect of rain events, which mainly enhance rapid carbonate and plagioclase weathering. The ratio in the outwash plain shows the lowest values, likely due to enhanced sulfide oxidation in those relatively young sediments, similarly to the distributed subglacial network.

Based on Ca^{2+}/SO_4^{2-}, we can conclude that the subglacial distributed system provides most of the SO_4^{2-}during the summer season. If $SO_4^{2-}$is conservative, as suggested by its inverse relationship with discharge, it could be used to estimate the baseflow contribution from the subglacial distributed system: We assume that the SO_4^{2-}concentration of the reservoir can be set equal to the winter concentration (28.5 mg L^{-1}) and that no $SO_4^{2-}$is dissolved in the channelized system. In this case, the baseflow simply corresponds to the measured concentration in summer divided by the winter SO_4^{2-}concentration times the measured discharge. This basic calculation leads to a winter baseflow discharge of 0.3 mm d^{-1} and a median summer baseflow of 1.25 d^{-1} (but varying between 0.65 and 2.3 mm d^{-1}) with the maximum baseflow in early June, followed by no significant trend in the entire summer.

This estimated value for winter baseflow is very similar to the estimated baseflow from the missing storage compartment, which we estimated based on recession analysis to a value of about 0.24 mm d^{-1} at GS3 (Müller et al., 2022a), which is equivalent to 0.35 mm d^{-1} at the glacier outlet (GS1) (due to the smaller catchment area at GS1). In Müller et al. (2022a), we also estimated a maximum early winter baseflow of about 0.5 mm d^{-1}, but we could not estimate summer baseflow due to the ice and snowmelt signal. If we retain the parameters of the non linear recession analysis estimated in that previous study, we can estimate summer groundwater storage (S) based on the summer baseflow (Q) estimated in this study, following $S=Q^c/\alpha$, with the recession coefficient α=115 d and the slope coefficient $c = 0.5$. With a baseflow of 1.25 mm d^{-1}, we obtain a summer storage of 75 mm (55 to 100 mm considering the extreme values of baseflow), which is very similar to the estimates of 70 mm made at the Aletsch glacier by Oestreicher et al. (2021).

Nevertheless, $SO_4^{2-}$is likely produced in a subglacial system rather than from older bedrock weathering, which would suggest that the missing storage discussed previously is maintained by the drainage of the subglacial distributed system, most likely in the subglacial till sediments, and not in the bedrock.

6.3.3 Noble gases

Between the 23 August and 11 September 2021, the GE-MIMS mass spectrometer recorded nobles gases day and night. The results of the NGRT shows no clear variations, neither with the time of the day nor with the advancing season, despite lower average discharge in early September. For all wells, a depletion in O_2 is observed, likely due to a strong microbial activity in the floodplain, as documented in other floodplains (Schilling et al., 2021). For well B1, all pairs of noble gases lead to the same NGRT between 0 and 3 °C. For well B2 and B3, the NGRT is located at around 10 °C. ^{4}He concentra tion is higher than the ASW but seems to remain on the excess air line of 10°C. Due to the strong groundwater diel variations, the enrichment by excess air is plausible although it could not be observed at well B1.

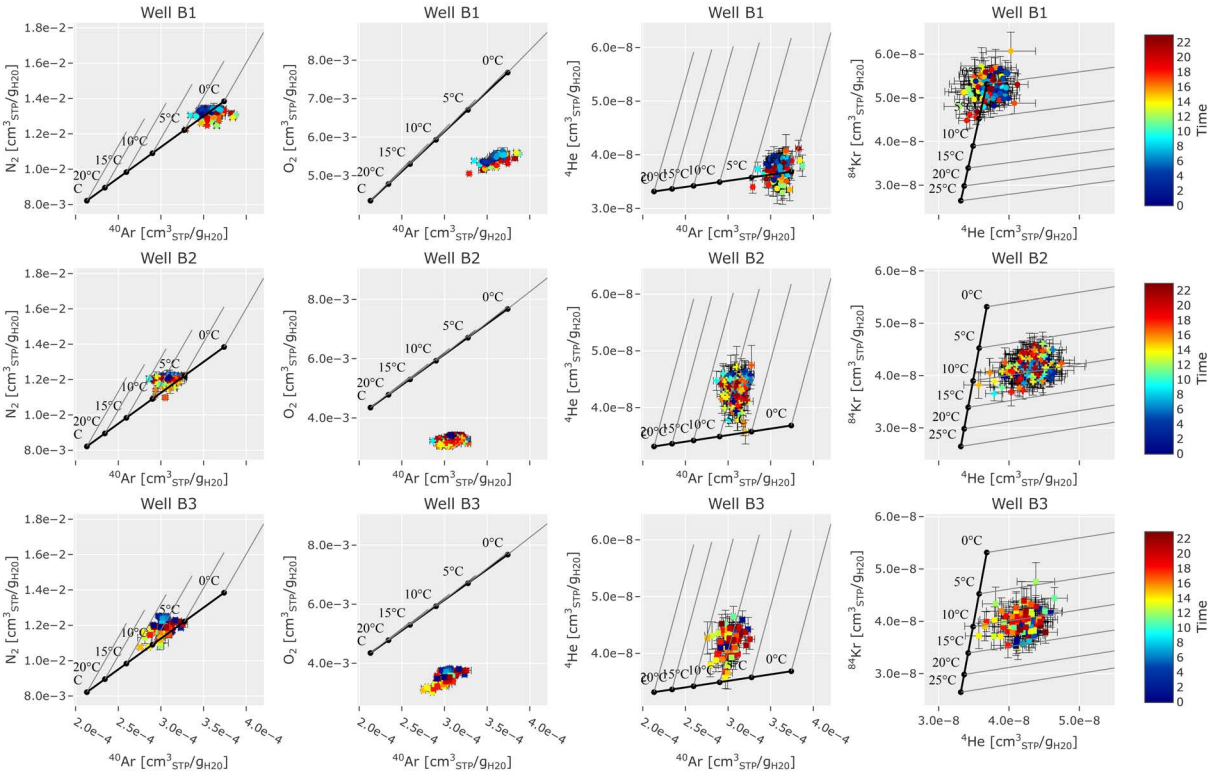

Figure 6.11: Result of dissolved noble gases concentrations for pairs of noble gases for well B1 (top), B2 (center) and B3 (bottom). The black line represents the corresponding air-saturated water (ASW) concentrations for a recharge temperature from 0 to 20 °C. The grey lines represent the impact of additional excess air to ASW at different temperatures.

To establish a mixing model, the recharge temperature of the hillslope water needs to be defined. Based on Fig. 6.3, the temperature of tributary 3 mainly varies between 10 and 15 °C, which is similar to the groundwater temperature at well B3. From this analysis, we can assume that groundwater at well B2 and B3 is mainly recharged by hillslope infiltration, while well B1 is strongly connected to the river.

6.3.4 Mixing model of subglacial EC variations

The simple mixing model described in Sect. 6.2.5 relies on the assumption that EC is mainly influenced by the relative contribution of its three components, which mainly evolve due the expansion of the subglacial channelised system, as suggested in the work of Lane and Nienow (2019). This is supported by the fact that the magnitude of EC variations are strongly correlated to discharge variations (Fig.C3). Similarly, most solutes show a correlation with discharge with a slope larger than -1 in log space. More importantly, the magnitude of the daily EC and discharge variations are also highly correlated with the f_{chann} (Pearson correlation of 0.85). Based on this observation, we propose to substitute time with f_{chann} and analyze the peak and low flow discharge and corresponding EC only. The left plot of figure 6.12b & c illustrates the measured discharge and EC for year 2021 as well as the fraction of the channelized system. The plots on the right transpose f_{chann} to the x-axis and and show only the corresponding measured and modelled values for low and peak flow. In order to match the stream EC during measured peak and low flow jointly, an EC value of 23 μS cm^{-1} was estimated for the distributed system and 8 μS cm^{-1} for the channelized system, while measured baseflow EC during winter had a value of 120 μS cm^{-1}. Moreover, a baseflow discharge of 1 mm d^{-1}, similarly to the estimation using SO_4^{2-}, is found here to correctly reproduce stream EC during daily low flow. However, during peak flow, this baseflow needs to be set to zero in order to correctly represent the magnitude of EC variations during the whole summer. Using a fixed baseflow leads to only small variations of EC and can not represent the observed

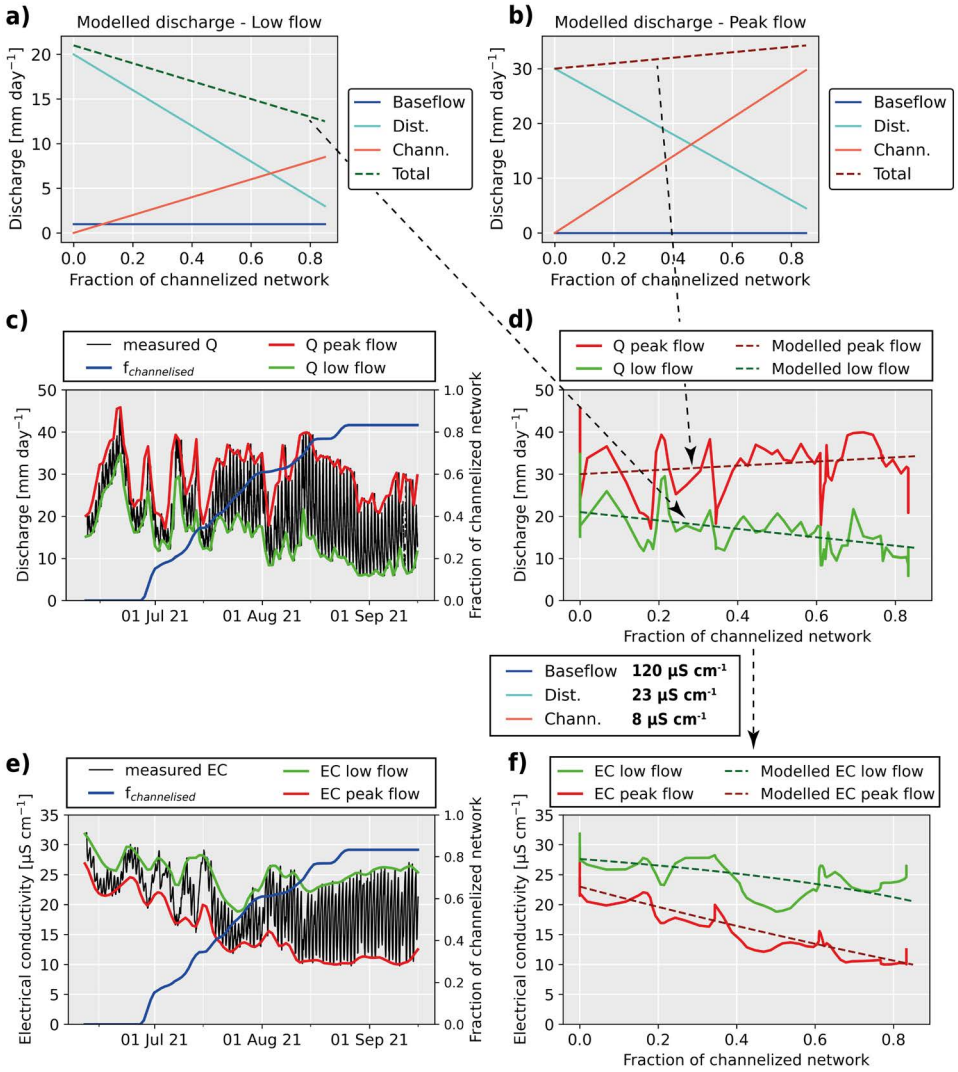

Figure 6.12: Observed and modelled EC and discharge at the glacier outlet during peak flow and low flow. **a)** Modelled discharge from the three subglacial component for low flow. **b)** Modelled discharge from the three subglacial component for peak flow. **c)** Observed discharge for year 2021, identification of daily peak and low flow and estimation of the fraction of channelized network ($f_{\text{channelized}}$). **d)** Comparison of observed and modelled peak and low flow discharge against $f_{\text{channelized}}$. **e)** Observed EC for year 2021, identification of daily EC during peak and low flow. **f)** Comparison of observed and modelled EC during peak and low flow against $f_{\text{channelized}}$.

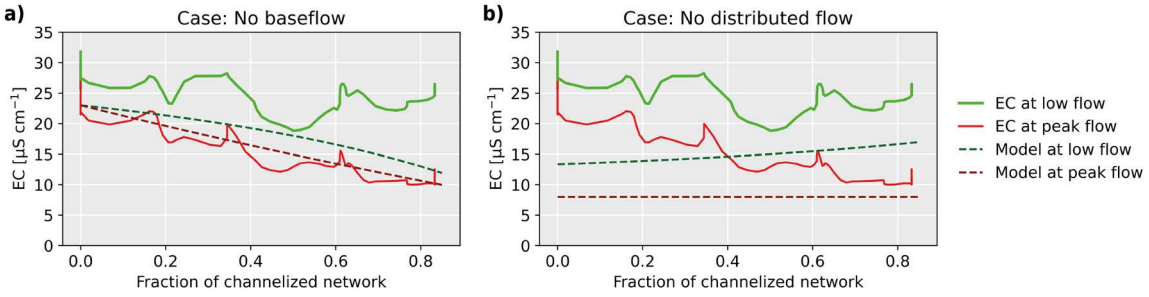

Figure 6.13: Sensitivity analysis of observed and modelled EC at the glacier outlet. **a)** Impact if no baseflow is considered (Q_{base}=0). **b)** Impact if no distributed flow is considered (Q_{dist}=0)

EC values. Finally, Fig. 6.13 illustrates how baseflow and the distributed system both impact the EC results in different ways. In particular, the distributed system seems to be responsible for the observed decline of EC at peak flow.

6.4 Discussion

6.4.1 Groundwater connectivity in the outwash plain

We explored different tracers in order to assess groundwater recharge in the outwash plain aquifer. Results from isotopic and EC data show that tributaries flowing at the surface or inside the lateral morainic deposits may show a strong spatial variability, either being recharged from the bedrock, from higher hanging valleys and from rapid snowmelt runoff directed downstream at locations where bedrock topography concentrates the flow. These mechanisms lead to a complex combination of recharge with water showing different geochemical and isotopic compositions. Moreover, even if the hillslope appears to deliver runoff rather quickly, limited chemical weathering may still occur and thereby further complicate the use of a mixing model (which typically relies on fixed end-member concentrations). These limitations were already pointed out previously (e.g. Carroll et al., 2019; Kiewiet et al., 2019; Zuecco et al., 2019). Nevertheless, we have shown here that the different types of tributaries can be easily identified based on δ^2H and on their geochemical signature and that the impact of lateral tributaries on the outwash plain groundwater recharge can be qualitatively identified. We have shown that groundwater wells near the stream, as expected, always behave similarly to the stream water. Near the hillslope, some tributaries respond clearly to hillslope recharge, especially in the downstream part (well A1 and A2). However, in the central part of the outwash plain, contribution from the hillslope are more uncertain. For instance, based on the Ca^{2+}/Mg^{2+} ratio (Fig. 6.9), we estimate that a maximum of 50 % of the water originated from the hillslope for wells B1, B2, B3, C2 and D2. Based on δ^2H, wells closer to the hillslope (A1, C2, D2, and slightly less B2, B3 in Fig. 6.4) showed in 2021 a more enriched signal compared to the stream water. However, In 2020, only wells A1 and C2 were significantly higher than stream δ^2H, mainly during the early melt. Since 2021 was subject to much more heavy rain events, it is likely that the isotopic enrichment was due to recharge from rain-fed hillslope runoff, and especially wells A1 and C2 may be more impacted by bedrock-fed sources. Nonetheless, in mid-August to September 2021, weather conditions were drier but the isotopic values of the tributaries remained more enriched than those of the stream water. We can here only postulate that groundwater flow in the outwash plain is relatively slow and that rain water is only slowly replaced by more stream infiltration to the outwash plain aquifer in late summer.

Finally, the noble gas temperature of recharge indicates that almost 100 % of groundwater in B2 and B3 was recharged by the warmer hillslope tributaries. This is consistent with a strong impact of rain-fed hillslope recharge. Interestingly, no diel variations were observed in those wells; this also supports relatively slow groundwater flow, which effectively dampens the diel stream infiltration patterns, as discussed in the work of Müller (2022a). Based on our previous modelling work (Müller, 2022a), a mean transit time from upstream river infiltration to well B2 of about 10 days can be estimated, which is coherent with the present results that point towards slow groundwater flow.

Nevertheless, even if we have shown here that hillslope recharge may dominate the outwash plain groundwater near the hillslope, our previous modelling work clearly showed that the groundwater levels are tightly correlated with stream discharge and with infiltration in the upper part of the outwash plain. Since our groundwater wells were shallow (they usually only reached about 1 to 1.5 m deep into the aquifer), it is also possible that hillslope recharge mainly influences the upper part of the aquifer, while deeper groundwater may be more influenced by stream water.

6.4.2 A simple model of coupled bedrock - subglacial groundwater storage

We have shown that winter baseflow is more similar to subglacial water than bedrock exfiltrations, mainly based on SO_4^{2-}. It remains, however, unclear if subglacial till can store and release such rather large amounts of water. It was indeed previously discussed that subglacial till in this Alpine area is characterized by a rather rocky bed (Maisch et al., 1999) and that subglacial till thickness is

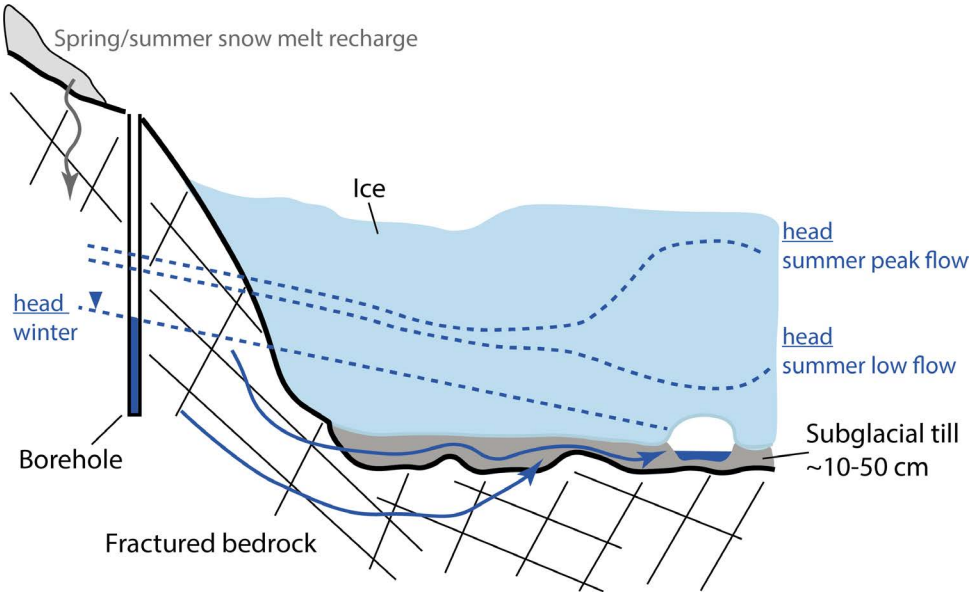

Figure 6.14: Conceptual representation of the proposed model of subglacial-bedrock groundwater connectivity. Dashed lines represent water heads during different periods. The small cavity below the ice represent a subglacial channel. Arrows represent groundwater flowpaths. Note that the borehole observations were made in the Aletsch glacier (Hugentobler et al., 2022), but it was added here to illustrate the processes likely similar in Otemma.

in the order of 10 to 30 cm e.g. under the Glacier d'Arolla (Harbor, 1997). Another study showed a till thickness of 40 to 70 cm for a temperate glacier in Sweden (Brand et al., 1987). Based on the estimation of 40 mm of winter storage (Müller et al., 2022a), and assuming a till porosity of 0.3 (Fountain, 1994), this would represent about 35 cm of continuously saturated till below the whole glacier surface. However, subglacial till hydraulic conductivity (K_s) is low and usually shows a gradient from values around 10^{-4} to 10^{-5} m s^{-1} near subglacial channels due eluviation of fine sediments in summer (Fischer and Hubbard, 1999) to 10^{-7} to 10^{-9} m s^{-1} (Hubbard et al., 1995). If subglacial hydraulic gradients can be assumed to be low in winter, groundwater flow would be driven by the bedrock slope. Further assuming that subglacial groundwater flows through a distributed network composed of linked cavities (Covington et al., 2012; Flowers, 2015) with a mean flowpath length of 100 m through the till until it reaches such a cavity, we can estimate a mean transit time in the till using Darcy's law. Using a relatively high K_s of 10^{-5} m s^{-1} and a gradient of 10 % representative of the Otemma bedrock slope (based on bedrock maps from Grab et al. (2021)), we obtain a mean transit time of 350 days. Compared with the recession time of about 100 days estimated from the recession analysis (Müller et al., 2022a), this transit time seems clearly too large.

To reconcile the winter storage, which seems to match better subglacial sediment weathering, and to obtain a faster mean transit time (or recession constant), we hypothesize that groundwater storage is maintained in the glacier area by the coupling of water that is stored in bedrock fractures on each side of the glacier and that is connected to subglacial till. Water stored in the bedrock has a water table higher than the glacier bed and therefore increases the hydraulic gradient in the subglacial till, leading to faster groundwater flow and constant recharge from the bedrock. This hypothesis matches well the borehole observations in the Aletsch glacier (Switzerland), where bedrock water heads declined by several meters during the winter season (Hugentobler et al., 2022; Oestreicher et al., 2021). In summer, it is possible that groundwater flow from the subglacial till is partially inverted during daily peak flow. This is due to an increase of the pressure head in the subglacial drainage system, which is inefficient to evacuate the heavy daily meltwater amounts, as suggested by Hubbard et al. (1995) or Perolo et al. (2019). This mechanism would provide a satisfying explanation for the results obtained from the EC model, where baseflow discharge during peak flow needed to be significantly reduced. The increased pressure near subglacial channels

during afternoon peak flow likely pushes meltwater into the subglacial sediments and thus prevents groundwater contribution from subglacial till and thus leads to lower EC. During morning low flow, pressure decreases substantially allowing for more subglacial till water exfiltration, which leads to a further increase in total dissolved solutes and in EC. In Figure. 6.14, we illustrate this perceptual model of groundwater connectivity in summer and in winter in the glaciated part of the catchment.

6.5 Conclusion

Based on our previous estimations of groundwater storage in the Otemma catchment (Müller, 2022a; Müller and Miesen, 2022), this work aimed to evaluate those results based on a detailed analysis of various natural tracers. Based on previous geochemical work in other glacier catchments (e.g. Anderson et al., 2000; Mitchell et al., 2006; Sharp et al., 1995), we carefully analyzed the main weathering processes at work in such a typical silicate-rock dominated catchment. As already discussed by others, we stress that the concentration of dissolved solutes and thus EC cannot be considered purely conservative and may lead to large biases if geochemical enrichment is not properly addressed. Nonetheless, while strict quantitative estimates are difficult to obtain, we synthesize here the results from different natural tracers (δ^2H, ratio Ca^{2+}/Mg^{2+}, SO_4^{2-}, NGRT, EC model) to attempt to better constrain groundwater connectivity and groundwater recharge contributions mainly in the outwash plain region but also for subglacial water storage. These two compartments are of special interest because previous work has highlighted their potential to store groundwater at seasonal timescales and that they could be able to maintain baseflow during future drier conditions (Müller and Miesen, 2022). We have shown here that the outwash plain aquifer seems to be recharged from multiple sources, which are difficult to constrain due to the complex combinations of water sources. Nonetheless, we can conclude that, near the hillslope, groundwater recharge is dominated by rain-fed or bedrock recharge, while closer to the stream network, stream water infiltration dominates. Since previous results have shown that such aquifers are mainly recharged by stream infiltration, we postulate here that groundwater is likely to be not well mixed and that a gradient with depth may exist, with deeper groundwater being potentially more similar to the stream. In this regard, novel methods based on noble gases recharge temperature may provide a promising, more conservative tracer to assess groundwater recharge in contexts where large differences of the water temperature at the point of recharge exist. Our observations were unfortunately only limited to a short period and to shallow groundwater wells. We suggest that this method could be improved by sampling groundwater at different depths, at different locations and for a complete melt season, which could be undertaken with the use of such a portable field mass-spectrometer, similarly to the work of Schilling et al. (2021).

We furthermore focused on subglacial groundwater storage and showed that three groundwater compartments are essential to reproduce stream EC measurements and that we need to account for a certain amount of weathering in all compounds. Here the ratio of $Ca^{2+}/SO_4^{2-}$and SO_4^{2-}concentrations may provide a more conservative tracer approach to estimate groundwater contributions, as previously suggested by (Mitchell et al., 2006); this approach might, however, also be relatively site-specific based on the local lithologies. Other natural tracers could also be used, in particular the ratio of $^{87}Sr/^{86}Sr$, which can be used as a marker of carbonate versus silicate weathering (de Souza et al., 2010; Hindshaw et al., 2011). Building on this work and on previous works in the Otemma catchment (Müller and Miesen, 2022) and on borehole observations in the Aletsch glacier (Hugentobler et al., 2022), we propose a perceptual model of coupled bedrock-subglacial groundwater flow which allows to resolve some of the key conflicting observations.

Finally, this work highlights that the largest groundwater storage is most likely located in the bedrock and connected to subglacial sediments. With future glacier retreat, ice-free subglacial till may be covered by coarser debris and the pressurized flow discussed previously will cease, so

that its water conveying role will fade out. This suggests that bedrock storage will likely remain the major driver of baseflow at a seasonal scale and may become increasingly important during potential future late summer droughts. It still remains unclear how glacier retreat and the subsequent reduction in subglacial water head will impact bedrock storage. Outwash plains are expected to maintain their role to store water during long periods due to their strong connection to both stream and hillslope recharge and their relatively slow drainage (Müller, 2022a). In this context, their role to promote suitable habitat conditions for alpine species (Brighenti et al., 2019b; Roncoroni et al., 2023) will likely become increasingly relevant in a context of rapid climate warming.

C Appendix

C.1 Additional EC and water stable isotopes data

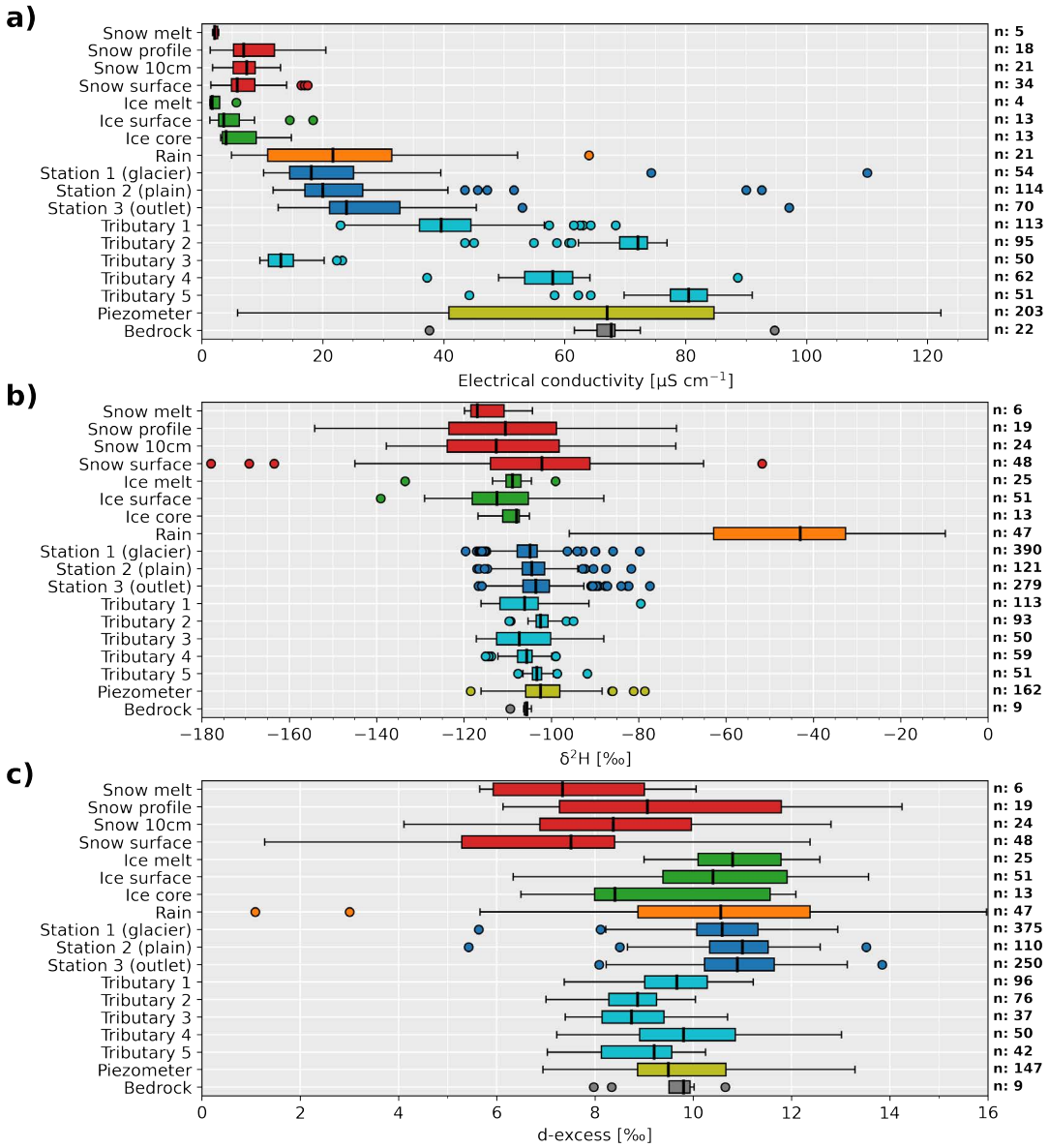

Figure C1: Boxplot of all samples for EC, δ^2H and d-excess collected between June 2019 and October 2021. n represents the number of samples.

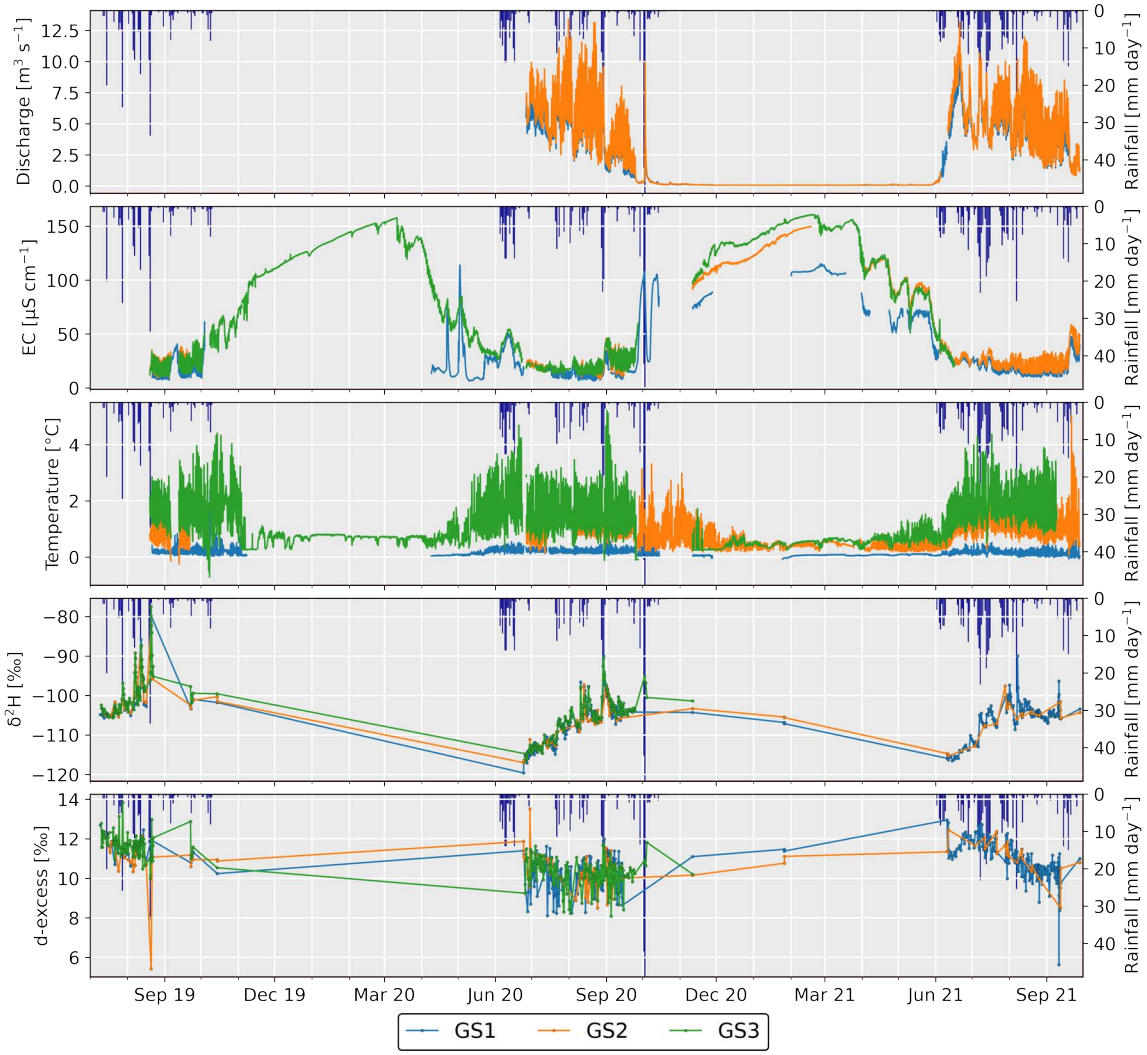

Figure C2: Stream discharge, water temperature, EC, δ^2H and d-excess at the three gauging stations from July 2019 to October 2021.

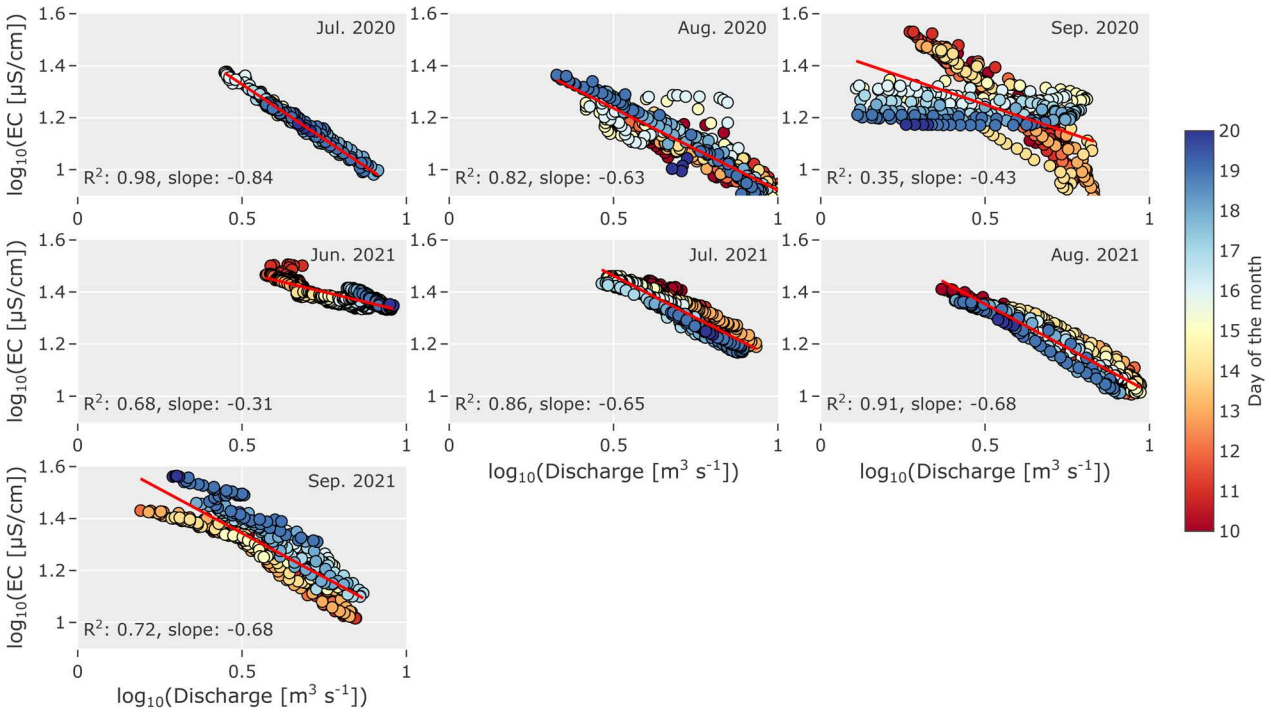

Figure C3: Stream EC at GS1 against river discharge in logarithmic scale separated by month. The colorscale represents the day of the month and for better visibility we only plot day 10 to 20. Regression lines are also provided with the coefficient of correlation (R^2) and slope of the regression.

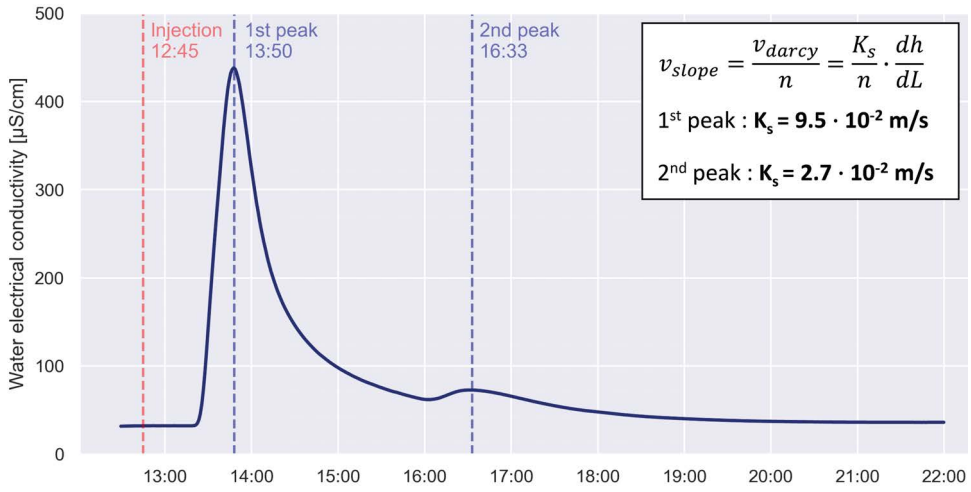

Figure C4: Electrical conductivity at the base of the hillslope near Tributary 2 after the injection of 2 kg of dissolved salt near the the bedrock sampling location (Fig. 6.1). The corresponding hydraulic conductivity (K_s) was estimated for both peaks following Darcy's law.

C.2 Additional geochemical data

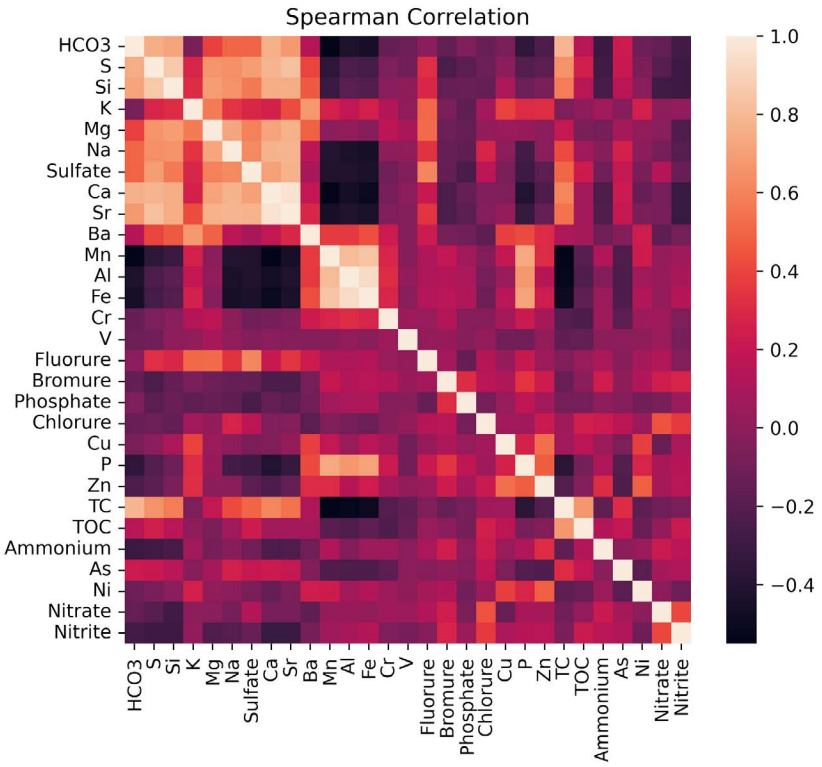

Figure C5: Spearman cross-correlation of all water solutes.

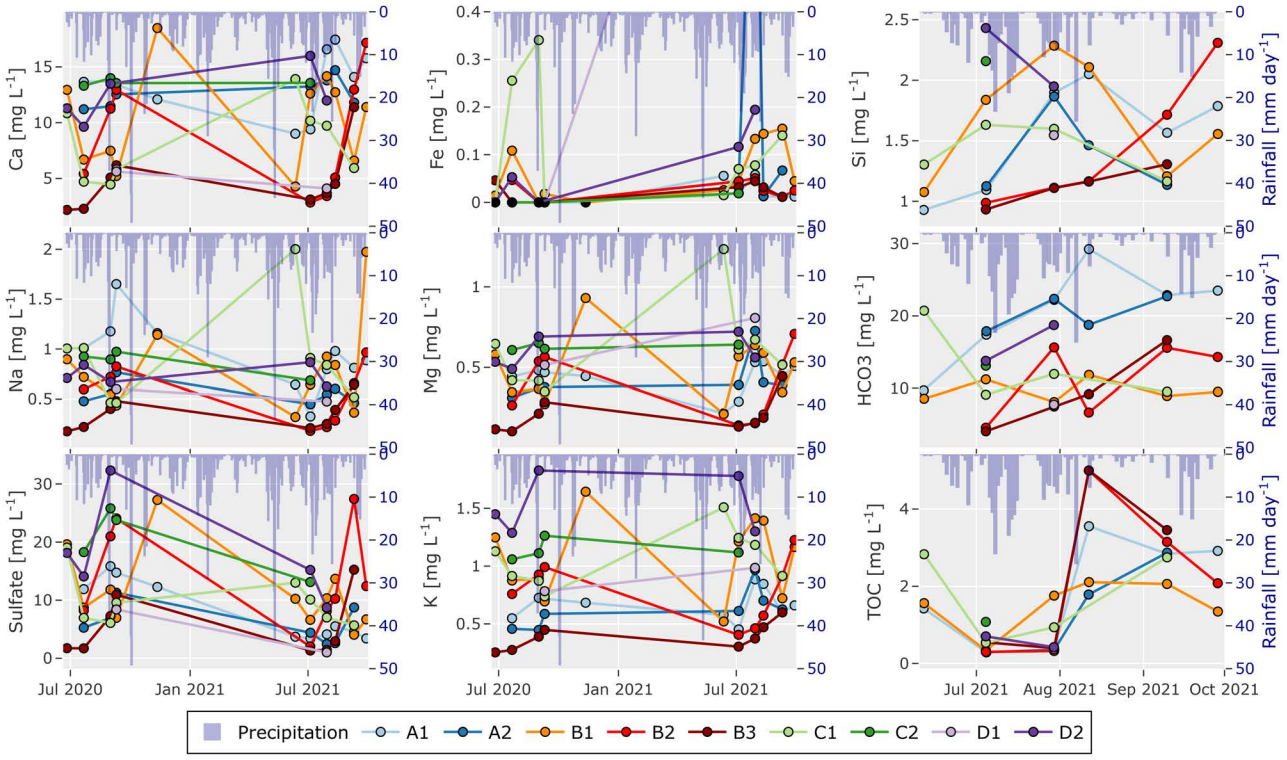

Figure C6: Temporal evolution of the main dissolved solutes in the groundwater wells.

Figure C7: Boxplots of the main water solutes for all sampling sites from 2020 and 2021. Note that for the last column data were only available in 2021.

7 Discussion

7.1 A synthesis of the hydrogeological functioning of an Alpine glaciated catchment

This work focused on an in-depth analysis of the hydrogeological functioning of a typical Alpine glaciated catchment. Our main focus was to identify the different hydrogeological units within its boundaries which are responsible for storing and releasing water. In order to assess how future groundwater and surface water availability will evolve in the future, we focused on characterizing the potential volumes of water stored and the timescales at which water is released. This allowed better assessment of which aquifers contribute more to baseflow, on daily, seasonal or annual time scales. During this work, we attempted to take an integrated approach, where we not only look at each unit individually, but also at how they are interconnected and finally at their combined hydrological response at the catchment-scale. For this purpose, we relied on a wide range of field methods in order to provide a multifaceted range of sources of information and to improve our interpretations by comparing results from different approaches. In Alpine environments, it is well known that the assemblage of landforms and their subsequent release of water is complex, water sources overlapping, mixing and leading to large spatial variability in their composition even at a very local scale (Carroll et al., 2019; Zuecco et al., 2019). In the following chapter, I provide a synthesis of the main outcomes of the different chapters.

7.1.1 The role of superficial landforms to store and release water

Review of the literature, from both a geomorphological and hydrological perspective, helped to identify more clearly the key landforms involved in and to formulate hypotheses about proglacial hydrological systems (Chapt. 2). Due to significant sediment release and rapid reworking in such areas, we first focused our analysis on the groundwater storage capacity of surface deposits, which are thought to play an important role at seasonal time-scales (Hayashi, 2020).

In the first research article (Chapt. 3), we built on this review to create a simple model of the hydrological response of the main superficial landforms based on the theory of recession analysis and compared the results of this analysis with the catchment-scale winter recession. From this work, we show that combining slope, estimates of hydraulic conductivities and flowpaths length to assess mean transit time appears as a simple, yet easily reproducible approach, which allows assessment of the rates of aquifer drainage and, coupled to a simple recharge routine, may provide rough estimates of storage. Relatively large uncertainties clearly arise from such a simple approach due, for instance, to the heterogeneous nature of aquifers (Roques et al., 2022) and the complex processes partitioning recharge and overland flow (Carroll et al., 2019). Nonetheless the trends and the timescales which we highlighted are likely representative of realistic physical processes. The main findings can be summarized in a few points:

- All deposits in such recently deglaciated environments have rapid hydraulic conductivities and water storage is very likely strongly limited on steep slopes with water transit times of the order of days.
- Mostly flatter morainic or glaciofluvial deposits (outwash plain) have the potential to store water for a few months.
- Storage decreases rapidly in all landforms once snowmelt disappears in the late summer season.

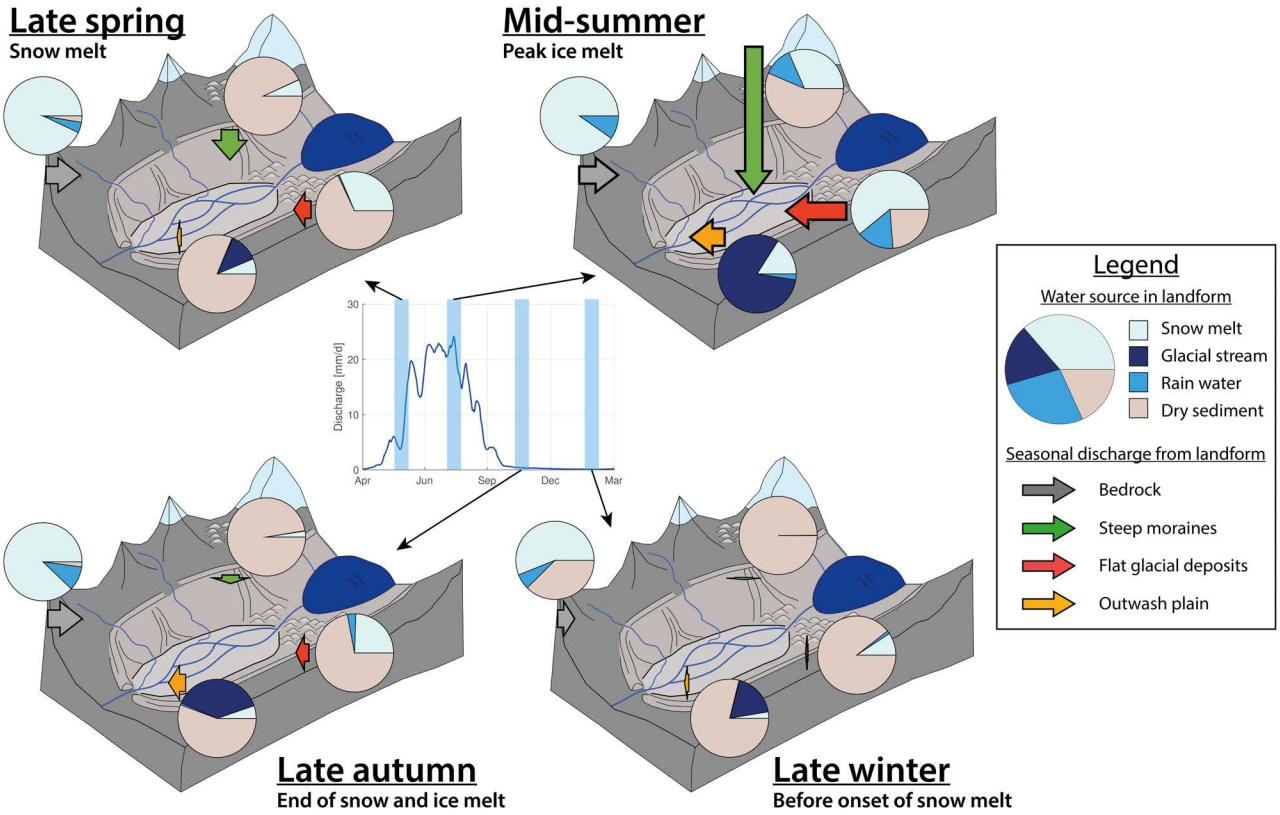

Figure 7.1: Perceptual model of groundwater dynamics in the Otemma catchment during four key hydrological periods. The central hydrograph represents the mean daily catchment-scale river discharge for the year 2015. The pie charts represent the seasonal partitioning of the three water sources (rainwater, snowmelt, glacial stream) calculated based on recharge and outflow for the three main superficial landforms as well as a bedrock aquifer. The source "Glacial stream" represents the mixed discharge leaving the glacier outlet and is an undefined mix of icemelt and snowmelt as well as of any rain transiting through the glacier. The share of dry sediments represents the percentage of aquifer storage drained compared to the calculated maximum storage, which is 40 mm for bedrock (missing storage), 23 mm for the steep lateral moraines, 19 mm for flatter glacial deposits, and 11 mm for the outwash plain. The length of the arrows represents the relative magnitude of the baseflow discharge estimated in Fig. 3.12 for each landform.

- Only the outwash plain receives a more constant recharge from glacier meltwater leading to greater saturation depths within such aquifers, which may result in a more constant source of baseflow in winter.
- None of the superficial aquifers allows explained the catchment-scale response in winter, which suggests that a deeper aquifer or subglacial mechanism maintain baseflow for several months.

In Fig. 7.1, we recall the perceptual model presented in Chapt. 3, which summarizes the main processes discussed above.

This first assessment strongly highlighted the role of outwash plains in collecting various sources of water and potentially providing baseflow at a more seasonal timescale. Since very limited literature exists for such post-LIA glacial deposits, we further deepened this analysis in the second research paper (Chapt.4). Secondly, while we hypothesize that there is a major contribution from a bedrock aquifer, the nature of such an aquifer remained unclear so that we attempted to provide a more detailed analysis based on natural tracers (Chapt.6).

7.1.2 Characterizing groundwater dynamics in the outwash plain

In chapter 4, we investigated the groundwater dynamics of the outwash plain aquifer, its surface water-groundwater exchange rates and their future importance for water storage and baseflow generation. Based on field observations and a physical model, we conclude that such an aquifer is mainly recharged by stream

infiltration. While hillslope contributions may be locally important, they do not drive the seasonal groundwater heads in such an aquifer. Their potential to significantly contribute to baseflow appears relatively limited as most of the water seems to be stored in a bedrock depression, so that only the fraction located above the lower bedrock edge may drain. Moreover, groundwater levels appear to be almost at equilibrium with river discharge so that, at a daily scale, they produce a similar amount of water exfiltration downstream compared to the amounts infiltrated upstream. Developing a simplified 3D model of the studied aquifer means that Brunner et al. (2019); Schilling et al. (2017), model development could make the representation more realistic modelling of flowpaths; for instance using a more complex representation of heterogeneities or by including more information from natural tracers. Nonetheless, a reasonable representation of summer and winter heads seems to indicate that the model appropriately represented the seasonal dynamics of groundwater. The main findings are summarized as :

- The outwash plain in Otemma stores significant water amounts relative to its small size (about 10 mm), but only about a third of this groundwater can be mobilized to maintain baseflow.
- Future outwash plains may appear with glacier retreat but the cascading effect of their cumulative groundwater contribution will remain marginal as long as stream discharge is above ~0.5 mm d^{-1}.
- Groundwater levels in the outwash plain are closely linked to stream bed levels. Geomorphological processes of sediments erosion and deposition have therefore a strong impact on groundwater levels. It is however expected that only limited upstream discharge is required to maintain water heads close to the surface and this should not be greatly impacted by future drier conditions since such aquifers drain slowly and from their upstream part first.
- Groundwater levels appear to be currently too deep to provide moisture for most pioneer species. It is possible that vegetation may profit from such shallow aquifer in the future with succession to deeper routing species and that could mean that proglacial alluvial plains become future hotspots of biodiversity similarly to the role of older Quaternary deposits (Hauer et al., 2016). However, the fact that water levels remain below the floodplain surface explains why primary colonisation of deglaciated alluvial plains can remain extremely slow, as in the case of Otemma.

7.1.3 Groundwater connectivity in the outwash plain

We investigated groundwater connectivity between landforms based on multiple natural tracers (Chapt. 5), which we discuss in the next section. Measurements performed in some tributaries near the outwash plain highlighted the large heterogeneities in their water compositions. Three main pathways were discussed:

1. rain water or snowmelt driven by topography in zones of depression where surface flow rapidly reaches the outwash plain or the stream directly;
2. rain water or snowmelt which infiltrates into the shallow soils and/or in the lateral deposits and either re-emerges at the foot of the hillslopes (if bedrock is close the surface) or directly enters the outwash plain below ground and
3. rain water or snowmelt which reaches bedrock fractures, follows longer and slower flowpaths and re-merges either at the bedrock outcrop, where it may re-infiltrate into the lateral deposits, or directly recharges the outwash plain.

All subsurface flowpaths described here are only hypotheses since they could not be observed during the work. Water seemed only to be transmitted in the lateral deposits as illustrated by a rapid recession of the δ^2H signal in exfiltrations at the base of those deposits and by a rapid return of the EC to its pre-event value in the outwash plain. The δ^2H response is very rapid and did not show signs of preferentially releasing older water as often observed in catchments at lower elevations, likely due to the absence of soils and the fast travel times.

The partitioning between hillslope recharge and stream infiltration in the outwash plain appeared to be very challenging to quantify based on natural tracers, due to the variability of the tributaries, the potential weathering occurring in the outwash plain and similar isotopic signals between most tributaries and the outwash

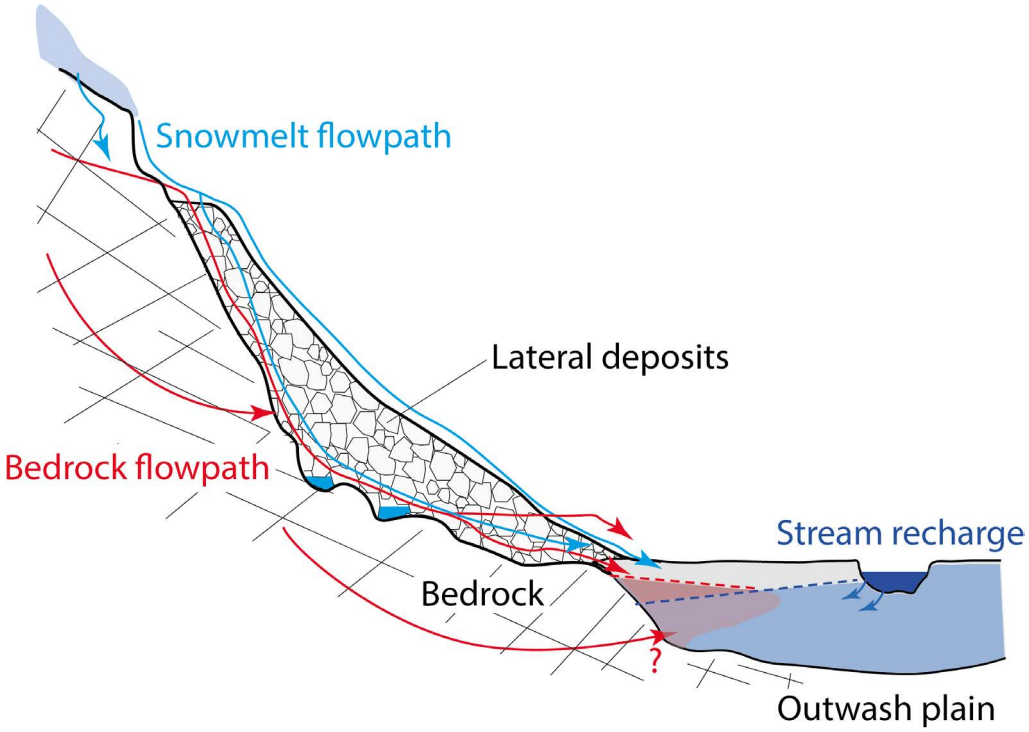

Figure 7.2: Conceptual representation of groundwater connectivity of the bedrock-hillslope-outwash plain complex. Red arrows indicate flowpaths from the bedrock, light blue from the snowmelt or rain, and dark blue from the glacial stream. The blue area in the outwash plain represents groundwater preferentially recharged by the outwash plain and the red area groundwater dominated by hillslope drainage. Note the opposite direction of the water tables (dashed lines). We added at the base of the lateral deposits some pockets of water to be consistent with previous work on talus slopes (Muir et al., 2011), although no mechanism of fill and spill (Tromp-Van Meerveld and McDonnell, 2006) could be observed in this study.

plain signals. Nonetheless, noble gas recharge temperature, which appears as a promising approach for such aquifers, showed a strong dominance of hillslope water near the hillslope and up to mid-way between the hillslope and the stream.

Results from the MODFLOW modeling work in Chapt. 4 suggest that groundwater recharge originates predominantly from upstream river infiltration. To resolve these partly conflicting conclusions, we argue that hillslope recharge occurs mostly near the top of the outwash plain such that the water composition of the first meters of the aquifer near the hillslope is composed of hillslope waters. These processes are summarized in Fig. 7.2.

Finally, we did not analyze in further details the composition of the water in the bedrock. Since both its EC and δ^2H were relatively stable in time, it seems that flowpaths are relatively long, although EC remained at low values, around 70 μS cm^{-1}. Its isotopic composition, around -105‰, seems to represent a larger share of snowmelt (for which δ^2H gradually increases from about -130‰ in the early season to -90‰ based on results of Chapt. 5) and rainwater (with a median value of -45‰). However, our samples of bedrock leakages are all from the bedrock outcrop above the outwash plain, which may not be representative of other locations.

7.1.4 Bedrock-subglacial till connectivity

Further building on the analysis of natural tracers, and by analyzing the varying rates of weathering of certain minerals in the glacial stream, we estimated a relatively constant baseflow during the melt season of about 1 mm d^{-1}, which is more similar to subglacial till weathering rather than to bedrock. Based on this baseflow, we further estimate a summer bedrock storage of about 75 mm. Additionally, we show that stream EC variations are strongly correlated with the extension of the channelized subglacial network and that measured EC at the glacier outlet can only be simulated by three compartments: a baseflow discharge resulting

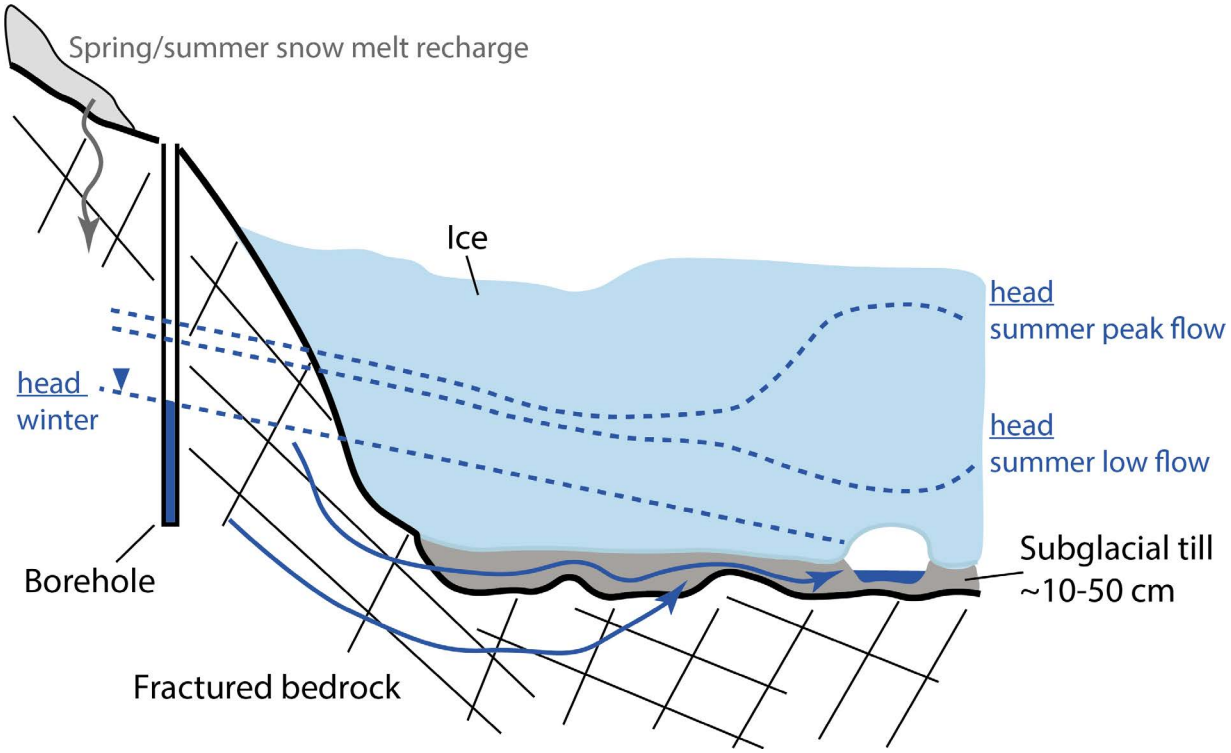

Figure 7.3: Conceptual representation of the proposed model of subglacial-bedrock-groundwater connectivity. Dashed lines represent water heads during different periods. The small cavity below the ice represents a subglacial channel. Arrows represent groundwater flowpaths. Note that the borehole observations were made in the Aletsch glacier (Hugentobler et al., 2022), but it was added here to illustrate likely similar processes in Otemma.

from the drainage of subglacial sediments, a (slow) distributed drainage system and a fast channelized network. The baseflow discharge seems to be at least partially reduced during daily peak flow from the glacier. We suggest that this is due to an increased water head in the subglacial system during the peak flow period, which prevents the drainage of the till. However, relying on a rough estimation of water transit time in the till, it seems that a strong hydraulic gradient is needed to increase the mean transit time of subglacial flow in the till such that it matches recession rates estimated in Chapt. 3. Based on these observations, we propose a conceptual model on groundwater connectivity between subglacial groundwater storage in the till and the bedrock. In that representation (Fig. 7.3), water head in the bedrock increases and supplies subglacial sediments. More widely, the need to invoke subglacial sediments to explain subglacial hydrological response suggests that this glacier at least has some subglacial till cover, something that touches wider debates regarding glacial erosion.

7.1.5 Groundwater connectivity from the glacier outlet to the catchment outlet

Due to the large amounts of water released at the glacier snout in summer, once groundwater reaches the main stream, it is largely diluted, making comparisons along the stream difficult. Indeed, the δ^2H observations along the stream all show a very similar response. EC shows, however, a slight increase in summer during low-flows, which we attribute to groundwater exfiltration from the outwash plain. After the outwash plain, the stream flows in a steeper valley with a bedrock-constrained cross-section, and no clear change in EC can be observed. Nonetheless, in winter, the variability of stream EC along the stream becomes more pronounced. The baseflow supplied from below the ice rapidly reaches the outwash plain, where we estimated that about 50 % of the associated discharge infiltrates in the sediments, while a slightly larger amount exfiltrates at the downstream end of the outwash plain, so that baseflow is only slightly larger downstream compared to upstream. This process leads to a significant increase in stream EC as weathering enriches the groundwater in the outwash plain. In essence, what we observe here is that upstream baseflow originates from bedrock, flows downstream until it re-enters into another aquifer (the outwash plain). This infiltration maintains a a hydraulic gradient in the outwash plain, which leads to groundwater exfiltration at the other

end of the outwash plain, leading to an increase in EC.

As such, the net increase in groundwater along the stream, considering the entire outwash plain, would be the difference between the upstream surface water infiltration and the downstream groundwater exfiltration. Practically, this estimation is challenging because infiltration does not change the stream water composition, and the losing stream reach is thus difficult to quantify.

Finally, in winter, we also observe a small increase in EC between the station located just downstream of the outwash plain (GS2) and the catchment outlet (GS3). At this stage, this small increase remains unexplained, and we can only attribute it to a bedrock recharge composed of significantly older water than what we observe in the catchment.

7.2 Uncertainties in the use of natural tracers

In addition to the main focus of this work on groundwater characterization, we also attempted to establish sound methodologies to overcome the important limitations of the use of natural tracers. Here we illustrate some of these challenges and discuss how some limitations may be overcome.

7.2.1 Electrical conductivity and other geochemical tracers

The use of EC to identify groundwater contribution in Alpine environments is certainly the most wide spread method (e.g. Engel et al., 2016; He et al., 2019; Kobierska et al., 2015b; Schmieder et al., 2018). Most studies acknowledge that the concentration in the water sources (end-members) may show a certain degree of spatial variation, which is usually accounted for by have a large number of samples in the catchment and by estimating the mean and standard deviation. Using such an approach, a simple procedure of error propagation is used, in most cases based on the work of Lemieux et al. (2008). This procedure appears to be insufficient in many regards, for the range of reasons highlighted below. These comments also hold true for most dissolved solutes.

Chemical weathering

Even in high alpine catchments, which are often dominated by crystalline lithologies, we have shown in Chapt. 6, along with many others (e.g. Carroll et al., 2018; Hindshaw et al., 2011; Mitchell and Brown, 2007; Sharp et al., 1995), that rock-water interactions always lead to some degree of weathering, which is difficult to quantify. This may be even more important in the case of glaciated catchments, where the suspended sediment load is large and relatively recently added to the water, which leads to a rapid enrichment in solutes Sharp et al. (1995). Therefore, not accounting for weathering will always lead to an overestimation of groundwater source importance.

Temporal variability

Groundwater water storage is usually considered as showing little seasonal variation, so that this variation is usually not considered. However, it is commonly assumed, especially in the case of bedrock storage, that a hydraulic gradient with increasing depth (Achtziger-Zupančič et al., 2017; Roques et al., 2022) leads to slower flowpaths, increased residence time and thus weathering. As groundwater storage becomes depleted, EC may therefore increase significantly. Even the EC of the other end-members may vary with time. For instance, EC in the snowpack always shows lower values than in rain, and this phenomenon is at least partially due to the preferential release (ions elution) of some solutes during snowmelt Costa et al. (2020); Marsh and Pomeroy (1999). Finally, there may be significant delays between the moment of supply of groundwater and its arrival at the stream outlet.

Varying groundwater sources and potential interactions

The sources of groundwater may change over the season or superimpose along the stream (Kiewiet et al., 2019; Zuecco et al., 2019). We showed for instance that, in summer, hillslope drainage recharged by snowmelt provides large amounts of water, while the outwash plain and the bedrock become more dominant in winter. Moreover, it remains very challenging to define the actual concentration of the groundwater when bedrock samples are difficult to obtain. Most research uses the lowest stream EC in winter (e.g. He

et al., 2019; Schmieder et al., 2018) as a proxy for the composition of the bedrock water, but there is no guarantee that such an approach is correct. We illustrated this with the example of the outwash plain in winter, where stream EC increases due to the re-infiltration of part of the baseflow (Sect. 7.1.5). It is here that the cumulative effect of two aquifers which leads to the observed stream EC; the stream EC at the end of the outwash plain is thus not indicative of the bedrock EC. Other studies alternatively use EC in springs (e.g. Engel et al., 2016), but these values might be influenced by snowmelt recharge in summer and not representative of the deeper aquifers. Here we can acknowledge the work of Penna et al. (2017), who discussed these two approaches.

All these limitations lead to serious concerns regarding the validity of using EC as a conservative tracer for mixing model.

We propose here a few good practices which should provide a better framework to interpret EC data:

- First, we advocate that a perceptual understanding of the hydrogeological processes is essential before initializing any sampling campaigns, in order to correctly identify the major sources of surface and groundwater flow and to assess at which time-scales groundwater drainage occurs. In this regard, the perceptual model presented in Chapt. 3 provides a simple methodology easily reproducible elsewhere.
- While the internal variability within a groundwater source can be estimated based on multiple sampling and on an error propagation model(Lemieux et al., 2008), integrating the temporal variability in the uncertainty quantification is more challenging. Here, Bayesian mixing frameworks appear to be promising to better integrate the spatio-temporal uncertainties in the model (Beria et al., 2020). It this case, samples need to be repeated over time to constrain this evolution.
- Analyzing weathering rates of different solutes may provide interesting information about the sources of groundwater. In particular, the relative ratio between certain solutes may be a good indicator of different processes, as discussed in Chapt. 6. In addition, certain isotopes ratios may also be of particular relevance in alpine environments, such as the ratio of $^{87}Sr/^{86}Sr$, which could provide further information on weathering of different silicate minerals (de Souza et al., 2010; Hindshaw et al., 2011),
- Relying on dissolved solutes, multivariate mixing approaches may provide better information than EC alone (Baraer et al., 2009, 2015; Carroll et al., 2018). If possible, developing multiple mixing models along the stream may provide further insights into the role of different aquifers (Carroll et al., 2018).

7.2.2 Water stable isotopes

In chapter 5, we provided a detailed analysis of the evolution of water stable isotopes. While isotopes are more conservative than EC, the spatio-temporal variability of the end-member sources is also a major challenge. In the corresponding chapter we made the following conclusions:

- The spatial variability in surface snow δ^2H on a single day was found to be similar to the annual δ^2H variability in the stream. This is due to progressive snow melt, snow redistribution and due to the strong snow metamorphic processes which lead to different degrees of isotopic fractionation. Samples taken 10 to 20 cm below the snowpack surface showed completely different values to surface samples, with no clear trends. This suggests that any sound estimation of the snowpack isotopic composition should be based on bulk samples of the whole snow column. This is supported by the extensive work recently provided by Carroll et al. (2022), who considered the isotopic profile of several snow packs.
- We successfully modelled gradual snowmelt isotopic enrichment over an entire melt season, at an hourly resolution, by relying on a relatively parsimonious glacio-hydrological modelling framework. Whilst the model remains based on a statistical calibration, the main physical processes of snow enrichment (snow sublimation, snow melt and rain on snow) could be relatively well constrained and show promising results.

- Nonetheless, we show that in the case the Otemma glaciated catchment, snow and ice melt contributions remain poorly constrained by isotopes only, as their isotopic signals overlap during a substantial part of the season. This observation is likely true for most medium-size glaciers in the Alps, where ice is mainly younger than the last glacial period, as suggested by Jenk et al. (2009).
- The separation of ice and snow appears to be even more complex because the response to rain events at the glacier outlet is complex, and a small rain fraction may largely influence the stream δ^2H signal. This complexity arises from the complex mechanisms of rain integration into the snowpack, which depends on its thermal state, its water holding capacity and thickness (Juras et al., 2017; Rücker et al., 2019a). In addition, we have shown that the glacier preferentially released older water during short rain events, which suggests complex mechanisms of water storage and delayed flow.

Based on these observations, as well as based on observations made in the last research paper (Chapt. 6), we can affirm that relying on water stable isotopes in such environments to identify water sources is difficult. If coupled in a modelling framework, isotopes can help to better constrain some of the internal mechanisms of water transport inside the glacier or within the catchment, but establishing such models is not simple. To the best of our knowledge, few studies have proposed alternative tracers for snow and ice separation, such as Bhatia et al. (2011), who suggests the use atmospherically derived Beryllium-7 (^{7}Be), which could only be measured in snow.

Finally, d-excess was shown to usually be lower in the snowpack than in the ice. This is due to different rates of fractionation of the isotopologues of waters during isotopic enrichment in heavy isotopes in the snowpack (sublimation and melt) (Beria et al., 2018). However, based on observations at the glacier outlet, d-excess appeared to be more similar to ice even when the water is snowmelt-dominated, which indicates complex processes of meltwater refreezing within the snowpack or within the ice and shows that d-excess is not a satisfying conservative tracer.

7.3 Future research and perspectives

In this chapter, we discuss unanswered or new questions which arise from this work and propose some perspectives for future research.

7.3.1 Water stable isotopes in snow- and ice-dominated catchments

In the third research paper (Chapt. 5), building on the previous work by Ala-aho et al. (2017), we developed a physically-based approach that combined a glacio-hydrological model with isotopes to better constrain model calibration and to estimate the shares of snowmelt, icemelt and rain. This research highlighted the promising potential of such a method to simulate snowmelt reliably, especially if the model can be calibrated against a limited but relevant number of isotopic bulk snow samples through the season.

In this context, this approach could provide interesting insights for future glacier mass balance work, in particular in contexts where melt rates are more heterogeneous and more difficult to observe from supraglacial ablation measurements, such as in the case of heavily debris-covered glaciers (Ferguson and Vieli, 2021; Jouvet et al., 2011).

In non-glaciated catchments, a more precise modelling framework of the snowmelt, as proposed here, would allow to better constrain flowpath length and to quantify subsurface flow (Carroll et al., 2019) or to estimate superficial and deep groundwater recharge and exfiltration rates, as suggested by Ala-Aho et al. (2017).

We suggest here that such an isotopic model could be further explored and applied to other contexts. Major uncertainties remain, such as (i) a sound characterization of the bulk snowpack isotopic heterogeneity, although a large contribution was provided recently by Carroll et al. (2022); (ii) the complex mechanisms of rain-on-snow by building on the work of Juras et al. (2017); Rücker et al. (2019a); (iii) exploring the potential improvements of integrating an energy balance snow module; (iv) the complex role of vegetation when considering lower catchments Ala-aho et al. (2017).

7.3.2 Future hydrological response of alpine catchments

This work used multiple approaches to highlight the main mechanisms of groundwater storage and water connectivity within a typical alpine glaciated catchment and offered a more precise conceptual understanding of such areas. To some extent, we were also able to provide an estimate of some of the storage volumes within the catchment. We focused on two major hydrological systems.

First, a detailed assessment of the hydrological importance of outwash plains was provided, along with an assessment of their future evolution. Yet some questions remain.

- How will biogeomorphic feedbacks influence stream channel evolution (Miller and Lane, 2018; Roncoroni et al., 2019) ? Stream channel incision may evolve in the future, driven eventually by reduced discharge variability and volumes and lower bed and suspended loads. The likely result is stream incision. This should lower the water table, further isolating the alluvial plain surface from groundwater supply; but high magnitude reductions in water table elevation, especially in the lower part of the outwash plain, are likely limited due to the hydraulic gradient maintained by the preferential upstream stream infiltration into the aquifer.
- Groundwater drainage rates relied on limited observations and the modelling results therefore depend on limited data concerning the water age or the contribution of older sources. While we believe that the seasonal dynamics are accurate, more detailed insights could be acquired with the use of noble gases, for instance using Radon (^{222}Rn) to estimate short water flowpaths (<15 days), such as in the work of Kobierska et al. (2015a), using noble gas recharge temperature to assess hillslope contributions (Schilling et al., 2021) or the use of ^{4}He to quantify water age (Popp et al., 2021b).

Secondly, this work also highlighted that the largest groundwater storage is most likely located in bedrock fractures, which are connected to subglacial sediments. The processes responsible for its recharge were however not assessed. Since this storage will likely remain the main contributor for baseflow, but also for water supply to small springs on the valley sides, its response to future climate conditions remains unclear. In particular, more research is needed on the following topics:

- How does the behavior of the bedrock aquifer differ in the proglacial zone, where the glacier has recently retreated, compared to the coupled bedrock-subglacial store which we discussed previously ?

  Since drainage is likely not limited by subglacial till and high subglacial water pressure, it is likely that bedrock drainage is faster in the proglacial zone than above the ice. If this holds true, baseflow recession rates should gradually increase with retreating ice volumes, which would have a significant impact on future baseflow generation. Such mechanisms were not observed based on our 12-year recession analysis in Chapt. 3, but may be observable elsewhere based on longer timeseries.

- How, where and when does bedrock recharge occur in such catchments ?

  This is likely one of the major questions for alpine hydrology and is of particular interest since many studies have shown the increasing potential for groundwater storage with elevation. For instance, Staudinger et al. (2017) showed that catchments at high elevation had a larger dynamic storage, but do not specifically point out the underlying mechanisms. Sayama et al. (2011) proposes a conceptual model of this phenomenon showing that steeper, high elevated catchments may store more water in the bedrock due to a smaller area of groundwater seepage in their lower part, which leads to an increased capacity to store larger amounts of groundwater. Jasechko et al. (2016) also showed, based on isotopes, that young water fraction in streamflow decreases with steeper landscapes, potentially due to more fractured bedrock and long flowpaths. In addition, Carroll et al. (2019, 2018) found that baseflow was correlated with steeper slopes and increased SWE accumulation due to (i) a rapid melt of the snowpack, which leads to soil saturation and larger flux to the bedrock, (ii) limited evapotranspiration and (iii) the small soil retention capacity, which promotes subsurface flow until it reaches zones of topographic convergence where bedrock infiltration occurs. On the other hand, Beria (2020)

indicate that cold season recharge is higher at lower elevations and suggest that in the future, more ephemeral snowpacks at higher elevations may increase groundwater recharge.

This illustrates that recharge mechanisms are complex and that the interactions between snowmelt rates, soil infiltration and deeper bedrock recharge may evolve significantly with changes in climatic conditions, especially in alpine environments.

- How will soil and vegetation development influence soil water retention capacity and evapotranspiration ?

  This question links to the previous statement. As vegetation establishment increases with time, changes in sediment granulometry and soil organic matter should reduce infiltration rates and lead to more water retention in the soil pores (Maier et al., 2020), which will increase evapotranspiration and modify groundwater recharge processes. While deeper aquifer characteristics seem to evolve on time-scales of thousands of years (Maier et al., 2021), surface conditions may influence local hydrology.

- How will permafrost and relict rock glacier thaw influence water infiltration and baseflow ?

  In this study, we mostly neglected the role of permafrost, whose effect can be assumed to be limited to the summer months and marginal compared to snowmelt. Rogger et al. (2017) suggested, however, that the loss of permafrost will increase water storage capacity of hillslopes, which may lead to more storage in debris cones. Furthermore, the behavior of glacier melt may be influenced by supraglacial sediments accumulation and the subsequent isolation and burial of large dead ice. Since traditional models do not include such phenomena, relict ice may be preserved during longer periods than what is currently modelled and, depending on the scale of these processes, the gradual thawing of those ice volumes may increase baseflow.

  Although slow colonization from surface vegetation may build shallow soils, changes in sediment granulometry (Maier et al., 2020) and improved channel stability (Roncoroni et al., 2019), deeper aquifer characteristics evolve on time-scales of thousands of years (Maier et al., 2021), making the hydrological conclusions applicable to other fluvial systems.

8 Conclusion

During this research, we have attempted to shed new light on the hydrogeological processes which govern groundwater storage, connectivity and release in a typical high-elevation glaciated catchment. We developed an integrated approach to revisit the groundwater functioning of a series of specific hydro-geomorphological landforms and to link them together in order to provide a detailed perceptual model of the spatial and temporal scales at which they influence the catchment-scale hydrological response. We based our approach on the collection and analysis of a large range of relevant hydrogeological data, which we tried to exploit as optimally as possible via their integration into simple conceptual or more detailed models. Studying the dominant processes through different methods greatly contributed to improve and confirm our interpretation of the complex processes at play and to provide more sound process understanding of the groundwater connectivity between landforms. We finally highlighted the challenges and uncertainties inherent to each field method used and proposed different ways to improve the sampling strategies and to integrate them in relatively simple models.

In the following, we summarize the insight gained into the hydrogeological functioning of recently deglaciated proglacial areas and provide the main take-home messages of this work:

The functioning of recently deglaciated proglacial areas is governed by multiple hydrogeological structures, which release water at different timescales and seasons. Steep superficial landforms mostly transmit rain and meltwater especially during the early melt season and have a rapid discharge recession of the order of days. As water converges towards the bottom of the valley, we observe a diversity of water sources, either generated by rapid surface flow, slow bedrock leakages or rapid subsurface flow in the coarse hillslope deposits. Flatter deposits appear to have a larger potential release groundwater at seasonal timescales (weeks to months) and, in Otemma, such deposits are mostly represented by a braided alluvial floodplain, the outwash plain, which collects hillslope water and show strong stream water - groundwater interactions. However, we estimated a rather limited mobile storage of only about 5 mm, so that such zones have only a limited potential to supply baseflow. Finally, we identified that, with about 75 mm of storage in summer, the largest groundwater aquifer at a seasonal to annual scale is located in bedrock fractures. Results show that baseflow in winter is mostly dominated by the connection of such bedrock aquifer to a subglacial sediment system which slowly release water in winter and maintain a residual baseflow of the order of 0.5 mm d^{-1}.

With the exception of the outwash plain which is in direct contact with the main proglacial stream, most aquifers are recharged by snowmelt during the early season. The gradual decline in snowmelt cover during the summer implies reduced recharge to the hillslope leading to a depletion of most aquifers (lateral deposits, flatter moraine deposits in elevated hanging valleys, bedrock). Here, large rain events may contribute to temporarily increase storage in hillslope but drainage usually occurs in a week. Rainfall also partially contributes to recharge the bedrock aquifer, although the amount of recharge remains unknown. Finally, the outwash plain system displays a unique behavior as its composition reflects that of the proglacial stream. We have shown that only a limited stream discharge (~0.5 mm d^{-1}) maintains high groundwater levels in the outwash plain so that storage remains high until the end of the melt period.

In the context of rapid glacier retreat, we expect the formation of more superficial deposits and flat outwash plains. Here, the formation of potential future outwash plains are not expected to provide a significant additional baseflow, but will maintain relatively high groundwater levels throughout the year. Overall, at the seasonal scale, the larger extent of superficial deposits will not greatly modify the active groundwater storage at the catchment-scale, so that drier conditions are expected, especially in late summer, due to ear-

lier snowmelt and reduced surface available for icemelt. In that perspective, while catchment-scale bedrock storage should not significantly change and bedrock exfiltration will maintain a limited baseflow seasonally, the mechanisms of bedrock recharge and drainage remain more uncertain. In particular the interplay of more liquid precipitation and earlier and more ephemeral snow and early soil development are still poorly understood. Moreover, the gradual disconnection of the bedrock aquifer system from the subglacial system due to glacier recession may also prove to increase drainage rates and thus lead to faster baseflow recession in winter.

With this work, I hope to a have provided a better process understanding of the hydrogeological functioning of a typical high elevated catchment. I also attempted to provide simple methods which are transposable to other elevated areas and guidelines for a better use of natural tracers. Altogether, this should allow future hydrological research to design better perceptual or physical models with more sound hypothesis about their internal processes and thus contribute to better constrain future groundwater fluxes in different alpine context. At the scale of proglacial zones, this work should provide useful information for other fields, such as ecological studies or geomorphological research on sediment transport in such environment. On a more regional scale, we have shown that bedrock storage is likely the largest contributor to baseflow and such aquifer likely extends to catchments at much larger scale, underlining the need to assess its role to provide water downstream especially for studies focusing on extreme events.

References

Achtziger-Zupančič, P., Loew, S., and Mariéthoz, G. (2017). A new global database to improve predictions of permeability distribution in crystalline rocks at site scale. *Journal of Geophysical Research: Solid Earth*, 122:3513–3539. https://doi.org/10.1002/2017JB014106.

Ala-aho, P., Tetzlaff, D., McNamara, J. P., Laudon, H., Kormos, P., and Soulsby, C. (2017). Modeling the isotopic evolution of snowpack and snowmelt: Testing a spatially distributed parsimonious approach. *Water Resources Research*, 53(7):5813–5830. https://doi.org/10.1002/2017WR020650.

Ala-Aho, P., Tetzlaff, D., McNamara, J. P., Laudon, H., and Soulsby, C. (2017). Using isotopes to constrain water flux and age estimates in snow-influenced catchments using the STARR (Spatially distributed Tracer-Aided Rainfall-Runoff) model. *Hydrology and Earth System Sciences*, 21(10):5089–5110. https://doi.org/10.5194/hess-21-5089-2017.

Alley, R., Cuffey, K., Evenson, E., Strasser, J., Lawson, D., and Larson, G. (1997). How glaciers entrain and transport basal sediment: Physical constraints. *Quaternary Science Reviews*, 16(9):1017–1038. https://doi.org/10.1016/S0277-3791(97)00034-6.

Andermann, C., Longuevergne, L., Bonnet, S., Crave, A., Davy, P., and Gloaguen, R. (2012). Impact of transient groundwater storage on the discharge of Himalayan rivers. *Nature Geoscience*, 5(2):127–132. https://doi.org/10.1038/ngeo1356.

Anderson, M. P. (1989). Hydrogeologic facies models to delineate large-scale spatial trends in glacial and glaciofluvial sediments. *Geological Society of America Bulletin*, 101(4):501–511. https://doi.org/10.1130/0016-7606(1989)101<0501:HFMTDL>2.3.CO;2.

Anderson, S. P. (2007). Biogeochemistry of glacial landscape systems. *Annual Review of Earth and Planetary Sciences*, 35:375–399. https://doi.org/10.1146/annurev.earth.35.031306.140033.

Anderson, S. P., Drever, J. I., Frost, C. D., and Holden, P. (2000). Chemical weathering in the foreland of a retreating glacier. *Geochimica et Cosmochimica Acta*, 64:1173–1189. https://doi.org/10.1016/S0016-7037(99)00358-0.

Arthur, D. and Vassilvitskii, S. (2007). k-means++: the advantages of careful seeding. *SODA '07: Proceedings of the eighteenth annual ACM-SIAM symposium on Discrete algorithms*, pages 1027–1035.

Ayala, A., Pellicciotti, F., MacDonell, S., McPhee, J., Vivero, S., Campos, C., and Egli, P. (2016). Modelling the hydrological response of debris-free and debris-covered glaciers to present climatic conditions in the semiarid andes of central chile. *Hydrological Processes*, 30:4036–4058. https://doi.org/10.1002/hyp.10971.

Baewert, H. and Morche, D. (2014). Coarse sediment dynamics in a proglacial fluvial system (Fagge River, Tyrol). *Geomorphology*, 218:88–97. https://doi.org/10.1016/j.geomorph.2013.10.021.

Bakker, M., Post, V., Langevin, C. D., Hughes, J. D., White, J. T., Starn, J. J., and Fienen, M. N. (2016). Scripting MODFLOW Model Development Using Python and FloPy. *Groundwater*, 54(5):733–739. https://doi.org/10.1111/gwat.12413.

Ballantyne, C. K. (2002). Paraglacial geomorphology. *Quaternary Science Reviews*, 21(18-19):1935–2017. https://doi.org/10.1016/S0277-3791(02)00005-7.

Baraer, M., McKenzie, J. M., Mark, B. G., Bury, J., and Knox, S. (2009). Characterizing contributions of glacier melt and groundwater during the dry season in a poorly gauged catchment of the Cordillera Blanca (Peru). *Advances in Geosciences*, 22:41–49. https://doi.org/10.5194/adgeo-22-41-2009.

Baraer, M., Mckenzie, J., Mark, B. G., Gordon, R., Bury, J., Condom, T., Gomez, J., Knox, S., and Fortner, S. K. (2015). Contribution of groundwater to the outflow from ungauged glacierized catchments: A multi-site study in the tropical Cordillera Blanca, Peru. *Hydrological Processes*, 29(11):2561–2581. https://doi.org/10.1002/hyp.10386.

Barandun, M., Huss, M., Usubaliev, R., Azisov, E., Berthier, E., Kääb, A., Bolch, T., and Hoelzle, M. (2018). Multi-decadal mass balance series of three Kyrgyz glaciers inferred from modelling constrained with repeated snow line observations. *Cryosphere*, 12(6):1899–1919. https://doi.org/10.5194/tc-12-1899-2018.

Barnett, T. P., Adam, J. C., and Lettenmaier, D. P. (2005). Potential impacts of a warming climate on water availability in snow-dominated regions. *Nature*, 438(7066):303–309. https://doi.org/10.1038/nature04141.

Benettin, P., Soulsby, C., Birkel, C., Tetzlaff, D., Botter, G., and Rinaldo, A. (2017). Using SAS functions and high-resolution isotope data to unravel travel time distributions in headwater catchments. *Water Resources Research*, 53(3):1864–1878. https://doi.org/10.1002/2016WR020117.

Beniston, M., Farinotti, D., Stoffel, M., Andreassen, L. M., Coppola, E., Eckert, N., Fantini, A., Giacona, F., Hauck, C., Huss, M., Huwald, H., Lehning, M., López-Moreno, J. I., Magnusson, J., Marty, C., Morán-Tejéda, E., Morin, S., Naaim, M., Provenzale, A., Rabatel, A., Six, D., Stötter, J., Strasser, U., Terzago, S., and Vincent, C. (2018). The European mountain cryosphere: A review of its current state, trends, and future challenges. *Cryosphere*, 12(2):759–794. https://doi.org/10.5194/tc-12-759-2018.

Bennett, M. R. (2009). *Glacial geology : ice sheets and landforms*. Chichester : Wiley, 2nd ed.. edition. ISBN 9780470516904.

Berghuijs, W. R., Woods, R. A., and Hrachowitz, M. (2014). A precipitation shift from snow towards rain leads to a decrease in streamflow. *Nature Climate Change*, 4(7):583–586. https://doi.org/10.1038/nclimate2246.

Beria, H. *Improving hydrologic model realism using stable water isotopes in the swiss alps*. Doctoral thesis, University of Lausanne, (2020).

Beria, H., Larsen, J. R., Ceperley, N. C., Michelon, A., Vennemann, T., and Schaefli, B. (2018). Understanding snow hydrological processes through the lens of stable water isotopes. *Wiley Interdisciplinary Reviews: Water*, 5(6):1–23. https://doi.org/10.1002/wat2.1311.

Beria, H., Larsen, J. R., Michelon, A., Ceperley, N. C., and Schaefli, B. (2020). HydroMix v1.0: A new Bayesian mixing framework for attributing uncertain hydrological sources. *Geoscientific Model Development*, 13(5):2433–2450. https://doi.org/10.5194/gmd-13-2433-2020.

Berne, A., Uijlenhoet, R., and Troch, P. A. (2005). Similarity analysis of subsurface flow response of hillslopes with complex geometry. *Water Resources Research*, 41(9):1–10. https://doi.org/10.1029/2004WR003629.

Berthling, I. (2011). Beyond confusion: Rock glaciers as cryo-conditioned landforms. *Geomorphology*, 131(3-4):98–106. https://doi.org/10.1016/j.geomorph.2011.05.002.

Bhatia, M. P., Das, S. B., Kujawinski, E. B., Henderson, P., Burke, A., and Charette, M. A. (2011). Seasonal evolution of water contributions to discharge from a greenland outlet glacier: insight from a new isotope-mixing model. *Journal of Glaciology*, 57:929–941. https://doi.org/10.3189/002214311798043861.

Biemans, H., Siderius, C., Lutz, A. F., Nepal, S., Ahmad, B., Hassan, T., von Bloh, W., Wijngaard, R. R., Wester, P., Shrestha, A. B., and Immerzeel, W. W. (2019). Importance of snow and glacier meltwater for agriculture on the indo-gangetic plain. *Nature Sustainability*, 2:594–601. https://doi.org/10.1038/s41893-019-0305-3.

Boeckli, L., Brenning, A., Gruber, S., and Noetzli, J. (2012). Permafrost distribution in the European Alps: Calculation and evaluation of an index map and summary statistics. *Cryosphere*, 6(4):807–820. https://doi.org/10.5194/tc-6-807-2012.

Bosson, J.-B., Deline, P., Bodin, X., Schoeneich, P., Baron, L., Gardent, M., and Lambiel, C. (2015). The influence of ground ice distribution on geomorphic dynamics since the Little Ice Age in proglacial areas of two cirque glacier systems. *Earth Surface Processes and Landforms*, 40(5):666–680. https://doi.org/10.1002/esp.3666.

Boussinesq, J. (1904). Recherches théoriques sur l'écoulement des nappes d'eau infiltrées dans le sol et sur le débit des sources. *Journal de Mathématiques Pures et Appliquées*, 10:5–78.

Bovis, M. J. (1990). Rock-slope deformation at Affliction Creek, southern Coast Mountains, British Columbia. *Canadian Journal of Earth Sciences*, 27(2):243–254. https://doi.org/10.1139/e90-024.

Brand, G., Pohjola, V., and Hooke, R. L. (1987). Evidence for a Till Layer Beneath Storglaciären, Sweden, Based on Electrical Resistivity Measurements. *Journal of Glaciology*, 33(115):311–314. https://doi.org/10.1017/S0022143000008881.

Brennwald, M. S., Schmidt, M., Oser, J., and Kipfer, R. (2016). A Portable and Autonomous Mass Spectrometric System for On-Site Environmental Gas Analysis. *Environmental Science & Technology*, 50(24):13455–13463. https://doi.org/10.1021/acs.est.6b03669.

Brighenti, S., Tolotti, M., Bruno, M. C., Engel, M., Wharton, G., Cerasino, L., Mair, V., and Bertoldi, W. (2019)a. After the peak water: the increasing influence of rock glaciers on alpine river systems. *Hydrological Processes*, 33(21):2804–2823. https://doi.org/10.1002/hyp.13533.

Brighenti, S., Tolotti, M., Bruno, M. C., Wharton, G., Pusch, M. T., and Bertoldi, W. (2019)b. Ecosystem shifts in Alpine streams under glacier retreat and rock glacier thaw: A review. *Science of the Total Environment*, 675:542–559. https://doi.org/10.1016/j.scitotenv.2019.04.221.

Brunner, M. I., Gurung, A. B., Zappa, M., Zekollari, H., Farinotti, D., and Stähli, M. (2019). Present and future water scarcity in switzerland: Potential for alleviation through reservoirs and lakes. *Science of The Total Environment*, 666:1033–1047. https://doi.org/10.1016/j.scitotenv.2019.02.169.

Brunner, P., Therrien, R., Renard, P., Simmons, C. T., and Franssen, H.-J. H. (2017). Advances in understanding river-groundwater interactions. *Reviews of Geophysics*, 55(3):818–854. https://doi.org/10.1002/2017RG000556.

Burri, M., Allimann, M., Chessex, R., Piaz, G. V. D., Valle, G. D., Bois, L. D., Gouffon, Y., A., G., Hagen, T., Krummenacher, D., and Looser, M.-O. (1999). Chanrion (cn 1346) avec partie nord de la feuille mont vélan (cn 1366). *Atlas géologique de la Suisse 1:25 000*.

Buytaert, W., Moulds, S., Acosta, L., De Bièvre, B., Olmos, C., Villacis, M., Tovar, C., and Verbist, K. M. J. (2017). Glacial melt content of water use in the tropical Andes. *Environmental Research Letters*, 12(11). https://doi.org/10.1088/1748-9326/aa926c.

Caballero, Y., Jomelli, V., Chevallier, P., and Ribstein, P. (2002). Hydrological characteristics of slope deposits in high tropical mountains (Cordillera Real, Bolivia). *CATENA*, 47(2):101–116. https://doi.org/10.1016/S0341-8162(01)00179-5.

Carrivick, J. L. and Heckmann, T. (2017). Short-term geomorphological evolution of proglacial systems. *Geomorphology*, 287:3–28. https://doi.org/10.1016/j.geomorph.2017.01.037.

Carrivick, J. L., Heckmann, T., Turner, A., and Fischer, M. (2018). An assessment of landform composition and functioning with the first proglacial systems dataset of the central European Alps. *Geomorphology*, 321:117–128. https://doi.org/10.1016/j.geomorph.2018.08.030.

Carroll, R. W., Deems, J. S., Niswonger, R., Schumer, R., and Williams, K. H. (2019). The Importance of Interflow to Groundwater Recharge in a Snowmelt-Dominated Headwater Basin. *Geophysical Research Letters*, 46(11):5899–5908. https://doi.org/10.1029/2019GL082447.

Carroll, R. W. H., Bearup, L. A., Brown, W., Dong, W., Bill, M., and Willlams, K. H. (2018). Factors controlling seasonal groundwater and solute flux from snow-dominated basins. *Hydrological Processes*, 32:2187–2202. https://doi.org/10.1002/hyp.13151.

Carroll, R. W. H., Deems, J., Maxwell, R., Sprenger, M., Brown, W., Newman, A., Beutler, C., Bill, M., Hubbard, S. S., and Williams, K. H. (2022). Variability in observed stable water isotopes in snowpack across a mountainous watershed in colorado. *Hydrological Processes*, 36. https://doi.org/10.1002/hyp.14653.

Clark, M. P., Rupp, D. E., Woods, R. A., Tromp-van Meerveld, H. J., Peters, N. E., and Freer, J. E. (2009). Consistency between hydrological models and field observations: linking processes at the hillslope scale to hydrological responses at the watershed scale. *Hydrological Processes*, 23(2):311–319. https://doi.org/10.1002/hyp.7154.

Clow, D., Schrott, L., Webb, R., Campbell, D., Torizzo, A., and Dornblaser, M. (2003). Ground Water Occurrence and Contributions to Streamflow in an Alpine Catchment, Colorado Front Range. *Ground Water*, 41 (7):937–950. https://doi.org/10.1111/j.1745-6584.2003.tb02436.x.

Clow, D. W. and Mast, M. A. (2010). Mechanisms for chemostatic behavior in catchments: Implications for co2 consumption by mineral weathering. *Chemical Geology*, 269:40–51. https://doi.org/10.1016/j.chemgeo.2009.09.014.

Cochand, M., Christe, P., Ornstein, P., and Hunkeler, D. (2019). Groundwater Storage in High Alpine Catchments and Its Contribution to Streamflow. *Water Resources Research*, 55(4):2613–2630. https://doi.org/10.1029/2018WR022989.

Coplen, T. B. (1994). Reporting of stable hydrogen, carbon, and oxygen isotopic abundances (technical report). *Pure and Applied Chemistry*, 66:273–276. https://doi.org/10.1351/pac199466020273.

Costa, D., Sexstone, G. A., Pomeroy, J. W., Campbell, D. H., Clow, D. W., and Mast, A. (2020). Preferential elution of ionic solutes in melting snowpacks: Improving process understanding through field observations and modeling in the rocky mountains. *Science of The Total Environment*, 710:136273. https://doi.org/10.1016/j.scitotenv.2019.136273.

Covington, M. D., Banwell, A. F., Gulley, J., Saar, M. O., Willis, I., and Wicks, C. M. (2012). Quantifying the effects of glacier conduit geometry and recharge on proglacial hydrograph form. *Journal of Hydrology*, 414-415:59–71. https://doi.org/10.1016/j.jhydrol.2011.10.027.

Cozzetto, K. D., Bencala, K. E., Gooseff, M. N., and McKnight, D. M. (2013). The influence of stream thermal regimes and preferential flow paths on hyporheic exchange in a glacial meltwater stream. *Water Resources Research*, 49(9):5552–5569. https://doi.org/10.1002/wrcr.20410.

Crossman, J., Bradley, C., Boomer, I., and Milner, A. (2011). Water flow dynamics of groundwater-fed streams and their ecological significance in a glacierized catchment. *Arctic, Antarctic, and Alpine Research*, 43(3): 364–379. https://doi.org/10.1657/1938-4246-43.3.364.

de Souza, G. F., Reynolds, B. C., Kiczka, M., and Bourdon, B. (2010). Evidence for mass-dependent isotopic fractionation of strontium in a glaciated granitic watershed. *Geochimica et Cosmochimica Acta*, 74:2596–2614. https://doi.org/10.1016/j.gca.2010.02.012.

Dewandel, B., Lachassagne, P., Bakalowicz, M., Weng, P., and Al-Malki, A. (2003). Evaluation of aquifer thickness by analysing recession hydrographs. Application to the Oman ophiolite hard-rock aquifer. *Journal of Hydrology*, 274(1-4):248–269. https://doi.org/10.1016/S0022-1694(02)00418-3.

Doherty, J. (2015). Calibration and Uncertainty Analysis for Complex Environmental Models. Watermark Numerical Computing, Brisbane, Australia.

Duethmann, D., Blöschl, G., and Parajka, J. (2020). Why does a conceptual hydrological model fail to correctly predict discharge changes in response to climate change? *Hydrology and Earth System Sciences*, 24: 3493–3511. https://doi.org/10.5194/hess-24-3493-2020.

Dusik, J.-M., Neugirg, F., and Haas, F. (2019). Geomorphology of Proglacial Systems. In Heckmann, T. and Morche, D., editors, *Geomorphology of Proglacial Systems. Geography of the Physical Environment.*, pages 177–196. Springer, Cham. ISBN 978-3-319-94184-4. https://doi.org/10.1007/978-3-319-94184-4_11.

Egli, P. E., Irving, J., and Lane, S. N. (2021). Characterization of subglacial marginal channels using 3-d analysis of high-density ground-penetrating radar data. *Journal of Glaciology*, 67:759–772. https://doi.org/10.1017/jog.2021.26.

Engel, M., Penna, D., Bertoldi, G., Dell'Agnese, A., Soulsby, C., and Comiti, F. (2016). Identifying run-off contributions during melt-induced run-off events in a glacierized alpine catchment. *Hydrological Processes*, 30(3):343–364. https://doi.org/10.1002/hyp.10577.

Engel, M., Penna, D., Bertoldi, G., Vignoli, G., Tirler, W., and Comiti, F. (2019). Controls on spatial and temporal variability in streamflow and hydrochemistry in a glacierized catchment. *Hydrology and Earth System Sciences*, 23(4):2041–2063. https://doi.org/10.5194/hess-23-2041-2019.

Evans, D., Phillips, E., Hiemstra, J., and Auton, C. (2006). Subglacial till: Formation, sedimentary characteristics and classification. *Earth-Science Reviews*, 78(1-2):115–176. https://doi.org/10.1016/j.earscirev.2006.04.001.

Eyles, N., Eyles, C. H., and Miall, A. D. (1983). Lithofacies types and vertical profile models; an alternative approach to the description and environmental interpretation of glacial diamict and diamictite sequences. *Sedimentology*, 30(3):393–410. https://doi.org/10.1111/j.1365-3091.1983.tb00679.x.

Farinotti, D., Pistocchi, A., and Huss, M. (2016). From dwindling ice to headwater lakes: Could dams replace glaciers in the european alps? *Environmental Research Letters*, 11. https://doi.org/10.1088/1748-9326/11/5/054022.

Farinotti, D., Huss, M., Fürst, J. J., Landmann, J., Machguth, H., Maussion, F., and Pandit, A. (2019)a. A consensus estimate for the ice thickness distribution of all glaciers on Earth. *Nature Geoscience*, 12(March): 168–173. https://doi.org/10.1038/s41561-019-0300-3.

Farinotti, D., Round, V., Huss, M., Compagno, L., and Zekollari, H. (2019)b. Large hydropower and water-storage potential in future glacier-free basins. *Nature*, 575(7782):341–344. https://doi.org/10.1038/s41586-019-1740-z.

Fatichi, S., Rimkus, S., Burlando, P., and Bordoy, R. (2014). Does internal climate variability overwhelm climate change signals in streamflow? the upper po and rhone basin case studies. *Science of The Total Environment*, 493:1171–1182. https://doi.org/10.1016/j.scitotenv.2013.12.014.

Fayad, A., Gascoin, S., Faour, G., López-Moreno, J. I., Drapeau, L., Page, M. L., and Escadafal, R. (2017). Snow hydrology in Mediterranean mountain regions: A review. *Journal of Hydrology*, 551:374–396. https://doi.org/10.1016/j.jhydrol.2017.05.063.

Fellman, J. B., Hood, E., Raymond, P. A., Hudson, J., Bozeman, M., and Arimitsu, M. (2015). Evidence for the assimilation of ancient glacier organic carbon in a proglacial stream food web. *Limnology and Oceanography*, 60(4):1118–1128. https://doi.org/10.1002/lno.10088.

Feng, X., Taylor, S., Renshaw, C. E., and Kirchner, J. W. (2002). Isotopic evolution of snowmelt 1. a physically based one-dimensional model. *Water Resources Research*, 38:35–1–35–8. https://doi.org/10.1029/2001WR000814.

Ferguson, J. C. and Vieli, A. (2021). Modelling steady states and the transient response of debris-covered glaciers. *The Cryosphere*, 15:3377–3399. https://doi.org/10.5194/tc-15-3377-2021.

Fischer, M., Huss, M., Barboux, C., and Hoelzle, M. (2014). The New Swiss Glacier Inventory SGI2010: Relevance of Using High-Resolution Source Data in Areas Dominated by Very Small Glaciers. *Arctic, Antarctic, and Alpine Research*, 46(4):933–945. https://doi.org/10.1657/1938-4246-46.4.933.

Fischer, U. H. and Hubbard, B. (1999). Subglacial sediment textures: Character and evolution at Haut Glacier d'Arolla, Switzerland. *Annals of Glaciology*, 28(1987):241–246. https://doi.org/10.3189/172756499781821977.

Flowers, G. E. (2015). Modelling water flow under glaciers and ice sheets. *Proceedings of the Royal Society A: Mathematical, Physical and Engineering Sciences*, 471(2176):20140907. https://doi.org/10.1098/rspa.2014.0907.

Flowers, G. E. and Clarke, G. K. C. (2002). A multicomponent coupled model of glacier hydrology 1. Theory and synthetic examples. *Journal of Geophysical Research: Solid Earth*, 107(B11):ECV 9—-1—-ECV 9—-17. https://doi.org/10.1029/2001jb001122.

Fountain, A. G. (1994). Borehole water-level variations and implications for the subglacial hydraulics of South Cascade Glacier, Washington State, USA. *Journal of Glaciology*, 40(135):293–304. https://doi.org/10.1017/S0022143000007383.

Frey, H., Machguth, H., Huss, M., Huggel, C., Bajracharya, S., Bolch, T., Kulkarni, A., Linsbauer, A., Salzmann, N., and Stoffel, M. (2014). Estimating the volume of glaciers in the Himalayan–Karakoram region using different methods. *The Cryosphere*, 8(6):2313–2333. https://doi.org/10.5194/tc-8-2313-2014.

Gabbi, J., Farinotti, D., Bauder, A., and Maurer, H. (2012). Ice volume distribution and implications on runoff projections in a glacierized catchment. *Hydrology and Earth System Sciences*, 16(12):4543–4556. https://doi.org/10.5194/hess-16-4543-2012.

Gabbi, J., Carenzo, M., Pellicciotti, F., Bauder, A., and Funk, M. (2014). A comparison of empirical and physically based glacier surface melt models for long-term simulations of glacier response. *Journal of Glaciology*, 60(224):1199–1207. https://doi.org/10.3189/2014JoG14J011.

Galewsky, J. (2009). Orographic precipitation isotopic ratios in stratified atmospheric flows: Implications for paleoelevation studies. *Geology*, 37(9):791–794. https://doi.org/10.1130/G30008A.1.

Gärtner-Roer, I. and Bast, A. (2019). (Ground) Ice in the Proglacial Zone. In Heckmann, T. and Morche, D., editors, *Geomorphology of Proglacial Systems. Geography of the Physical Environment.*, pages 85–98. Springer, Cham. ISBN 978-3-319-94184-4. https://doi.org/10.1007/978-3-319-94184-4_6.

GLAMOS (1881-2020). The Swiss Glaciers 1880-2018/19, Glaciological Reports No 1-140, Yearbooks of the Cryospheric Commission of the Swiss Academy of Sciences (SCNAT), published since 1964 by VAW / ETH Zurich. https://doi.org/10.18752/glrep_series.

Glas, R., Lautz, L., McKenzie, J., Mark, B., Baraer, M., Chavez, D., and Maharaj, L. (2018). A review of the current state of knowledge of proglacial hydrogeology in the Cordillera Blanca, Peru. *WIREs Water*, 5(5):e1299. https://doi.org/10.1002/wat2.1299.

Godsey, S. E., Kirchner, J. W., and Clow, D. W. (2009). Concentration-discharge relationships reflect chemostatic characteristics of us catchments. *Hydrological Processes*, 23:1844–1864. https://doi.org/10.1002/hyp.7315.

Gordon, R. P., Lautz, L. K., McKenzie, J. M., Mark, B. G., Chavez, D., and Baraer, M. (2015). Sources and pathways of stream generation in tropical proglacial valleys of the Cordillera Blanca, Peru. *Journal of Hydrology*, 522:628–644. https://doi.org/10.1016/j.jhydrol.2015.01.013.

Grab, M., Mattea, E., Bauder, A., Huss, M., Rabenstein, L., Hodel, E., Linsbauer, A., Langhammer, L., Schmid, L., Church, G., Hellmann, S., Délèze, K., Schaer, P., Lathion, P., Farinotti, D., and Maurer, H. (2021). Ice thickness distribution of all Swiss glaciers based on extended ground-penetrating radar data and glaciological modeling. *Journal of Glaciology*, 67(266):1074–1092. https://doi.org/10.1017/jog.2021.55.

Grämiger, L. M., Moore, J. R., Gischig, V. S., Ivy-Ochs, S., and Loew, S. (2017). Beyond debuttressing: Mechanics of paraglacial rock slope damage during repeat glacial cycles. *Journal of Geophysical Research: Earth Surface*, 122(4):1004–1036. https://doi.org/10.1002/2016JF003967.

Greuell, W. and Böhm, R. (1998). 2 m temperatures along melting mid-latitude glaciers, and implications for the sensitivity of the mass balance to variations in temperature. *Journal of Glaciology*, 44:9–20. https://doi.org/10.3189/S0022143000002306.

GTZ. (1989). *Deutsche Gesellschaft für Technische Zusammenarbeit (GTZ) GmbH. Planning of Water and Hydropower Intake Structures*. ISBN 3-528-02042-3.

Guido, Z., McIntosh, J. C., Papuga, S. A., and Meixner, T. (2016). Seasonal glacial meltwater contributions to surface water in the Bolivian Andes: A case study using environmental tracers. *Journal of Hydrology: Regional Studies*, 8:260–273. https://doi.org/10.1016/j.ejrh.2016.10.002.

Guillon, H., Mugnier, J.-L., Buoncristiani, J.-F., Carcaillet, J., Godon, C., Prud'homme, C., van der Beek, P., and Vassallo, R. (2015). Improved discrimination of subglacial and periglacial erosion using 10 Be concentration measurements in subglacial and supraglacial sediment load of the Bossons glacier (Mont Blanc massif, France). *Earth Surface Processes and Landforms*, 40(9):1202–1215. https://doi.org/10.1002/esp.3713.

Gupta, H. V., Kling, H., Yilmaz, K. K., and Martinez, G. F. (2009). Decomposition of the mean squared error and nse performance criteria: Implications for improving hydrological modelling. *Journal of Hydrology*, 377:80–91. https://doi.org/10.1016/j.jhydrol.2009.08.003.

Haeberli, W. and Weingartner, R. (2020). In full transition: Key impacts of vanishing mountain ice on water-security at local to global scales. *Water Security*, 11:100074. https://doi.org/10.1016/j.wasec.2020.100074.

Haeberli, W., Hallet, B., Arenson, L., Elconin, R., Humlum, O., Kääb, A., Kaufmann, V., Ladanyi, B., Matsuoka, N., Springman, S., and Mühll, D. V. (2006). Permafrost creep and rock glacier dynamics. *Permafrost and Periglacial Processes*, 17(3):189–214. https://doi.org/10.1002/ppp.561.

Haeberli, W., Schaub, Y., and Huggel, C. (2017). Increasing risks related to landslides from degrading permafrost into new lakes in de-glaciating mountain ranges. *Geomorphology*, 293:405–417. https://doi.org/10.1016/j.geomorph.2016.02.009.

Hallet, B., Hunter, L., and Bogen, J. (1996). Rates of erosion and sediment evacuation by glaciers: A review of field data and their implications. *Global and Planetary Change*, 12(1-4):213–235. https://doi.org/10.1016/0921-8181(95)00021-6.

Hammer, K. M. and Smith, N. D. (1983). Sediment production and transport in a proglacial stream: Hilda Glacier, Alberta, Canada. *Boreas*, 12(2):91–106. https://doi.org/10.1111/j.1502-3885.1983.tb00441.x.

Hanus, S., Hrachowitz, M., Zekollari, H., Schoups, G., Vizcaino, M., and Kaitna, R. (2021). Future changes in annual, seasonal and monthly runoff signatures in contrasting alpine catchments in austria. *Hydrology and Earth System Sciences*, 25:3429–3453. https://doi.org/10.5194/hess-25-3429-2021.

Harbor, J. (1997). Influence of subglacial drainage conditions on the velocity distribution within a glacier cross section. *Geology*, 25(8):739–742. https://doi.org/10.1130/0091-7613(1997)025<0739:IOSDCO>2.3.CO;2.

Harman, C. and Sivapalan, M. (2009)a. A similarity framework to assess controls on shallow subsurface flow dynamics in hillslopes. *Water Resources Research*, 45(1):1–12. https://doi.org/10.1029/2008WR007067.

Harman, C. and Sivapalan, M. (2009)b. Effects of hydraulic conductivity variability on hillslope-scale shallow subsurface flow response and storage-discharge relations. *Water Resources Research*, 45(1):1–15. https://doi.org/10.1029/2008WR007228.

Harman, C. J., Sivapalan, M., and Kumar, P. (2009). Power law catchment-scale recessions arising from heterogeneous linear small-scale dynamics. *Water Resources Research*, 45(9):1–13. https://doi.org/10.1029/2008WR007392.

Harrington, J. S., Mozil, A., Hayashi, M., and Bentley, L. R. (2018). Groundwater flow and storage processes in an inactive rock glacier. *Hydrological Processes*, 32(20):3070–3088. https://doi.org/10.1002/hyp.13248.

Hart, J. K. (1998). The deforming bed/debris-rich basal ice continuum and its implications for the formation of glacial landforms (Flutes) and sediments (Melt-out till). *Quaternary Science Reviews*, 17(8):737–754. https://doi.org/10.1016/S0277-3791(98)00065-6.

Hartmann, A., Semenova, E., Weiler, M., and Blume, T. (2020). Field observations of soil hydrological flow path evolution over 10 millennia. *Hydrology and Earth System Sciences*, 24(6):3271–3288. https://doi.org/10.5194/hess-24-3271-2020.

Hauer, F. R., Locke, H., Dreitz, V. J., Hebblewhite, M., Lowe, W. H., Muhlfeld, C. C., Nelson, C. R., Proctor, M. F., and Rood, S. B. (2016). Gravel-bed river floodplains are the ecological nexus of glaciated mountain landscapes. *Science Advances*, 2(6):1–14. https://doi.org/10.1126/sciadv.1600026.

Hayashi, M. (2020). Alpine Hydrogeology: The Critical Role of Groundwater in Sourcing the Headwaters of the World. *Groundwater*, 58(4):498–510. https://doi.org/10.1111/gwat.12965.

He, Z., Unger-Shayesteh, K., Vorogushyn, S., Weise, S. M., Kalashnikova, O., Gafurov, A., Duethmann, D., Barandun, M., and Merz, B. (2019). Constraining hydrological model parameters using water isotopic compositions in a glacierized basin, Central Asia. *Journal of Hydrology*, 571(November 2018):332–348. https://doi.org/10.1016/j.jhydrol.2019.01.048.

Heckmann, T. and Morche, D. (2019). *Geomorphology of Proglacial Systems*. Geography of the Physical Environment. Springer International Publishing, Cham. ISBN 978-3-319-94182-0. https://doi.org/10.1007/978-3-319-94184-4.

Heckmann, T., Mccoll, S., and Morche, D. (2016). Retreating ice: Research in pro-glacial areas matters. *Earth Surface Processes and Landforms*, 41(2):271–276. https://doi.org/10.1002/esp.3858.

Heckmann, T., Morche, D., and Becht, M. (2019). Introduction. In *Geomorphology of Proglacial Systems. Geography of the Physical Environment.*, pages 1–19. Springer. ISBN 978-3-319-94184-4. https://doi.org/10.1007/978-3-319-94184-4_1.

Hindshaw, R. S., Tipper, E. T., Reynolds, B. C., Lemarchand, E., Wiederhold, J. G., Magnusson, J., Bernasconi, S. M., Kretzschmar, R., and Bourdon, B. (2011). Hydrological control of stream water chemistry in a glacial catchment (Damma Glacier, Switzerland). *Chemical Geology*, 285(1-4):215–230. https://doi.org/10.1016/j.chemgeo.2011.04.012.

Hock, R. (1999). Including Potential Direct Solar Radiation. *Journal of Glaciology*, 45(149):101–111.

Hogarth, W. L., Li, L., Lockington, D. A., Stagnitti, F., Parlange, M. B., Barry, D. A., Steenhuis, T. S., and Parlange, J.-Y. (2014). Analytical approximation for the recession of a sloping aquifer. *Water Resources Research*, 50(11):8564–8570. https://doi.org/10.1002/2014WR016084.

Hood, E., Battin, T. J., Fellman, J., O'neel, S., and Spencer, R. G. (2015). Storage and release of organic carbon from glaciers and ice sheets. *Nature Geoscience*, 8(2):91–96. https://doi.org/10.1038/ngeo2331.

Hood, J. L. and Hayashi, M. (2015). Characterization of snowmelt flux and groundwater storage in an alpine headwater basin. *Journal of Hydrology*, 521:482–497. https://doi.org/10.1016/j.jhydrol.2014.12.041.

Hubbard, B. P., Sharp, M. J., Willis, I. C., Nielsen, M. K., and Smart, C. C. (1995). Borehole water-level variations and the structure of the subglacial hydrological system of Haut Glacier d'Arolla, Valais, Switzerland. *Journal of Glaciology*, 41(139):572–583. https://doi.org/10.1017/S0022143000034894.

Hugentobler, M., Loew, S., Aaron, J., Roques, C., and Oestreicher, N. (2020). Borehole monitoring of thermo-hydro-mechanical rock slope processes adjacent to an actively retreating glacier. *Geomorphology*, 362: 107190. https://doi.org/10.1016/j.geomorph.2020.107190.

Hugentobler, M., Aaron, J., Loew, S., and Roques, C. (2022). Hydro-mechanical interactions of a rock slope with a retreating temperate valley glacier. *Journal of Geophysical Research: Earth Surface*, 127. https://doi.org/10.1029/2021JF006484.

Huss, M. (2011). Present and future contribution of glacier storage change to runoff from macroscale drainage basins in europe. *Water Resour. Res.*, 47(7):W07511. https://doi.org/10.1029/2010WR010299.

Huss, M. and Hock, R. (2018). Global-scale hydrological response to future glacier mass loss. *Nature Climate Change*, 8(2):135–140. https://doi.org/10.1038/s41558-017-0049-x.

Huss, M., Farinotti, D., Bauder, A., and Funk, M. (2008). Modelling runoff from highly glacierized alpine drainage basins in a changing climate. *Hydrological Processes*, 22(19):3888–3902. https://doi.org/10.1002/hyp.7055.

Huss, M., Bookhagen, B., Huggel, C., Jacobsen, D., Bradley, R. S., Clague, J. J., Vuille, M., Buytaert, W., Cayan, D. R., Greenwood, G., Mark, B. G., Milner, A. M., Weingartner, R., and Winder, M. (2017). Toward mountains without permanent snow and ice. *Earth's Future*, 5(5):418–435. https://doi.org/10.1002/2016EF000514.

Immerzeel, W. W., van Beek, L. P. H., Konz, M., Shrestha, A. B., and Bierkens, M. F. P. (2012). Hydrological response to climate change in a glacierized catchment in the himalayas. *Climatic Change*, 110:721–736. https://doi.org/10.1007/s10584-011-0143-4.

Immerzeel, W. W., Lutz, A. F., Andrade, M., Bahl, A., Biemans, H., Bolch, T., Hyde, S., Brumby, S., Davies, B. J., Elmore, A. C., Emmer, A., Feng, M., Fernández, A., Haritashya, U., Kargel, J. S., Koppes, M., Kraaijenbrink, P. D. A., Kulkarni, A. V., Mayewski, P. A., Nepal, S., Pacheco, P., Painter, T. H., Pellicciotti, F., Rajaram, H., Rupper, S., Sinisalo, A., Shrestha, A. B., Viviroli, D., Wada, Y., Xiao, C., Yao, T., and Baillie, J. E. M. (2020). Importance and vulnerability of the world's water towers. *Nature*, 577(7790):364–369. https://doi.org/10.1038/s41586-019-1822-y.

Iverson, N. R., Jansson, P., and Hooke, R. L. (1994). In-situ measurement of the strength of deforming subglacial till. *Journal of Glaciology*, 40(136):497–503. https://doi.org/10.1017/S0022143000012375.

Jasechko, S. (2019). Global Isotope Hydrogeology—Review. *Reviews of Geophysics*, 57(3):835–965. https://doi.org/10.1029/2018RG000627.

Jasechko, S., Kirchner, J. W., Welker, J. M., and McDonnell, J. J. (2016). Substantial proportion of global streamflow less than three months old. *Nature Geoscience*, 9:126–129. https://doi.org/10.1038/ngeo2636.

Jefferson, A., Nolin, A., Lewis, S., and Tague, C. (2008). Hydrogeologic controls on streamflow sensitivity to climate variation. *Hydrological Processes*, 22(22):4371–4385. https://doi.org/10.1002/hyp.7041.

Jenk, T. M., Szidat, S., Bolius, D., Sigl, M., Gäggeler, H. W., Wacker, L., Ruff, M., Barbante, C., Boutron, C. F., and Schwikowski, M. (2009). A novel radiocarbon dating technique applied to an ice core from the Alps indicating late Pleistocene ages. *Journal of Geophysical Research Atmospheres*, 114(14):1–8. https://doi.org/10.1029/2009JD011860.

Jenkin, M., Mancini, D., Miesen, F., Hofmann, M., Hubbard, B., Herman, F., and Lane, S. N. (2022). Subglacial export of coarse sediment from temperate alpine glaciers by meltwater. *EGU General Assembly 2022, Vienna, Austria, 23–27 May 2022, EGU22-3854*. https://doi.org/https://doi.org/10.5194/egusphere-egu22-3854.

Jordi, C., Doetsch, J., Günther, T., Schmelzbach, C., and Robertsson, J. O. (2018). Geostatistical regularization operators for geophysical inverse problems on irregular meshes. *Geophysical Journal International*, 213 (2):1374–1386. https://doi.org/10.1093/gji/ggy055.

Jouvet, G., Huss, M., Funk, M., and Blatter, H. (2011). Modelling the retreat of grosser aletschgletscher, switzerland, in a changing climate. *Journal of Glaciology*, 57:1033–1045. https://doi.org/10.3189/002214311798843359.

Juras, R., Würzer, S., Pavlásek, J., Vitvar, T., and Jonas, T. (2017). Rainwater propagation through snowpack during rain-on-snow sprinkling experiments under different snow conditions. *Hydrology and Earth System Sciences*, 21:4973–4987. https://doi.org/10.5194/hess-21-4973-2017.

Kalbus, E., Reinstorf, F., and Schirmer, M. (2006). Measuring methods for groundwater - Surface water interactions: A review. *Hydrology and Earth System Sciences*, 10(6):873–887. https://doi.org/10.5194/hess-10-873-2006.

Käser, D. and Hunkeler, D. (2016). Contribution of alluvial groundwater to the outflow of mountainous catchments. *Water Resources Research*, 52(2):680–697. https://doi.org/10.1002/2014WR016730.

Kern, Z., Kohán, B., and Leuenberger, M. (2014). Precipitation isoscape of high reliefs: Interpolation scheme designed and tested for monthly resolved precipitation oxygen isotope records of an Alpine domain. *Atmospheric Chemistry and Physics*, 14(4):1897–1907. https://doi.org/10.5194/acp-14-1897-2014.

Kiewiet, L., von Freyberg, J., and van Meerveld, H. J. (2019). Spatiotemporal variability in hydrochemistry of shallow groundwater in a small pre-alpine catchment: The importance of landscape elements. *Hydrological Processes*, 33(19):2502–2522. https://doi.org/10.1002/hyp.13517.

Kipfer, R., Aeschbach-hertig, W., Peeters, F., and Stute, M. (2002). Noble Gases in Lakes and Ground Waters. *Reviews in Mineralogy and Geochemistry*, 47(1):615–700. https://doi.org/10.2138/rmg.2002.47.14.

Kirchner, J. W. (2003). A double paradox in catchment hydrology and geochemistry. *Hydrological Processes*, 17(4):871–874. https://doi.org/10.1002/hyp.5108.

Kirchner, J. W. (2009). Catchments as simple dynamical systems: Catchment characterization, rainfall-runoff modeling, and doing hydrology backward. *Water Resources Research*, 45(2). https://doi.org/10.1029/2008WR006912.

Kirchner, J. W., Godsey, S. E., Solomon, M., Osterhuber, R., McConnell, J. R., and Penna, D. (2020). The pulse of a montane ecosystem: Coupling between daily cycles in solar flux, snowmelt, transpiration, groundwater, and streamflow at Sagehen Creek and Independence Creek, Sierra Nevada, USA. *Hydrology and Earth System Sciences*, 24(11):5095–5123. https://doi.org/10.5194/hess-24-5095-2020.

Klaus, J. and McDonnell, J. (2013). Hydrograph separation using stable isotopes: Review and evaluation. *Journal of Hydrology*, 505:47–64. https://doi.org/10.1016/j.jhydrol.2013.09.006.

Klein, G., Vitasse, Y., Rixen, C., Marty, C., and Rebetez, M. (2016). Shorter snow cover duration since 1970 in the Swiss Alps due to earlier snowmelt more than to later snow onset. *Climatic Change*, 139(3-4):637–649. https://doi.org/10.1007/s10584-016-1806-y.

Knoben, W. J. M., Freer, J. E., and Woods, R. A. (2019). Technical note: Inherent benchmark or not? comparing nash–sutcliffe and kling–gupta efficiency scores. *Hydrology and Earth System Sciences*, 23:4323–4331. https://doi.org/10.5194/hess-23-4323-2019.

Kobierska, F., Jonas, T., Griessinger, N., Hauck, C., Huxol, S., and Bernasconi, S. M. (2015)a. A multi-method field experiment to determine local groundwater flow in a glacier forefield. *Hydrological Processes*, 29(6): 817–827. https://doi.org/10.1002/hyp.10188.

Kobierska, F., Jonas, T., Kirchner, J. W., and Bernasconi, S. M. (2015)b. Linking baseflow separation and groundwater storage dynamics in an alpine basin (Dammagletscher, Switzerland). *Hydrology and Earth System Sciences*, 19(8):3681–3693. https://doi.org/10.5194/hess-19-3681-2015.

Kraaijenbrink, P. D., Bierkens, M. F., Lutz, A. F., and Immerzeel, W. W. (2017). Impact of a global temperature rise of 1.5 degrees celsius on asia's glaciers. *Nature*, 549:257–260. https://doi.org/10.1038/nature23878.

Kulessa, B., Hubbard, B., Williamson, M., and Brown, G. H. (2005). Hydrogeological analysis of slug tests in glacier boreholes. *Journal of Glaciology*, 51(173):269–280. https://doi.org/10.3189/172756505781829458.

Kurylyk, B. L. and Hayashi, M. (2017). Inferring hydraulic properties of alpine aquifers from the propagation of diurnal snowmelt signals. *Water Resources Research*, 53(5):4271–4285. https://doi.org/10.1002/2016WR019651.

Lane, S., Richards, K., and Chandler, J. (1996). Discharge and sediment supply controls on erosion and deposition in a dynamic alluvial channel. *Geomorphology*, 15(1):1–15. https://doi.org/10.1016/0169-555X(95)00113-J.

Lane, S. N. (2014). Acting, predicting and intervening in a socio-hydrological world. *Hydrology and Earth System Sciences*, 18:927–952. https://doi.org/10.5194/hess-18-927-2014.

Lane, S. N. and Nienow, P. W. (2019). Decadal-Scale Climate Forcing of Alpine Glacial Hydrological Systems. *Water Resources Research*, 55(3):2478–2492. https://doi.org/10.1029/2018WR024206.

Lane, S. N., Bakker, M., Gabbud, C., Micheletti, N., and Saugy, J. N. (2017). Sediment export, transient landscape response and catchment-scale connectivity following rapid climate warming and Alpine glacier recession. *Geomorphology*, 277:210–227. https://doi.org/10.1016/j.geomorph.2016.02.015.

Langevin, C., Hughes, J., Provost, A., Russcher, M., Niswonger, R., Panday, S., Merrick, D., and Banta, E. (2022). MODFLOW 6 Modular Hydrologic Model version 6.3.0: U.S. Geological Survey Software Release, 4 March 2022. https://doi.org/https://doi.org/10.5066/P97FFF9M.

Langston, G., Bentley, L. R., Hayashi, M., McClymont, A., and Pidlisecky, A. (2011). Internal structure and hydrological functions of an alpine proglacial moraine. *Hydrological Processes*, 2982(May):n/a–n/a. https://doi.org/10.1002/hyp.8144.

Langston, G., Hayashi, M., and Roy, J. W. (2013). Quantifying groundwater-surface water interactions in a proglacial moraine using heat and solute tracers. *Water Resources Research*, 49(9):5411–5426. https://doi.org/10.1002/wrcr.20372.

Lemieux, J.-M., Sudicky, E. A., Peltier, W. R., and Tarasov, L. (2008). Dynamics of groundwater recharge and seepage over the Canadian landscape during the Wisconsinian glaciation. *Journal of Geophysical Research*, 113(F1):F01011. https://doi.org/10.1029/2007JF000838.

Levy, A., Robinson, Z., Krause, S., Waller, R., and Weatherill, J. (2015). Long-term variability of proglacial groundwater-fed hydrological systems in an area of glacier retreat, Skeiðarársandur, Iceland. *Earth Surface Processes and Landforms*, 40(7):981–994. https://doi.org/10.1002/esp.3696.

Liljedahl, A. K., Gädeke, A., O'Neel, S., Gatesman, T. A., Douglas, T. A., and Liljedahl, A. K. (2017). Glacierized headwater streams as aquifer recharge corridors, subarctic Alaska. *Geophysical Research Letters*, 44(13): 6876–6885. https://doi.org/10.1002/2017gl073834.

Linsbauer, A., Huss, M., Hodel, E., Bauder, A., Fischer, M., Weidmann, Y., Bärtschi, H., and Schmassmann, E. (2021). The New Swiss Glacier Inventory SGI2016: From a Topographical to a Glaciological Dataset. *Frontiers in Earth Science*, 9(October):1–22. https://doi.org/10.3389/feart.2021.704189.

Liu, F., Williams, M. W., and Caine, N. (2004). Source waters and flow paths in an alpine catchment, Colorado Front Range, United States. *Water Resources Research*, 40(9):1–16. https://doi.org/10.1029/2004WR003076.

Lukas, S. (2012). Processes of annual moraine formation at a temperate alpine valley glacier: Insights into glacier dynamics and climatic controls. *Boreas*, 41(3):463–480. https://doi.org/10.1111/j.1502-3885.2011.00241.x.

Lukas, S. and Sass, O. (2011). The formation of alpine lateral moraines inferred from sedimentology and radar reflection patterns: A case study from Gornergletscher, Switzerland. *Geological Society Special Publication*, 354:77–92. https://doi.org/10.1144/SP354.5.

Lukas, S., Graf, A., Coray, S., and Schlüchter, C. (2012). Genesis, stability and preservation potential of large lateral moraines of Alpine valley glaciers – towards a unifying theory based on Findelengletscher, Switzerland. *Quaternary Science Reviews*, 38:27–48. https://doi.org/10.1016/j.quascirev.2012.01.022.

MacDonald, A. M., Maurice, L., Dobbs, M. R., Reeves, H. J., and Auton, C. A. (2012). Relating in situ hydraulic conductivity, particle size and relative density of superficial deposits in a heterogeneous catchment. *Journal of Hydrology*, 434-435:130–141. https://doi.org/10.1016/j.jhydrol.2012.01.018.

Macdonald, A. M., Black, A. R., Ó Dochartaigh, B. E., Everest, J., Darling, W. G., Flett, V., and Peach, D. W. (2016). Using stable isotopes and continuous meltwater river monitoring to investigate the hydrology of a rapidly retreating Icelandic outlet glacier. *Annals of Glaciology*, 57(72):151–158. https://doi.org/10.1017/aog.2016.22.

Mackay, J. D., Barrand, N. E., Hannah, D. M., Krause, S., Jackson, C. R., Everest, J., MacDonald, A. M., and Ó Dochartaigh, B. (2020). Proglacial groundwater storage dynamics under climate change and glacier retreat. *Hydrological Processes*, 34(26):5456–5473. https://doi.org/10.1002/hyp.13961.

Magnusson, J., Jonas, T., and Kirchner, J. W. (2012). Temperature dynamics of a proglacial stream: Identifying dominant energy balance components and inferring spatially integrated hydraulic geometry. *Water Resources Research*, 48(6):1–16. https://doi.org/10.1029/2011WR011378.

Magnusson, J., Kobierska, F., Huxol, S., Hayashi, M., Jonas, T., and Kirchner, J. W. (2014). Melt water driven stream and groundwater stage fluctuations on a glacier forefield (Dammagletscher, Switzerland). *Hydrological Processes*, 28(3):823–836. https://doi.org/10.1002/hyp.9633.

Maier, F., van Meerveld, I., Greinwald, K., Gebauer, T., Lustenberger, F., Hartmann, A., and Musso, A. (2020). Effects of soil and vegetation development on surface hydrological properties of moraines in the Swiss Alps. *Catena*, 187(December 2019):104353. https://doi.org/10.1016/j.catena.2019.104353.

Maier, F., van Meerveld, I., Meerveld, I., Weiler, M., van Meerveld, I., Meerveld, I., and Weiler, M. (2021). Long-Term Changes in Runoff Generation Mechanisms for Two Proglacial Areas in the Swiss Alps I: Overland Flow. *Water Resources Research*, 57(12):1–30. https://doi.org/10.1029/2021WR030221.

Maisch, M., Haeberli, W., Hoelzle, M., and Wenzel, J. (1999). Occurrence of rocky and sedimentary glacier beds in the Swiss Alps as estimated from glacier-inventory data. *Annals of Glaciology*, 28:231–235. https://doi.org/10.3189/172756499781821779.

Maizels, J. (2002). Sediments and landforms of modern proglacial terrestrial environments. In *Modern and Past Glacial Environments*, number 4, pages 279–316. Elsevier. https://doi.org/10.1016/B978-075064226-2/50012-X.

Maizels, J. K. (1977). Experiments on the Origin of Kettle-holes. *Journal of Glaciology*, 18(79):291–303. https://doi.org/10.3189/S0022143000021365.

Malard, F., Tockner, K., and Ward, J. V. (1999). Shifting dominance of subcatchment water sources and flow paths in a glacial floodplain, Val Roseg, Switzerland. *Arctic, Antarctic, and Alpine Research*, 31(2):135–150. https://doi.org/10.2307/1552602.

Mancini, D. and Lane, S. N. (2020). Changes in sediment connectivity following glacial debuttressing in an Alpine valley system. *Geomorphology*, 352:106987. https://doi.org/10.1016/j.geomorph.2019.106987.

Mancini, D., Dietze, M., Jenkin, M., Miesen, F. M., Müller, T., and Lane, S. N. (2021). Bedload export from an alpine glacier inferred from seismic methods. *EGU General Assembly 2021, online, 19–30 Apr 2021, EGU21-4000*. https://doi.org/https://doi.org/10.5194/egusphere-egu21-4000.

Mariethoz, G., Renard, P., and Straubhaar, J. (2010). The direct sampling method to perform multiple-point geostatistical simulations. *Water Resources Research*, 46(11):1–14. https://doi.org/10.1029/2008WR007621.

Marren, P. M. (2005). Magnitude and frequency in proglacial rivers: A geomorphological and sedimentological perspective. *Earth-Science Reviews*, 70(3-4):203–251. https://doi.org/10.1016/j.earscirev.2004.12.002.

Marsh, P. and Pomeroy, J. W. (1999). Spatial and temporal variations in snowmelt runoff chemistry, northwest territories, canada. *Water Resources Research*, 35:1559–1567. https://doi.org/10.1029/1998WR900109.

Marshall, S. J., Sharp, M. J., Burgess, D. O., and Anslow, F. S. (2007). Near-surface-temperature lapse rates on the prince of wales icefield, ellesmere island, canada: implications for regional downscaling of temperature. *International Journal of Climatology*, 27:385–398. https://doi.org/10.1002/joc.1396.

Masset, O. and Loew, S. (2010). Hydraulic conductivity distribution in crystalline rocks, derived from inflows to tunnels and galleries in the Central Alps, Switzerland. *Hydrogeology Journal*, 18(4):863–891. https://doi.org/10.1007/s10040-009-0569-1.

Maurya, A. S., Shah, M., Deshpande, R. D., Bhardwaj, R. M., Prasad, A., and Gupta, S. K. (2011). Hydrograph separation and precipitation source identification using stable water isotopes and conductivity: River ganga at himalayan foothills. *Hydrological Processes*, 25:1521–1530. https://doi.org/10.1002/hyp.7912.

Mavris, C., Egli, M., Plötze, M., Blum, J. D., Mirabella, A., Giaccai, D., and Haeberli, W. (2010). Initial stages of weathering and soil formation in the morteratsch proglacial area (upper engadine, switzerland). *Geoderma*, 155:359–371. https://doi.org/10.1016/j.geoderma.2009.12.019.

Mazurkiewicz, A. B., Callery, D. G., and McDonnell, J. J. (2008). Assessing the controls of the snow energy balance and water available for runoff in a rain-on-snow environment. *Journal of Hydrology*, 354:1–14. https://doi.org/10.1016/j.jhydrol.2007.12.027.

McClymont, A. F., Roy, J. W., Hayashi, M., Bentley, L. R., Maurer, H., and Langston, G. (2011). Investigating groundwater flow paths within proglacial moraine using multiple geophysical methods. *Journal of Hydrology*, 399(1-2):57–69. https://doi.org/10.1016/j.jhydrol.2010.12.036.

McGuire, K. J. and McDonnell, J. J. (2006). A review and evaluation of catchment transit time modeling. *Journal of Hydrology*, 330(3-4):543–563. https://doi.org/10.1016/j.jhydrol.2006.04.020.

McGuire, K. J., McDonnell, J. J., Weiler, M., Kendall, C., McGlynn, B. L., Welker, J. M., and Seibert, J. (2005). The role of topography on catchment-scale water residence time. *Water Resources Research*, 41(5):1–14. https://doi.org/10.1029/2004WR003657.

Miall, A. D. (1977). A review of the braided-river depositional environment. *Earth Science Reviews*, 13(1):1–62. https://doi.org/10.1016/0012-8252(77)90055-1.

Michelon, A., Ceperley, N., Beria, H., Larsen, J., Vennemann, T., and Schaefli, B. (2023). Hydrodynamics of a high alpine catchment characterized by four natural tracers. *Hydrology and Earth System Sciences*, 27(7):1403–1430. https://doi.org/10.5194/hess-27-1403-2023.

Miller, H. R. and Lane, S. N. (2018). Biogeomorphic feedbacks and the ecosystem engineering of recently deglaciated terrain. *Progress in Physical Geography*, 43(1):24–45. https://doi.org/10.1177/0309133318816536.

Milner, A. M., Brown, L. E., and Hannah, D. M. (2009). Hydroecological response of river systems to shrinking glaciers. *Hydrological Processes*, 23(1):62–77. https://doi.org/10.1002/hyp.7197.

Milner, A. M., Khamis, K., Battin, T. J., Brittain, J. E., Barrand, N. E., Füreder, L., Cauvy-Fraunié, S., Gíslason, G. M., Jacobsen, D., Hannah, D. M., Hodson, A. J., Hood, E., Lencioni, V., Ólafsson, J. S., Robinson, C. T., Tranter, M., and Brown, L. E. (2017). Glacier shrinkage driving global changes in downstream systems. *Proceedings of the National Academy of Sciences*, 114(37):9770–9778. https://doi.org/10.1073/pnas.1619807114.

Mitchell, A., Brown, G. H., and Fuge, R. (2001). Minor and trace element export from a glacierized alpine headwater catchment (haut glacier d'arolla, switzerland). *Hydrological Processes*, 15:3499–3524. https://doi.org/10.1002/hyp.1041.

Mitchell, A. C. and Brown, G. H. (2007). Diurnal hydrological - physicochemical controls and sampling methods for minor and trace elements in an Alpine glacial hydrological system. *Journal of Hydrology*, 332 (1-2):123–143. https://doi.org/10.1016/j.jhydrol.2006.06.026.

Mitchell, A. C., Brown, G. H., and Fuge, R. (2006). Minor and trace elements as indicators of solute provenance and flow routing in a subglacial hydrological system. *Hydrological Processes*, 20(4):877–897. https://doi.org/10.1002/hyp.6112.

Moeck, C., Popp, A. L., Brennwald, M. S., Kipfer, R., and Schirmer, M. (2021). Combined method of 3H/3He apparent age and on-site helium analysis to identify groundwater flow processes and transport of perchloroethylene (PCE) in an urban area. *Journal of Contaminant Hydrology*, 238(January):103773. https://doi.org/10.1016/j.jconhyd.2021.103773.

Muir, D. L., Hayashi, M., and McClymont, A. F. (2011). Hydrological storage and transmission characteristics of an alpine talus. *Hydrological Processes*, 25(19):n/a–n/a. https://doi.org/10.1002/hyp.8060.

Müller, T. (2022)a. Weather dataset from Otemma glacier forefield, Switzerland (from 14 July 2019 to 18 November 2021) (v1.2021.02). *Zenodo [Data set]*. https://doi.org/10.5281/zenodo.6106778.

Müller, T. (2022)b. Water table elevation and groundwater temperature from the outwash plain of the Otemma glacier forefield (Switzerland) from 2019 to 2021 (v1.2022.03). *Zenodo [Data set]*. https://doi.org/10.5281/zenodo.6355474.

Müller, T. (2022)c. Electrical Resistivity Tomography (ERT) datasets from the Otemma glacier forefield and outwash plain (v1.2022.03). *Zenodo [Data set]*. https://doi.org/10.5281/zenodo.6342767.

Müller, T. (2023). Water stable isotope, temperature and electrical conductivity dataset (snow, ice, rain, surface water, groundwater) from a high alpine catchment (2019-2021). (v1.2023.01). *Zenodo [Data set]*. https://doi.org/10.5281/zenodo.7529792.

Müller, T. and Miesen, F. (2022). Stream discharge, stage, electrical conductivity & temperature dataset from Otemma glacier forefield, Switzerland (from July 2019 to October 2021) (v1.2021.02). *Zenodo [Data set]*. https://doi.org/10.5281/zenodo.6202732.

Müller, T., Roncoroni, M., Mancini, D., Lane, S. N., and Schaefli, B. (2023). Current and future role of meltwater-groundwater dynamics in a proglacial alpine outwash plain. *EGUsphere*, 2023:1–34. https://doi.org/10.5194/egusphere-2022-1503.

Müller, T., Lane, S. N., and Schaefli, B. (2022)a. Towards a hydrogeomorphological understanding of proglacial catchments: an assessment of groundwater storage and release in an alpine catchment. *Hydrology and Earth System Sciences*, 26:6029–6054. https://doi.org/10.5194/hess-26-6029-2022.

Müller, T., Schaefli, B., and Lane, S. N. (2022)b. A simple low-cost arduino based lorawan automatic weather station, egu general assembly 2022, vienna, austria, 23–27 may 2022, egu22-940. https://doi.org/10.5194/egusphere-egu22-940.

Nan, Y., He, Z., Tian, F., Wei, Z., and Tian, L. (2022). Assessing the influence of water sampling strategy on the performance of tracer-aided hydrological modeling in a mountainous basin on the tibetan plateau. *Hydrology and Earth System Sciences*, 26:4147–4167. https://doi.org/10.5194/hess-26-4147-2022.

Nie, Y., Liu, Q., Wang, J., Zhang, Y., Sheng, Y., and Liu, S. (2018). An inventory of historical glacial lake outburst floods in the Himalayas based on remote sensing observations and geomorphological analysis. *Geomorphology*, 308:91–106. https://doi.org/10.1016/j.geomorph.2018.02.002.

Nie, Y., Pritchard, H. D., Liu, Q., Hennig, T., Wang, W., Wang, X., Liu, S., Nepal, S., Samyn, D., Hewitt, K., and Chen, X. (2021). Glacial change and hydrological implications in the himalaya and karakoram. *Nature Reviews Earth and Environment*, 2:91–106. https://doi.org/10.1038/s43017-020-00124-w.

Nienow, P., Sharp, M., and Willis, I. (1998). Seasonal changes in the morphology of the subglacial drainage system, haut glacier d'arolla, switzerland. *Earth Surface Processes and Landforms*, 23:825–843. https://doi.org/10.1002/(SICI)1096-9837(199809)23:9<825::AID-ESP893>3.0.CO;2-2.

Ó Dochartaigh, B. É., MacDonald, A. M., Black, A. R., Everest, J., Wilson, P., Darling, W. G., Jones, L., and Raines, M. (2019). Groundwater–glacier meltwater interaction in proglacial aquifers. *Hydrology and Earth System Sciences*, 23(11):4527–4539. https://doi.org/10.5194/hess-23-4527-2019.

Oestreicher, N., Loew, S., Roques, C., Aaron, J., Gualandi, A., Longuevergne, L., Limpach, P., and Hugentobler, M. (2021). Controls on Spatial and Temporal Patterns of Slope Deformation in an Alpine Valley. *Journal of Geophysical Research: Earth Surface*, 126(12). https://doi.org/10.1029/2021JF006353.

Orsi, G., Burger, U., Marschallinger, R., and Nocker, C. (2016). Geological model of an alpine lateral valley with implications for the design of a groundwater monitoring network – the example of the padaster valley (Eastern Alps, Austria). *Austrian Journal of Earth Sciences*, 109(1). https://doi.org/10.17738/ajes.2016.0003.

Otto, J.-C. (2019). Proglacial Lakes in High Mountain Environments. In Heckmann, T. and Morche, D., editors, *Geomorphology of Proglacial Systems. Geography of the Physical Environment.*, pages 231–247. Springer, Cham. ISBN 978-3-319-94184-4. https://doi.org/10.1007/978-3-319-94184-4_14.

Otto, J.-C., Schrott, L., Jaboyedoff, M., and Dikau, R. (2009). Quantifying sediment storage in a high alpine valley (Turtmanntal, Switzerland). *Earth Surface Processes and Landforms*, 34(13):1726–1742. https://doi.org/10.1002/esp.1856.

Park, Y., Reichel, L., Rodriguez, G., and Yu, X. (2018). Parameter determination for tikhonov regularization problems in general form. *Journal of Computational and Applied Mathematics*, 343:12–25. https://doi.org/10.1016/j.cam.2018.04.049.

Parriaux, A. and Nicoud, G. (1990). Hydrological behaviour of glacial deposits in mountainous areas. *IAHS Publication 190*, 1(190):291—-312.

Penna, D., Engel, M., Mao, L., Dell'agnese, A., Bertoldi, G., and Comiti, F. (2014). Tracer-based analysis of spatial and temporal variations of water sources in a glacierized catchment. *Hydrology and Earth System Sciences*, 18(12):5271–5288. https://doi.org/10.5194/hess-18-5271-2014.

Penna, D., Engel, M., Bertoldi, G., and Comiti, F. (2017). Towards a tracer-based conceptualization of meltwater dynamics and streamflow response in a glacierized catchment. *Hydrology and Earth System Sciences*, 21(1):23–41. https://doi.org/10.5194/hess-21-23-2017.

Perolo, P., Bakker, M., Gabbud, C., Moradi, G., Rennie, C., and Lane, S. N. (2019). Subglacial sediment production and snout marginal ice uplift during the late ablation season of a temperate valley glacier. *Earth Surface Processes and Landforms*, 44(5):1117–1136. https://doi.org/10.1002/esp.4562.

Pfeffer, W. T., Arendt, A. A., Bliss, A., Bolch, T., Cogley, J. G., Gardner, A. S., Hagen, J. O., Hock, R., Kaser, G., Kienholz, C., Miles, E. S., Moholdt, G., Mölg, N., Paul, F., Radić, V., Rastner, P., Raup, B. H., Rich, J., Sharp, M. J., Andreassen, L. M., Bajracharya, S., Barrand, N. E., Beedle, M. J., Berthier, E., Bhambri, R., Brown, I., Burgess, D. O., Burgess, E. W., Cawkwell, F., Chinn, T., Copland, L., Cullen, N. J., Davies, B., De Angelis, H., Fountain, A. G., Frey, H., Giffen, B. A., Glasser, N. F., Gurney, S. D., Hagg, W., Hall, D. K., Haritashya, U. K., Hartmann, G., Herreid, S., Howat, I., Jiskoot, H., Khromova, T. E., Klein, A., Kohler, J., König, M., Kriegel, D., Kutuzov, S., Lavrentiev, I., Le Bris, R., Li, X., Manley, W. F., Mayer, C., Menounos, B., Mercer, A., Mool, P., Negrete, A., Nosenko, G., Nuth, C., Osmonov, A., Pettersson, R., Racoviteanu, A., Ranzi, R., Sarikaya, M. A., Schneider, C., Sigurdsson, O., Sirguey, P., Stokes, C. R., Wheate, R., Wolken, G. J., Wu, L. Z., and Wyatt, F. R. (2014). The randolph glacier inventory: A globally complete inventory of glaciers. *Journal of Glaciology*, 60(221):537–552. https://doi.org/10.3189/2014JoG13J176.

Phillips, J. V. and Tadayon, S. (2006). *Selection of Manning's roughness coefficient for natural and constructed vegetated and non-vegetated channels, and vegetation maintenance plan guidelines for vegetated channels in central Arizona.* US Geological Survey.

Planet Team. Planet Application Program Interface: In Space for Life on Earth, (2017).

Pomeroy, J. W., Fang, X., and Marks, D. G. (2016). The cold rain-on-snow event of june 2013 in the canadian rockies - characteristics and diagnosis. *Hydrological Processes*, 30:2899–2914. https://doi.org/10.1002/hyp.10905.

Popp, A. L., Scheidegger, A., Moeck, C., Brennwald, M. S., and Kipfer, R. (2019). Integrating Bayesian Groundwater Mixing Modeling With On-Site Helium Analysis to Identify Unknown Water Sources. *Water Resources Research*, 55(12):10602–10615. https://doi.org/10.1029/2019WR025677.

Popp, A. L., Manning, C. C., and Knapp, J. L. (2021)a. Rapid Advances in Mobile Mass Spectrometry Enhance Tracer Hydrology and Water Management. *Water Resources Research*, 57(6). https://doi.org/10.1029/2021WR029890.

Popp, A. L., Pardo-Álvarez, Á., Schilling, O. S., Scheidegger, A., Musy, S., Peel, M., Brunner, P., Purtschert, R., Hunkeler, D., and Kipfer, R. (2021)b. A Framework for Untangling Transient Groundwater Mixing and Travel Times. *Water Resources Research*, 57(4):1–16. https://doi.org/10.1029/2020WR028362.

Pritchard, H. D. (2019). Asia's shrinking glaciers protect large populations from drought stress. *Nature*, 569:649–654. https://doi.org/10.1038/s41586-019-1240-1.

Robinson, Z. P., Fairchild, I. J., and Russell, A. J. (2008). Hydrogeological implications of glacial landscape evolution at Skeiðarársandur, SE Iceland. *Geomorphology*, 97(1-2):218–236. https://doi.org/10.1016/j.geomorph.2007.02.044.

Rogger, M., Chirico, G. B., Hausmann, H., Krainer, K., Brückl, E., Stadler, P., and Blöschl, G. (2017). Impact of mountain permafrost on flow path and runoff response in a high alpine catchment. *Water Resources Research*, 53(2):1288–1308. https://doi.org/10.1002/2016WR019341.

Rolland, C. (2003). Spatial and seasonal variations of air temperature lapse rates in alpine regions. *Journal of Climate*, 16:1032–1046. https://doi.org/10.1175/1520-0442(2003)016<1032:SASVOA>2.0.CO;2.

Roncoroni, M., Brandani, J., Battin, T. I., and Lane, S. N. (2019). Ecosystem engineers: Biofilms and the ontogeny of glacier floodplain ecosystems. *Wiley Interdisciplinary Reviews: Water*, 6(6):e1390. https://doi.org/10.1002/wat2.1390.

Roncoroni, M., Mancini, D., Kohler, T. J., Miesen, F., Gianini, M., Battin, T. J., and N. Lane, S. (2022). Centimeter-scale mapping of phototrophic biofilms in glacial forefields using visible band ratios and UAV imagery. *International Journal of Remote Sensing*, 00(00):1–35. https://doi.org/10.1080/01431161.2022.2079963.

Roncoroni, M., Mancini, D., Miesen, F., Müller, T., Gianini, M., Ouvry, B., Clémençon, M., Lardet, F., Battin, T. J., and Lane, S. N. (2023). Decrypting the stream periphyton physical habitat of recently deglaciated floodplains. *Science of The Total Environment*, 867:161374. https://doi.org/10.1016/j.scitotenv.2022.161374.

Roques, C., Rupp, D. E., de Dreuzy, J.-R., Longuevergne, L., Jachens, E. R., Grant, G., Aquilina, L., and Selker, J. S. (2022). Recession discharge from compartmentalized bedrock hillslopes. *Hydrology and Earth System Sciences*, 26:4391–4405. https://doi.org/10.5194/hess-26-4391-2022.

Rücker, C., Günther, T., and Wagner, F. M. (2017). pyGIMLi: An open-source library for modelling and inversion in geophysics. *Computers & Geosciences*, 109(August):106–123. https://doi.org/10.1016/j.cageo.2017.07.011.

Rupp, D. E. and Selker, J. S. (2005). Drainage of a horizontal Boussinesq aquifer with a power law hydraulic conductivity profile. *Water Resources Research*, 41(11):1–8. https://doi.org/10.1029/2005WR004241.

Rupp, D. E. and Selker, J. S. (2006). On the use of the Boussinesq equation for interpreting recession hydrographs from sloping aquifers. *Water Resources Research*, 42(12):1–15. https://doi.org/10.1029/2006WR005080.

Rücker, A., Boss, S., Kirchner, J. W., and Freyberg, J. V. (2019)a. Monitoring snowpack outflow volumes and their isotopic composition to better understand streamflow generation during rain-on-snow events. *Hydrology and Earth System Sciences*, 23:2983–3005. https://doi.org/10.5194/hess-23-2983-2019.

Rücker, A., Zappa, M., Boss, S., and von Freyberg, J. (2019)b. An optimized snowmelt lysimeter system for monitoring melt rates and collecting samples for stable water isotope analysis. *Journal of Hydrology and Hydromechanics*, 67:20–31. https://doi.org/10.2478/johh-2018-0007.

Saberi, L., McLaughlin, R. T., Crystal Ng, G. H., La Frenierre, J., Wickert, A. D., Baraer, M., Zhi, W., Li, L., and Mark, B. G. (2019). Multi-scale temporal variability in meltwater contributions in a tropical glacierized watershed. *Hydrology and Earth System Sciences*, 23(1):405–425. https://doi.org/10.5194/hess-23-405-2019.

Santos, A. C., Portela, M. M., Rinaldo, A., and Schaefli, B. (2018). Analytical flow duration curves for summer streamflow in Switzerland. *Hydrology and Earth System Sciences*, 22(4):2377–2389. https://doi.org/10.5194/hess-22-2377-2018.

Sass, O. (2006). Determination of the internal structure of alpine talus deposits using different geophysical methods (Lechtaler Alps, Austria). *Geomorphology*, 80(1-2):45–58. https://doi.org/10.1016/j.geomorph.2005.09.006.

Sass, O. (2007). Bedrock detection and talus thickness assessment in the European Alps using geophysical methods. *Journal of Applied Geophysics*, 62(3):254–269. https://doi.org/10.1016/j.jappgeo.2006.12.003.

Sayama, T., McDonnell, J. J., Dhakal, A., and Sullivan, K. (2011). How much water can a watershed store? *Hydrological Processes*, 25(25):3899–3908. https://doi.org/10.1002/hyp.8288.

Schaefli, B., Hingray, B., Niggli, M., and Musy, A. (2005). A conceptual glacio-hydrological model for high mountainous catchments. *Hydrology and Earth System Sciences*, 9:95–109. https://doi.org/10.5194/hess-9-95-2005.

Schaefli, B., Harman, C. J., Sivapalan, M., and Schymanski, S. J. (2011). HESS Opinions: Hydrologic predictions in a changing environment: Behavioral modeling. *Hydrology and Earth System Sciences*, 15(2):635–646. https://doi.org/10.5194/hess-15-635-2011.

Schaefli, B., Nicótina, L., Imfeld, C., Da Ronco, P., Bertuzzo, E., and Rinaldo, A. (2014). SEHR-ECHO v1.0: A spatially explicit hydrologic response model for ecohydrologic applications. *Geoscientific Model Development*, 7(6):2733–2746. https://doi.org/10.5194/gmd-7-2733-2014.

Schaefli, B., Manso, P., Fischer, M., Huss, M., and Farinotti, D. (2019). The role of glacier retreat for Swiss hydropower production. *Renewable Energy*, 132:615–627. https://doi.org/10.1016/j.renene.2018.07.104.

Schilling, O. S., Gerber, C., Partington, D. J., Purtschert, R., Brennwald, M. S., Kipfer, R., Hunkeler, D., and Brunner, P. (2017). Advancing Physically-Based Flow Simulations of Alluvial Systems Through Atmospheric Noble Gases and the Novel 37 Ar Tracer Method. *Water Resources Research*, 53(12):10465–10490. https://doi.org/10.1002/2017WR020754.

Schilling, O. S., Parajuli, A., Tremblay Otis, C., Müller, T. U., Antolinez Quijano, W., Tremblay, Y., Brennwald, M. S., Nadeau, D. F., Jutras, S., Kipfer, R., and Therrien, R. (2021). Quantifying Groundwater Recharge Dynamics and Unsaturated Zone Processes in Snow-Dominated Catchments via On-Site Dissolved Gas Analysis. *Water Resources Research*, 57(2):1–24. https://doi.org/10.1029/2020WR028479.

Schmieder, J., Hanzer, F., Marke, T., Garvelmann, J., Warscher, M., Kunstmann, H., and Strasser, U. (2016). The importance of snowmelt spatiotemporal variability for isotope-based hydrograph separation in a high-elevation catchment. *Hydrology and Earth System Sciences*, 20(12):5015–5033. https://doi.org/10.5194/hess-20-5015-2016.

Schmieder, J., Garvelmann, J., Marke, T., and Strasser, U. (2018). Spatio-temporal tracer variability in the glacier melt end-member - How does it affect hydrograph separation results? *Hydrological Processes*, 32 (12):1828–1843. https://doi.org/10.1002/hyp.11628.

Schmieder, J., Seeger, S., Weiler, M., and Strasser, U. (2019). 'Teflon Basin' or Not? A High-Elevation Catchment Transit Time Modeling Approach. *Hydrology*, 6(4):92. https://doi.org/10.3390/hydrology6040092.

Schäppi, B. *Measurement and analysis of rainfall gradients along a hillslope transect in the Swiss Alps*. Doctoral thesis, ETH Zurich, Zürich, (2013).

Sharp, M., Brown, G. H., Tranter, M., Willis, I. C., and Hubbard, B. (1995). Comments on the use of chemically based mixing models in glacier hydrology. *Journal of Glaciology*, 41(138):241–246. https://doi.org/10.1017/S0022143000016142.

Shokory, J. A. N., Schaefli, B., and Lane, S. N. (2023). Water resources of afghanistan and related hazards under rapid climate warming: a review. *Hydrological Sciences Journal*, pages 1–19. https://doi.org/10.1080/02626667.2022.2159411.

Shukla, T., Sundriyal, S., Stachnik, L., and Mehta, M. (2018). Carbonate and silicate weathering in glacial environments and its relation to atmospheric co ₂ cycling in the himalaya. *Annals of Glaciology*, 59:159–170. https://doi.org/10.1017/aog.2019.5.

Singh, P., Spitzbart, G., Hübl, H., and Weinmeister, H. (1997). Hydrological response of snowpack under rain-on-snow events: a field study. *Journal of Hydrology*, 202:1–20. https://doi.org/10.1016/S0022-1694(97)00004-8.

Somers, L. D., Gordon, R. P., McKenzie, J. M., Lautz, L. K., Wigmore, O., Glose, A. M., Glas, R., Aubry-Wake, C., Mark, B., Baraer, M., and Condom, T. (2016). Quantifying groundwater–surface water interactions in a proglacial valley, Cordillera Blanca, Peru. *Hydrological Processes*, 30(17):2915–2929. https://doi.org/10.1002/hyp.10912.

Staudinger, M., Stoelzle, M., Seeger, S., Seibert, J., Weiler, M., and Stahl, K. (2017). Catchment water storage variation with elevation. *Hydrological Processes*, 31(11):2000–2015. https://doi.org/10.1002/hyp.11158.

Stewart, M. K. (2015). Promising new baseflow separation and recession analysis methods applied to streamflow at Glendhu Catchment, New Zealand. *Hydrology and Earth System Sciences*, 19(6):2587–2603. https://doi.org/10.5194/hess-19-2587-2015.

Stigter, E. E., Litt, M., Steiner, J. F., Bonekamp, P. N., Shea, J. M., Bierkens, M. F., and Immerzeel, W. W. (2018). The importance of snow sublimation on a himalayan glacier. *Frontiers in Earth Science*, 6. https://doi.org/10.3389/feart.2018.00108.

Strasser, U., Bernhardt, M., Weber, M., Liston, G. E., and Mauser, W. (2008). Is snow sublimation important in the alpine water balance? *The Cryosphere*, 2:53–66. https://doi.org/10.5194/tc-2-53-2008.

Swift, D. A., Nienow, P. W., Hoey, T. B., and Mair, D. W. F. (2005). Seasonal evolution of runoff from Haut Glacier d'Arolla, Switzerland and implications for glacial geomorphic processes. *Journal of Hydrology*, 309(1-4):133–148. https://doi.org/10.1016/j.jhydrol.2004.11.016.

SwissTopo. (2019). swissALTI3D - The high precision digital elevation model of Switzerland. Federal Office of Topography (swisstopo). Available at https://www.swisstopo.admin.ch/en/geodata/height/alti3d.html (last accessed 11 May 2021).

SwissTopo. (2020)a. SWISSIMAGE 10 cm - The Digital Color Orthophotomosaic of Switzerland. Federal Office of Topography (swisstopo). Available at https://www.swisstopo.admin.ch/en/geodata/images/ortho/swissimage10.html (last accessed 30 March 2021).

SwissTopo. (2020)b. Swiss Map Vector 1000. Federal Office of Topography (swisstopo). Available at https://www.swisstopo.admin.ch/en/geodata/maps/smv/smv1000.html (last accessed 03 January 2023).

Tassaux, A. Incipient pedogenesis and weathering processes in the context of alpine retreating glaciers. Mater thesis, University of Lausanne, Lausanne, (2022).

Taylor, S., Feng, X., Kirchner, J. W., Osterhuber, R., Klaue, B., and Renshaw, C. E. (2001). Isotopic evolution of a seasonal snowpack and its melt. *Water Resources Research*, 37(3):759–769. https://doi.org/10.1029/2000WR900341.

Temme, A. J. A. M. (2019). *The Uncalm Development of Proglacial Soils in the European Alps Since 1850*, pages 315–326. Springer, Cham. ISBN 978-3-319-94184-4. https://doi.org/10.1007/978-3-319-94184-4_18.

Tockner, K., Malard, F., Uehlinger, U., and Ward, J. V. (2002). Nutrients and organic matter in a glacial river-floodplain system (val roseg, switzerland). *Limnology and Oceanography*, 47:266–277. https://doi.org/10.4319/lo.2002.47.1.0266.

Troch, P. A., Berne, A., Bogaart, P., Harman, C., Hilberts, A. G., Lyon, S. W., Paniconi, C., Pauwels, V. R., Rupp, D. E., Selker, J. S., Teuling, A. J., Uijlenhoet, R., and Verhoest, N. E. (2013). The importance of hydraulic groundwater theory in catchment hydrology: The legacy of Wilfried Brutsaert and Jean-Yves Parlange. *Water Resources Research*, 49(9):5099–5116. https://doi.org/10.1002/wrcr.20407.

Tromp-Van Meerveld, H. J. and McDonnell, J. J. (2006). Threshold relations in subsurface stormflow: 2. The fill and spill hypothesis. *Water Resources Research*, 42(2):1–11. https://doi.org/10.1029/2004WR003800.

Uehlinger, U., Robinson, C. T., Hieber, M., and Zah, R. (2010). The physico-chemical habitat template for periphyton in alpine glacial streams under a changing climate. *Hydrobiologia*, 657(1):107–121. https://doi.org/10.1007/s10750-009-9963-x.

van Tiel, M., Kohn, I., Van Loon, A. F., and Stahl, K. (2020)a. The compensating effect of glaciers: Characterizing the relation between interannual streamflow variability and glacier cover. *Hydrological Processes*, 34(3):553–568. https://doi.org/10.1002/hyp.13603.

van Tiel, M., Stahl, K., Freudiger, D., and Seibert, J. (2020)b. Glacio-hydrological model calibration and evaluation. *WIREs Water*, 7(6):e1483. https://doi.org/https://doi.org/10.1002/wat2.1483.

Van Tiel, M., Van Loon, A. F., Seibert, J., and Stahl, K. (2021). Hydrological response to warm and dry weather: do glaciers compensate? *Hydrology and Earth System Sciences*, 25(6):3245–3265. https://doi.org/10.5194/hess-25-3245-2021.

Verhoest, N. E. C. and Troch, P. A. (2000). Some analytical solutions of the linearized Boussinesq equation with recharge for a sloping aquifer. *Water Resources Research*, 36(3):793–800. https://doi.org/10.1029/1999WR900317.

Vincent, A., Violette, S., and Aðalgeirsdóttir, G. (2019). Groundwater in catchments headed by temperate glaciers: A review. *Earth-Science Reviews*, 188(June 2018):59–76. https://doi.org/10.1016/j.earscirev.2018.10.017.

Viviroli, D., Dürr, H. H., Messerli, B., Meybeck, M., and Weingartner, R. (2007). Mountains of the world, water towers for humanity: Typology, mapping, and global significance. *Water Resources Research*, 43(7):1–13. https://doi.org/10.1029/2006WR005653.

Viviroli, D., Kummu, M., Meybeck, M., Kallio, M., and Wada, Y. (2020). Increasing dependence of lowland populations on mountain water resources. *Nature Sustainability*, 3(11):917–928. https://doi.org/10.1038/s41893-020-0559-9.

von Freyberg, J., Knapp, J. L. A., Rücker, A., Studer, B., and Kirchner, J. W. (2020). Technical note: Evaluation of a low-cost evaporation protection method for portable water samplers. *Hydrology and Earth System Sciences*, 24:5821–5834. https://doi.org/10.5194/hess-24-5821-2020.

Vuille, M., Carey, M., Huggel, C., Buytaert, W., Rabatel, A., Jacobsen, D., Soruco, A., Villacis, M., Yarleque, C., Elison Timm, O., Condom, T., Salzmann, N., and Sicart, J. E. (2018). Rapid decline of snow and ice in the tropical Andes – Impacts, uncertainties and challenges ahead. *Earth-Science Reviews*, 176(May 2017):195–213. https://doi.org/10.1016/j.earscirev.2017.09.019.

Wagener, T., Sivapalan, M., Troch, P., and Woods, R. (2007). Catchment Classification and Hydrologic Similarity. *Geography Compass*, 1(4):901–931. https://doi.org/10.1111/j.1749-8198.2007.00039.x.

Wagner, T., Kainz, S., Helfricht, K., Fischer, A., Avian, M., Krainer, K., and Winkler, G. (2021). Assessment of liquid and solid water storage in rock glaciers versus glacier ice in the Austrian Alps. *Science of The Total Environment*, 800:149593. https://doi.org/10.1016/j.scitotenv.2021.149593.

Ward, J. V., Malard, F., Tockner, K., and Uehlinger, U. (1999). Influence of ground water on surface water conditions in a glacial flood plain of the Swiss Alps. *Hydrological Processes*, 13(3):277–293. https://doi.org/10.1002/(SICI)1099-1085(19990228)13:3<277::AID-HYP738>3.0.CO;2-N.

Werder, M. A., Hewitt, I. J., Schoof, C. G., and Flowers, G. E. (2013). Modeling channelized and distributed subglacial drainage in two dimensions. *Journal of Geophysical Research: Earth Surface*, 118(4):2140–2158. https://doi.org/10.1002/jgrf.20146.

Wijngaard, R. R., Biemans, H., Lutz, A. F., Shrestha, A. B., Wester, P., and Immerzeel, W. W. (2018). Climate change vs. socio-economic development: Understanding the future south asian water gap. *Hydrology and Earth System Sciences*, 22:6297–6321. https://doi.org/10.5194/hess-22-6297-2018.

Williams, M. W., Hood, E., Molotch, N. P., Caine, N., Cowie, R., and Liu, F. (2015). The 'teflon basin' myth: hydrology and hydrochemistry of a seasonally snow-covered catchment. *Plant Ecology & Diversity*, 8(5-6):639–661. https://doi.org/10.1080/17550874.2015.1123318.

Windsor, F. M., Grocott, M. T., and Milner, A. M. (2017). An inter-catchment assessment of macroinvertebrate communities across groundwater-fed streams within Denali National Park, interior Alaska. *Hydrobiologia*, 785(1):373–384. https://doi.org/10.1007/s10750-016-2944-y.

Winkler, G., Wagner, T., Pauritsch, M., Birk, S., Kellerer-Pirklbauer, A., Benischke, R., Leis, A., Morawetz, R., Schreilechner, M. G., and Hergarten, S. (2016). Identification and assessment of groundwater flow and storage components of the relict Schöneben Rock Glacier, Niedere Tauern Range, Eastern Alps (Austria). *Hydrogeology Journal*, 24(4):937–953. https://doi.org/10.1007/s10040-015-1348-9.

Wittenberg, H. and Sivapalan, M. (1999). Watershed groundwater balance estimation using streamflow recession analysis and baseflow separation. *Journal of Hydrology*, 219(1-2):20–33. https://doi.org/10.1016/S0022-1694(99)00040-2.

WPA. (2022). 814.20 Federal Act of 24 January 1991 on the Protection of Waters (Waters Protection Act, WPA). Available at https://www.fedlex.admin.ch/eli/cc/1992/1860_1860_1860/en (last accessed 21 December 2022).

Yao, Y., Zheng, C., Andrews, C. B., Scanlon, B. R., Kuang, X., Zeng, Z., Jeong, S. J., Lancia, M., Wu, Y., and Li, G. (2021). Role of Groundwater in Sustaining Northern Himalayan Rivers. *Geophysical Research Letters*, 48(10):1–10. https://doi.org/10.1029/2020GL092354.

You, J., Qin, X., Ranjitkar, S., Lougheed, S. C., Wang, M., Zhou, W., Ouyang, D., Zhou, Y., Xu, J., Zhang, W., Wang, Y., Yang, J., and Song, Z. (2018). Response to climate change of montane herbaceous plants in the genus rhodiola predicted by ecological niche modelling. *Scientific Reports*, 8:5879. https://doi.org/10.1038/s41598-018-24360-9.

Zekollari, H., Huss, M., and Farinotti, D. (2019). Modelling the future evolution of glaciers in the european alps under the euro-cordex rcm ensemble. *The Cryosphere*, 13:1125–1146. https://doi.org/10.5194/tc-13-1125-2019.

Zielinski, T. and Van Loon, A. (2003). Pleistocene sandur deposits represent braidplains, not alluvial fans. *Boreas*, 32(4):590–611. https://doi.org/10.1080/03009480310004170.

Zuecco, G., Carturan, L., De Blasi, F., Seppi, R., Zanoner, T., Penna, D., Borga, M., Carton, A., and Dalla Fontana, G. (2019). Understanding hydrological processes in glacierized catchments: Evidence and implications of highly variable isotopic and electrical conductivity data. *Hydrological Processes*, 33(5):816–832. https://doi.org/10.1002/hyp.13366.

Łukasz Stachnik, Yde, J. C., Krzemień, K., Łukasz Uzarowicz, Sitek, S., and Kenis, P. (2022). Sem-eds and water chemistry characteristics at the early stages of glacier recession reveal biogeochemical coupling between proglacial sediments and meltwater. *Science of The Total Environment*, 835:155383. https://doi.org/10.1016/j.scitotenv.2022.155383.